



THE EFFECTS OF TRAVELING IONOSPHERIC DISTURBANCES ON SUPERDARN NEAR RANGE ECHOES

by

**Alicreance HIYADUTUJE
(218087701)**

**A thesis submitted in fulfillment of the
academic requirements for the degree of Doctor of Philosophy (Space Physics)**

School of Chemistry and Physics

College of Agriculture, Engineering and Science

**University of KwaZulu Natal
Westville SOUTH AFRICA**

May 2022

Preface

The work described in this thesis was carried out in the School of Chemistry and Physics, University of KwaZulu Natal, under the supervision of Prof. Michael J. Kosch and Dr Judy A.E. Stephenson.



Signed.....
Alicreance HIYADUTUJE (Author)

Date. 22 August 2022

As the candidate's Supervisor I agree to the submission of this thesis.



Signed.....
Prof. Michael J. Kosch (Supervisor)

Date. 22/08/2022



Signed....
Dr A.E. Judy Stephenson (Co-supervisor)

Date. 24/08/2022

Declaration - PLAGIARISM

I, Alicreance HIYADUTUJE, declare that:

1. The research reported in this thesis, except where otherwise indicated, is my original research.
2. This thesis has not been submitted for any degree or examination at any other university.
3. This thesis does not contain other persons' data, pictures, graphs or other information, unless specifically acknowledged as being sourced from other persons.
4. This thesis does not contain other persons' writing, unless specifically acknowledged as being sourced from other researchers. Where other written sources have been quoted, then: a. Their words have been re-written but the general information attributed to them has been referenced b. Where their exact words have been used, then their writing has been placed in italics and inside quotation marks, and referenced.
5. This thesis does not contain text, graphics or tables copied and pasted from the Internet, unless specifically acknowledged, and the source being detailed in the thesis and in the References section.

Signed:



PUBLICATION from this thesis

DETAILS OF CONTRIBUTION TO PUBLICATIONS that form part and/or include research presented in this thesis (include publications in preparation, submitted, in press and published and give details of the contributions of each author to the experimental work and writing of each publication).

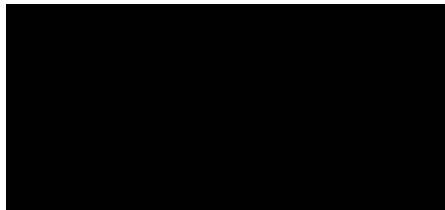
Data collection and analysis was done by Alicreance HIYADUTUJE (first author). Guidance, ideas and suggestions were given by Prof. Michael J. Kosch (second author) and Dr. Judy A.E. Stephenson (third author) in the preparation of the following manuscript.

Publication:

- First observations of *E*-region Near Range Echoes partially modulated by *F*-region Traveling Ionospheric Disturbances observed by the same SuperDARN HF radar “published by Journal of Geophysical Research (JGR)”

Authors: Alicreance HIYADUTUJE^{1,2}, Michael J. Kosch^{1,2,3,4}, Judy A.E. Stephenson²

1. South African National Space Agency, Hermanus, South Africa
2. Department of Chemistry and Physics, University of KwaZulu Natal, Durban, South Africa
3. Department of Physics and Astronomy, University of the Western Cape, Cape Town, South Africa
4. Department of Physics, University of Lancaster, UK



Signed:

Acknowledgement

I would like to express my most profound appreciation to my supervisors Prof. Michael Kosch and Dr. Judy Stephenson, for their valuable support and guidance throughout this project. I am especially grateful to the staff of the National Astrophysics and Space Science Programme (NASSP) for the scholarship awarded to me for my honours and masters studies. I am happy to thank the South African National Space Agency (SANSA) and the South African National Antarctic Programme (SANAP) for the scholarship awarded to me. Without this scholarship, this research would not have been accomplished. I would like to thank the management of the South African National Space Agency (SANSA) for financial assistance and support during my period of study.

I am grateful to the University of KwaZulu Natal for both academic and financial support. Many thanks to Dr. Zama Katamzi, Dr. Pierre Cilliers, Prof. Manfred Hellberg, Dr. John Bosco Habarulema, Dr. Pieter Kotze, Dr. Shimul Maharaj, and Dr. Stephan Lotz for their academic contributions to my study. I am grateful for the support I received from Dr. Alireza Mahmoudian in running the DUSTY model. I acknowledge J.-P. St.-Maurice for his valuable comments during my SuperDARN virtual workshop presentation and for his work on the Gradient Drift Instability (GDI), which was of great help in this study. I also acknowledge the National Space Weather Program for its space weather definition (“used and quoted in this thesis”), which was presented in a book by (Goodman, 2004).

I would also like to thank my past and present colleagues and fellow students for their motivation and support. These include Mr. Dakalo Casca Mashao, Mr. Ntlakanipho Ngwane, Ms. Tsige Atilaw, Mr. Taiwo Ojo, Mr. Golekamang Thaganyana, Ms. Sarah McKee and other students who have now achieved their MSc and PhD degrees. Thanks to our student administrator Ms Juchelle Ontong for the guidance and motivation throughout this journey.

Finally, I would like to acknowledge with gratitude the love, prayers and support of my wife, my sons, and other family members.

Dedication

This thesis is primarily dedicated to my father, Hungulimana Cyprien, who sacrificed his life so that we could live. Thank you for the love you showed me in that short time we spent together. You were my first teacher. You taught me how to count, even though it was tough. Your hard work always guided me during my journey. Thank you for teaching us to get up early and help you with the crop irrigation before going to work every morning. I will not forget the truths you taught us during our discussions, your help in making our traditional soccer ball and your guitar that I often broke. I wish you were still with us to see the fruits of the seeds that you sowed.

I also dedicate this thesis to my mother, Ntakaziraho Spèceiose, who fought hard to raise us. I still hear her lovely songs in my dreams. Your training to work harder after the war changed everything; it is an outstanding lesson to your children. My thesis is also dedicated to Hiyaturokoye Amina, my youngest sister, who died due to the harsh situation that followed the war. I believe that they are all resting in peace.

Finally, this thesis is dedicated to my wife, Uwineza Providence, my sons Hiyadutuje Alliance, Hiyadutije Crispin and Hiyadutoje Archelaus, and also to siblings, Hiyadukunze Blandine, Hiyaduhaye Dieudonné, Hiyadutunze Adeline and Hiyaduhanze Clarentus who supported and encouraged me.

Abstract

Traveling Ionospheric Disturbances (TIDs) and Near Range Echoes (NREs) are both natural phenomena observed by SuperDARN High Frequency (HF) radars. This study presents for the first time observations of NREs in the lower E -region whose amplitudes are moderately modulated by medium-scale TIDs propagating in the F -region that have been observed by the same radar at another time in the far ranges. Two events during geomagnetic storms in winter recorded by the SANAE radar and two events during quiet times in summer recorded by the Zhongshan radar, both radars in the southern hemisphere, are described. The Gradient Drift Instability (GDI) proved to be the likely mechanism. The GDI is driven by the velocity difference between neutrals and plasma in the E -region ionosphere, due to the global convection electric field, and can be modulated by the polarization electric field of a passing TID via the near-vertical equipotential magnetic field lines.

Contents

Declaration	ii
Acknowledgement	iv
Dedication	v
List of Figures	ix
List of Tables	xiv
List of Abbreviations	xvi
1 INTRODUCTION	1
1.1 Introduction	1
1.2 SuperDARN HF radars TIDs and NREs	1
1.3 Motivation for this research	2
1.4 Objectives of the study	2
1.5 Thesis outline	2
2 THEORETICAL BACKGROUND	4
2.1 Space weather	4
2.1.1 Introduction	4
2.1.2 Solar activity	4
2.1.3 Solar wind and Earth's magnetosphere	6
2.1.4 Bow shock, magnetotail, plasma sheet of the magnetosphere and field line reconnection	7
2.1.5 The ring current within the magnetosphere	9
2.2 Geomagnetic storms	9
2.3 Thermosphere and ionosphere	11
2.3.1 Introduction	11
2.3.2 Thermosphere	11
2.3.3 The Earth's ionosphere	12
2.3.3.1 Introduction	12
2.3.3.2 Regions of ionosphere	12
2.3.3.3 Variation of the ionosphere	14
2.3.3.4 Radio wave absorption in the ionosphere	17
2.4 Atmospheric waves and traveling ionospheric disturbances	20
2.4.1 Introduction	20
2.4.2 Planetary waves	20
2.4.3 Tides	20
2.4.4 Sound waves	20
2.4.5 Atmospheric gravity waves (AGWs)	21
2.4.5.1 Origin of AGWs	21
2.4.5.2 Buoyancy force	23
2.4.5.3 The dispersion relation of AGWs	24
2.4.5.4 AGW dissipation	27
2.4.5.5 Ionospheric behavior under the influence of internal gravity waves	28
2.4.6 Other waves related to the sound waves	29
2.4.6.1 Ion acoustic waves	29
2.4.6.2 Electron plasma waves	30
2.4.6.3 Hydromagnetic and magnetosonic waves	31
2.5 Summary	31

3 INSTRUMENTS AND MODELS	32
3.1 SuperDARN HF radars	32
3.1.1 Introduction	32
3.1.2 Ray tracing of SuperDARN HF radars	33
3.1.2.1 Interferometry method for measurement of the elevation angle	34
3.1.2.2 Multi-pulse radars and the auto-correlation function	35
3.1.2.3 Parameters of the SuperDARN HF radar	35
3.1.3 Multi-hop propagation	38
3.1.4 Ionospheric (IS) and ground or sea (GS) scatters	38
3.1.5 Differentiating between ground and ionospheric scatters	39
3.1.6 TIDs identified by means of GS or IS of SuperDARN	40
3.1.7 Advantages of the use of GS and IS for studying ionospheric irregularities	40
3.1.8 Disadvantages of the use of GS and IS for studying ionospheric irregularities	42
3.1.9 Convection maps	42
3.2 SuperDARN HF and satellite measurements	43
3.2.1 POES Satellites	43
3.2.2 DMSP Satellites	44
3.3 Ground-based magnetometers	44
3.3.1 Introduction	44
3.3.2 SANAe magnetometers	45
3.3.3 Zhongshan magnetometer	46
3.4 Ionosonde	47
3.4.1 Introduction	47
3.4.2 Ionograms	47
3.4.3 Zhongshan ionosonde	48
3.5 Models	49
3.5.1 Dusty model	49
3.5.1.1 Introduction	49
3.5.1.2 Input and output of the DUSTY model	49
3.5.2 Mass-Spectrometer-Incoherent-Scatter model (MSISE)	50
3.5.3 International Reference Ionosphere (IRI)	51
3.5.4 Horizontal Wind Model (HWM)	51
3.6 Summary	52
4 PREVIOUS TID and NRE STUDIES	53
4.1 Introduction	53
4.2 Observations of traveling ionospheric disturbances	53
4.2.1 Propagation modes of TIDs and AGWs	53
4.2.2 Perkins instability	56
4.3 SuperDARN HF radar near range echoes	59
4.3.1 Meteor echoes	60
4.3.2 Polar mesospheric summer echoes	60
4.3.2.1 Origin of polar mesospheric summer echoes	60
4.3.2.2 Measurement of PMSEs	62
4.3.2.3 Correlation between high energy particles precipitation and PMSEs	62
4.3.3 Instabilities in the <i>E</i> -region	63
4.3.3.1 Introduction	63
4.3.3.2 Farley Buneman and gradient drift instabilities	64
4.3.3.3 FBI dispersion relation	64
4.3.3.4 GDI dispersion relation	65
4.3.3.5 The instability growth rate	66
4.3.3.6 High-aspect angle irregularity regions (HAIR) and far-aspect angle irregularity region (FAIR) echoes	67
4.4 Summary	72

5	OBSERVATIONS AND MODEL OUTPUTS	73
5.1	Introduction	73
5.2	Backscatter power, Doppler velocity and spectral width	73
5.2.1	Ray-tracing	76
5.2.2	Geomagnetic indices during both winter and summer events	78
5.3	Particle precipitation	79
5.4	Electron density derived from IRI-2016	80
5.4.1	Winter events	80
5.4.2	Summer events	80
5.5	Wind parameters derived from the HWM-14	82
5.5.1	Winter events	84
5.5.2	Summer events	85
5.6	Sporadic- <i>E</i> layers	86
5.7	Electric field in the southern hemisphere	86
5.8	Summary	89
6	RELATIONSHIP BETWEEN MSTIDs AND NREs	91
6.1	Introduction	91
6.1.1	Periods of TIDs and NREs	91
6.1.2	Wavenumbers of MSTIDs	92
6.1.3	Characteristics of MSTID	99
6.2	Cross-correlation between NREs (N) and TIDs (T)	100
6.3	Spearman Correlation Coefficients of NREs and TIDs	103
6.4	Summary	110
7	MECHANISM RELATING MSTIDs AND NREs	114
7.1	Introduction	114
7.2	Mechanisms unlikely to cause NREs	114
7.2.1	Meteor trail echoes, HAIR echoes and PMSEs	114
7.2.2	DUSTY model output for the event on 17 December 2013	115
7.3	Primary waves that are responsible for the NREs	118
7.4	Cross-correlation using detrended data	122
7.5	Summary	122
8	CONCLUSIONS AND SUGGESTIONS	126
8.1	Introduction	126
8.2	Conclusions	126
8.3	Suggestions for further research	127

List of Figures

2.1	Solar activity (https://za.pinterest.com/pin/377035800023905531/)	5
2.2	Solar energy streams to the surrounding space (Goodman, 2004).	6
2.3	The top panel shows the IMF, bow shock and magnetic reconnection within the magnetosphere. The bottom panel shows the structures of the Pedersen and Hall currents (Gillies, 2012).	7
2.4	Magnetotail, magnetosheath and two lobes after the reconnection of magnetic field lines (Moldwin, 2008).	8
2.5	Earth's magnetosphere with its electrical currents. This shows both equatorial and noon-midnight meridional planes (adapted from Figure 4.3 in Moldwin (2008))	9
2.6	The mid-latitude ionospheric regions and their electron density. The solid lines show solar maximum values during the day and night, while the dashed lines show the solar minimum values	13
2.7	The top panel illustrates the ion-neutral, electron-neutral collision and gyro-frequencies while the bottom panel shows different directions of current caused by different relative motion between ions and electrons in the magnetic and electric fields (Leake et al., 2014; Gillies, 2012).	16
2.8	Radio wave propagation in the ionosphere, showing the comparison between vertical and oblique sounding systems (Hargreaves, 1995; Fabrizio, 2013).	19
2.9	Examples of atmospheric gravity wave, namely the observed (top) and simulated gravity waves (bottom) of instability structures in the noctilucent cloud (Fritts and Alexander, 2003).	22
3.1	Fields of view of the southern hemisphere SuperDARN HF radars, with SANA E (left) and Zhongshan (right) in red.	32
3.2	The geometry of the interferometry technique to measure the elevation angle (Iserhienrhien, 2016).	34
3.3	The eight SuperDARN pulses, with the vertical dashes showing the transmission time between the pulses (Ribeiro et al., 2013)	36
3.4	The blue, red, and green squares show that the SuperDARN pulses P_1 and P_2 are returned from distances d_- , d_o , and d_+ , respectively. The arrows show that the pulses return after some time (Iserhienrhien, 2016).	37
3.5	Ray paths of simulated signals using Chapman E and F layers for a spherical Earth geometry. The blue shading is a spatial distribution of the refractive index n . The yellow contour shows an area where the aspect angle condition is satisfied to within 1° . Black contours/dots show group range marks at 400-km intervals (Ponomarenko et al., 2009).	39
3.6	Ray-tracing for beam 7 of the Syowa East at 11 MHz on 19 February 2012 (http://vt.superdarn.org/tiki-index.php?page=Ray-tracing)	40
3.7	Difference between GS (A) and IS (B) on 17 December 2013. Beam 12 of Zhongshan HF radar was used. The top panels show the power, the middle panels show the Doppler velocity and the bottom panels show the spectral width.	41
3.8	Convection maps (a) for 28 May 2011 between 10:58 and 12:00 UT, (b) for 15 July 2012 between 13:28 and 13:30 UT (c) for 22 November 2013 between 14:58 and 15:00 UT and (d) for 17 December 2013 between 19:00 and 19:02 UT.	43
3.9	The footprint of four (15, 16, 18, and 19) NOAA POES and MetOp-02 satellites in the northern and southern hemispheres plotted on ILAT versus MLT coordinates (Søråas et al., 2018).	44
3.10	Two SAPS events observed by midlatitude SuperDARN radars during times with different Dst values: (a) on 9 April 2015 at 06:30 UT (quiet time) and (b) on 17 March 2013 at 20:00 UT (storm time). Velocity vectors of convection flow derived from mid-latitude SuperDARN measurements are overlaid on each panel using the color bar on the right (Kunduri et al., 2017).	45
3.11	Elements of the geomagnetic field (http://wdc.kugi.kyoto-u.ac.jp/element/eleexp.html).	46
3.12	A fluxgate magnetometer at Zhongshan station (Liu et al., 2016)	47
3.13	Ionogram interpretation (Witvliet et al., 2015)	48

4.1	Sources and propagation modes of AGWs/TIDs in the atmosphere. Upper modes (1 and 2) and lower modes (3 and 4) are illustrated in the top panel, while waves (with other parameters) and their directions are shown in the bottom panel. The figures were adopted from Hocke et al. (1996) and Iserhienrhien (2016).	54
4.2	SuperDARN MSTID illustration: (a) Ground focusing and defocusing of HF radar's ray paths during a passing TID. (b) Ground backscatter power of beam 8 of the Falkland Islands radar between 11:00 and 21:00 UT (Grocott et al., 2013).	56
4.3	(a) Figure 1 and caption from Perkins (1973), page 219: "Geometry of the coordinate systems. The view is toward the east in a northern hemisphere magnetic meridian plane. The unit vectors \hat{l} and \hat{h} are in the horizontal and vertical directions, respectively. The unit vectors \hat{z} and \hat{x} are, respectively, parallel and perpendicular to the magnetic field \mathbf{B} , which has a dip angle D ." (b) Figure 2 from Hamza (1999), page 22,572: electric field \mathbf{E} , wave vector \mathbf{k} and neutral wind velocity \mathbf{U}	58
4.4	Noctilucent Clouds over the northern part of Sweden on 10-11 August 2000. AGWs are seen in these photos (Dalin et al., 2004).	62
4.5	Cartoon illustrating PMSE at the mesopause height. The radar signal is backscattered when the structure fulfils Bragg's scatter condition (Routledge, 2011).	63
4.6	Cartesian coordinate system for the electric field \mathbf{E} (which is antiparallel to the X-axis), and parallel to ∇n_e , and magnetic field \mathbf{B} (which is parallel to the Z-axis) in the southern polar hemisphere (see Schmidt and Gary (1973)). The wave vector \mathbf{k} , together with its aspect (β) and flow (θ) angles, are represented.	66
4.7	The formation of linear instabilities: (a) The FBI is produced in the presence of a strong electric field, magnetic field and the relative velocity between electrons and ions and (b) GDI is produced under the condition that both the electric field and density gradient pointing in the same direction (Kelley, 2009).	68
4.8	GDI driven by (a) an electric field and (b) a neutral wind. Light regions have lower electron density than the dark regions (Kelley, 2009).	69
4.9	A demonstration of the FAIR mechanisms, as an eastward neutral wind and/or westward $\mathbf{E} \times \mathbf{B}$ drift create a westward polarization electric field (St.-Maurice and Nishitani, 2020).	71
5.1	Range-Time-Intensity plot of backscatter power (top), Doppler velocity (middle) and spectral width (bottom) based on data from the SANA E HF radar and showing TIDs and NRE; (A) from 11:00 to 13:00 UT on 28 May 2011 from beam 7 and (B) from 12:00 to 17:00 UT on 15 July 2012 from beam 15.	74
5.2	RTI plot of backscatter power (top), Doppler velocity (middle) and spectral width (bottom) based on data from beam 15 of the Zhongshan HF radar and showing TIDs and NREs; (A) from 00:00 to 04:00 UT on 22 November 2013 and (B) from 19:00 to 21:00 UT on 17 December 2013.	75
5.3	Near range echoes of odd numbered beams showing the backscatter power (left panels), Doppler velocity (middle panels) and the spectral width (right panels). A) shows SANA E HF radar data for 28 May 2011 from 11:00 to 12:46 UT. B) shows SANA E HF radar data for 15 July 2012 from 12:30 to 16:30 UT.	76
5.4	Near range echoes of odd numbered beams showing the backscatter power (left panels), Doppler velocity (middle panels) and the spectral width (right panels). A) shows Zhongshan HF radar data for 22 November 2013 from 00:00 to 04:00 UT. B) shows Zhongshan HF radar data for 17 December 2013 from 19:00 to 21:00 UT.	77
5.5	The estimation of the backscatter echo reflection points using ray tracing at 12.0 MHz (SANA E) and 10.0 MHz (Zhongshan). Panel A) at 11:00 UT on 28 May 2011, panel B) at 12:00 UT on 15 July 2012, panel C) at 00:00 UT on 22 November 2013, and panel D) at 19:00 UT on 17 December 2013.	78
5.6	The AE, Dst and Kp indices on A) 28 May 2011, B) 15 July 2012 during a geomagnetic storm, and C) 22 November 2013 and 17 December 2013 during quiet time conditions.	79

5.7	Potential map plot showing the vectors of convection plasma flow derived from the southern hemisphere SuperDARN measurements and overlaid on a MLT-MLAT grid, along with particle precipitation data from the TED instrument of the POES satellites. The equatorward auroral oval boundary (red dot-dash line) determined by from POES. The equatorward edge of the auroral oval boundary was estimated by fitting a circle to the POES TED data. The green dot-dash line shows the poleward boundary: A) at 10:58-11:00 UT on 28 May 2011, B) at 11:58-12:00 UT on 15 July 2012, C) at 00:02-00:04 on 22 November 2013, and D) at 19:00-19:02 on 17 December 2013.	81
5.8	The electron density as derived from the IRI model for altitudes of between 80 and 160 km for 28 May 2011 (A) and 15 July 2012 (B), LT \approx UT +2 hr at (-72.50°, -2.76°) geographic coordinates.	82
5.9	The electron density as derived from the IRI model for altitudes of between 80 and 160 km for 22 November 2013 (A) and 17 December 2013 (B), LT \approx UT +5 hr at (-69.40°, 82.60°) geographic coordinates.	83
5.10	The meridional and zonal winds at altitudes between 80 and 160 km on 28 May 2011 (A and B) and on 15 July 2012 (C and D) LT \approx UT +2h at (-72.50°, -2.76°) geographic coordinates, as modeled by the HWM-14.	84
5.11	The meridional and zonal winds at altitudes between 80 and 160 km altitude on 22 November 2013 (A and B) and on 17 December 2013 (C and D), LT \approx UT +5h at (-69.40°, 82.60°) geographic coordinates, as modeled by the HWM-14.	85
5.12	An ionogram showing an <i>Es</i> -layer at 6.50 MHz on 17 December 2013 at 20:00 UT	86
5.13	Electric field magnitudes derived from SuperDARN convection plasma velocity over the southern hemisphere on A) 28 May 2011 at 12:00 UT, B) 15 July 2012 at 15:30 UT, C) 22 November 2013, and D) 17 December 2013.	87
5.14	The first four gates of each beam of SANA E SuperDARN radar and their range gates (A) and a comparison of their magnetic coordinates with the electric field coordinates (B). The electric field and other parameters are found on the SuperDARN webpage (http://vt.superdarn.org/tiki-index.php?page=ASCIIData) where the magnetic coordinates are also provided.	89
5.15	The northward (dashed green line) and eastward (dotted black line) electric field and the power of gate 0 (solid red line) and gate 1 (dash-dotted blue line) of beam 7 on 22 November 2013 from 00:00 to 03:48 UT.	90
6.1	Average of power amplitudes (dB) calculated by the FFT for gate numbers 0-20 (i.e., NREs and TIDs) of beams 0 (A), 1 (B), 4 (C) and 7 (D). The horizontal dotted (red) line shows the mean power level of TIDs and NREs. The significant frequencies of MSTIDs are at 0.05 min ⁻¹ (20 min) and 0.02 min ⁻¹ (50 min) for the period 19:00 - 20:48 UT on 17 December 2013.	92
6.2	Stack plots of power amplitudes (dB) calculated by FFT for gates 0-3 (i.e., NREs) of beam 0 (A) and beam 1 (B) of the Zhongshan radar. Stack plots are also shown for gates 4-20 (i.e., TIDs) of beam 0 (C) and beam 1 (D) of the Zhongshan radar. The colors show the gates from 0-20. The vertical lines show periods of 20 and 50 minutes for the period between 19:00 - 20:48 UT on 17 December 2013.	93
6.3	Stack plots of power amplitudes (dB) calculated by the FFT for gates 0-3 (i.e., NREs) of beam 4 (A) and beam 9 (B) of the Zhongshan radar. Stack plots are also shown for gates 4-20 (i.e., TIDs) of beam 4 (C) and beam 9 (D) of the Zhongshan radar. The colors show the gates from 0-20. The vertical lines show periods of 20 and 50 minutes for the period between 19:00 - 20:48 UT on 17 December 2013.	94
6.4	Stack plots of power amplitudes (dB) calculated by the FFT for NREs (A) and MSTIDs (B) of beam 10 of the SANA E HF radar on 28 May 2011 between 11:00 and 12:46 UT, for NREs (C) and MSTIDs (D) of beam 7 of the SANA E HF radar on 15 July 2012 between 12:30 and 16:30 UT, and for NREs (E) and MSTIDs (F) of beam 7 of the Zhongshan HF radar on 22 November 2013 for the period between 00:00 and 03:48 UT. The colors show the gates from 0-20. The vertical lines show periods 15.9, 27.8, and 66.7 minutes (A and B); 17.5, 27.8, and 66.7 minutes (C and D); and 10.0, 14.5, 20.0, and 30.3 minutes (E and F).	95
6.5	The analyses of two times series (6,8) and (7,6) (left panels) and another two time series (8,8) and (7,6) (right panels). The panels (A) show the time series of each pair, panels (B) show their CSD, panels (C) show their coherence and panels (D) show phase difference between 19:00 and 20:48 UT, on 17 December 2013 at Zhongshan.	96

6.6	The analyses of two times series (3,47) and (5,45) (left panels) and another two time series (7,47) and (5,45) (right panels). The panels (A) show the time series of each pair, panels (B) show their CSD, panels (C) show their coherence and panels (D) show phase difference between 11:40 and 12:40 UT, on 28 May 2011 at SANA E.	96
6.7	The analyses of two times series (0,40) and (2,38) (left panels) and another two time series (4,40) and (2,38) (right panels). The panels (A) show the time series of each pair, panels (B) show their CSD, panels (C) show their coherence and panels (D) show phase difference between 12:30 and 16:30 UT, on 15 July 2012 at SANA E.	97
6.8	Phase differences of two times series (7,14) and (9,12) (left panels) and another two time series (11,14) and (9,12) (right panels). The panels (A) show the time series of each pair, panels (B) show their CSD, panels (C) show their coherence and panels (D) show phase difference between 00:00 and 03:00 UT, on 22 November 2013 at Zhongshan.	97
6.9	The three cells combination of the Zhongshan HF radar used for cross-spectral analysis. The boresight beam (beam 7) points nearly to the -x direction and perpendicular to y axis.	98
6.10	Cross-correlation between the power received by gate 0 (NREs) and gates 10-15 (TIDs) of beam 7 (A) of the SANA E radar for the time period 12:30 - 16:30 UT on 15 July 2012; and gate 0 (NREs) and gates 13-18 (TIDs) of beam 1 (B) of the Zhongshan radar for the time period 00:00 - 03:48 UT on 22 November 2013.	102
6.11	Cross-correlation between the power of gates 0-3 (NREs) of different beams with various gates (TIDs) of the SANA E radar for 28 May 2011 for the time period 11:00 - 12:46 UT (A) and for 15 July 2012 from 12:30 to 16:30 UT (B).	103
6.12	Cross-correlation between the power of gates 0-3 (NREs) of different beams with various gates (TIDs) of the Zhongshan radar for 22 November 2013 for the time period 00:00 - 03:48 UT (A) and for 17 December 2013 from 19:00 to 20:48 UT (B).	104
6.13	SCC, LRCC, and p-values of range gates 3 (NREs) and 40 (TIDs) of beam 0 (A), and of range gates 2 (NREs) and 10 (TIDs) of beam 4 (B) for the time period 12:30 - 16:30 UT on 15 July 2012 at SANA E. The plane in the plots is defined by the time series power received by near gates for NREs and far gates for MSTIDs.	105
6.14	SCC, LRCC, and p-values of range gates 1 (NREs) and 21 (TIDs) of beam 14 (A), and of range gates 1 (NREs) and 23 (TIDs) of beam 15 (B) for the time period 00:00 - 03:48 UT on 22 November 2013 at Zhongshan. The plane in the plots is defined by the time series power received by near gates for NREs and far gates for MSTIDs.	106
6.15	SCC, LRCC, and p-values of range gates 1 (NREs) and 12 (TIDs) of beam 7 (A), and of range gates 1 (NREs) and 13 (TIDs) of beam 12 (B) for the time period 11:00 - 12:45 UT on 28 May 2011 at SANA E. The plane in the plots is defined by the time series power received by near gates for NREs and far gates for MSTIDs.	108
6.16	SCC, LRCC, and p-values of range gates 3 (NREs) and 11 (TIDs) of beam 0 (A), and of range gates 1 (NREs) and 8 (TIDs) of beam 15 (B) for the time period 19:00 - 20:50 UT on 17 December 2013 at Zhongshan. The plane in the plots is defined by the time series power received by near gates for NREs and far gates for MSTIDs.	109
6.17	The SCC of range gate 1 (NREs) and TIDs of gates of beams 7, 8, 10, and 12 of the SANA E radar for 28 May 2011	110
6.18	The SCC (A) of range gate 1 (NREs) and TIDs of gates from all beams of the SANA E radar on 15 July 2012; and (B) of range gate 2 and TIDs of gates of all beams of the SANA E radar for 15 July 2012	111
6.19	The SCC (A) of range gate 1 (NREs) and TIDs of gates of all beams of the Zhongshan radar for 22 November 2013, and (B) of range gate 2 and TIDs of gates of all beams of the Zhongshan radar for 22 November 2013	112
6.20	The SCC (A) of range gate 1 (NREs) and TIDs of gates of all beams of the Zhongshan radar for 17 December 2013, and (B) range gate 2 and TIDs of gates of all beams of the Zhongshan radar for 17 December 2013	113
7.1	A) Mean power and FFT of beam 3 of the Zhongshan HF radar. B) Radii and density of dust particles given by DUSTY model for the same beam. <i>rdi</i> and <i>rdf</i> are the initial and final radii of the icy dust particle.	116

7.2	Radius and density variations of dust particles together with the variation in backscatter power (dB) received by beams 0-14 of the Zhongshan HF radar on 17 December 2013. The results of beam 3 of the radar is shown in a rectangular block.	118
7.3	Panel A) shows the primary wave wavelengths as derived from data for 15 July 2012, supplied by the SuperDARN HF radar (SANA) operating at 12.57 MHz and panel B) shows the wavelengths of the data for 22 November 2013 supplied by the Zhongshan radar operating at 10.25 MHz. The relative velocity between electrons and ions is (a) $V_d = 50$ m/s, (b) $V_d = 100$ m/s, (c) $V_d = 200$ m/s and (d) $V_d = 400$ m/s . The relative amplitude (compared to the background) of the primary waves are assumed to be 5% (blue), 10% (orange), 20% (green), and 40% (red) and $L_y = 500$ (blue-violet), 1000 (brown), 2000 (violet), and 4000 m (gray).	120
7.4	Panel A) shows the primary wave wavelengths as derived from data for 28 May 2011, supplied by the SuperDARN HF radar (SANA) operating at 12.57 MHz, and panel B) shows the wavelengths of the data for 17 December 2013 supplied by the Zhongshan radar operating at 10.25 MHz. The relative velocity between electrons and ions is (a) $V_d = 50$ m/s, (b) $V_d = 100$ m/s, (c) $V_d = 200$ m/s and (d) $V_d = 400$ m/s . The relative amplitude (compared to the background) of the primary waves are assumed to be 5% (blue), 10% (orange), 20% (green) and 40% (red), and $L_y = 500$ (blue-violet), 1000 (brown), 2000 (violet) and 4000 m (gray).	121
7.5	For 15 July 2012 from 12:30 to 16:30 UT at an altitude of 100 km altitude (case S1): (a) modeled eastward neutral wind, (b) Z-component of the Earth's magnetic field at ground level, (c) the linear detrended observed northward electric field (E_{yd}), (d) the linear detrended calculated plasma density scale height (Lzd), (e) the linear detrended average backscatter power of all beams for range gate 2 (p2), (f) the cross-correlation between E_{yd} (panel c) and p2d (panel e), and (g) cross-correlation between Lzd (panel d) and p2d (panel e).	123
7.6	For 22 November 2013 from 00:00 to 02:48 UT at an altitude of 100 km (case Z1): (a) modeled eastward neutral wind, (b) Z-component of the Earth's magnetic field at ground level, (c) the linear detrended observed northward electric field (E_{yd}), (d) the linear detrended calculated plasma density scale height (Lzd), (e) the linear detrended average backscatter power of all beams for range gate 2 ($p2d$), (f) the cross-correlation between E_{yd} (panel c) and p2 (panel e), and (g) cross-correlation between Lz (panel d) and $p2d$ (panel e).	124
7.7	For 17 December 2013 from 19:00 to 20:48 UT at an altitude of 100 km (case Z2): (a) modeled eastward neutral wind, (b) Z-component of the Earth's magnetic field at ground level, (c) the linear detrended observed northward electric field (E_{yd}), (d) the linear detrended calculated plasma density scale height (Lzd), (e) the linear detrended average backscatter power of all beams for range gate 2 ($p2d$), (f) the cross-correlation between E_{yd} (panel c) and p2 (panel e), and (g) cross-correlation between Lz (panel d) and $p2d$ (panel e).	125

List of Tables

2.1	Layers of Earth's atmosphere	11
6.1	MSTID parameters estimated on 15 July 2012 for the period from 11:30 to 17:30 UT, 22 November 2013 for the period from 00:00 to 03:48 UT and on 17 December 2013 for the period from 19:00 to 20:48 UT for the F region.	99
6.2	Frequency and virtual height derived from the Zhongshan ionosonde data on 17 December 2013	100
6.3	Earlier studies on the parameters of TIDs/AGWs.	101
7.1	The change in the output of radar backscatter power (dB) as derived by the DUSTY model for the Zhongshan HF radar. The radii of dust particles is rd and ratio of density of dust particles and background electrons is $nd/ne0$	115

List of Abbreviations

- AACGC: Altitude-Adjusted Corrected Geomagnetic Coordinates
- ABT-2009: Assimilation Bottomside Thickness model-2009
- ACF: Auto Correlation Function
- AE-B: Atmosphere Explorer-B
- AE-C: Atmosphere Explorer-C
- AE: Auroral Electrojet Index
- AGWs: Atmospheric Gravity Waves
- AL: Auroral Lower limit index
- AMTB2013: Assimilation Model electron Temperature B model-2013
- Ap: Apest index
- ARTIST: Automatic Real-Time Ionogram Scaler with True height
- AU: Auroral Upper limit index
- CAM: Compact Atomic Magnetometer
- CAS: Chinese Academy of Sciences
- CC: Cross-Correlation
- CCD: Charge Coupled Device
- CGM: Corrected GeoMagnetic
- CIRA: COSPAR International Reference Atmosphere
- CIRs: Corotating Interacting Regions
- CMEs: Coronal Mass Ejections
- COSPAR: Committee on Space Research
- CSD: Cross-Spectra Density
- DPS-4: Digisonde Portable Sounder-4
- Dst: Disturbance storm time
- DWM: Disturbance Wind Model
- EIA: Equatorial Ionization Anomaly
- EISCAT: European Incoherent Scatter Radar
- Es: Sporadic *E*-region
- ESV: Effective Scatter Volume
- EUV: Extreme Ultraviolet
- FAIR: Far-Aspect Angle Irregularity Region
- FAIs: Field-Aligned Irregularities
- FBI: Farley-Buneman Instability

FFT:	Fast Fourier Transform
FIR:	Falkland Islands Radar
FITACF:	Fitted Auto Correlation Function
FOV:	Field Of View
FPI:	Fabry Perot Interferometer
GDI:	Gradient Drift Instability
GEONET:	GPS Earth Observation Network
GI:	Ground Scatter
GICs:	Geomagnetically Induced Currents
GNSS:	Global Navigation Satellite System
GPS:	Global Positioning System
HAIR:	High Aspect Irregularity Region
HF:	High Frequency
HWM:	Disturbance Wind Model
IDM:	Ion Drift Meter
IF:	Intermediate Frequency
IG:	Global Ionospheric index
IGG:	Institute of Geology and Geophysics
IGRF:	International Geomagnetic Reference Field
IGS:	International GNSS Service
IGWs:	Internal Gravity Waves
ILAT:	Invariant Latitude
IMF:	Interplanetary Magnetic Field
INTERMAGNET:	INTERNational Real-time MAGnetic Observatory NETwork
IP:	Initial Phase
IRI:	International Reference Ionosphere
IS:	Ionospheric Scatter
ISO:	International Organization for Standardization
JGR:	Journal of Geophysical Research
Kp:	Kennziffer planetary index
LOS:	Line Of Sight
LRCC:	Linear Regression Correlation Coefficient
LSAGWs:	Large-Scale Atmospheric Gravity Waves
LSTIDs:	Large-Scale Traveling Ionospheric Disturbances
LT:	Local Time

- MF: Medium Frequency
- MHD: Magnetohydrodynamics
- MLAT: Magnetic Latitude
- MLT: Magnetic Local Time
- MP: Main Phase
- MPC: Polar Mesospheric Clouds
- MSAGWs: Medium-Scale Atmospheric Gravity Waves
- MSIS: Mass-Spectrometer-Incoherent-Scatter model
- MSTIDs: Medium-Scale Traveling Ionospheric Disturbances
- MUF: Maximum Usable Frequency
- NASSP: National Astrophysics and Space Science Programme
- NLC: Noctilucent Cloud
- NNSS: Navy Navigation Satellite System
- NOAA: National Oceanic and Atmospheric Administration
- NREs: Near Range Echoes
- NSWP: National Space Weather Program
- PIC: Particle-In-Cell
- PMSEs: Polar Mesospheric Summer Echoes
- PMWEs: Polar Mesospheric Winter Echoes
- POES: Polar Operational Environmental Satellites
- PSD: Power Spectral Density
- Q_e: Effective Q index
- QP: Quasi-Periodic
- RKN: Rankin Inlet
- RP: Recovery Phase
- RS-232: Recommended Standard 232
- RTI: Range-Time-Intensity
- SANAE: South African National Antarctic Expedition
- SANAP: South African National Antarctic Programme
- SANSA: South African National Space Agency
- SAPS: Subauroral Polarization Stream
- SCC: Spearman rank Correlation Coefficient
- SEM: Space Environment Monitor
- SNR: Signal-to-Noise Ratio
- SSIES: Special Sensor Topside Ionosphere Plasma Sensor

- SSJ: Special Sensor J
- SSM: Special Sensor Magnetometer
- SSN: Sunspot Number
- SuperDARN: Super Dual Auroral Radar Network
- SYE Syowa East
- TBT2012+SA: Temperature B Topside model with Solar Activity variations
- TDU: Technical University of Denmark
- TEC: Total Electron Content
- TECU: TEC Unit
- TED: Total Energy Detector
- TIDs: Traveling Ionospheric Disturbances
- UHF: Ultra-High Frequency
- URSI: International Union of Radio Science
- UT: Universal Time
- UV: Ultraviolet
- VHF: Very High Frequency
- VT: Virginia Tech
- Zcomp: Z-component

Chapter 1

INTRODUCTION

1.1 Introduction

This chapter introduces the Traveling Ionospheric Disturbances (TIDs) and Near Range Echoes (NREs) observed by Super Dual Auroral Radar Network (SuperDARN) coherent High Frequency (HF) radars, operating at 8-20 MHz. It also presents the scientific motivation, objectives and the thesis outline.

1.2 SuperDARN HF radars TIDs and NREs

SuperDARN, ionosondes, Global Positioning System (GPS) and other instruments observe ionospheric wave-like structures that travel from the high-latitudes to the mid-latitudes (Hunsucker, 1982; Miyoshi et al., 2018) and sometimes propagate across the equator (Habarulema et al., 2015). TIDs are observed within the SuperDARN backscatter echoes beyond 350 km slant range at altitudes above 150 km. Hines (1960) proposed that Atmospheric Gravity Waves (AGWs) are the source of these wave-like structures, named Traveling Ionospheric Disturbances (TIDs). Others sources of TIDs are associated with electrodynamic processes such as instabilities, for example the Perkins instability, and other mechanisms involving the electric field (Liu et al., 2019). In short, TIDs may be caused by any number of energetic phenomena (strong enough to cause TIDs) caused by interaction with the ionosphere. Examples of the energy input include Joule heating in the E -region, thunderstorms below the ionosphere, and geomagnetic storms (Ding et al., 2008), and etc.

SuperDARN Near Ranges Echoes (NREs) are observed by SuperDARN HF radars within a 315 km slant range, at altitudes between 100 and 120 km (Ponomarenko et al., 2016). E -sporadic layers (E_s) may be associated with E region Field-Aligned Irregularities (FAIs) in the nighttime ionosphere. The formation of FAI is affected by steep E_s gradients, strong neutral wind shear and the polarization electric field (Liu et al., 2021). Radio waves transmitted by HF instruments such as SuperDARN radars are Bragg backscattered by those irregularities on a scale between ~ 7.5 and ~ 18.7 m. Other irregularities are observed by SuperDARN radars when the orthogonality condition is met. For example, meteor trails (Hall et al., 1997; Jenkins and Jarvis, 1999; Hussey et al., 2000) and Polar Mesospheric Summer Echoes (PMSEs) (Ogawa et al., 2003; Hosokawa et al., 2005) have been reported as observed by SuperDARN radars. Icy particles originating from ablated meteors cause strong backscatter in radar data at an altitude range of 80-90 km, known as Polar Mesospheric Summer Echoes. PMSEs require very low temperatures (< 200 K) and therefore can only appear in summer when adiabatic cooling is strongest due to global air circulation. PMSEs and meteor ablation may be used to study the neutral atmosphere and mesospheric dynamics. SuperDARN HF radar backscatter in the near range gates (180 - 350 km) have been reported to come from PMSEs. This is consistent with well-established Very High Frequency (VHF) radar data (Ogawa et al., 2003). Ogunjobi also reported radar backscatter due to PMSEs in SuperDARN HF radar data (Ogunjobi et al., 2015, 2017). PMSEs can be used in the study of energy coupling between the lower and upper atmosphere, or vice versa. This is critical to understand the upper atmospheric energy balance, which forms the interface between terrestrial and space weather. Other types of NREs are the High Aspect Irregularity Region (HAIR) echoes (Milan et al., 2004; Drexler and St.-Maurice, 2005; St.-Maurice and Nishitani, 2020) and the Far-Aspect Angle Irregularity Regions (FAIR) echoes (St.-Maurice and Nishitani, 2020) associated with plasma instabilities. Gradient Drift Instability (GDI) triggered by the density gradient and $\mathbf{E} \times \mathbf{B}$ drift causes NREs, which are observed by SuperDARN at altitudes near 100 km (St.-Maurice and Nishitani, 2020).

1.3 Motivation for this research

TIDs carry energy and momentum and may propagate horizontally, obliquely or vertically in the ionosphere. TIDs may also generate a polarization electric field in the F -region (Otsuka et al., 2004, 2007; Liu et al., 2019). Between the F -region, where TIDs are observed, and the bottom of the E -region, where NREs take place, there is a distance of $\sim 100 - 200$ km. This thesis focuses on TIDs traveling horizontally and offers the first report of TIDs propagating overhead that moderately modulate the backscatter power of NREs. Our conclusion is that GDI is the most probable mechanism.

Both TIDs and NREs relate to the dynamics of space weather such as geomagnetic storms and particle precipitation. Understanding the effects of TIDs on NREs would enhance our understanding of the effect of space weather on space-based technology, such as HF communication satellites (McNamara, 1991; Goodman, 2004). It also enhances our understanding of the coupling between the E - and F -regions.

1.4 Objectives of the study

The main objectives of the project were to:

- Find TID and NRE events which occurred concurrently,
- Compute the correlation between TIDs and NREs,
- Quantify the impact of TIDs on NREs, and
- Explain the physical mechanisms behind the effect of TIDs on NREs.

1.5 Thesis outline

This thesis has eight chapters.

- Chapter 1 introduces the study of this thesis focused on TIDs and NREs as observed by SuperDARN HF radars. It also gives examples of the sources of TIDs and NREs. The scientific motivation behind the reason for undertaking this study is explained. The main objectives and the thesis outline are presented.
- In chapter 2, the interaction between the Sun and Earth is discussed. Geomagnetic storms are defined and the thermosphere and ionosphere is described, focusing on the high-latitude regions. Atmospheric waves such as AGWs and TIDs are described.
- Chapter 3 concerns the instruments and data that were used in this study. The SuperDARN HF radars, satellites, ground-based magnetometers, and ionosondes together with their measurements are introduced. Models relating to the ionosphere, such as the DUSTY model, Mass-Spectrometer-and-Incoherent-Scatter Radar (MSIS), International Reference Ionosphere (IRI) and the Horizontal Wind Model (HWM) are explained.
- Chapter 4 offers an overview of research relating to TIDs and NREs and also describes methods that have been used to study these phenomena. This chapter also introduces SuperDARN NREs, such as PMSEs and GDI-related echoes. Cross-correlation is one of the methods that has been used to relate these two phenomena. The Spearman correlation coefficients is another method that has been used to statistically investigate how one phenomenon may contribute to the other quantitatively.
- Chapter 5 discusses four observed events which concurrently showed both TIDs and NREs, based on the HF radar backscatter power, Doppler velocity and spectral width at both SANAE and Zhongshan. The particle precipitation, electron density based on the International Reference Ionosphere model (IRI-16), the neutral wind derived from the Horizontal Wind Model (HWM-14), the sporadic E layers, and the convection electric field during these events are also described.
- The relationship between TIDs and NREs are discussed in chapter 6. The periodicity of both TIDs and NREs are estimated. TIDs parameters, such as wavenumber, phase velocity, propagation azimuth angle, wavelength and amplitude derivation are explained. This chapter highlights the cross-correlation and Spearman correlation coefficients of TIDs and NREs.

- In chapter 7, meteor trail echoes and PMSEs as the unlikely mechanisms that cause NREs are discussed. GDIs as the most plausible mechanism to cause NREs are discussed. The estimated modulation of the plasma density scale height is presented. The chapter also focuses on the electrodynamic coupling between the E and F regions by means of mapping of the polarization electric field caused by F region TIDs.
- Chapter 8 describes the conclusions that the research led to and offers suggestions for future research. Included at the end is the paper published by the Journal of Geophysical Research on the results of this thesis.

Chapter 2

THEORETICAL BACKGROUND

2.1 Space weather

2.1.1 Introduction

Space weather may have harmful effects on our day-to-day life here on the Earth. The National Space Weather Program (NSWP), which was established in 1995, defines space weather as “*conditions on the Sun and in the solar wind, magnetosphere, ionosphere, and thermosphere that can influence the performance and reliability of space-borne and ground-based technological systems and can endanger human life or health*” (<http://www.spaceweathercenter.org/swop/NSWP/1.html>). Another definition of space weather is offered by Goodman (2004). Space weather can negatively or positively influence our lifestyle by interrupting/terminating or favoring space- and ground-based technology (such as navigation, surveillance or telecommunication systems), much like terrestrial weather. Coronal Mass Ejection (CME), solar radiation, particles, flares and the solar wind are related to solar magnetic activity, which can cause geomagnetic storms and are sources of space weather (Manchester IV et al., 2004; Xie et al., 2004).

Geomagnetic storms disturb the magnetosphere (Gonzalez et al., 1994), which generally protects the Earth from high energy particles from the surrounding space. The magnetosphere is the space enclosed by the Earth’s magnetic field. The transportation of energy and momentum during space-atmosphere coupling participates in the magnetosphere disturbances, where the reflection and absorption of solar particles as well as magnetic field reconnection might occur (see Figure 2.1 (<https://www.noaa.gov/explainers/space-weather-storms-from-sun>)). The disturbed magnetosphere may cause a large disruption; however, its magnetic field acts as armor, shielding the Earth from solar activity (Goodman, 2004; Marov, 2020). The magnetic field at the Earth’s surface is roughly 50 times larger than the change in the magnetic field during a severe geomagnetic storm ($K_p = 9$, which has ~ 1000 nT).

Solar activity may reach our atmosphere and cause electrodynamic phenomena by means of energy and momentum exchange (Gonzalez et al., 1994). The sunspots are visible as dark spots on the Sun since they are cooler than the surrounding surface of the Sun. The magnetic field surrounding the sunspots protrude from the visible surface of the Sun. From time to time the magnetic field lines erupt in the form of flares. The energy lost due to frequent reconnection between oppositely directed magnetic field lines produces a massive explosion (Innes et al., 1997). As a result, some particles traveling close to the speed of light are ejected from the so-called solar flares and energetic X-ray radiation results from the blast. An abundance of magnetized plasma, of several billions of tons, known as CME (Forbes, 2000; Schindler, 2006) and/or solar wind move within interplanetary space at the speed of hundreds to thousands of kilometers per second, and occasionally collide with the magnetosphere to give rise to a geomagnetic storm. Damage to space-based electronics may occur due to the enhanced particle population in the radiation belts, depending on where the satellites are. During these disturbances, Atmospheric Gravity Waves (AGWs), Traveling Ionospheric Disturbances (TIDs) and instabilities may arise from the interaction between neutral and charged particles, respectively. Solar activity and its impact is described in more detail in the following sub-section.

2.1.2 Solar activity

Sunspots are a great source of information on the level of activity of the Sun. Sunspots differ in size; the largest recorded sunspot was 230×10^6 m in diameter (Goodman, 2004). Sunspots may be seen with the naked eye when they are big enough (at least 40×10^6 m). Sunspots indicate the direction of the Sun’s rotation. Generally, sunspots may last for a few hours or a few weeks. A sunspot has an umbra (its very dark inner region) with a

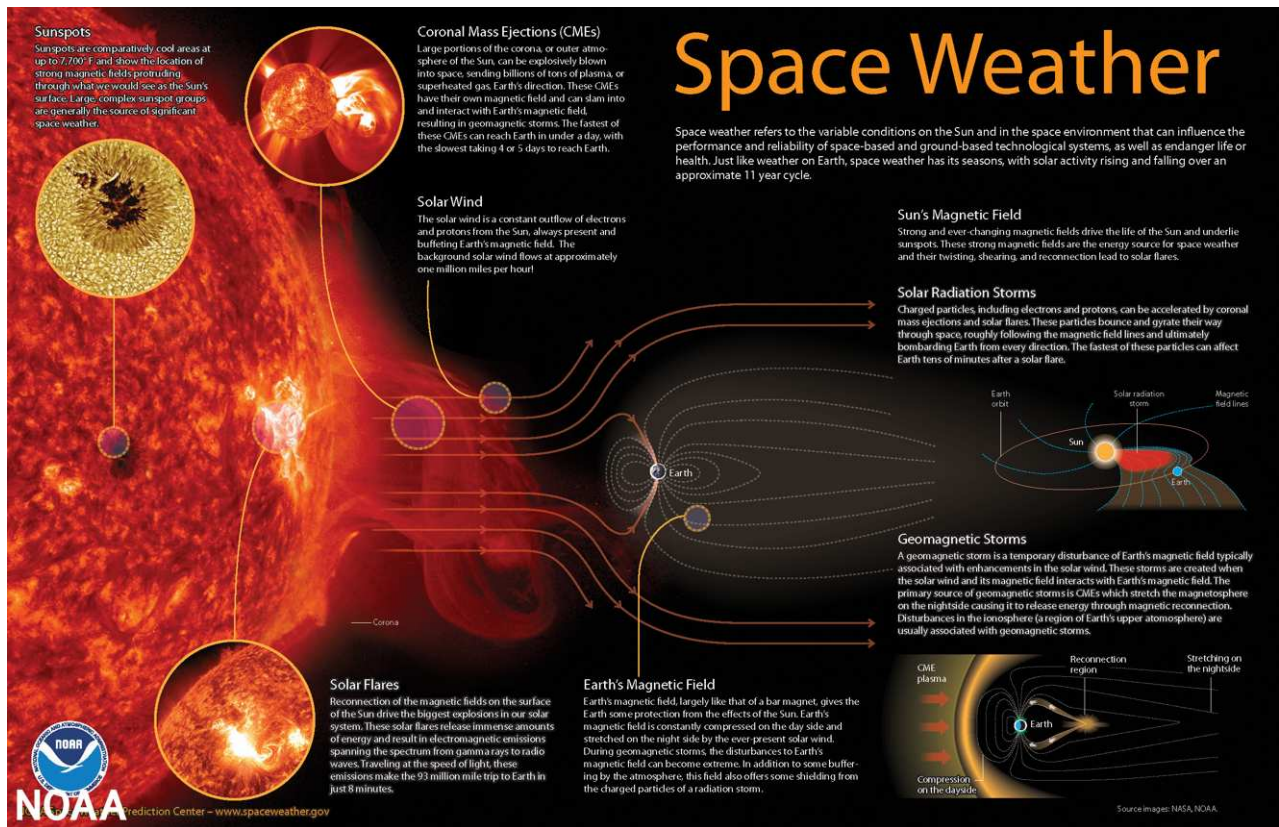


Figure 2.1: Solar activity (<https://za.pinterest.com/pin/377035800023905531/>)

temperature of $\sim 3230^\circ\text{C}$ and a penumbra (the lighter region surrounding the umbra) with a temperature of $\sim 5000^\circ\text{C}$ (Wilson, 1968). These temperatures are lower than that of the outer surface of the Sun ($\sim 5,537.8^\circ\text{C}$) (Wilson, 1968). This temperature difference makes the sunspots appear dark. Sunspots are generated through the disorderly displacement of gases which twist and deform the magnetic field of the Sun (Moldwin, 2008). Moreover, the hot gases are repelled inward by the twisted field's power to prevent the temperature enhancement at the photosphere, as a result, they produce sunspots. On average, the number of sunspots reaches its minimum or maximum every 11 years, a period known as the solar cycle. As the cycle moves towards solar minimum, the number of sunspots decrease, and towards solar maximum, the number increases. Due to hot plasma in the Sun's convection zone, sunspots retain tremendous energy which produces and launches solar flares, the solar wind and CMEs (Moldwin, 2008).

Between the Sun and the Earth, solar flares, the solar wind and CMEs may interact physically with other objects (Li et al., 2008). These particles have a magnetic field, electric field, speeds and masses, and may interact with other matter in space. Particles in a collisionless (i.e., the conductivity is ∞) plasma interact via their electric fields. When the conductivity is infinite, plasma and magnetic field move together (i.e., frozen-in plasma), so that the Interplanetary Magnetic Field (IMF) (\mathbf{B}) moves at the same bulk speed as the solar wind (\mathbf{u}) (i.e., the electric field (\mathbf{E}) is in this case given by $\mathbf{E} = -\mathbf{u} \times \mathbf{B}$). After reaching the magnetopause (the boundary between Earth's magnetosphere and the surrounding plasma), solar wind IMF may reconnect to the geomagnetic field and allow particles to enter into the Earth's atmosphere.

There are physical and chemical interactions in the interior part of the Sun, that allow its energy to escape into space. Figure 2.2 illustrates the Sun's physical phenomena. The temperature of the Sun drops from $1.5 \times 10^7\text{K}$ in its core to $\sim 10^6\text{K}$ at its corona. This is not a linear trend because, at a 0.86 solar radius, the temperature profoundly decreases and increases again beyond the solar radius (Goodman, 2004). Several physical activities such as radiation, diffusion, convection and turbulence occur in different parts of the Sun, creating energy loss into space. Gravity waves, sound waves and magnetohydrodynamic (MHD) waves, CMEs, solar flares and solar

wind participate in moving solar energy from the convection zone to its surroundings. The Sun's outer region is called the corona which is fundamental to the occurrence of a geomagnetic storm.

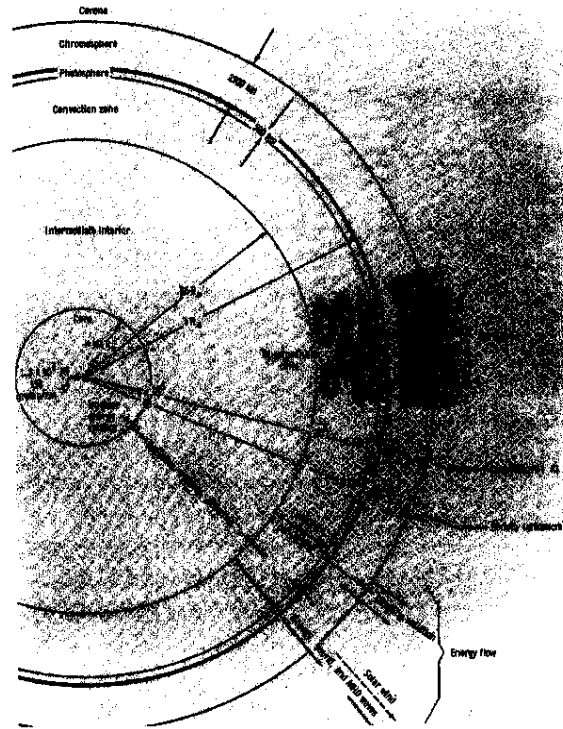


Figure 2.2: Solar energy streams to the surrounding space (Goodman, 2004).

2.1.3 Solar wind and Earth's magnetosphere

Coronal holes are regions in the Sun's corona, mainly at the poles, which are darker and less dense than the surrounding areas. A magnetic field which extends far from its source is known as an open magnetic field. The open magnetic field lines of solar coronal holes extends into interplanetary space (Chapman and Bartels, 1940; Bertotti and Farinella, 2012). There is a direct connection between the structure of the Sun's magnetic field and these coronal holes, and sometimes they may occur at low latitudes. Solar plasma moves radially. The magnetic field lines, that are anchored to the Sun, are then wound into a spiral by solar rotation (Moldwin, 2008; Gillies, 2012). The solar wind consists of protons, electrons, heavy ions, atomic nuclei of carbon, helium, nitrogen, oxygen, neon and magnesium moving radially at a speed of between 300 and 700 km/s (see Figures 2.1, 2.3 and 2.4 (Moldwin, 2008; Gillies, 2012)).

The magnetosphere is a region surrounding the Earth, with a magnetic field generated mostly by electrical currents circulating in the Earth's metallic core. Another part of the magnetic field is generated by the currents in the magnetosphere, such as the magnetopause and distributed currents (Olson and Pfitzer, 1974). Within the inner magnetosphere, the magnetic field has greater control over the motion of charged particles than other factors, i.e., the density of the energy of the geomagnetic field is greater than the density of the energy of its surrounding plasma (Goodman, 2004). The following equation summarizes this statement:

$$\frac{B^2}{2\mu_0} > nk_B T, \quad (2.1)$$

where B is the magnetic induction, μ_0 is the vacuum permeability, k_B is the Boltzmann's constant and n is plasma density at temperature T . The magnetic pressure is greater than the plasma pressure.

2.1.4 Bow shock, magnetotail, plasma sheet of the magnetosphere and field line reconnection

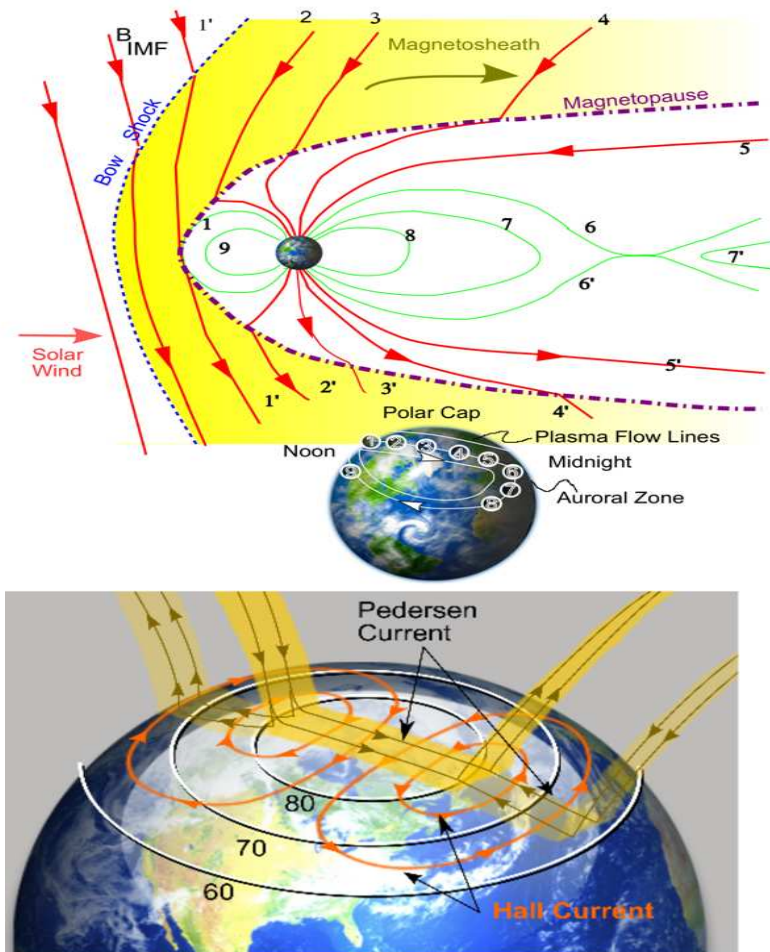


Figure 2.3: The top panel shows the IMF, bow shock and magnetic reconnection within the magnetosphere. The bottom panel shows the structures of the Pedersen and Hall currents (Gillies, 2012).

Figure 2.3 (top panel) shows the bow shock of the Earth's magnetosphere, a shock caused by solar wind. The latter normally moves at a supersonic speed $\gtrsim 340$ km/s on the day-side of the magnetosphere. The magnetosheath is a space between the bow shock and magnetopause. The magnetopause is located where solar wind pressure (ρv^2) and magnetospheric pressure are equal but opposite. When solar wind pressure becomes stronger in terms of its velocity and density, it causes the magnetopause to shift toward the Earth.

Magnetic reconnection happens when two field lines of opposite directions are brought together, just like magnets of opposite poles. When the IMF, which results from magnetized solar winds, interacts with one of the geomagnetic field lines to make a new common field, this is called magnetic reconnection (Moldwin, 2008; Gillies, 2012). It causes heightened magnetic activity. It tends to occur when the IMF is southward. Reconnection may also happen during northward IMF during relatively quiet magnetic activity. The solar wind (line 1') is connected with the Earth's northward-directed magnetic field (line 1) (see the top panel of Figure 2.3). After reconnection, two new field lines (2 and 2') are produced. One open field line sweeps out to the Earth's north pole (line 2), the other sweeps out to the southern pole, toward the outer space (line 2') after reconnection (Moldwin, 2008; Gillies, 2012). These open field lines guide some particles into the space outside of the magnetosphere. Different positions taken by these field lines are shown by lines 3-3', 4-4' and end with 5-5'. The open field lines formed by 5-5' with a cylindrical shape are known as the magnetotail. The magnetotail is made up of two magnetic lobe regions, one connected to the north polar cap (line 5) pointing toward Earth and the second one attached to the south polar cap (line 5') pointing away from the Earth. The separation between

the two lobes is a region of magnetic field and is called the plasmashet (Moldwin, 2008; Gillies, 2012). There are also plasmashet low-latitude boundary layer and high-latitude boundary layer regions.

The ionospheric plasma moves with the magnetic field in the polar cap F -region, from the noon sector towards the midnight sector, creating the background electric field. F -region dynamo is due to the solar wind, heating and gravitational lunar forcing. The convection plasma patterns moving across the magnetic field create the background convection electric field $\mathbf{E} = -\mathbf{u} \times \mathbf{B}$. Figure 2.3 (bottom panel) shows two components of the ionospheric currents. The first one is the current moving parallel to the electric field and it is known as the Pedersen current. The second one moves perpendicular to both the electric field and the magnetic field and it is known as the Hall current. The electric field that points from dawn to dusk in the magnetosphere is generated by the solar wind-magnetosphere interaction as shown in Figure 2.4. Plasma sheet flux tubes shift toward the Earth in a convective motion. This convective (or flux tube) motion takes place just after the reconnection as illustrated in Figure 2.3 (Moldwin, 2008; Gillies, 2012). These fluxes move back as lines 2', 2, 3',

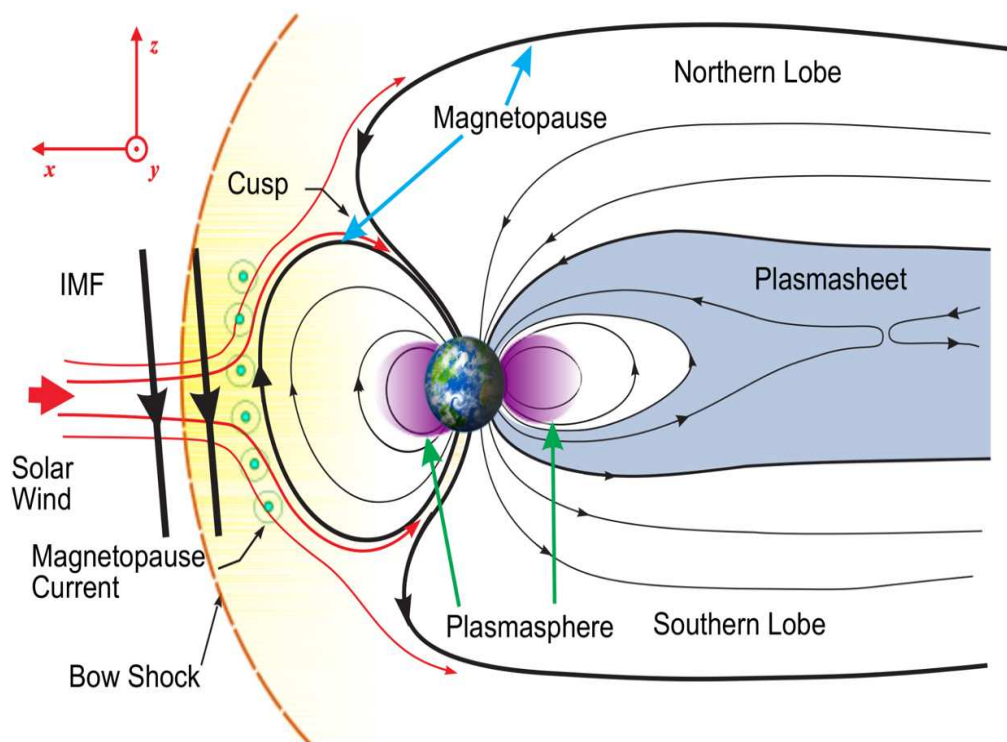


Figure 2.4: Magnetotail, magnetosheath and two lobes after the reconnection of magnetic field lines (Moldwin, 2008).

3, 4', 4 and finally form 5' and 5 (the magnetotail) during the night. The magnetotail in its convective motion towards the plasmashet, i.e., lines 6' from the south and 6 from the north, reconnects again at a neutral point as shown in Figure 2.4. They form a new field line 7 that takes energized particles into both polar regions, and another new field line 7' away from the Earth (see Figure 2.3) (Moldwin, 2008; Gillies, 2012). This process of reconnection and convection caused by the IMF and geomagnetic field results in energy transformation from a low-energy solar wind to a high-energy plasma sheet particles. In the case of the convection towards the Earth, the reconnection provides the energy input into the magnetosphere, which may produce a geomagnetic storm.

2.1.5 The ring current within the magnetosphere

The ring current is caused by gradient drift and curvature drift of plasmasheet particles and the effect of the magnetization current due to the spatial gradient of gyrating charged particles in the magnetosphere (Hargreaves, 1979; Kivelson, 1995; Moldwin, 2008; Bertotti and Farinella, 2012). Pressure from both the plasma (which can compress the geomagnetic field) and from a stream of particles from the Sun (see Figure 2.5), known as the solar wind, affects the magnetosphere. Assuming that the magnetic field is uniform and constant, the uniform motion of a particle with charge q and mass m is expressed by:

$$m \frac{d\mathbf{v}}{dt} = q(\mathbf{E} + \mathbf{v} \times \mathbf{B}) \quad (2.2)$$

where \mathbf{v} is the particle's velocity. The particle could move in the direction, parallel, perpendicular or circular to the magnetic field line. The perpendicular drift generates electric current J (or ring current) that in turn also produces an induced magnetic field. This current is defined by Bertotti and Farinella (2012):

$$J = \frac{nm u^2}{Br} \quad (2.3)$$

where n is the electron density, u is the velocity of the particle along a line of force and r is the radial position of the particle. Figure 2.5 shows current directions in the magnetosphere. The currents within the noon-midnight

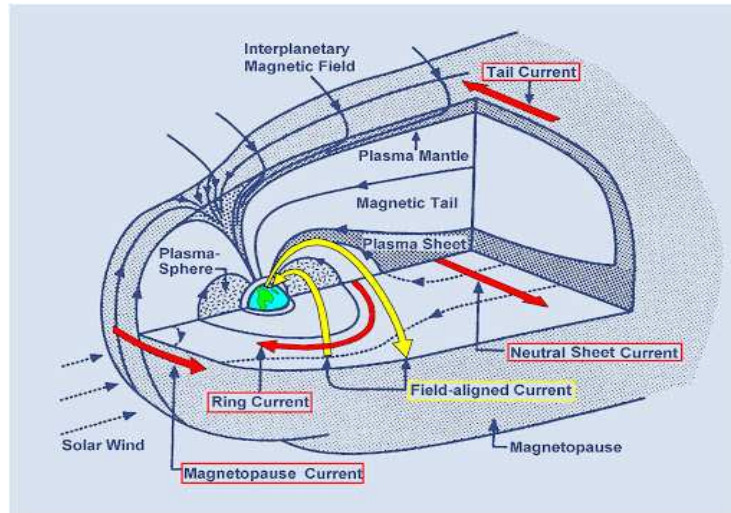


Figure 2.5: Earth's magnetosphere with its electrical currents. This shows both equatorial and noon-midnight meridional planes (adapted from Figure 4.3 in Moldwin (2008))

and equatorial planes are shown by solid arrows. The equatorial current indicated by a curved red line is referred to as the ring current, because it forms a circular path around the Earth. This current is caused by the magnetic gradient and curvature drift of plasma and the effect of the magnetization current due to the spatial gradient of gyrating charged particles. This current induces a magnetic field that weakens the geomagnetic field. The Disturbed Storm Time index (Dst) measures this field by using ground-based magnetometers located near the magnetic equator. When the Dst is negative, it indicates that the geomagnetic field has been weakened during an enhancement of the ring current. The field-aligned current links the ring current and the plasma sheet to the ionosphere and gives rise to the aurora as well as other phenomena.

2.2 Geomagnetic storms

A geomagnetic storm is induced when the magnetosphere energy input is associated with a southward IMF from ejected solar plasma, together with CMEs (defined in 2.1.2) or corotating interacting regions (CIRs). A CIR consists of high-speed charged particles ejected from the Sun's coronal holes. Other charged particles are injected into the magnetosphere by means of the solar wind. These particles generate a current in the magnetosphere, known as the ring current. When the ring current increases, it negatively affects the geomagnetic

field, i.e., it weakens. This current is measured by means of the Dst index based on the data generated by geomagnetic observatories located near the equator. The Dst index is a measure of the reduction of the horizontal component of the Earth's magnetic field. The Dst threshold that indicates a storm is usually less than ~ -30 nT (Borovsky and Denton, 2006) and sometimes, less than ~ -20 nT (Riley and Love, 2017). A geomagnetic storm displays three main phases:

- Initial Phase (IP): It is characterized by a rapid increase in the geomagnetic field due to the increase in the dynamic pressure caused by an increased stream of protons and electrons; in the solar wind, lasting for a few minutes. Upon hitting the Earth's magnetopause, a Sudden Commencement (SC) or Sudden Storm Commencement (SSC) is triggered. There is a sharp increase in the dynamic pressure of the solar wind which causes a rapid increase in the northward component of the Earth's surface magnetic field.
- Main Phase (MP): When the Z-component of IMF turns southward, the energy input into the magnetosphere is enhanced, which energizes the ring current. As a result of this energy input, there is a decrease in the horizontal component of the geomagnetic field, formed by the vector sum of the northward and the eastward components of the magnetic field at the equator. Due to differences in the velocities of the incoming solar wind particles, there is a variable delay of some of the particles, hence some of the particles interact with the magnetosphere at different times. Thus this phase may last for longer or less than a day.
- Recovery Phase (RP): The ring current weakens as the IMF turns to northward, resulting in geomagnetic field recovery. This phase may last for several hours and sometimes a few days.

Note that not all storms have all these three phases. Geomagnetic storms are classified according to their severity, represented by minimum Dst values. Storms could be weak, moderate, strong, severe, and great as indicated by their indices in the range, i.e., $[-30 -50]$ nT, $[-50 -100]$ nT, $[-100 -200]$ nT, $[-200 -350]$ nT, and $Dst < -350$ nT, respectively (Loewe and Prölss, 1997).

There is a relationship between geomagnetic storms and solar cycles, namely the closer in time to the solar maximum, the greater the number of storms, and conversely, the closer in time to the solar minimum, the smaller the number of storms (Hutchinson et al., 2011). The level of geomagnetic disturbance due to the solar wind is measured in the mid- and high-latitudes by the planetary index (Kp). The label 'K' comes from the German word "Kennziffer" meaning characteristic digit while 'p' is "planetarische" meaning planetary. This index characterizes geomagnetic activity on a scale of 0 (quiet) to 9 (extreme storm). It is derived from measurements of two horizontal geomagnetic components eight times in 24 hours (i.e., 0-3, 3-6, ..., 21-24 UT) at thirteen observatories (Matzka et al., 2021). The first three levels of Kp, i.e., Kp = 0 and 0+, Kp = 1-, 1, and 1+ and Kp = 2-, 2, and 2+, are associated with geomagnetically calm conditions. When such conditions exist the auroral oval, a big ring above the Earth's geomagnetic pole is faint, quiet, and barely visible to the unaided eye. The fourth and the fifth levels, i.e., Kp = 3-, 3, and 3+ and Kp = 4-, 4, and 4+ indicate unsettled and active conditions, respectively. The aurora changes color and becomes increasingly dynamic. At this stage, the northern lights are clearly visible with the naked eye. The sixth to tenth levels, i.e., Kp = 5-, 5, and 5+, Kp = 6-, 6, and 6+, Kp = 7-, 7, and 7+, Kp = 8-, 8, and 8+ and Kp = 9-, 9, and 9+, indicate storms from minor to intense. The brightness and movement of the aurora increase as it expands toward the mid-latitudes (<https://auroraforecast.is/kp-index/>).

Apart from geomagnetic storms, there are other smaller disturbances known as substorms. A substorm is a short disturbance in the geomagnetosphere that causes energy to be released from the "tail" of the magnetosphere and injected into the high-latitude ionosphere. At high latitudes the substorms may be visible in the auroras. Geomagnetic storms consist of many substorms, on average four times a day. They are characterized by increased in movement of auroral arcs. Auroral electrojets are horizontal electric currents that flow in the ionosphere of the auroral zone. They may cause intense geomagnetically induced currents (GICs) and are measured by considering global electrojet activity. GIC is the current induced by the variation in the electric currents in the magnetosphere and ionosphere during space weather events. Auroral electrojet (*AE*) indices estimates high-latitude auroral activity (Nakamura et al., 2015). The data of twelve observatories in the northern hemisphere are used to derive these *AE* indices. This index is defined by:

$$AE = AU - AL \quad (2.4)$$

with AU and AL defining the upper and the lower limits of the envelopes of the averaged values of the horizontal magnetic field components measured at stations in the polar regions. AU values indicate strong electrojet currents toward the east, while AL values indicate strong electrojet currents toward the west in the aurora. The AU and AL indices respectively increase and decrease under the aurora (Kamide and Rostoker, 2004; Nakamura et al., 2015).

2.3 Thermosphere and ionosphere

2.3.1 Introduction

The thermosphere and ionosphere are within the Earth's atmosphere. Life on Earth can be attributed to various gases, chemical phases, thermal and dynamical structures, resulting in organic molecules. The Earth's outer appearance is determined by its atmosphere. Fluid dynamics is affected by gravitational and the Coriolis force. The dynamics involve local meteorological conditions, global circulation and energy transfer. Changes in the Earth's atmosphere are controlled by the Sun's activities (Bertotti and Farinella, 2012).

The Earth's atmosphere is divided into five different regions (layers).

The first layer from the ground is the troposphere which varies between 0 and ~ 9 km (at the geographic pole) and ~ 17 km at the equator. Its average altitude range is ~ 12 km. The second layer from the ground is called the stratosphere. It follows the troposphere at ~ 12 km to the stratopause at an altitude of ~ 50 - ~ 55 km. The third layer from the ground is the mesosphere. It is located between ~ 50 and ~ 80 - ~ 90 km. The fourth layer is the thermosphere. This layer is located between ~ 80 - ~ 90 and ~ 500 - ~ 1000 km. The fifth layer from the ground is called the exosphere. It starts from ~ 700 km and goes up to $\sim 10\,000$ km. Table 2.1 shows five layers with their altitude range in km. The troposphere and stratosphere details are not given here because

Layer	altitude range (km)
Troposphere	0 to ~ 9 - 17
Stratosphere	~ 9 - 17 to ~ 50 - 55
Mesosphere	~ 50 - 55 to ~ 80 - 90
Thermosphere	~ 80 - 90 to ~ 400 - 700
Exosphere	~ 400 - 700 to 10000

Table 2.1: Layers of Earth's atmosphere

they are beyond the scope of this thesis. The chemical composition and thermal energy in thermosphere are discussed in the following subsection. Descriptions of the mesosphere, thermosphere and exosphere follow in the description of ionospheric layers.

2.3.2 Thermosphere

The Earth's thermosphere is a layer above the mesosphere. This region's chemical composition during the day is: H , H_e , O , O_2 , and N_2 . In this region, the solar EUV source causes various excitation mechanisms (Mayr and Harris, 1977; McNamara, 1991). This layer is mostly dominated by solar and tidal heating. The solar EUV photon absorption in the middle and upper thermosphere causes ionization through photoelectrons, which causes Coulomb collisions with electrons and ions and inelastic collisions with neutrals. When the photoelectrons slow down, there is a production of hot electron gas and an increase in the neutral gas temperature. In this region, solar radiation is the dominant heat source. Photons dissociate O_2 to produce metastable atomic oxygen and release their excess energy in the form of neutral heating. At high latitudes, the dominant thermal energy mechanisms are the following:

- Joule heating caused by friction due to differential ion and neutral motions,
- heating caused by auroral particle precipitation and
- Lorentz coupling due to the presence of particles moving within the electric and magnetic fields.

Neutral winds can change the Joule heating rate by changing the ion-neutral differential velocity. Mostly during solar maximum, the cooling effects are caused by radiative constituents, such as NO and CO_2 . The cooling effect takes place when there is a drop in species temperature. Thermospheric circulation is controlled by pressure-gradient forces, which also contribute to the increase in temperature. Energy is also transferred into the thermosphere from the lower part of the Earth's atmosphere via the upward propagation of tides and gravity waves.

2.3.3 The Earth's ionosphere

2.3.3.1 Introduction

The ionosphere is so-named because it is composed of ionized particles, mainly O^+ , N_2^+ , and O_2^+ (Schunk and Nagy, 2000, 2009). A great number of the ionospheric layers is formed by UV radiation through photoionization and photodissociation. The temperature in this region increases exponentially upward with altitude. The relative motion of electrons and ions, due to their differing collision rates with neutral particles, create different currents systems at different altitudes in the E -region of the ionosphere. A global electric field pointing from dawn to dusk of the Earth's polar regions is generated by the solar wind by means of the hydrodynamic dynamo process. In this region, the electric Pedersen currents may create Ohmic heating, also known as Joule heating, which may trigger TIDs in the ionosphere (Bertotti and Farinella, 2012). Appleton named the three essential regions of the ionosphere, known as the D -, E - and F -regions (Appleton and Barnett, 1925). He first discovered an area, now referred to as the E layer, which reflects the electric field of radio waves. Subsequently, he named the region on the top of the E region the F region. Finally, he discovered a layer below the E region, named the D region, in line with the alphabetic order (Schunk and Nagy, 2000, 2009).

The mesosphere, thermosphere and exosphere compose the neutral part of the ionosphere. It is made up of plasma (ions and electrons) with neutrals, at an altitude of between ~ 50 and ~ 1000 km and encircles the Earth. When high-frequency (HF) radio signals propagate through this natural layer, they may be reflected to the ground and/or be refracted to a higher altitude. Free electrons and ions in this region result from the interaction of energetic extreme ultraviolet (EUV) radiation and X-rays, mainly from the Sun, during the day. Atoms are energized by EUV radiation, freeing their electrons and leaving behind heavy ions. This process is called photoionization. This process is reversed when negatively charged electrons recombine with positively charged ions to form neutral atoms during the night. Recombination is a process that enables the restoration of neutral atoms and decreases the electron density. However, because the rate of recombination is a slower process than ionization, free electrons are available all the time, especially in the F -region.

Oxygen atoms are the most common species populating the F_2 -region (the upper layer of the ionosphere). This has been confirmed by satellite and rocket measurements. The O^+ ions are produced by means of photoionization and the process is described in the following expression:



where h is Planck's constant, ν is the frequency given by c/λ , $h\nu$ is the photon energy, the speed of light in a vacuum is denoted by c and λ is the wavelength (McNamara, 1991; Zolesi and Ljiljana R, 2014; Hiyadutuje et al., 2016).

2.3.3.2 Regions of ionosphere

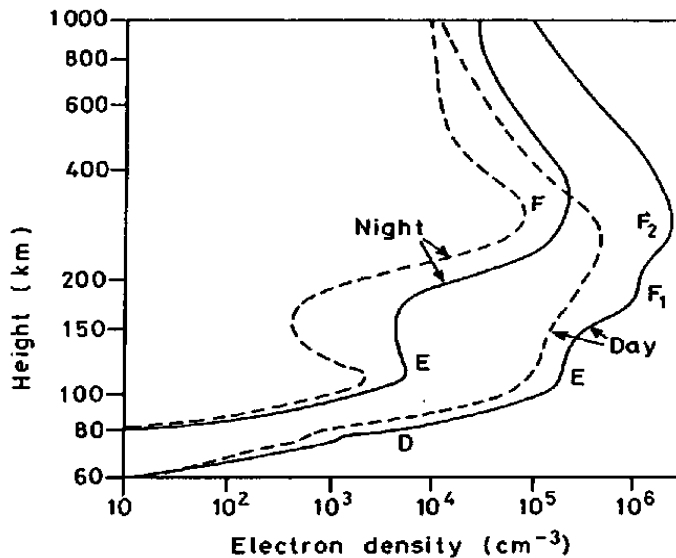
The ionosphere has a bottom side and a topside (McNamara, 1991). The plasma density of the topside depends mostly on the presence of neutral particles to be ionized and on the EUV intensity. Above 350 km, there are fewer neutral particles for ionization, hence this region is sparsely populated by electrons and ions. Below 200 km, despite the abundance of neutral atoms for ionization, the EUV is weak because a significant amount of its energy is absorbed before reaching this altitude, i.e., the ionization is not substantial. Maximum ionization takes place at altitudes between 200 and 350 km. Here there are sufficient species for ionization, and the EUV is strong enough to supply the required energy. Generally, the ionosphere has four layers known as the D , E , F_1 and F_2 regions during the day. They are differentiated by their particular type of species. Each species requires a specific wavelength of EUV radiation in order to be absorbed. A few minutes after sunset the F_2 and F_1 regions become a single layer known as the F region.

The D region is located between ~ 50 and ~ 90 km above the Earth's surface and has an electron density of

$10^2 - 10^3 \text{ cm}^{-3}$ (as shown in Figure 2.6) and the density of neutral species is in the order of 10^{14} cm^{-3} . There are numerous negative ions formed by electron attachment to O and O_2 , associative detachment ($O + O^- \rightarrow O_2 + e^-$) and mutual neutralization ($O^- + A^+ \rightarrow O + A$ where A stands for a neutral atom), may also occur.

Between ~ 90 and ~ 150 km, another layer called the E region, is found. The electron density in this region varies between 10^3 and 10^5 cm^{-3} (as shown in Figure 2.6). The F_1 region is found between ~ 150 and ~ 200 km, and has an electron density in the order of $10^5 - 10^6 \text{ cm}^{-3}$ (as shown in Figure 2.6). Another layer of the ionosphere, known as F_2 region, lies between ~ 200 and 350 km. Its electron density varies between 10^5 and 10^6 cm^{-3} (as shown in Figure 2.6), while its neutral atmosphere is $\sim 10^8 \text{ cm}^{-3}$ (McNamara, 1991; Zolesi and Ljiljana R, 2014; Hiyadutuje et al., 2016).

In E -region of the low-, mid- and high-latitudes, a sporadic ionospheric layer E_s may be formed. When the east-west neutral wind blows across the magnetic field in an electric field, heavy ions are moved up and down between ~ 90 and ~ 140 km in the E region, forming a layer at the height where the wind reverses occur. Wind shear is considered the mechanism by which the E_s -layer in the mid-latitude regions is formed. Due to the fact that the magnetic field is nearly vertical at the poles, E_s layers are not generally associated with the wind shear theory, but are mainly caused by solar radiation and particle precipitation (Gubenko and Kirillovich, 2019). Near the poles in the high latitudes, E_s layers are associated with the aurora, mostly at night, and their electron density is nearly the same as that of the F region (see Figure 2.6). Sunspot numbers, seasons, local time, and geographic location influence the appearance of E_s layers (Gubenko and Kirillovich, 2019). These layers may be used as mirrors to reflect radio waves. The topside ionosphere extends from 350 to 1000 km. Due to its high electron density, HF radio wave signals sent to this region may be absorbed. Instruments such as ground-based ionosondes are not used to study the topside ionosphere due to the F -region peak plasma frequency. Above the peak altitude, only waves with higher frequencies than the critical frequency can propagate and they are not reflected at all. A huge number of energetic particles enter the ionosphere and contribute



(Hargreaves, 1995; Zolesi

and Ljiljana R, 2014).

Figure 2.6: The mid-latitude ionospheric regions and their electron density. The solid lines show solar maximum values during the day and night, while the dashed lines show the solar minimum values

to the generation of more free particles. It is different during quiet conditions, when the solar zenith angle determines the level of ionization and the ionospheric electron density of these regions. The zenith angle is the angle between the vertical direction and the Sun's rays. From the Cancer and Capricorn tropical zones toward the poles, the zenith angle increases and as a result, photoionization reduces. The production rate of free particle is higher when the zenith angle is close to zero. At noontime, we expect the level of ionization is assumed to be at its maximum. During midnight, the zenith angle is $\geq 90^\circ$. This leads to a lower ionization level. The recombination rate, which removes ionospheric free electrons, increases progressively during the

period from sunset to midnight. Significant depletion of free electrons occurs during the night, but during the day, the ionosphere is again populated with many free electrons (see Figure 2.6). The D , E , F_1 and F_2 regions all appear during the day, however at night D and F_1 vanish while the E region sometimes doesn't, and only F_2 remains during the night.

The ionization of atmospheric species varies from season to season, due to the variation in the Sun's position relative to the Earth's rotation axis. In summer the Sun is almost overhead at noon at the equator and the lower part of the mid-latitude, thus ionizing more atoms. At the higher part of mid-latitude and the whole high-latitude, the Sun does not come overhead, hence the solar ionization is less into these regions. At high-latitude, there are other factors that may contribute to the ionization, such as particle precipitation, and others. The Sun is almost overhead at noon, but it disappears after sunset, hence the ionization is at its maximum at noon in the low- and mid-latitudes regions. At high latitudes, the ionization is higher in summer than in winter, when the only ionization mechanism is solar radiation. The zenith angle is always greater in winter than the equivalent zenith angle in summer. Therefore, ionization is lower in winter than in summer.

The ionization level also depends on the duration of the 11-year solar cycle, which is ~ 11 years. The minimum or maximum number of sunspots are related with the low or high ionospheric electron density, respectively. This was confirmed after a study of the monthly median of their respective values (McNamara, 1991; Zolesi and Ljiljana R, 2014). Sometimes the electrons are not equally distributed in the ionosphere, causing small-scale disturbances called ionospheric irregularities.

Electric and magnetic fields significantly contribute to the formation of ionospheric irregularities. Electrons are captured by the strong magnetic field, prohibiting the easy flow in a horizontal direction. This enables the neutral wind's steady motion to blow these particles along the magnetic field lines. A constant convection pattern is driven by the polar electric field together with the Earth's rotation. A continuous plasma density irregularity of higher concentration may be formed by global plasma convection within the polar cap regions. When there is high energy input efficiency and strong Joule heating a phenomenon called the tongue of ionization may take place (Horvath and Lovell, 2016). During geomagnetic storms, the convection pattern expands and the drift speeds increase. As a result of this expansion, a depletion and increase the plasma density occur, modifying the plasma structure in polar ionospheric regions.

Plasma density perturbations called Field-Aligned Irregularities (FAIs) in the E and F regions are associated with the magnetic field. The $\mathbf{E} \times \mathbf{B}$ drift velocity of the plasma in F_2 -region is measured to understand these convection patterns, for example, SuperDARN can provide these measurements. SuperDARN radars transmit signals which are coherently returned by these kinds of irregularities. Power transmitted and received by SuperDARN is discussed in greater detail in chapter 3.

2.3.3.3 Variation of the ionosphere

Latitude, diurnal cycle, seasons and solar activity contribute to the structure of the ionospheric plasma. The ionosphere at different latitudes has different features:

- Based on geomagnetic coordinates, the low latitudes are the regions from 0° to $\pm 20^\circ$, also known as equatorial regions (Huba et al., 2005; Imtiaz et al., 2020). Geomagnetic field lines are nearly parallel to the Earth's surface. In this region, at the altitude of the F_2 -region, a well-known phenomenon named the equatorial ionization anomaly (EIA) takes place. The pressure gradient and $\mathbf{E} \times \mathbf{B}$ together act against gravity to lift the plasma, which then diffuses downward following the field lines to the south and north of the equator. During the day, an eastward electric field is involved in this process, also known as the fountain effect. This anomaly greatly depletes the electrons near the geomagnetic equator and populates the region near 15° north and south of the trough. For example, there is a fountain effect at $\sim 50^\circ$ west longitude, where the magnetic and geographic equator cross each other (<https://svs.gsfc.nasa.gov/4617>). The anomaly may occur at different longitudes close to the equator.

The mid-latitudes cover the area between the geomagnetic latitudes $\pm 20^\circ$ and $\pm 60^\circ$ (Huba et al., 2005; Imtiaz et al., 2020). This is where photoionization and recombination processes are almost balanced. Upward thermospheric winds displace ions in the same direction, but electrons are pushed into an almost perpendicular direction. A drag force results from the collision between particles and neutral gases, and

in the presence of the magnetic field it produces the Lorentz force. The Lorentz force and electric current push ions and electrons in the wind's direction. This causes differential motion. The dynamo region is a result of an electric current associated with wind. The electric field and neutral winds disturb the plasma up and down, then enhancing/depleting mid-latitude electron density at the ionospheric altitudes. When the Sun rises, plasma shifts along the magnetic field lines to higher altitudes, while the protons flow back downward in the evening.

- The high latitudes are located between the geomagnetic latitudes $\pm 60^\circ$ and $\pm 90^\circ$, where the magnetic field is almost perpendicular to the Earth's surface, pointing downward and upward on the north and south poles, respectively. The Earth's magnetic field structure allows charged particles from the Sun to gyrate around field lines and reach the ionosphere through the cusp regions. A part of these charged particles comes from within the magnetosphere. The equation of motion of those particles at different altitudes is expressed by Schunk and Nagy (2000, 2009):

$$m_\alpha \frac{d\mathbf{v}_\alpha}{dt} = q_\alpha(\mathbf{E} + \mathbf{v}_\alpha \times \mathbf{B}) - \nu_{\alpha n} m_\alpha (\mathbf{v}_\alpha - \mathbf{u}_n) - \frac{\nabla(n_\alpha T_\alpha)}{n_\alpha} \pm m_\alpha \nu_{ei} (\mathbf{u}_e - \mathbf{u}_i) + m_\alpha \mathbf{g} \quad (2.6)$$

where \mathbf{E} , q_α , \mathbf{B} , \mathbf{u}_n , ν_{ei} , \mathbf{g} , $\nu_{\alpha n}$, m_α , \mathbf{v}_α , T_α (in eV), and n_α , are the electric field, charge of the particle, geomagnetic field, neutral wind velocity, electron/ion collision frequency with neutrals, acceleration due to gravity, momentum transfer collision (α -neutral) frequency, mass, velocity, temperature and number density of the particle α , respectively. Note that equation (2.6) is also valid at middle and low latitudes. Coulomb collisions between electrons and ions are neglected assuming that $\nu_{\alpha n} \gg \nu_{ei}$ valid below 200 km. The relative drift velocity $\mathbf{v}_{\alpha\perp}$ is expressed by:

$$\mathbf{v}_{\alpha\perp} = \frac{1}{1 + \left(\frac{\nu_{\alpha n}}{\Omega_\alpha}\right)^2} \left[\frac{\nu_{\alpha n}}{\Omega_\alpha} \frac{\mathbf{E}'_\perp}{B} + \frac{\mathbf{E}'_\perp \times \mathbf{B}}{B^2} \right] \quad (2.7)$$

where Ω_α or $\omega_B^\alpha = \frac{q_\alpha B}{m_\alpha}$ represents the gyrofrequency of the particle α , and $\mathbf{E}'_\perp = \mathbf{E}_\perp + \mathbf{u}_n \times \mathbf{B}$ (Gillies, 2012). The square of $\frac{\nu_{\alpha n}}{\Omega_\alpha}$ term greatly influences the relative velocity between ions and electrons. Equation (2.7) demonstrates the relative drift velocity between ion and electron motion when $\nu_{\alpha n}$ is high enough. The first term shows how those particles move along the electric field, while the last term indicates the drift associated with the cross product between electric and magnetic fields. The ratio of ion-neutral or electron-neutral collision frequencies to the ion or electron gyro-frequencies, respectively, affect the direction and magnitude of this drift velocity. Figure 2.7 (top panel) shows that at a near 100 km altitude, the electron gyro-frequency is much greater than the electron-neutral collision frequency. At the same altitude, its bottom panel shows that the electrons move faster than ions along the x-direction. At the same altitude the ion gyro-frequency is very much less than the ion-neutral collision frequency. Beyond an altitude of 150 km the electron density is the highest, but with less neutrals compared to the altitude below 150 km. At this altitude, particles are highly magnetized and are said to be "frozen-in" to the magnetic field. This magnetization is the result of an electron gyro-frequency that is much greater than the collision frequency of those particles. Considering this fact, the ratio between the two frequencies tends to approach zero, and from equation (2.7) the drift velocity \mathbf{v}_{EB} of those particles will only depend on its second term, i.e., convection:

$$\mathbf{v}_{EB} = \frac{\mathbf{E} \times \mathbf{B}}{B^2}. \quad (2.8)$$

Figure 2.7 (bottom panel), shows particle velocity and current at 100, 120, and 160 km altitudes. The magnetic field points along the z-axis, electric field along the y-axis and the x-axis points in the direction perpendicular to both \mathbf{B} and \mathbf{E} -fields. At 100 km, ions have a small component of \mathbf{v} along the \mathbf{E} -field direction, while the electrons take the \mathbf{v}_{EB} direction. This is due to the fact that the ion-neutral collision frequency is high at this altitude. The ion motion direction changes slightly from ~ 110 to ~ 150 km, due to the decrease in their collisions with neutrals, and the direction of their velocity is different to that of \mathbf{v}_{EB} , causing the current to move in the \mathbf{E} -field and $\mathbf{E} \times \mathbf{B}$ directions. The two components of this current is presented graphically in the bottom panel of Figure 2.3. In the E -region, the Hall current perturbs the magnetic field and its intensity can be monitored by ground-based magnetometers. The Pedersen cur-

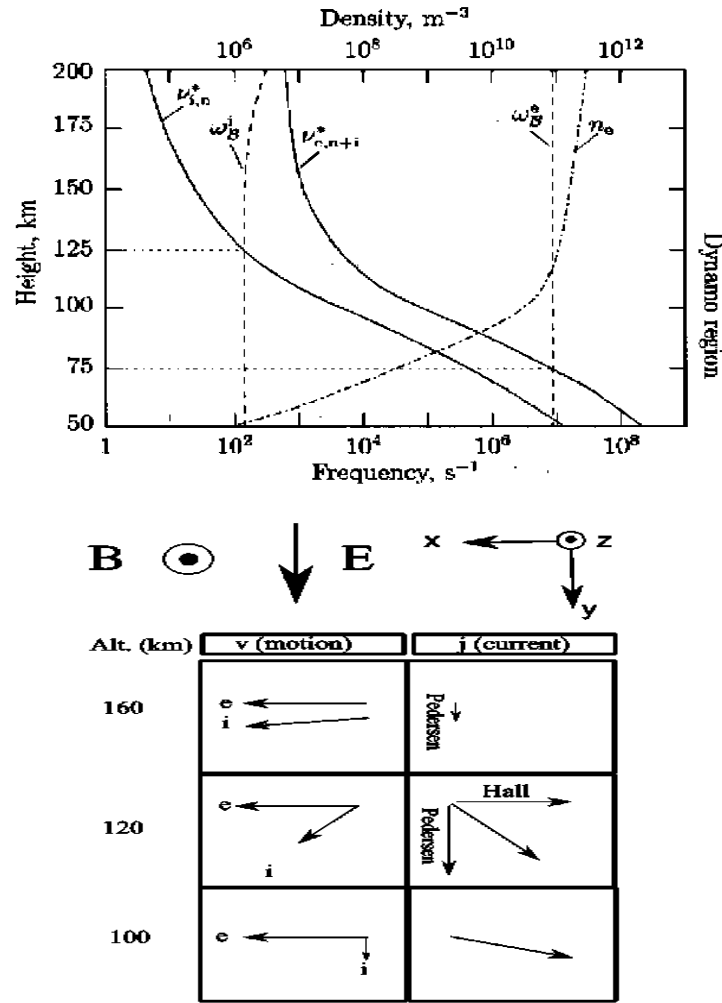


Figure 2.7: The top panel illustrates the ion-neutral, electron-neutral collision and gyro-frequencies while the bottom panel shows different directions of current caused by different relative motion between ions and electrons in the magnetic and electric fields (Leake et al., 2014; Gillies, 2012).

rent moves in the direction of \mathbf{E} -field and is very small at 100 km altitude. Despite its intensity, Pedersen current is very important in the generation of F -region irregularities. At around 160 km, the ions and electrons move nearly together in the same direction. The Hall (Σ_h) and Pedersen (Σ_p) conductivities are expressed by the following equations described by Schunk and Nagy (2000, 2009);

$$\Sigma_h = -\sum_i \sigma_i \frac{v_i \Omega_i}{v_i^2 + \Omega_i^2} + \sigma_e \frac{v_e \Omega_e}{v_e^2 + \Omega_e^2} \quad (2.9)$$

and

$$\Sigma_p = \sum_i \sigma_i \frac{v_i}{v_i^2 + \Omega_i^2} + \sigma_e \frac{v_e}{v_e^2 + \Omega_e^2}. \quad (2.10)$$

Where $\sigma_i = \frac{n_i e_i^2}{m_i v_i}$, $\sigma_e = \frac{n_e e_e^2}{m_e v_e}$, $\Omega_i = \frac{|e_i B|}{m_i}$, and $\Omega_e = \frac{|e_e B|}{m_e}$. Equations (2.9) and (2.10) can be re-written as integral forms:

$$\Sigma_h = \frac{q}{B} \int \left[\frac{1}{1 + v_{en}^2 / \Omega_e^2} + \frac{1}{1 + v_{in}^2 / \Omega_i^2} \right] n_e dh \quad (2.11)$$

and

$$\Sigma_p = \frac{q}{B} \int \left[\frac{v_{en}/\Omega_e}{1 + v_{en}^2/\Omega_e^2} + \frac{v_{in}/\Omega_i}{1 + v_{in}^2/\Omega_i^2} \right] n_e dh \quad (2.12)$$

where q , B , n_e and h are the charge, magnetic field intensity, electron density and altitude, respectively.

Upon moving into both polar regions, electrons produce collisional ionization with atoms of the neutral atmosphere. Collisional ionization then gives rise to a feature named auroral oval at an altitude of about 100 km. The auroral ovals are caused by particle precipitation from the plasmasheet in the magnetosphere. The solar wind variation affects the size of the auroral ovals by either contracting or expanding them. When the magnetosphere is not disturbed, the auroral oval shrinks to a small band of limited latitudinal degree. Its size increases toward the equator when the magnetosphere is affected by disturbances originating from solar activity.

2.3.3.4 Radio wave absorption in the ionosphere

A radio wave is transmitted as a form of energy which can be absorbed by the ionosphere. The atmosphere is made up of different species, including particles such as electrons. When the wave passes through them, its energy may be absorbed by those species by means of collision with neutral atoms. Wave absorption occurs when there are sufficient electrons and neutrals, for example in the D -region with elevated electron density due to a solar flare, substorm particle precipitation, or solar proton events etc. Electrons again release the energy in the same way as a radio wave. This energy transfer continues from one electron to another until the radio wave suffers either refraction or reflection. If the transmitted wave signal has the same intensity, frequency, amplitude and power as the received wave, the wave hasn't been absorbed. Absorption takes place when there is a decline in one, many or all of the above-mentioned wave parameters.

When the energetic electron encounters a positively charged ion, there will be a recombination to neutralize the electric charges. Some of the electron energy is lost during recombination and the remainder is converted to heat. Energy is also lost when there is a collision between the electron and a neutral atom. An atom is heavier than an electron. Consequently, the atom after collision with an electron vibrates at a frequency lower than a radio wave. When this happens, the atom increases its speed, transforming a part of the wave energy to mechanical energy, and causing radio wave energy loss. Electron collision with other species convert radio wave energy into heat. Absorption is significant in the D -region and bottom part of E -region, because the neutral density and collision frequency are higher than in F_2 region. The density of atmospheric particles in the D - and lower E -region is much higher than the density in the higher E - and F -regions. Hence, the chance of a collision between an electron and atom is higher in the D - and lower E -region. The absorption in the D and E regions is called non-deviative absorption, while in the F region it is due to the low refractive index and is called deviative absorption (Zawdie et al., 2017). Radio waves are better absorbed during the day than during the night, because the D -region disappears at night (see Figure 2.6). This is very important in the use of HF SuperDARN radars and ionosondes instruments. During the absorption, those instruments do not receive any backscatter, and hence causes a data gap.

An increase in electron density caused by intense solar activity significantly affects absorption. Geometrical orientation, also known as the polarization of a radio wave, is another parameter which influences absorption. Normally, electrons gyrate around the magnetic field lines in the absence of collisions. Electrons could speed up or slow down due to the electric field possessed by circularly polarized waves. Radio wave energy absorbed by gyrating electrons increases their mechanical energy, hence the increased possibility of colliding with neutrals and losing energy. Electrons accelerated by extraordinary waves, also known as X-waves, are decelerated by ordinary waves, also known as O-waves. As a consequence, X-waves are more affected in terms of absorption than the O-waves. X-wave energy can be absorbed when its frequency is the same as that of the electron moving around the magnetic field line, and such a wave is completely absorbed in that medium (McNamara, 1991; Zolesi and Ljiljana R, 2014; Hiyadutuje et al., 2016).

In its propagation through the atmosphere, the refractive index n of a radio wave is expressed by:

$$n = \frac{c}{v}. \quad (2.13)$$

In the case of macroscopic changes in n , refraction and/or reflection takes place, but microscopic changes result in the scattering of the radio wave signal. In the HF to UHF bands, n in the altitude range between the Earth's surface and the thermosphere can be estimated using the following equation:

$$n - 1 = \frac{3.75 \times 10^{-1} p_w}{T^2} + \frac{7.76 \times 10^{-5} P}{T} - \frac{N_e}{2N_c} \quad (2.14)$$

where p_w (mb), P (mb), T (K), N_e , and N_c is the water vapor partial pressure, the total atmospheric pressure, absolute temperature, electron number density, and the critical plasma density, respectively (Sato, 1989). The Appleton-Lassen dispersion relation for radio wave propagation describes the refractive index n of the plasma (Norman et al., 2013) and it is expressed by:

$$n^2 = 1 - \frac{X}{1 - iZ - \frac{(Y \sin \theta)^2}{2(1 - X - iZ)} \pm \sqrt{\frac{(Y \sin \theta)^4}{4(1 - X - iZ)^2} + (Y \cos \theta)^2}} \quad (2.15)$$

where the normalized frequencies X , Y , and Z are expressed by:

$$X = \frac{\omega_{pe}^2}{\omega^2} = \frac{n_e e^2}{\epsilon_0 m_e \omega^2}, \quad (2.16)$$

where ω_{pe} is the electron plasma frequency.

$$Y = \frac{\omega_{ge}}{\omega} = \frac{eB}{m_e \omega} \quad (2.17)$$

where ω_{ge} is the electron gyro-frequency, and

$$Z = \frac{v_{en}}{\omega}. \quad (2.18)$$

Where e , ϵ_0 , m_e , ω and B are the charge unit, permittivity of free space (vacuum), mass of electron, angular frequency of the radio wave and external magnetic field of the Earth obtained within a dipole field approximation, for this case, respectively (Sen and Wyller, 1960; Zawdie et al., 2017). The angle between the wave vector and the direction of the magnetic field is symbolized by θ . Here v_{en} is expressed by the following formula (Pashin et al., 1995):

$$v_{en} = 1.7 \times 10^{-11} [N_2] T_e + 3.8 \times 10^{-10} [O_2] \sqrt{T_e} + 1.4 \times 10^{-10} [O] \sqrt{T_e} \quad (2.19)$$

where the neutral densities in square brackets are measured in cm^{-3} , while electron temperature T_e is in Kelvin. The imaginary part of n shows the damping of a radio wave. The wave is damped because a part of its energy is absorbed by the plasma. The ionosphere is considered to have a series of layers with different refractive indices. For example, in communication systems, the HF radio wave velocity v changes with the altitude. Using Snell's law, it follows that:

$$\frac{\sin i_j}{\sin i_{j+1}} = \frac{v_j}{v_{j+1}} = \frac{n_{j+1}}{n_j} \quad (2.20)$$

where $j = D, E, F_1$ represents the ionospheric layers. Equation (2.20) $j + 1$ indicates the next layer from the bottom upward, for example, if $j = D$, then $j + 1 = E$, if $j = E$, then $j + 1 = F_1$, and if $j = F_1$, then $j + 1 = F_2$. Figure 2.8 shows a radio wave refraction and reflection from the transmitted T or D to the receiving R or D point, for oblique or vertical sounding systems, respectively. When the plasma frequency increases, the refractive index decreases. The radio wave reaches its reflection altitude before the virtual height (E), which is caused by the change of speed as it travels through the different layers. Only waves traveling at a constant speed can reach the point (E) (Davies, 1990; Hargreaves, 1995; Fabrizio, 2013). The refraction and/or reflection of a radio wave occurs in the ionospheric region when $\omega \leq \omega_{pe}$ (see equation 2.16) for vertical propagation. When the propagation is oblique, the refraction or reflection occurs even when $\omega > \omega_{pe}$. Otherwise, the wave continues straight through the ionosphere without reflection and goes into outer space. There are two absorption modes: The first mode is non-deviative (i.e., $v_e/\omega > 0$) absorption in the lower part of the ionosphere. In this case, an

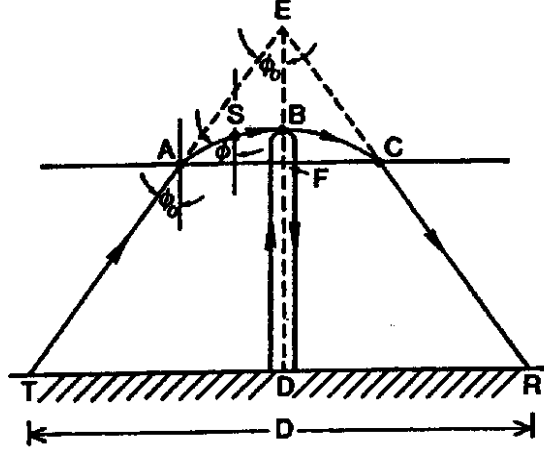


Figure 2.8: Radio wave propagation in the ionosphere, showing the comparison between vertical and oblique sounding systems (Hargreaves, 1995; Fabrizio, 2013).

approximation of the absorption coefficient κ is expressed by:

$$\kappa = \frac{e^2}{2\epsilon_0 m c} \frac{1}{\mu} \frac{n_e v_e}{v_e^2 + (2\pi f \pm \omega_{ecf} \cos \theta)^2}. \quad (2.21)$$

Here f is the wave frequency, ω_{ecf} is the electron cyclotron frequency, θ is the angle between the direction of propagation (\mathbf{k}) and the Earth's magnetic field, and the signs + and - indicate the O- and X-mode polarization of radio waves (Davies, 1990). The dispersion relation for ordinary waves is expressed by:

$$\omega^2 = \omega_{pe}^2 + c^2 k^2 \quad (2.22)$$

where $\mu_0 \epsilon_0 = 1/c^2$, its cut-off frequency occurs when $k \rightarrow 0$, i.e., $\omega = \omega_{pe}$ and it doesn't have a resonance frequency, i.e., for $k \rightarrow \infty$. These waves can only propagate when $\omega > \omega_{pe}$ (Schunk and Nagy, 2000, 2009; Francis, 2016). The dispersion relation of extraordinary waves is expressed by:

$$\omega^2 = k^2 c^2 + \omega_{pe}^2 \left[\frac{\omega^2 - \omega_{pe}^2}{\omega^2 - (\omega_{pe}^2 + \omega_{ce}^2)} \right]. \quad (2.23)$$

When wavenumber $k \rightarrow 0$, there is a cut-off frequency for these waves. In this case, the equation (2.23) is reduced to equation (2.24).

$$\omega^2 = \omega_{pe}^2 \left[\frac{\omega^2 - \omega_{pe}^2}{\omega^2 - (\omega_{pe}^2 + \omega_{ce}^2)} \right] \quad (2.24)$$

which can be rearranged to give:

$$\omega^2 \pm \omega \omega_{ce} - \omega_{pe}^2 = 0, \quad (2.25)$$

where the negative sign in equation (2.25) is for negative k , i.e., waves that propagate in the opposite direction. Frequencies with a positive sign are considered here only. Solving the quadratic equation (2.25), one would get two roots in equations (2.26) (the right-hand cut-off frequency) and (2.27) (the left-hand cut-off frequency):

$$\omega_R = \frac{1}{2} \left[\omega_{ce} + (\omega_{ce}^2 + 4\omega_{pe}^2)^{1/2} \right] \quad (2.26)$$

and

$$\omega_L = \frac{1}{2} \left[-\omega_{ce} + (\omega_{ce}^2 + 4\omega_{pe}^2)^{1/2} \right]. \quad (2.27)$$

When $\omega < \omega_L$ or $\omega_{pe}^2 + \omega_{ce}^2 < \omega < \omega_R$, there would be no propagation. By contrast, when $\omega_L < \omega < \omega_{pe}^2 + \omega_{ce}^2$ or $\omega_R < \omega$, the extraordinary waves propagate (Schunk and Nagy, 2000, 2009; Francis, 2016).

The second mode is deviative absorption (i.e., $v_e < \omega$) in the F layer. In this case the absorption coefficient κ is expressed by:

$$\kappa = \frac{v_e}{2c} \left(\frac{1}{\mu} - \mu \right) \quad (2.28)$$

where $\mu = 1 - X$. The absorption becomes very high as the radio wave comes closer to the reflection point, since μ reduces towards zero as the wave slows down. Radio wave absorption in decibel is expressed by: $A(\text{dB}) = 10 \log_{10} \left(\frac{P_T}{P_R} \right)$, where P_T and P_R are the transmitted and received power, respectively. SuperDARN signals are sometimes absorbed due to ionospheric irregularities, very low ionospheric electric field and sometimes through the D -region (Gauld et al., 2002). AGWs observed by these radars as TIDs may also affect the propagation of radio signals. More details on SuperDARN transmitted and received power is given in chapter 3.

2.4 Atmospheric waves and traveling ionospheric disturbances

2.4.1 Introduction

Waves in the Earth's atmosphere are generated by both external and internal perturbations. Planetary waves, tides, sound waves and atmospheric gravity waves are known as the main causes of traveling ionospheric disturbances, and are discussed here in detail. The AGWs dispersion relation, sources, and manifestation of AGWs in the ionosphere are highlighted. Based on their spatial scale lengths, atmospheric waves are classified into four groups:

2.4.2 Planetary waves

The first group of atmospheric waves are called planetary waves. These waves have periods between 2 and 16 days. Their wavelengths are between 3500 and 10000 km. They are caused by the temperature difference between polar air and tropical air as the Coriolis effect varies with latitude between the troposphere and mesosphere. Generally, they arise due to heating at the subsolar point and stationary modes, which are fixed with respect to a rotating planet (Schunk and Nagy, 2000, 2009).

2.4.3 Tides

The second group of atmospheric waves is tides. The periods of these waves vary between 8 and 24 hours (hr). Their existence is influenced by the Sun and the Moon. They can also be caused by gravity or heat. They are influenced by gravity and may be produced by the heat as a result of the absorption of solar radiation by water vapor and ozone in the mesosphere. These waves are divided into three types. Diurnal tides have a wavelength of ~ 40000 km and a period of 24 hr, semi-diurnal tides have a wavelength of ~ 20000 km and a period of 12 hr, and terdiurnal tides have a period of 8 hr (Smith, 2000; Schunk and Nagy, 2000, 2009). These tides are also grouped into migrating tides which move westward with the Sun (i.e., tides are caused by the pull of the Moon and Sun) and non-migrating tides which do not move with the Sun (Kato et al., 1982; Mayr et al., 2005; Miyoshi et al., 2017). The planetary and tidal waves are global-scale atmospheric oscillations (Schunk and Nagy, 2000, 2009).

2.4.4 Sound waves

The third group of atmospheric waves is called sound waves. Neglecting the viscosity of neutral atmosphere and use the Navier-Stokes equation, the sound waves are described by their equation of motion (EOM) (Francis, 2016):

$$\rho \left[\frac{\partial \mathbf{v}}{\partial t} + (\mathbf{v} \cdot \nabla) \mathbf{v} \right] = -\nabla p = -\frac{\gamma p}{\rho} \nabla \rho. \quad (2.29)$$

where ρ , \mathbf{v} and p are density, velocity and pressure, respectively. The continuity equation of sound waves is expressed by:

$$\frac{\partial \rho}{\partial t} + \nabla \cdot (\rho \mathbf{v}) = 0. \quad (2.30)$$

The sound waves are caused by pressure in the atmosphere to propagate from a layer of neutrals and another layer. Hence, the speed of a sound wave C_s is proportional to the square root of pressure;

$$C_s = \left(\frac{\gamma p_o}{\rho_o} \right)^{1/2} = \left(\frac{\gamma k_B T}{m_i} \right)^{1/2} = \frac{\omega}{k} \quad (2.31)$$

where p_o is the initial pressure, and it is expressed as $p_o = n_o k_B T_o$, ρ_o is the initial density, m_i is the ion mass and $m_i n = \rho$. γ stands for the ratio of a specific heat at constant pressure and specific heat at constant volume.

2.4.5 Atmospheric gravity waves (AGWs)

2.4.5.1 Origin of AGWs

Figure 2.9 shows examples of the fourth group of atmospheric waves, namely AGWs. The top panel shows the observed AGWs, while the bottom panel shows the simulated AGWs and instability in a noctilucent cloud. Streamwise-aligned instability structures are believed to account for the smaller-scale bright bands oriented approximately normally to the gravity wave phase fronts in the upper image (Fritts and Alexander, 2003). AGWs are caused by buoyancy forces (acting upward) against the gravitational force (acting downward). When there is any disturbance of the atmosphere, gravity acts as a restoring force to equilibrate the medium and causes waves which may propagate. These are local waves with limited wavelengths (Hocke et al., 1996).

AGWs are generated below or above the mesopause. Some AGWs are triggered in the Earth's stratosphere by meteorological forces to propagate upward into the mesosphere and may reach the upper thermosphere. Other sources are associated with the auroral zones when they originate from the upper atmosphere and propagate downward (Lintelman and Gardner, 1994; Vadas, 2007; Kaifler et al., 2017) or horizontally. Gravity waves of meteorological origin are waves that travel upward from below the ionosphere, for example, perturbations in the jetstream (also named the upper tropospheric jet). These include heated air parcels in the troposphere, known as tropical convection, airflow over mountains, known as topographic flow, cyclones, and tornadoes. There are also sporadic sources such as thunderstorms, volcanic eruptions, big explosions, tsunamis, earthquakes and the breaking of upward propagating tides (Röttger, 1981; Laštovička, 2006; Occhipinti et al., 2008; Schunk and Nagy, 2000, 2009). Like boiling water in a container, a heated air parcel from the troposphere rises into the stratosphere. Arriving at its lower part, the air's energy as heat may change into gravitational potential energy. This causes disturbances and while gravity is trying to stabilize the medium, it causes AGWs (Laštovička, 2006). Mountains deviate blowing winds, and on their leeward side, turbulence and instabilities are triggered. Mountain waves or AGWs are produced when gravity tries to equilibrate the air (Heale et al., 2020).

GWs of auroral origin are generated in the thermosphere and propagate downward to the mesosphere. They are caused by variations in Joule ($Q = \Sigma_p E^2$, where Σ_p is the Pedersen conductivity and E is the electric field) and precipitating particle heating, the effect of the Lorentz force at high latitudes, the breaking of downward propagating tides, in situ movement of the solar terminator passing and solar eclipses (Brekke, 1979; Laštovička, 2006). The solar terminator is a moving line that divides the daylit side and the dark night side of a planetary body. During the solar terminator, atmospheric temperature and pressure suddenly change and cause disturbances, whilst gravity, which normally acts towards the center of the Earth, tries to balance the medium and, as a result, some waves are generated and propagate from that region (Galushko et al., 1998). Geomagnetic storms are another source of AGWs. A significant number of high energy particles precipitate into the ionosphere during geomagnetic storms. Most of these particles are guided by the magnetic field into the polar ionospheric regions and heat the upper neutral atmosphere. Thermodynamically, when gas is heated, it expands and increases its volume. The heat stored in the neutral atmosphere is converted into a gravitational potential energy. Gravity then triggers AGWs traveling toward the lower altitudes. During a geomagnetic storm, AGWs that travel towards the equator are generated by the auroral electrojets during intense Joule heating, Lorentz force, particle precipitation and other mechanisms (Hunsucker, 1982; Ding et al., 2008). AGWs are grouped into three main classes; namely large-scale AGWs (LSAGWs), medium-scale AGWs (MSAGWs) and small-scale AGWs (SSAGWs):

- Characteristics of LSAGWs are:
 - horizontal wavelengths of about 1000 km

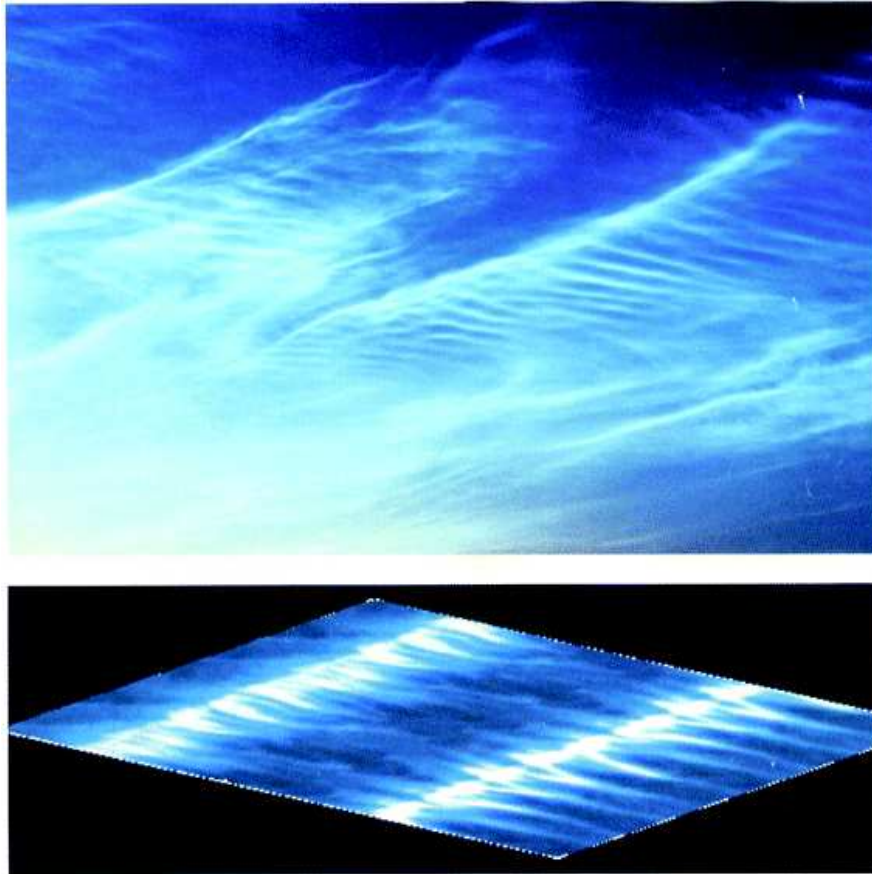


Figure 2.9: Examples of atmospheric gravity wave, namely the observed (top) and simulated gravity waves (bottom) of instability structures in the noctilucent cloud (Fritts and Alexander, 2003).

- wave periods of more than an hour
- horizontal velocities between 500 and 1000 ms^{-1}
- originate from polar regions during geomagnetic storms and propagate toward the equator (Hunsucker, 1982)
- Characteristics of MSAGWs are:
 - horizontal wavelengths of several hundred kilometers
 - wave periods between 5 and 60 minutes
 - horizontal velocities between 100 and 300 ms^{-1}
 - originate from the auroral zone and propagate from the winter polar regions (Hunsucker, 1982)
- Characteristics of SSAGWs are:
 - wave periods between 2 and 5 minutes
 - horizontal velocities between 300 and 3000 ms^{-1}
 - originate from severe convective activity and occur seasonally with their peak during the summer (Hunsucker, 1982)

The equations governing the dispersion of AGWs, equations (2.32) to (2.77), can be found in published papers (e.g., Hines, 1960), books (e.g., Schunk and Nagy, 2000, 2009), and theses (e.g., Mahlangu, 2017). TIDs are a manifestation of AGWs. The atmosphere of the Earth is assumed to be isothermal. Neglecting viscous effects,

thermal conduction, the Coriolis and centripetal accelerations, the continuity, momentum and energy equations for a single component of neutral gas are expressed by equations (2.32), (2.33) and (2.34), respectively:

$$\frac{\partial \rho}{\partial t} + \nabla \cdot (\rho \mathbf{u}) = 0, \quad (2.32)$$

$$\rho \left(\frac{\partial}{\partial t} + \mathbf{u} \cdot \nabla \right) \mathbf{u} + \nabla p - \rho \mathbf{G} = 0, \quad (2.33)$$

$$\left(\frac{\partial}{\partial t} + \mathbf{u} \cdot \nabla \right) p + \gamma p (\nabla \cdot \mathbf{u}) = 0. \quad (2.34)$$

Here $\gamma = 5/3$, ρ is the mass density, \mathbf{G} is the acceleration due to the gravity vector directed downward with magnitude g and \mathbf{u} is the velocity. Assuming a constant initial temperature (T_o), stationary gas ($\mathbf{u}_o = \mathbf{0}$), and horizontally stratified layers in hydrostatic equilibrium, the upward and downward forces balance is provided by:

$$\nabla p_o = \rho_o \mathbf{G} \quad (2.35)$$

This equation is written with the coordinates (x, y, z) corresponding to eastward, northward, and upward, as:

$$\frac{1}{n_o} \frac{dn_o}{dz} = -\frac{1}{H_o}, \quad (2.36)$$

where $H_o = kT_o/mg$ is the atmospheric scale height. Initial pressure and density vary exponentially as a function of H . After considering the ideal gas equation at a constant temperature: $p = \frac{nRT}{V}$, $n_o = \frac{m}{M}$ and $\rho = \frac{m}{V}$, then $p = \rho \frac{RT}{M}$. Here V is the volume, n_o is the number of moles, R is the ideal gas constant = 8.314462618 JK⁻¹mol⁻¹, m is the gas total mass, M is the gas molar mass, and T is the gas temperature.

Substituting these parameters into equation (2.36) (Schunk and Nagy, 2000, 2009), the expression becomes:

$$\frac{1}{\rho} \frac{d\rho}{dz} = -\frac{1}{H} \quad (2.37)$$

and

$$\frac{1}{p} \frac{dp}{dz} = -\frac{1}{H} \quad (2.38)$$

After integrating equations (2.37) and (2.38), the result is:

$$p, \rho \propto e^{-z/H} \quad (2.39)$$

Note that H is assumed to be constant.

2.4.5.2 Buoyancy force

Take an air parcel at altitude/height z and assume that the density (ρ_o) initially is constant. For a perturbation of the parcel moving from z to $z + \Delta z$, using the hydrostatic law of sound propagation with the assumption that there is no heat transfer (adiabatic), the perturbed density was expressed by Mahlangu (2017) as:

$$\Delta \rho' = \frac{\Delta p}{C_s^2} \quad (2.40)$$

where C_s is the speed of sound (see equation (2.101)). The surrounding medium is assumed to be in hydrostatic equilibrium with the gas in consideration, hence $\Delta p = -\rho g \Delta z$ and the density variation relative to the altitude is described by $\frac{d\rho_o}{dz}$. Considering the perturbed altitude (Δz), its change in density ($\Delta \rho''$) associated with the altitude change is expressed by:

$$\Delta \rho'' = \frac{d\rho_o}{dz} \Delta z. \quad (2.41)$$

The perturbed density of the air parcel in equation (2.40) and the density of the surrounding air defined by equation (2.41) are different. The required restorative force is called upthrust, known as the buoyancy force $F_b = g(\Delta \rho'' - \Delta \rho')$.

According to Newton's second law of motion the resultant force on the parcel accelerates it, therefore:

$$\rho_o \frac{d^2(\Delta z)}{dt^2} = g \left(\frac{d\rho_o}{dz} + \frac{\rho_o g}{C_s^2} \right) \Delta z \quad (2.42)$$

The solution of this (equation 2.42) is simple harmonic motion:

$$\Delta z(t) = A e^{i\omega_B t} + B e^{-i\omega_B t} \quad (2.43)$$

with A and B as constants, $i = \sqrt{-1}$ and ω_B the frequency of oscillations. The acceleration of the air parcel is expressed by the second-order time derivative of equation (2.43):

$$\frac{d^2(\Delta z)}{dt^2} = -\omega_B^2 \Delta z. \quad (2.44)$$

Replacing the second-order time derivative of equation (2.42) with the right-hand side term of equation (2.44), the equation becomes:

$$\omega_B^2 = -\frac{g}{\rho_o} \frac{d\rho_o}{dz} - \frac{g^2}{C_s^2} \quad (2.45)$$

where ω_B is the Brunt-Väisälä frequency. The sound speed squared in the neutral gas is expressed by $C_s^2 = \frac{\gamma p_o}{\rho_o} = \gamma g H_o = \frac{\gamma k T_o}{m}$. Inserting these parameters into equation (2.45), the equation becomes:

$$\omega_B^2 = \frac{\gamma p_o}{\rho_o} \left[\frac{1}{C_s^2} \frac{dp_o}{dz} + \frac{p_o}{C_s^4} \frac{dC_s^2}{dz} \right] - \frac{g^2}{C_s^2} \quad (2.46)$$

Substituting the ideal gas equation and the parameters defining the speed of sound to replace ρ_o and p_o in equation (2.46):

$$\omega_B^2 = \frac{\gamma g R T}{C_s^2 H} + \frac{g}{C_s^2} \frac{dC_s^2}{dz} - \frac{g^2}{C_s^2}. \quad (2.47)$$

Grouping terms of g and C_s^2 results in:

$$\omega_B^2 = \frac{(\gamma - 1)g^2}{C_s^2} + \frac{g}{C_s^2} \frac{dC_s^2}{dz} = \omega_g^2 + \frac{g}{C_s^2} \frac{dC_s^2}{dz}, \quad (2.48)$$

where ω_g is the buoyancy or isothermal Brunt-Väisälä frequency which defines the oscillation frequency of the air parcel, when it is dislodged from its equilibrium position.

2.4.5.3 The dispersion relation of AGWs

Equations representing the continuity, momentum and energy of air parcel can be rewritten in terms of small perturbations of the air parcel as represented by $\rho = \rho_o + \rho'$, $p = p_o + p'$ and $\mathbf{u} = \mathbf{u}'$, where $\mathbf{u}_o = 0$:

$$\frac{\partial \rho'}{\partial t} + \mathbf{u}' \cdot \nabla \rho_o + \rho_o \nabla \cdot \mathbf{u}' = 0, \quad (2.49)$$

$$\rho_o \frac{\partial \mathbf{u}'}{\partial t} + \nabla p' - \rho' \mathbf{G} = 0, \quad (2.50)$$

$$\frac{\partial p'}{\partial t} + \mathbf{u}' \cdot \nabla p_o + \gamma p (\nabla \cdot \mathbf{u}') = 0. \quad (2.51)$$

Equations (2.49), (2.50) and (2.51) can be expressed in terms of the relative density (i.e., $\frac{\rho'}{\rho_o}$), relative pressure ($\frac{p'}{p_o}$) and H_o along the vertical direction (z). Use u'_z as the vertical component of the perturbed velocity and use equation (2.39) to get:

$$u' \cdot \nabla \rho_o = -\frac{\rho_o}{H_o} u'_z$$

and

$$u' \cdot \nabla p_o = -\frac{p_o}{H_o} u'_z.$$

Using these two equations, the new equations are:

$$\frac{\partial}{\partial t} \left(\frac{\rho'}{\rho_o} \right) - \frac{1}{H_o} u'_z + (\nabla \cdot \mathbf{u}') = 0, \quad (2.52)$$

$$\frac{\partial \mathbf{u}'}{\partial t} + \frac{p'}{\rho_o p_o} \nabla p_o + \frac{p_o}{\rho_o} \nabla \left(\frac{p'}{p_o} \right) - \frac{\rho'}{\rho_o} \mathbf{G} = 0, \quad (2.53)$$

$$\frac{\partial}{\partial t} \left(\frac{p'}{p_o} \right) - \frac{1}{H_o} u'_z + \gamma (\nabla \cdot \mathbf{u}') = 0. \quad (2.54)$$

The relative density and pressure together with the perturbed velocity are given in a plane waves relation:

$$\left(\frac{\rho'}{\rho_o} \right), \left(\frac{p'}{p_o} \right), \mathbf{u}' \propto e^{i(\mathbf{k} \cdot \mathbf{r} - \omega t)}, \quad (2.55)$$

where \mathbf{k} and ω are the wave vector and wave frequency, respectively. Substituting each relative quantity of equation (2.55) into equations (2.52), (2.53) and (2.54) leads to:

$$-i\omega \left(\frac{\rho'}{\rho_o} \right) - \frac{1}{H_o} u'_z + i(\mathbf{k} \cdot \mathbf{u}') = 0, \quad (2.56)$$

$$-i\omega \mathbf{u}' + \frac{p'}{\rho_o p_o} \nabla p_o + \frac{p_o}{\rho_o} i\mathbf{k} \left(\frac{p'}{p_o} \right) - \frac{\rho'}{\rho_o} \mathbf{G} = 0, \quad (2.57)$$

$$-i\omega \left(\frac{p'}{p_o} \right) - \frac{1}{H_o} u'_z + i\gamma (\mathbf{k} \cdot \mathbf{u}') = 0. \quad (2.58)$$

Solving equations (2.56), (2.57) and (2.58) yield a general dispersion relation of an atmospheric wave, and after assuming that $H_o = \infty$ and $\mathbf{G} = 0$ (i.e., absence of gravity), the new equations are:

$$-\omega \rho' + \rho_o (\mathbf{k} \cdot \mathbf{u}') = 0, \quad (2.59)$$

$$k^2 p' - \omega \rho_o (\mathbf{k} \cdot \mathbf{u}') = 0, \quad (2.60)$$

$$-\omega p' + \gamma p_o (\mathbf{k} \cdot \mathbf{u}') = 0. \quad (2.61)$$

The matrix formed by equations (2.59), (2.60) and (2.61) is solved by using linear algebra to get the dispersion relation relating the wave vector to wave frequency.

$$\omega^2 = C_s^2 k^2 \quad (2.62)$$

When k and ω are real and if $\frac{\omega}{k} = \frac{d\omega}{dk} = \pm C$ it shows that the wave is a sound wave. This implies that there is no dispersion relation since C is constant.

Neglecting the perturbed pressure ($p' = 0$) from equations (2.56), (2.57) and (2.58), leads to the wave equations which depend on gravity and other external forces:

$$-i\omega \rho' + \rho_o \left(ik_z - \frac{1}{H_o} \right) u'_z = 0, \quad (2.63)$$

$$-i\omega \rho_o u'_z + g \rho' = 0, \quad (2.64)$$

$$\left(i\gamma k_z - \frac{1}{H_o} \right) u'_z = 0. \quad (2.65)$$

Solving equations (2.63), (2.64) and (2.65), calculates the buoyancy frequency (ω_g) as defined in equation (2.48), if vertical motion is assumed. For an AGW moving in an x-z plane with k_z and k_x , the perturbed velocity also would have two components (i.e., u'_z and u'_x). Thus equation (2.57) can be written in terms of both components and be split into two equations. The unknown perturbed quantities in equations (2.56), (2.57) and (2.58) would be $\left(\frac{\rho'}{\rho_o}, \frac{p'}{p_o}, u'_x \text{ and } u'_z \right)$.

These linear equations can be used to form a matrix that can be solved (by determinant). When written in the columns (the coefficients of $\frac{\rho'}{\rho_o}, \frac{p'}{p_o}, u'_x$ and u'_z) and the rows (the continuity, x-momentum, z-momentum

and energy equations), the result is:

$$\begin{vmatrix} -i\omega & 0 & ik_x & \left(ik_z - \frac{1}{H_o}\right) \\ 0 & ik_x \frac{C_s^2}{\gamma} & -i\omega & 0 \\ g & \left(ik_z - \frac{1}{H_o}\right) \frac{C_s^2}{\gamma} & 0 & -i\omega \\ 0 & -i\omega & i\gamma k_x & \left(i\gamma k_z - \frac{1}{H_o}\right) \end{vmatrix} = 0. \quad (2.66)$$

From this equation, after its expansion, the dispersion relation in terms of k and ω can be obtained:

$$\omega^4 - \omega^2 C_s^2 (k_x^2 + k_z^2) + (\gamma - 1)g^2 k_x^2 - i\gamma g \omega^2 k_z = 0. \quad (2.67)$$

Neglecting g from equation (2.67) yields the sound wave dispersion relation with k and ω real. Including gravity g in equation (2.67), leads to complex wave vectors and wave frequencies. When a wave propagates in a horizontal direction, only k_z is considered complex (i.e., $k_z = k_{zr} + k_{zi}$), with k_{zr} and k_{zi} the real and imaginary parts of k_z , respectively (Schunk and Nagy, 2000, 2009). AGWs are often assumed to propagate horizontally, in the x-z plane, but they may have a small vertical component. k_x and ω are still real, and the equation (2.67) now becomes:

$$\omega^4 - \omega^2 C_s^2 (k_x^2 + k_{zr}^2 - k_{zi}^2) + \gamma g k_{zi} \omega^2 + (\gamma - 1)g^2 k_x^2 - i\omega^2 k_{zr} (\gamma g + 2C_s^2 k_{zi}) = 0. \quad (2.68)$$

From equation (2.68), the imaginary part is equal to zero, hence:

$$k_{zi} = -\frac{\gamma g}{2C_s^2} = -\frac{1}{2H_o}. \quad (2.69)$$

Its perturbed velocity is then expressed as:

$$\mathbf{u}' \propto e^{z/2H_o} e^{i(k_x x + k_{zr} z - \omega t)}. \quad (2.70)$$

These kinds of waves are called internal gravity waves (IGWs). Their wave perturbation energy is $\frac{1}{2}\rho_o u_z'^2$ (with $u_z' \propto e^{z/2H_o}$) and their amplitudes increase exponentially as they propagate to higher altitudes. For example, Senior et al. (2006) when discussing the effects of AGWs disturbances on an artificial HF backscatter, presented an equation of the electron density perturbation (n) as the wave propagates. The equation is as follows:

$$n = n_o \left[1 + \sigma A_r A_\theta \cos 2\pi \left(t' + \left(\frac{\pi}{2} - \theta \right) \frac{R_E}{\lambda_x} + \frac{R_E}{\lambda_z} \right) \right] \quad (2.71)$$

where n_o , σ , λ_x , λ_z , θ , R_E , A_r , A_θ , and t' are the undisturbed background electron density, amplitude of the perturbation, horizontal/meridional wavelength of the wave, the vertical wavelength of the wave, co-latitude, Earth's radius, and the time variation, respectively (Senior et al., 2006). A_r is expressed as:

$$A_r = \exp \left[-\left(\frac{z - z_o}{H_{wave}} \right)^2 \right] \quad (2.72)$$

where z , z_o , and H_{wave} are the altitude, the peak height, and the scale height of the amplitude, respectively. A_θ is expressed as:

$$A_\theta = \exp \left[-\left(\frac{\theta - \theta_o}{\theta_c} \right) \right] \quad (2.73)$$

where θ_o and θ_c are the initial co-latitude and scale latitude, respectively. θ_o can be estimated using:

$$\theta_o = \theta_{oo} + \frac{\lambda_x t' v_{gx}}{v_x R_E} \quad (2.74)$$

where v_{gx} , v_x , and θ_{oo} are the group speed, horizontal phase speed, and the initial co-latitude at $t' = 0$. Equation (2.67) is rearranged as:

$$k_z^2 = \left(\frac{\omega_g^2 - \omega^2}{\omega^2} \right) k_x^2 + \left(\frac{\omega^2 - \omega_a^2}{C_s^2} \right), \quad (2.75)$$

where $\omega_a = \frac{\gamma g}{2C_s}$ is the minimum frequency of sound waves, while ω_g as defined in equation (2.48) is related to the oscillation of AGWs. For k_z , which is real, if $\omega_g < \omega < \omega_a$ it shows that AGWs are impermanent waves, i.e., they dissipate as their amplitudes grow to infinity. As a result of this property, AGWs only appear when either $\omega > \omega_a$ ($\sim 0.0042 \text{ s}^{-1}$) or $\omega < \omega_g$ ($\sim 0.00009 \text{ s}^{-1}$). ω_a and ω_g is the frequency mode for either sound waves and AGWs, respectively. For AGWs, the dispersion relation in equation (2.75) is simplified to:

$$k_z^2 \approx \frac{\omega_g^2 k_x^2}{\omega^2} - \frac{\omega_a^2}{C_s^2}. \quad (2.76)$$

Equation (2.76) represents the simplified AGWs dispersion relation. When substituting equation (2.69) into equation (2.67), the result is:

$$\omega^4 - \omega^2 C_s^2 (k_x^2 + k_z^2) + (\gamma - 1) g^2 k_x^2 - \frac{\gamma^2 g^2 \omega^2}{4 C_s^2} = 0. \quad (2.77)$$

Its solution is:

$$\frac{(p' - p_o)}{p_o P} = \frac{(\rho' - \rho_o)}{\rho_o R} = \frac{u_x}{X} = \frac{u_z}{Z} = A e^{(z\gamma g/2C_s^2)} \cdot e^{i(\omega t - k_x x - k_z z)} \quad (2.78)$$

where

$$\begin{aligned} P &= \gamma \omega^2 \left[k_z - \frac{i(1-\gamma/2)g}{C_s^2} \right] \\ R &= \omega^2 k_z + i(\gamma - 1)g k_x^2 - \frac{i\gamma g \omega^2}{2C_s^2} \\ X &= \omega k_x C_s^2 \left[k_z - \frac{i(1-\gamma/2)g}{C_s^2} \right] \\ Z &= \omega [\omega^2 - k_x^2 C_s^2] \end{aligned}$$

(Hines, 1960; Treumann and Baumjohann, 1997).

2.4.5.4 AGW dissipation

The dissipation of internal gravity waves such as AGWs is controlled by the molecular viscosity (equation (2.79)) and thermal conductivity (equation (2.80)), which explains the rate of heat transfer.

$$\rho_o \left(\frac{\partial \mathbf{u}}{\partial t} \right) = \rho \mathbf{G} - \nabla p \quad (2.79)$$

$$\frac{\partial p}{\partial t} + \mathbf{u} \cdot \nabla p_o = C_s^2 \left[\frac{\partial \rho}{\partial t} + \mathbf{u} \cdot \nabla \rho_o \right]. \quad (2.80)$$

Assuming that the viscous losses are not significant, the energy dissipation rate is estimated by considering the law of conservation of energy. The rate of dissipation of the energy per unit mass (D_r) as caused by kinematic viscosity in three (x,y,z) dimensions is:

$$D_r = \eta(2a^2 + 2b^2 + 2c^2 + d^2 + e^2 + f^2) - (2\eta/3)(a + b + c)^2. \quad (2.81)$$

These variables are defined as follows:

$$a = \frac{\partial u_x}{\partial x}, \quad b = \frac{\partial u_y}{\partial y}, \quad c = \frac{\partial u_z}{\partial z},$$

$$d = \frac{\partial u_z}{\partial y} + \frac{\partial u_y}{\partial z},$$

$$e = \frac{\partial u_x}{\partial z} + \frac{\partial u_z}{\partial x},$$

$$f = \frac{\partial u_y}{\partial x} + \frac{\partial u_x}{\partial y},$$

where η is the kinematic viscosity and u_x, u_y, u_z are the components of the velocity vector \mathbf{u} (Hines, 1960). When AGWs propagate toward a medium with a high electron density, they break while heating the local region. Energy loss by the AGWs may also contribute to the turbulent process in the region (Borchevskina et al.,

2020). As the AGWs propagate upward toward a less dense region, their amplitudes increase exponentially and they eventually dissipate (Liu and Swenson, 2003). Ion drag and wave-induced diffusion may contribute to the dissipation of the AGW's (Vadas, 2007). For AGWs with a period of less than a few hours, the ion drag is not very important during the night and for those with a period of less than an hour, the same is true during the day (Vadas, 2007). For AGWs with a period of an hour or two hours, wave-induced diffusion is not valid. It is only important for altitudes between 140 and 220 km altitude. The dissipation of AGWs also depends on solar activity: AGWs tend to dissipate more during active solar conditions and daytime than during extreme solar minimum and nighttime (Vadas, 2007).

2.4.5.5 Ionospheric behavior under the influence of internal gravity waves

To explain the effects of Internal Gravity Waves (IGWs) such as AGWs on the ionosphere, an example of a tsunamigenic IGW in the neutral atmosphere as modeled by Occhipinti et al. (2008) is given. The model shows that a tsunami in the ocean produced a wave that propagated upward and reached an altitude of 100 km. Its propagation time depended on the ocean's depth and the period of the tsunami.

Assume ions i with $i=1, 2, 3$ representing O_2^+ , NO^+ , O^+ , respectively. The tsunami initially has a velocity \mathbf{u}_n in the neutral atmosphere. Upon entering of the wave into the ionosphere, induced plasma velocity \mathbf{u}_i , ion pressure p_i and ion density ρ_i are expected.

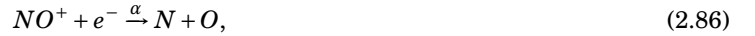
The continuity and momentum equations are rewritten as:

$$\frac{\partial n_i}{\partial t} + \nabla \cdot (n_i \mathbf{u}_i) = \pm \beta n_i - \alpha n_i^2 \quad (2.82)$$

$$\rho_i \frac{\partial \mathbf{u}_i}{\partial t} = -\nabla p_i + \rho_i \mathbf{G} + n_i q_i (\mathbf{E} + \mathbf{u}_i \times \mathbf{B}) - \rho_i v_{in} (\mathbf{u}_i - \mathbf{u}_n) \quad (2.83)$$

$$n_e = \sum_{i=1}^3 n_i \quad (2.84)$$

where \mathbf{E} , \mathbf{B} and v_{in} are the electric field, magnetic field and the collision frequency of ions and neutrals, respectively. α is the dissociative recombination processes (equations (2.85) and (2.86)) and β is a chemical ion loss by charge exchange (equations (2.87) and (2.88)). They are used in the chemical reaction to support in the ion equilibrium and long-term evolution of plasma density. In this case, solar ionization is neglected.



A linear dependence between ion \mathbf{u}_i and neutral velocities \mathbf{u}_n is expressed as follows:

$$u_{i\parallel} = u_{n\parallel} + \frac{F_{i\parallel}}{\rho_i v_{in}}, \quad (2.89)$$

$$u_{i\odot} = u_{n\odot} + \frac{\Omega_i}{v_{in}} u_{i\perp} + \frac{F_{i\odot}}{\rho_i v_{in}}, \quad (2.90)$$

$$u_{i\perp} = u_{n\perp} + \frac{\Omega_i}{v_{in}} u_{i\odot} + \frac{F_{i\perp}}{\rho_i v_{in}}, \quad (2.91)$$

where $F_{i\parallel}$, $F_{i\odot}$ and $F_{i\perp}$ are the components of forcing term \mathbf{F} independent of the magnetic field. Their orientations are shown by \parallel parallel to, and \odot, \perp perpendicular to, the magnetic field $\mathbf{B}(B, 0, 0)$. In this case, $\Omega_i = \frac{qn_i B}{\rho_i}$ is the magnetic gyro-frequency.

Similarly, electrons are also affected by moving IGWs, such as AGWs. Their continuity equation is:

$$\frac{\partial n_e}{\partial t} + \nabla \cdot (n_e \mathbf{u}_e) = P - L, \quad (2.92)$$

where P is the production rate, L is the loss rate and \mathbf{u}_e is the electron velocity. The perturbed electron density (n'_e) and perturbed velocity \mathbf{u}'_e are defined as:

$$n_e = n_{e0} + n'_e, \quad (2.93)$$

$$\mathbf{u}_e = \mathbf{u}_{e0} + \mathbf{u}'_e, \quad (2.94)$$

where n_{e0} and \mathbf{u}_{e0} are the unperturbed (initial) electron density and velocity, respectively. The continuity equation after perturbation of AGWs is expressed by the following formula, after assuming that $\mathbf{u}_{e0} = 0$:

$$\frac{\partial n'_e}{\partial t} = -\nabla \cdot (n_{e0} \mathbf{u}'_e). \quad (2.95)$$

Newton's second law of motion for an electron can be written to show that this particle of mass (m_e) accelerates due to the external forces acting on it.

$$m_e \frac{\partial \mathbf{u}'_e}{\partial t} \mathbf{e}_B = \mathbf{F}_c + \mathbf{F}_f + \mathbf{F}_m + \mathbf{F}_g + \mathbf{F}_p, \quad (2.96)$$

where \mathbf{F}_c , \mathbf{F}_f , \mathbf{F}_m , \mathbf{F}_g and \mathbf{F}_p are the Coriolis, friction, Lorentz, gravity, and gradient force, respectively, and \mathbf{e}_B is a unit vector pointing in the direction of the magnetic field \mathbf{B} .

A passing gravity wave perturbs electrons in a such a way that:

$$n'_e = n_{e0} \left(\frac{\mathbf{u}_n \cdot \mathbf{e}_B}{\omega} \right) \left\{ (\mathbf{k} \cdot \mathbf{e}_B) + i(\mathbf{e}_B \cdot \mathbf{e}_B) \left[\frac{1}{2H} \frac{d(\ln n_{e0})}{dz} \right] \right\}. \quad (2.97)$$

The instantaneous fluctuation of electrons is estimated by considering the real part of the equation (2.97) and n'_e is expressed as:

$$n'_e = \frac{i}{\omega} \nabla \cdot [n_{e0} (\mathbf{u}_n \cdot \mathbf{e}_B) \mathbf{e}_B]. \quad (2.98)$$

Perturbed electron density will vary exponentially as the relative density, pressure, and the velocity of AGWs do (equation (2.55)).

$$n'_e \propto \exp(k_x x + k_y y + \omega t) \quad (2.99)$$

These passing fluctuations in the ionosphere are known as TIDs (Hooke, 1970). The electron density perturbation under the influence of AGWs was described by Davis (1973), Porter and Tuan (1974), and Mahlangu (2017).

2.4.6 Other waves related to the sound waves

2.4.6.1 Ion acoustic waves

Sound waves moving in a plasma, i.e., where the assumption of $n_i = n_e = n$ holds, and with few collisions with neutral particles, are called ion acoustic waves. To derive their equations, further assumptions are necessary (Francis, 2016): unmagnetized plasma (i.e., $\mathbf{B} = 0$), ions moving in one-dimensional compressional motion (i.e., $\gamma_i = \frac{N+2}{N} = 3$, where $N = 1$ is the degree of freedom), isothermal electrons ($\gamma_e = 1$), massless electrons, low frequency oscillations, and electrostatic and longitudinal waves. Their EOM is written as:

$$m_i n \left[\frac{\partial \mathbf{v}_i}{\partial t} + (\mathbf{v}_i \cdot \nabla) \mathbf{v}_i \right] = en \mathbf{E} - \nabla p = -en \nabla \phi - \gamma_i k_B T_i \nabla n \quad (2.100)$$

where the electric field $\mathbf{E} = -\nabla \phi$ and ϕ is the electrostatic potential.

The speed of sound in a plasma is expressed by:

$$C_s = \frac{\omega}{k} = \left(\frac{k_B T_e + \gamma_i k_B T_i}{m_i} \right)^{1/2} \quad (2.101)$$

where T_e and T_i are electron and ion temperature, respectively (Francis, 2016).

When the plasma is magnetized, i.e., $\mathbf{B} \neq 0$, those waves are said to be: (a) parallel or perpendicular waves to indicate the direction of \mathbf{k} relative to \mathbf{B}_0 and (b) longitudinal or transverse waves to indicate the direction

of \mathbf{k} relative to the oscillating electric field \mathbf{E}_1 . Hence, if the oscillating magnetic field $\mathbf{B}_1 = 0$, the waves are electrostatic, and if $\mathbf{B}_1 \neq 0$, the waves are electromagnetic (Kotsarenko et al., 1996; Huba et al., 2000; Francis, 2016).

Assume that \mathbf{k} is almost perpendicular to \mathbf{B} , and electrostatic waves ($\mathbf{k} \times \mathbf{E} = 0$), $T_i = 0$, $v_o = 0$ and $E_o = 0$. Consider \mathbf{E} and $\nabla = ik$ along the x direction and \mathbf{B}_o along the z direction. The electric field $\mathbf{E} = -\nabla\phi$, k_z is neglected for ions, and electrons would move along \mathbf{B}_o to preserve charge neutrality. In this case, the EOM of ions would be expressed as:

$$m_i \frac{\partial \mathbf{v}_{i1}}{\partial t} = -e\nabla\phi_1 + e\mathbf{v}_{i1} \times \mathbf{B}_o. \quad (2.102)$$

The dispersion relation for electrostatic ion cyclotron waves is expressed by:

$$\omega^2 = \Omega_c^2 + k^2 v_s^2 \quad (2.103)$$

where $\Omega_c = \frac{eB_o}{M}$ is the cyclotron frequency.

2.4.6.2 Electron plasma waves

There are also electron plasma waves. To derive their equations, the following assumptions are made: unmagnetized plasma, warm electrons ($k_B T_e \neq 0$), electrons exhibiting a one-dimensional motion ($\gamma_e = 3$), mobile electrons and stationary ions, high-frequency oscillations, and electrostatic and longitudinal waves (Francis, 2016). Electron plasma waves are described by their EOM;

$$m_e n_e \left[\frac{\partial \mathbf{v}_e}{\partial t} + (\mathbf{v}_e \cdot \nabla) \mathbf{v}_e \right] = -en_e \mathbf{E} - \nabla p. \quad (2.104)$$

The equation for electron plasma waves, based on Gauss's Law, is written as:

$$\nabla \cdot \mathbf{E} = -\frac{n_e e}{\epsilon_o} \quad (2.105)$$

and the continuity equation is

$$\frac{\partial n_e}{\partial t} + \nabla \cdot (n_e \mathbf{v}_e) = 0. \quad (2.106)$$

Their dispersion relation is expressed by:

$$\omega^2 = \omega_{pe}^2 + \frac{3}{2} k^2 v_{th}^2 \quad (2.107)$$

where $v_{th} = \frac{2k_B T_e}{m}$ is the electron thermal velocity.

For magnetized plasma, i.e., $\mathbf{B} \neq 0$, these waves could be longitudinal (when $\mathbf{k} \times \mathbf{E}_1 = 0$), and electrostatic. Assuming that $k_B T_e = 0$ and $\mathbf{E}_o = 0$, the electrons are described by the following equations (Francis, 2016):

$$m \frac{\partial \mathbf{v}_{e1}}{\partial t} = -e(\mathbf{E}_1 + \mathbf{v}_{e1} \times \mathbf{B}_o), \quad (2.108)$$

$$\frac{\partial n_{e1}}{\partial t} + n_o \nabla \cdot \mathbf{v}_{e1} = 0, \quad (2.109)$$

and

$$\epsilon_o \nabla \cdot \mathbf{E}_1 = -en_{e1}. \quad (2.110)$$

For longitudinal waves with $\mathbf{k} \parallel \mathbf{E}_1$, their dispersion relation is expressed by:

$$\omega^2 = \omega_{pe}^2 + \omega_{ce}^2 = \omega_h^2 \quad (2.111)$$

where ω_h is the upper hybrid frequency and ω_{ce} is the frequency of electrostatic waves across the magnetic field \mathbf{B} (Francis, 2016). Waves along \mathbf{B} usually oscillate with $\omega = \omega_{pe}$.

When electrons are not allowed to move along \mathbf{B} to preserve charge neutrality, $T_e = 0$ and $\nabla \mathbf{p}_e = 0$, electron plasma waves will obey the full EOM instead of the Boltzmann relation. The lower hybrid frequency (ω_l) is

expressed as:

$$\omega^2 = \Omega_c \omega_{ce} = \omega_l^2. \quad (2.112)$$

For a very low plasma density, ω_l is expressed as:

$$\frac{1}{\omega_l^2} = \frac{1}{\omega_{ce}\Omega_c} + \frac{1}{\Omega_p^2} \quad (2.113)$$

2.4.6.3 Hydromagnetic and magnetosonic waves

Other plasma waves that propagate in a magnetized plasma include hydromagnetic (Alfvén) and magnetosonic waves. They are low frequency, transverse, electromagnetic waves. The Alfvén wave propagates along the magnetic field and the magnetosonic wave propagates across the magnetic field. Alfvén and magnetosonic waves are linearly polarized (Schunk and Nagy, 2000, 2009; Francis, 2016). The dispersion relation of Alfvén waves is:

$$\omega^2 = k^2 V_A^2 \quad (2.114)$$

where $V_A = \left(\frac{\mathbf{B}_0}{\mu_0 n_i m_i} \right)^{1/2}$ is the Alfvén speed.

The dispersion relation of magnetosonic waves is:

$$\omega^2 = k^2 \frac{v_s^2 + V_A^2}{1 + V_A^2/c^2} \quad (2.115)$$

where c is the speed of light (Schunk and Nagy, 2000, 2009).

2.5 Summary

In this chapter, the origin of space weather and its impact on the ionosphere was described. The space weather effects in the magnetosphere, known as geomagnetic storms, were introduced. The phases of a geomagnetic storm were characterized. Atoms, molecules and the energy distribution in the mesosphere, thermosphere and ionosphere were highlighted. The formation and morphology of four regions of Earth's ionosphere were discussed. Planetary waves and tides were briefly introduced, but AGWs and TIDs were discussed in more detail. AGWs/TIDs transport energy and momentum heat the bottom of the ionosphere through their breaking. Their sources, dispersion relations, and dissipation modes were discussed in detail. All of the above theories were introduced to help in the understanding of TID, which is one of the two phenomena discussed in this thesis.

Chapter 3

INSTRUMENTS AND MODELS

3.1 SuperDARN HF radars

3.1.1 Introduction

In this study, Zhongshan and SANAE HF radars were used. They provide better data sets than the other radar stations in Antarctica. Figure 3.1 shows the fields of view (FOV) of 13 southern hemisphere SuperDARN radars, as well as those of the South African SANAE and Chinese Zhongshan radars (in red). SANAE is located

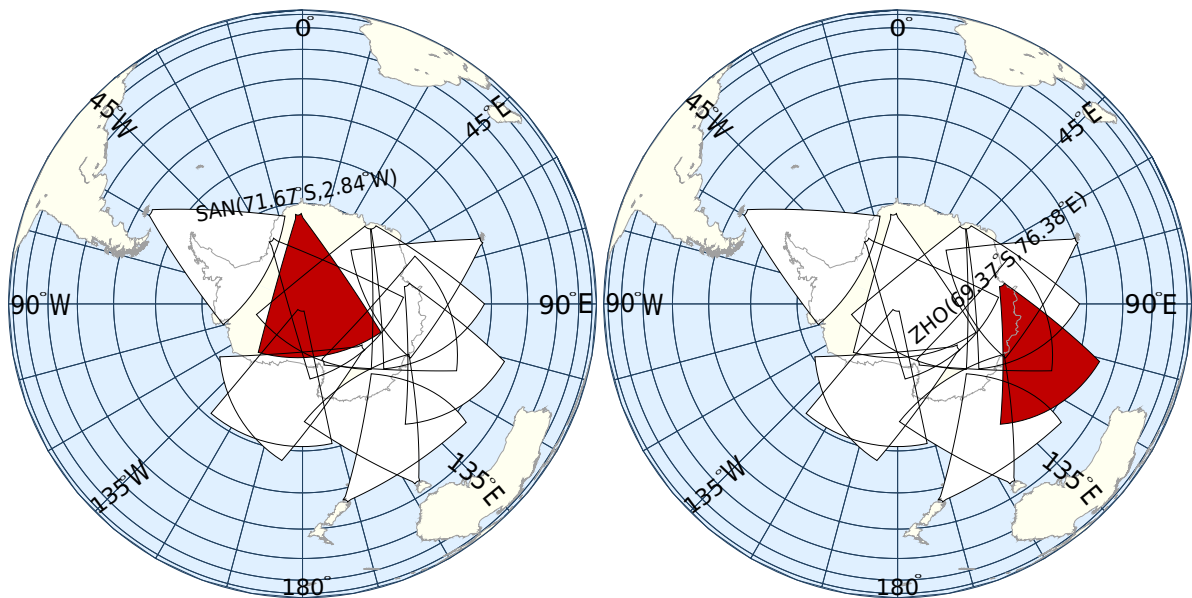


Figure 3.1: Fields of view of the southern hemisphere SuperDARN HF radars, with SANAE (left) and Zhongshan (right) in red.

at 71.67°S, 2.84°W (66.64°S, 48.51°E geomagnetic coordinates) and Zhongshan is located at 69.38°S, 76.38°E (74.5°S, 96.0°E geomagnetic coordinates). For SANAE, $LT = UT + 2h$ and $MLT \approx UT - 2h$. For Zhongshan, $LT = UT + 5h$, and $MLT \approx UT + 2h$. The SANAE and Zhongshan radars' geographic boresight directions are 173.2° and 72.5°, i.e., approximately southward and eastward, respectively. The Zhongshan and SANAE SuperDARN HF radars are part of a global network of 38 radars in the southern and northern hemispheres owned by 10 countries. Each radar normally operates in the 8-20 MHz frequency range, has at least 16 beams arranged in a fan $\sim 53^\circ$ wide, has a typical range resolution of 45 km, and observes at typical range distances from ~ 180 to ~ 3500 km at an altitude of ~ 80 to ~ 300 km. Its operating height can extend up to ~ 400 km (i.e., in F -region of the ionosphere) (Ponomarenko et al., 2009). The operating mode scans all 16 beams in 1 or 2 minutes. The radars can all operate over the horizon because of the refraction of the high-frequency waves in the ionosphere. This over-the-horizon propagation can be optimized for each radar by varying the frequency of operation and is usually done automatically.

Routine data products for each beam and range gate are backscatter power, Doppler velocity, and spectral width. In order to study the effects of AGWs/TIDs on NREs, backscatter power and Doppler velocity data of

the radar are used. The default operation is a 1- to 2-minute scan of all 16 beams with a 45 km range resolution, which is suitable for the study of AGWs/TIDs due to their long wavelength and low velocity. A coherent backscatter radar such as a SuperDARN radar transmits radio waves to the ionosphere and gets ionospheric information within the received echoes. This transmission is usually well above the critical frequency of the ionospheric E and F regions (several MHz). In the absence of plasma irregularities, there are no ionospheric echoes. In a following section ground/sea scatter echoes which rely on the aspect condition are discussed. In a case of an irregularity structure, such as a quasi-periodic electron density perturbation that meets a Bragg condition, the wavefront is scattered and could evoke a weak but detectable backscatter signal. Both momentum and energy, shown by Equations (3.1) and (3.2), are conserved during the radio wave-plasma irregularity scattering process.

$$\hbar k_{tr} = \hbar k_{re} + \hbar k_{ir} \quad (3.1)$$

$$\hbar \omega_{tr} = \hbar \omega_{re} + \hbar \omega_{ir} \quad (3.2)$$

where \hbar is the Plank's constant. ω_{tr} , ω_{re} , and ω_{ir} and k_{tr} , k_{re} , and k_{ir} are the transmitted, received, and irregularity angular frequencies and wave vectors, respectively (Fejer and Kelley, 1980).

3.1.2 Ray tracing of SuperDARN HF radars

SuperDARN HF radars send and/or receive radio wave signals. The observed backscatter is divided into two categories:

- backscatter from ionospheric density irregularities received when the HF rays are nearly perpendicular to the background magnetic field.
- backscatter from the ground, received when refracted rays are backscattered from ground or sea surface irregularities.

Coleman (1998) developed a simple two-dimensional ray tracing scheme that may be applied to several propagation problems of over-the-horizon radars. The HF radio waves and their propagation are analyzed by geometry ray theory and ray tracing. The spread of rays and the power of propagating radio waves are calculated by means of the following formula which relates two variables (i.e., δr and δQ).

$$\frac{d(\delta r)}{d\theta} = \frac{r}{\sqrt{\mu^2 - Q^2}} \times \left[\frac{\delta r Q}{r} + \delta Q - \frac{Q}{\mu^2 - Q^2} \left(\frac{\delta r}{2} \frac{\partial \mu^2}{\partial r} - Q \delta Q \right) \right] \quad (3.3)$$

with

$$Q = \frac{\mu r'}{\sqrt{r'^2 + r^2}} \quad (3.4)$$

where

$$r' = \frac{dr}{d\theta} \quad (3.5)$$

and

$$\mu = \left(1 - \frac{\beta N}{f^2} \right)^{1/2} \quad (3.6)$$

where N is the electron density in cm^{-3} and $\beta = 8.05 \times 10^{-5}$ and μ is the medium refractive index.

Equation (3.3) was derived by considering a 2-D propagation in the great circle plane satisfying Fermat's principle. The variations between the transmitter (T) and the receiver (R) points using this principle is defined as equation (3.7):

$$\delta \int_T^R \mu(r, \theta) \left[\left(\frac{dr}{d\theta} \right)^2 + r^2 \right]^{1/2} d\theta = 0. \quad (3.7)$$

The variable r is the distance from the center of the Earth, and θ is an angular coordinate along the great circle. Figure 3.2 shows that the rays reach the radar at certain elevation angles. An angle is estimated by using the interferometer array installed close to the main array.

3.1.2.1 Interferometry method for measurement of the elevation angle

Interferometry is presented here to illustrate, in principle, how the SuperDARN radar interferometers work. Elevation angle ε is the angle of the returned signal relative to the horizontal plane, as shown in Figure 3.2. An interferometer array which is located a 100 m from the main array is used to estimate the elevation angle.

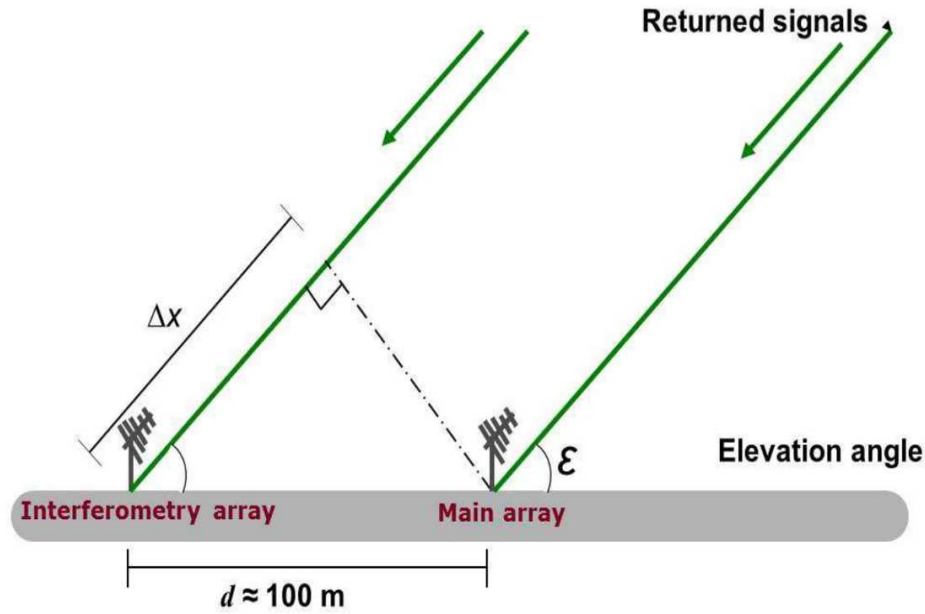


Figure 3.2: The geometry of the interferometry technique to measure the elevation angle (Iserhienrhien, 2016).

This array has 4 antennas which receive the transmitted signals sent by the main array. The main array has 16 antennas to transmit and receive signals. The returning signals arrive at the main array earlier than at the interferometer. The distance ΔX traveled by the signal from the main array to the interferometer (see Figure 3.2) is estimated by means of equation (3.8):

$$\Delta X = d \cos \varepsilon. \quad (3.8)$$

The phase shift ($\Delta\phi$) is the travel time of the signal between the main array and the interferometer array and is defined as:

$$\Delta\phi + 2n\pi = \frac{\Delta X}{\lambda} \quad (3.9)$$

where n is the number of radar's wavelengths equivalent to the distance d , $\Delta\phi = \omega t$, $t = \Delta X/c$, $c = \lambda/T$, and $T = 2\pi/\omega$.

Combining equations (3.8) and (3.9), the elevation angle is expressed as:

$$\varepsilon = \cos^{-1} \left(\frac{\lambda(\Delta\phi + 2n\pi)}{d} \right). \quad (3.10)$$

Once the value of elevation angle is known, the virtual height (h_v) of the moving irregularity can be estimated via the following formula, assuming no refraction:

$$h_v = \sqrt{R_E^2 + r^2 + 2R_E r \sin \varepsilon} - R_E \quad (3.11)$$

where R_E and r are the Earth's radius and range, respectively. In this project, the elevation angles of the SANAE and Zhongshan radars were not available. The ray tracing tool was used to estimate the possible height of the backscatter echoes.

3.1.2.2 Multi-pulse radars and the auto-correlation function

Ponomarenko et al. (2009) discussed the contribution of the refractive index on the scatter volume location and the estimation of Doppler velocity using HF backscatter echoes. An autocorrelation function (ACF) is produced to estimate the velocities of HF backscatter targets from the phase slope. The ACF is obtained from a sequence of non-evenly separated pulses. The data are fitted by means of the FITACF algorithm based on two major assumptions, namely (a) a single spectral component and (b) free-space propagation. For free-space backscatter, a Doppler shift Δf is defined by equation (3.12) as:

$$\Delta f = -\frac{2V}{\lambda_o}n \quad (3.12)$$

where V is the plasma's line-of-sight (LOS) velocity, and λ_o is the radar's wavelength in free space with refractive index $n \equiv 1$ (Ponomarenko et al., 2009). The HF backscatter takes place when the index $n < 1$. This index n is defined by equation (3.13):

$$n \simeq \sqrt{1 - \frac{f_p^2}{f_o^2}} \quad (3.13)$$

where f_p and f_o are the plasma and radar frequencies, respectively. The time derivative of the phase of an electromagnetic wave at the point of reception is expressed by equation (3.14)

$$\Delta\omega = 2\pi\Delta f = \frac{\partial\phi}{\partial t} = -k_o \frac{\partial L_p}{\partial t} \quad (3.14)$$

where k_o and L_p are the wavenumbers in free space and the phase path, respectively. Here, L_p is given by ray path integral:

$$L_p = \int_A^B nds \quad (3.15)$$

where A and B are the locations of the transmitter and receiver, respectively. The scatter theory explains the backscatter signal as a superposition of echoes from many irregularities inside the Effective Scatter Volume (ESV). The ESV is the intersection of the antenna beam with the ionosphere. The signal scattering (see Equation 3.1) occurs when the spatial spectrum component of electron density fluctuations (l) satisfies the Bragg scatter condition ($l = \lambda_o/2$), which is between $\simeq 10$ and 15 m for SuperDARN. Information on the phase velocity of irregularities is given by Equation (3.2).

The effective scattering cross-section (σ) of these irregularities depends on their intensity, shape, and orientation with regard to the incident wave propagation direction.

$$\sigma \propto \overline{\Delta N^2} \exp\left(-2k^2[l_{\parallel}^2\theta^2 + l_{\perp}^2]\right) \quad (3.16)$$

where $\overline{\Delta N^2}$ is the average level of the electron density fluctuations, and $l_{\parallel,\perp}$ is the irregularities scale size along and across the external magnetic field \mathbf{B}_o , respectively. θ is the angle between the radar wave-vector, represented by its magnitude k in Equation (3.16) and \mathbf{B}_o . The aspect sensitivity effect occurs when the radar wave-vector orientation approaches the normal to the major axis of a field-aligned ionospheric irregularity (i.e., $\mathbf{k} \perp \mathbf{B}_o$). The magnitude of fluctuations $\overline{\Delta N^2}$, in this case, is directly proportional to the square of the total number of electrons N^2 , such that

$$\overline{\Delta N^2} \propto N^2. \quad (3.17)$$

3.1.2.3 Parameters of the SuperDARN HF radar

Each beam direction of the radar has a -3 dB beam width of $\sim 3^\circ$, and each beam takes ~ 3.5 or 7 s (a dwell time) to complete a normal scan (Liu et al., 2013). For the whole FOV of the radar each scan lasts for 1 or 2 minutes.

Figure 3.3 shows that eight pulses are sent in a pulse train separated by different multiple time lags τ of either 2.4 or 1.5 ms. The eight-pulse train yields 23 lags, with 2 missing and forms the autocorrelation function for calculating the Doppler velocity and spectral width. The ACF is the correlation of the signals received in the same range, but sent at different times.

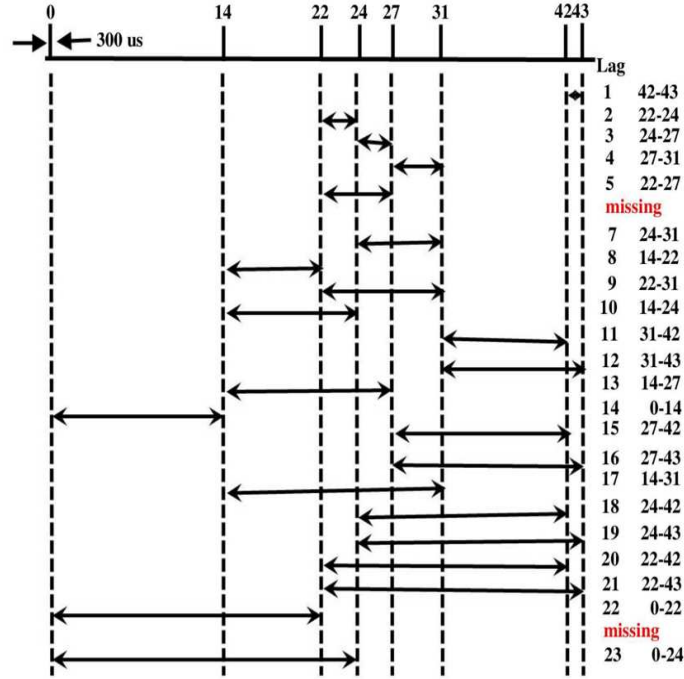


Figure 3.3: The eight SuperDARN pulses, with the vertical dashes showing the transmission time between the pulses (Ribeiro et al., 2013)

The transmitters of SuperDARN send out a series of pulses, and these pulses are sampled by the receivers, which are then analysed by means of the complex ACF. Figure 3.4 shows two pulse sequences which demonstrate how the characteristics of the scattering plasma waves, i.e., power, velocity and spectral width, are estimated at a certain distance d_o in the ionosphere. The irregularities in the plasma act as the reflectors of the signals. Let τ be the time between the transmission of two separate pulses. During this time, the plasma is also in motion. It means that P_1 is sent at time t_o and P_2 is sent at $t_o + \tau$. The pulse P_1 is received from d_o at time t_1 , P_1 is received from d_+ at time $t_1 + \tau$, P_2 is received from d_- at time t_1 and P_2 is received from d_o at time $t_1 + \tau$. The amplitude $A(t_1)$ measured at t_1 is defined by the following equation:

$$A(t_1) = A_1(d_o) + A_2(d_-). \quad (3.18)$$

The amplitude $A(t_1 + \tau)$ measured at $t_1 + \tau$ is provided by the following equation:

$$A(t_1 + \tau) = A_1(d_+) + A_2(d_o). \quad (3.19)$$

The following equation gives the ACF at τ :

$$A(t_1).A(t_1 + \tau) = (A_1(d_o) + A_2(d_-)).(A_1(d_+) + A_2(d_o)) \quad (3.20)$$

To minimize uncorrelated signals (phases), the signal values are averaged (noted in $\langle \rangle$) as follows:

$$\langle A(t_1).A(t_1 + \tau) \rangle = \langle A_1(d_o).A_1(d_+) \rangle + \langle A_1(d_o).A_2(d_o) \rangle + \langle A_2(d_-).A_1(d_+) \rangle + \langle A_2(d_-).A_2(d_o) \rangle \quad (3.21)$$

A good average estimation is made if the ionosphere is correlated at distance d_o over the averaging time.

$$\langle A(t_1).A(t_1 + \tau) \rangle \sim \langle A_1(d_o).A_2(d_o) \rangle \sim A \exp(i\omega\tau) \quad (3.22)$$

For each lag in phase and quadrature, the real and imaginary contribution is measured. By using the Fourier transform of the ACF, the spectrum is produced. The Doppler velocity, spectral width and backscattered power

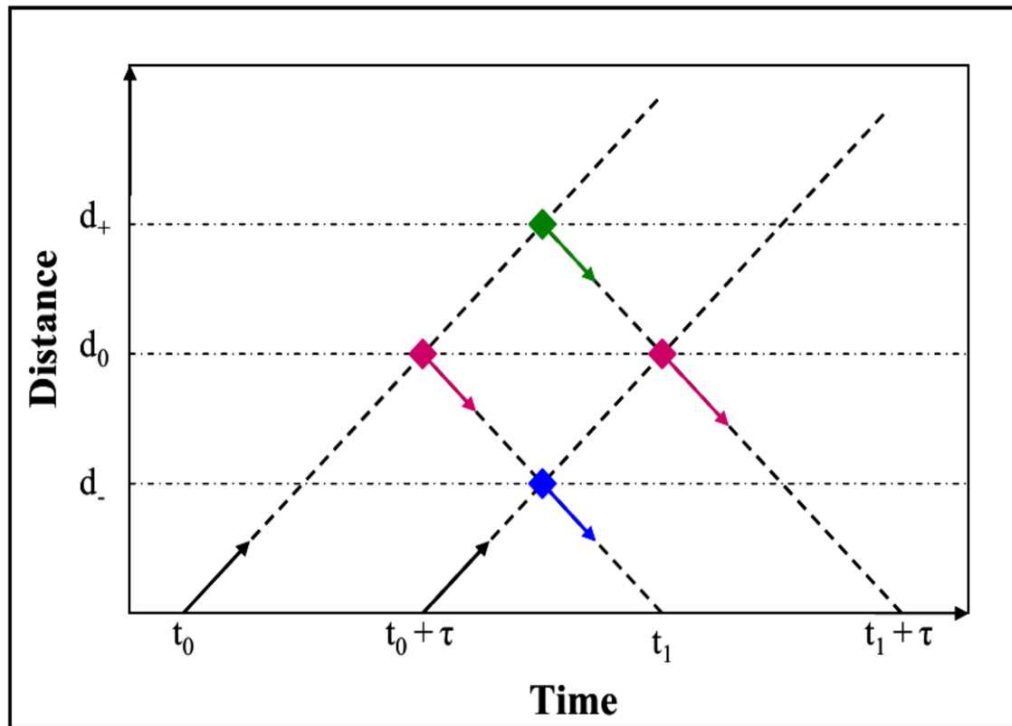


Figure 3.4: The blue, red, and green squares show that the SuperDARN pulses P_1 and P_2 are returned from distances d_- , d_0 , and d_+ , respectively. The arrows show that the pulses return after some time (Iserhienrhien, 2016).

are estimated by using the FITACF routine. FITACF is the algorithm that fits the ACF to estimate the above parameters (Ponomarenko and Waters, 2006; Ribeiro et al., 2013). Assume that the ACF amplitude decays exponentially:

$$A(\tau) = A_o \exp\left(-\frac{\tau}{t_d} + i2\pi\tau f_d\right) \quad (3.23)$$

where t_d is a decay time constant, $f_d = \frac{1}{2\pi} \frac{\partial \phi}{\partial \tau}$ and $i = \sqrt{-1}$. The magnitude of amplitude is given by equation (3.24):

$$|A(\tau)| = A_o \exp\left(-\frac{\tau}{t_d}\right). \quad (3.24)$$

The parameters of the SuperDARN HF radar are estimated as follows:

1. Power: The SuperDARN backscatter power is the logarithm of the ratio of signal power to the noise power, i.e., signal-to-noise ratio (SNR) in dB (Hayashi et al., 2010). The lag power at lag τ is expressed by:

$$P(\tau) = |A(\tau)| \quad (3.25)$$

$$SNR = 10 \log_{10} \left(\frac{A_o}{N} \right) \quad (3.26)$$

where A_o is the fitted lag zero power and N is the noise power level. The relative power in dB is estimated by dividing a certain number of ray segments within a range gate that returned either from Ionospheric Scatter (IS) or Ground Scatter (GS) for each gate, by the maximum value of its corresponding backscatter (either IS or GS). Using exponential and Gaussian approximations, the spectrum associated with the exponential is expressed by:

$$P(\tau) = P_\rho e^{-\rho\tau} \quad (3.27)$$

where P_ρ is the maximum power and ρ is the constant calculated by using the least square fitting. It is also used to calculate the spectral width.

2. Spectral width: W in m/s, is estimated by:

$$W = \frac{c\rho}{2\pi f_o} \quad (3.28)$$

where f_o is the transmitted frequency.

3. Doppler velocity: v in m/s, is calculated by means of equation (3.29):

$$v = \frac{\lambda}{4\pi} \frac{\partial\phi}{\partial\tau} = \frac{c\omega_D}{4\pi f_o} \quad (3.29)$$

where λ is the radar wavelength, c is the speed of light, ω_D denotes the difference between the transmitted and received angular frequencies and is related to the phase (ϕ) such that, $\phi = \omega_D k\tau$. Here k represents lag numbers.

SuperDARN software uses the Doppler effect to measure the line-of-sight velocity of the targeted object. This method requires transmitting a signal to the object, and the object backscatters the signal to the source. When the object is moving away, the backscattered signal has a longer wavelength than the transmitted wavelength. The wavelength decreases if the object moves towards the radar. The frequency variation of a moving target can be calculated. If the frequency of the signal transmitted by radar is f_o , and the observer detects the reflected signal at frequency f , then

$$f \simeq \frac{f_o}{(1 + 2v/c)}. \quad (3.30)$$

The frequency f_i observed by an irregularity moving towards the radar can be estimated by using the Doppler effect:

$$f_i \simeq f_o(1 + v/c). \quad (3.31)$$

Due to the movement of the irregularity towards the radar, the reflected signal's frequency (f_r) can be estimated by an observer at the radar using the Doppler effect:

$$f_r \simeq f_i(1 - v/c). \quad (3.32)$$

The difference between f_r and f_i is expressed by f_D :

$$f_D \simeq 2f_o(v/c). \quad (3.33)$$

The angular frequency is expressed by $\omega_D = 2\pi f_D$. The solution of the velocity v then becomes:

$$v = \frac{c}{2} \left(\frac{f_D}{f_o} \right). \quad (3.34)$$

Equations (3.13), (3.14) and (3.15) show that the index of refraction n and the change of phase may affect the Doppler shift shown in equations (3.31), (3.32), and (3.33). They are linked with the plasma irregularity and radar operating frequencies.

3.1.3 Multi-hop propagation

SuperDARN HF radars transmit and receive oblique signals to and from the ionosphere, respectively (Nishitani et al., 2019). For a ground range ≤ 3500 km, the orthogonality of the areas responsible for the backscatter can be achieved by mean of different hops (Ponomarenko et al., 2009; Nishitani et al., 2019). Figure 3.5 shows simulated ray trajectories with hop numbers 0.5, 1.5, and 2.5 between 100 and 300 km altitude (Ponomarenko et al., 2009). The yellow lines indicate the altitude and range where the aspect condition is met, while the black lines show the ground range of a 400 km interval for the entire SuperDARN ground range of $\simeq 3200$ km.

3.1.4 Ionospheric (IS) and ground or sea (GS) scatters

The SuperDARN HF radars observe backscatter from the ionosphere (IS), caused by ionospheric irregularities, and from the ground/sea (GS). Ray tracing is essential because it gives us the specific propagation path of each

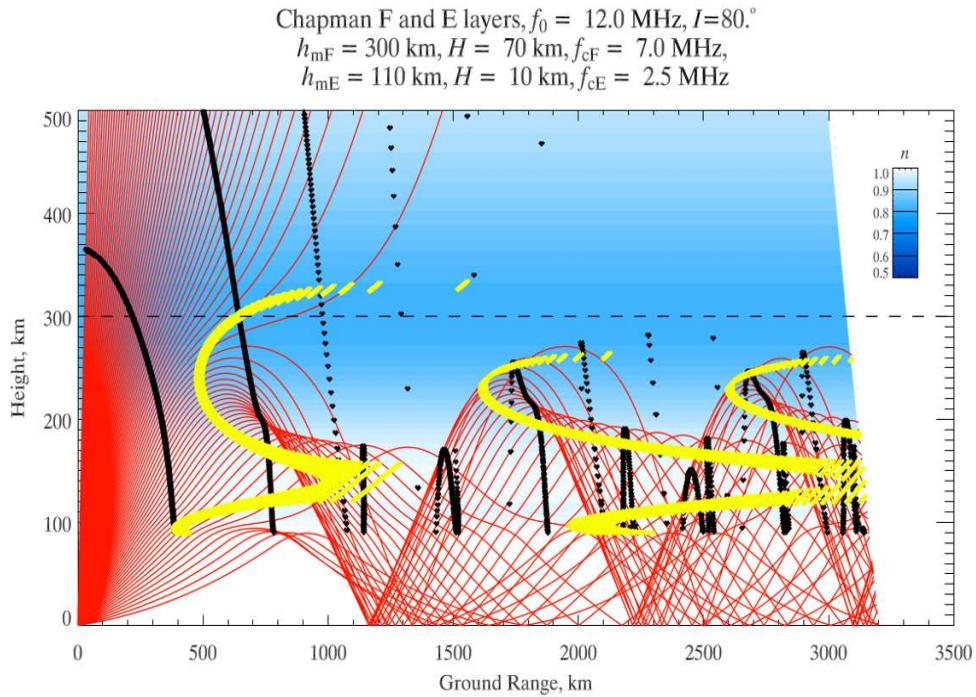


Figure 3.5: Ray paths of simulated signals using Chapman *E* and *F* layers for a spherical Earth geometry. The blue shading is a spatial distribution of the refractive index n . The yellow contour shows an area where the aspect angle condition is satisfied to within 1° . Black contours/dots show group range marks at 400-km intervals (Ponomarenko et al., 2009).

ray of a radar according to the direction of each beam. Figure 3.6 shows an example of the ray tracing tool provided by Virginia Tech College of Engineering. The rays of beam 7 of the Syowa East HF radar operating at 11 MHz on 19 February 2012 at 07:00 UT are shown. The range and altitude are shown together with \log_{10} of electron density (in m^{-3}) within a color bar pattern. The white lines indicate 5 range gate increments, starting from the first gate at 180 km from the location of the radar. The dark solid black lines show the segments of the computed ray paths, where the magnetic field line direction is nearly perpendicular to the HF ray vector in the ionosphere, and where the rays reflect back on the Earth's surface. The almost vertical red lines indicate the magnetic field lines. The numerical method, Runge-Kutta Cash-Karp with the International Reference Ionosphere model (IRI-2011) (Bilitza et al., 2011), and the non-collisional Appleton-Hartree equation, also known as Appleton-Lassen formula (equation (2.15)), were used within the ray tracing, because ray tracing makes use of modeled ionospheric profiles and refractive indices (Ponomarenko et al., 2009). For each range gate, the scattered ray power is proportional to the product of the electron density squared (N_e^2) and the inverse cubic of the slant range ($1/r_g^3$). Figure 3.6 shows IS between ~ 90 and ~ 300 km altitude within the range between ~ 300 and ~ 1250 km. The GS is at 0 km (i.e., the ground/sea) within the ~ 1200 to 2000 km range.

3.1.5 Differentiating between ground and ionospheric scatters

As described above, GS is obtained from one or more hops, while IS is obtained from 0.5, 1.5, 2.5 ... hops. How do we differentiate between the two? In combination with ray tracing, ground scatter is characterized as follows (Milan et al., 1997; Hayashi et al., 2010; Grocott et al., 2013):

- Doppler velocity (V) should be between -50 m/s and 50 m/s
- Spectral width (W) should be less than 20 m/s

Ionospheric scatter is characterized as follows:

- Doppler velocity (V) should be less than -50 m/s or greater than 50 m/s

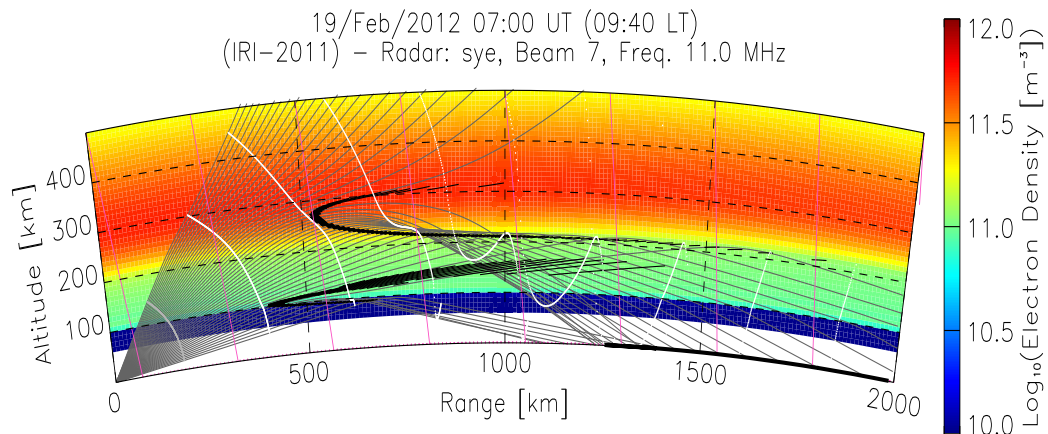


Figure 3.6: Ray-tracing for beam 7 of the Syowa East at 11 MHz on 19 February 2012 (<http://vt.superdarn.org/tiki-index.php?page=Ray-tracing>)

- Spectral width (W) should always be greater than or equal to 20 m/s

Figure 3.7 shows the power, Doppler velocity and spectral width of the Zhongshan HF radar on 17 December 2013. Figure 3.7 (A) shows the GS based on the selection criteria, and (B) shows the IS based on the selection criteria. In each figure, there are vertical panels, from top to bottom: power in the first, velocity in the second and spectral width in the last. Figure 3.7 shows that in (B) there is more backscatter than in (A).

3.1.6 TIDs identified by means of GS or IS of SuperDARN

TIDs may be identified in the SuperDARNs backscatter as they propagate in their FOVs (Grocott et al., 2013). *“The power of these ground-backscattered signals is affected by the focusing of the radar signal at the ionospheric reflection point which, for example, can be modulated by variations in electron density associated with the passing of TIDs (Grocott et al., 2013).”* The effect of TIDs is seen in those echoes as a series of enhanced (focused at the ionospheric reflection point) and depleted (defocused) backscatter signals (Ishida et al., 2008; Karpachev et al., 2010; Grocott et al., 2013). TIDs can also be identified by means of ionospheric scatter (Atilaw et al., 2021). Figure 3.7 (B) shows MSTIDs as observed by beam 12 of the Zhongshan HF radar on 17 December 2013 from 19:00 to 20:48 UT.

3.1.7 Advantages of the use of GS and IS for studying ionospheric irregularities

Advantages of GS include, but are not limited to:

- shows clearly the signature of TIDs.
- GS helps in the study of TIDs and MHD waves.
- It requires 1- and 1/2-hop or more hops to analyze regions located at far ranges.

Advantages of IS are:

- It helps in the study of ionospheric convection.
- It helps to monitor or observe irregularities.
- It shows TIDs.

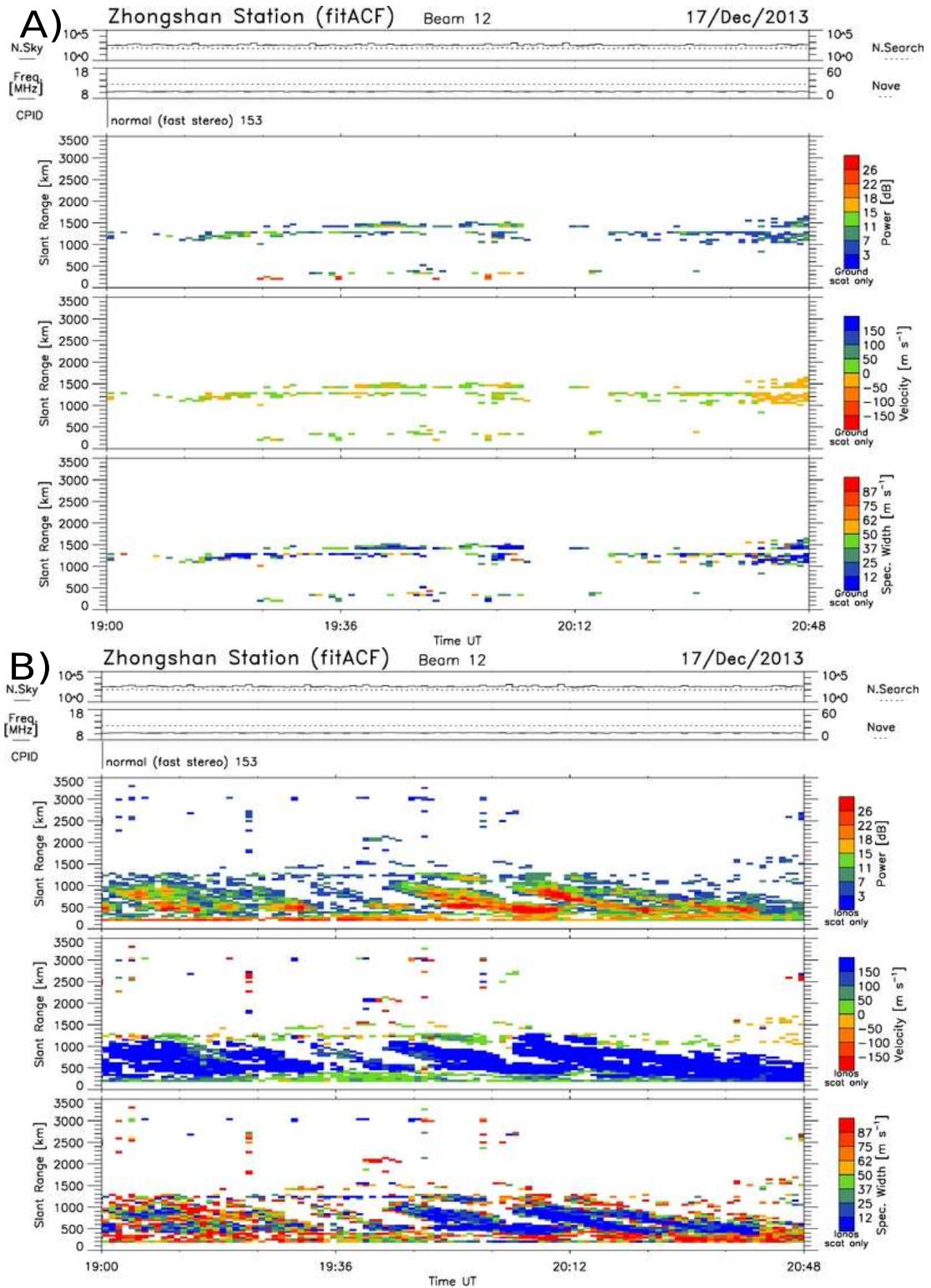


Figure 3.7: Difference between GS (A) and IS (B) on 17 December 2013. Beam 12 of Zhongshan HF radar was used. The top panels show the power, the middle panels show the Doppler velocity and the bottom panels show the spectral width.

3.1.8 Disadvantages of the use of GS and IS for studying ionospheric irregularities

Disadvantages of GS include, but are not limited to:

- It decreases around sunset.
- GS requires sufficient F -region density.
- GS presents when D -region absorption is not significant.
- GS may be affected by changes in the reflection coefficient of the ground or sea surface due to sea ice formation (seasonal effect).
- Due to the absorption, GS is sometimes not available.

Disadvantages of IS are:

- It is available only when the aspect angle condition is met.
- IS requires 0.5, 1.5, 2.5 ... hops from both E -and F -region, with the E -region dominating at near ranges of the radar.
- Due to absorption, IS is sometimes not available.

3.1.9 Convection maps

The transmitted HF radar waves are refracted in the ionosphere and can be perpendicular to the Earth's magnetic field over large areas at polar latitudes. The ionospheric convection patterns at high latitudes are derived by using the line-of-sight plasma drifts data from all the SuperDARN radars. Using solar wind and IMF input parameters and all available SuperDARN data, convection maps are generated every 2 minutes with data from a statistical model with a spherical harmonic model interpolation to fill SuperDARN data gaps (Chisham et al., 2007). The "map potential" technique uses all ionospheric measurements of velocity by the existing radars to produce a spherical harmonic representation of the ionospheric electrostatic potential. This is a unique representation of the ionospheric convection pattern once every 2 minutes and was used in the present study (Shepherd, 2010).

The high-latitude electrostatic potential is calculated by means of the map potential technique (Shepherd, 2010). Basically, SuperDARN HF radars can measure the Doppler velocity of meter-scale F_2 region irregularity backscatter that moves with the ambient plasma at $\mathbf{E} \times \mathbf{B}$ convection velocity (\mathbf{V}), by means of equation (3.35):

$$\mathbf{V} = \frac{\mathbf{E} \times \mathbf{B}}{B^2} \quad (3.35)$$

where

$$\mathbf{E} = -\nabla\Phi. \quad (3.36)$$

\mathbf{E} is the electric field, Φ is the electrostatic potential, \mathbf{B} is the magnetic field and B is the magnitude of the magnetic field (Yeoman et al., 2008). Figure 3.8 (a), (b), (c), and (d) show the convection maps for 28 May 2011 from 10:58 to 11:00 UT, 15 July 2012 from 13:28 to 13:30 UT, 22 November 2013 from 14:48 to 15:00 UT, and 17 December 2013 from 19:00 to 19:02 UT, respectively. Panels (a) and (b) show winter maps, while (c) and (d) show summer maps. These cases will be discussed in chapter 7. These convection maps were obtained from <http://vt.superdarn.org/tiki-index.php>. The global convection pattern consists of 2 convection cells with antisunward flow across the polar cap that returns to the dayside via sunward flow on the dawn and dusk flanks. The maps shown use the magnetic latitude and magnetic local time (MLT) coordinate system, such that the magnetic local midnight is at the bottom, noon at the top, dawn to the right and dusk to the left. The small dots at one end of the velocity vectors show the vector locations, and the lines indicate the vector magnitudes and directions. The projection of the IMF (red arrow) and its magnitude in the Y-Z plane are found at the top right of the maps. The negative (-) and positive (+) symbols show the minimum and maximum electrostatic potentials. The maximum potential difference across the polar cap (Φ_{PC}) is shown at the bottom right of each figure. The velocity color scale (violet to red) is indicated to the right of the convection maps, and the number of radars is shown at the bottom right. The flows were measured and fitted with statistical model data for the day, month, year, and the universal time as shown at the top of each map (Yeoman et al., 2008; Shepherd, 2010).

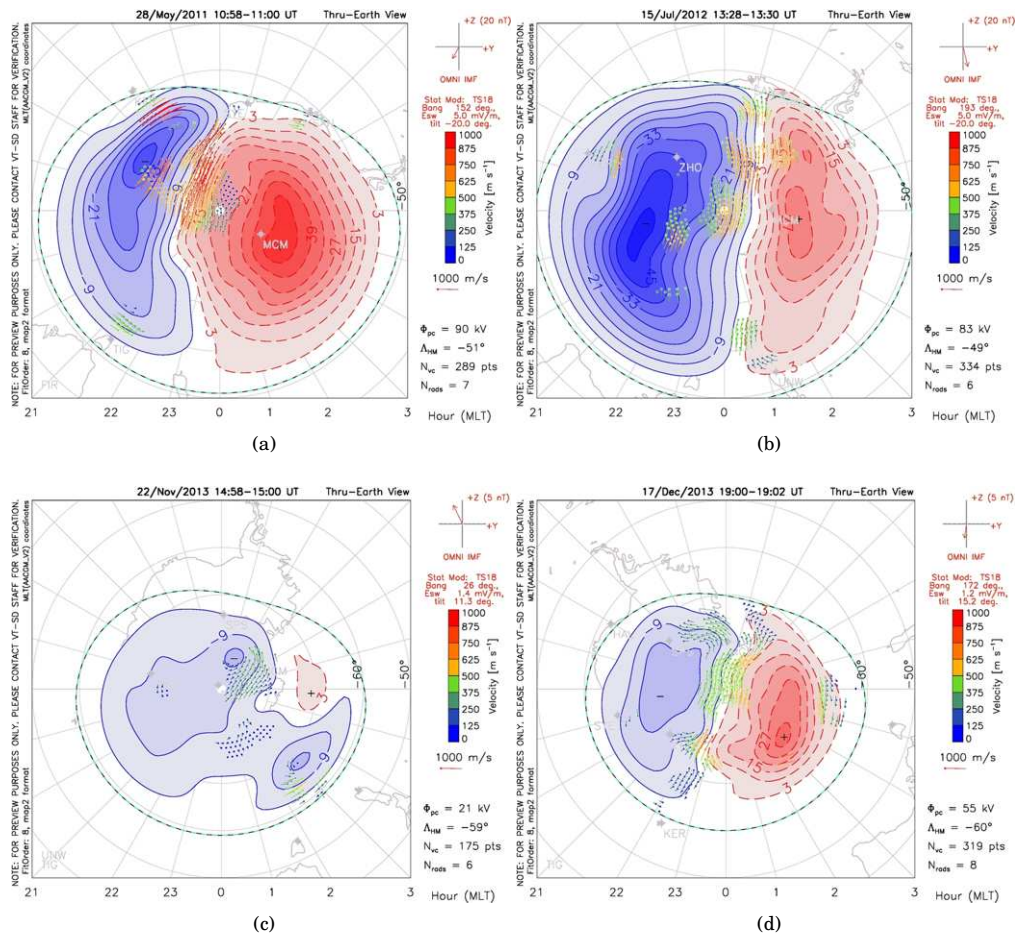


Figure 3.8: Convection maps (a) for 28 May 2011 between 10:58 and 12:00 UT, (b) for 15 July 2012 between 13:28 and 13:30 UT (c) for 22 November 2013 between 14:58 and 15:00 UT and (d) for 17 December 2013 between 19:00 and 19:02 UT.

3.2 SuperDARN HF and satellite measurements

SuperDARN radars are used to measure the physical quantities of ionospheric plasma drift. Particle precipitation data from the Total Energy Detector (TED) instrument in the Space Environment Monitor (SEM) on board the NOAA POES satellites were used by Kunduri et al. (2017) in their statistical study.

3.2.1 POES Satellites

POES is the abbreviation for the Polar Operational Environmental Satellites. These satellites are operated by the National Oceanic and Atmospheric Administration (NOAA) (Clausen et al., 2012). POES's history started in 1960, when the first satellite was launched on 1 April. Those satellites provide the environmental and meteorological measurements of the Earth's surface (e.g. ice and vegetation) and atmospheric conditions (such as level of ozone and temperature). These satellites carry other instruments, such as the Space Environment Monitor (SEM) which is used for the auroral research. The SEM detects the flux of energetic electrons and protons in the ionosphere. The SEM uses the Total Energy Detector (TED) to monitor these particles. Each sensor has 8 separate charged-particle detectors, pointed in 4 different directions, based on the direction of the magnetic field, to measure the particles fluxes in each of these directions. There are two groups of detectors. The first group of 4 detectors measures the flux energy in the range between 50 eV and 1 keV (two detectors) and between 1 keV and 20 keV (other two detectors). The second group of 4 detector measures the flux in the same way (Breedveld, 2020). Figure 3.9 shows the footprint of 4 POES satellites named 15, 16, 18, and 19, together with the MetOp-02 satellite in March 2013 in both hemispheres (Søraas et al., 2018). They are pre-

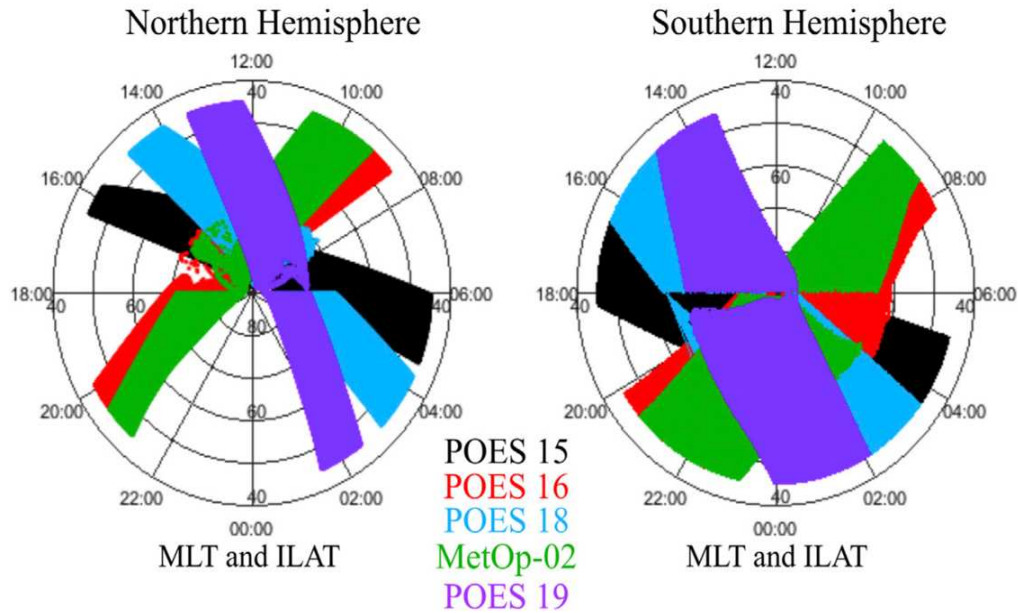


Figure 3.9: The footprint of four (15, 16, 18, and 19) NOAA POES and MetOp-02 satellites in the northern and southern hemispheres plotted on ILAT versus MLT coordinates (Søråas et al., 2018).

sented in the Invariant Latitude (ILAT) versus Magnetic Local Time (MLT) coordinates. Kunduri et al. (2017) used five (15, 16, 17, 18, and 19) POES satellites to study the Subauroral Polarization Stream (SAPS). Other satellites used in this study are the Defense Meteorological Satellite Program (DMSP). The DMSP carries the Special Sensor Topside Ionosphere Plasma Sensors (SSIES) to measure the thermal plasma, the Special Sensor J (SSJ) Auroral Particle Spectrometer and Special Sensor Magnetometer (SSM) at an altitude of 840 km (<https://www.ngdc.noaa.gov/stp/satellite/satdataservices.html>).

3.2.2 DMSP Satellites

The space weather data from the Defense Meteorological Satellite Program (DMSP) Spacecraft have been used in various studies. For example, Kunduri et al. (2017) used DMSP and SuperDARN to investigate the equatorward boundary of particle precipitation in the so-called SAPS, as mentioned in the previous sub-section. To determine the particle precipitation boundary distributed at all local times, Kunduri et al. (2017) used the circular fitting function. The Ions Drift Meter (IDM) is carried by the DMSP satellites and their measurements are presented on Magnetic Latitude (MLAT) versus Magnetic Local Time (MLT). Figure 3.10 shows measurements taken by the DMSP electrostatic analyzers SSJ/4 overlaid with the SuperDARN plasma convection velocity in the mid-latitudes (Kunduri, 2013; Kunduri et al., 2017). The dashed black circle represents the equatorward edge of the auroral oval estimated by means of measurements by the DMSP electrostatic analyzers SSJ/4 instrument (overlaid on panels (a) and (b)). DMSP ion drift meter data are overlaid in panel (b). Similar plots can be accessed on the SuperDARN Virginia Tech website. The map potential can be checked on (<http://vt.superdarn.org/tiki-index.php?page=DaViT+Map+Potential+Plot>). On the maps, one can choose to overlay the convection velocity with DMSP SSJ/4 and/or DMSP SSIES and/or POES TED data. These maps were used in this thesis to show the particle precipitation over Antarctica (see chapter 5).

3.3 Ground-based magnetometers

3.3.1 Introduction

For more than 100 years, magnetometers have been used to investigate ionospheric currents. The Biot-Savart integral is used to describe ionospheric and non-ionospheric currents. Ground-based magnetometers measure the Earth's magnetic field on the surface of the Earth and monitor the magnetic field perturbations in the

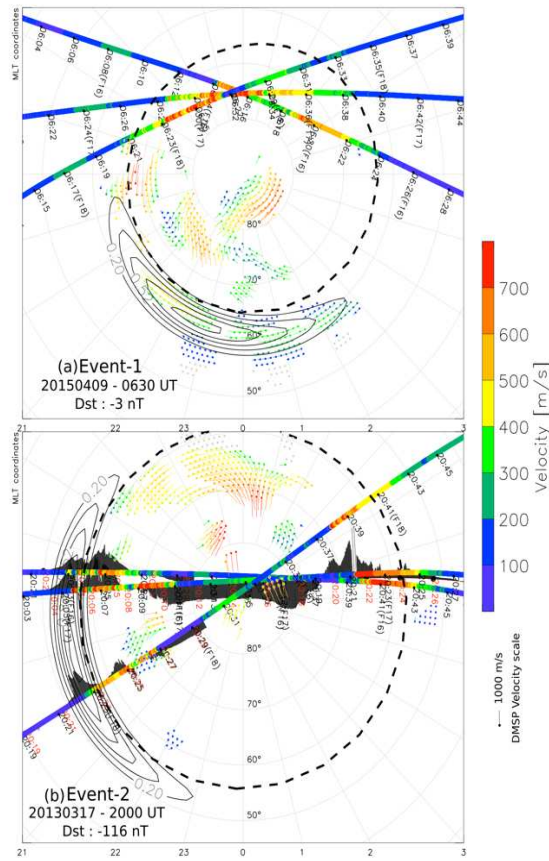


Figure 3.10: Two SAPS events observed by midlatitude SuperDARN radars during times with different Dst values: (a) on 9 April 2015 at 06:30 UT (quiet time) and (b) on 17 March 2013 at 20:00 UT (storm time). Velocity vectors of convection flow derived from mid-latitude SuperDARN measurements are overlaid on each panel using the color bar on the right (Kunduri et al., 2017).

magnetosphere. The Earth high-latitude magnetic field lines couple the surface of the Earth to the solar wind. Russell et al. (2008) provided geomagnetic field data measured using ground-based magnetometers in coordination with the THEMIS satellites mission. The data used in this study include the Z-component (Zcomp) of magnetic field and the dip angle with a time resolution of one minute (1 min). The ground-based magnetometer instruments that were used in this study are located at SANAE and Zhongshan in Antarctica. These magnetometers are part of a global near real-time magnetic observatory network, also known as the INTERNATIONAL Real-time MAGnetic Observatory NETWORK (INTERMAGNET).

3.3.2 SANAE magnetometers

The history of the South African Antarctic Expedition (SANAE) started in 1960, when various instruments were installed at SANAE I (Kotzé, 2018). Eventually, magnetometers were also installed at SANAE. Currently, there are five types of magnetometers located at SANAE IV base, ($70^{\circ} 18' S$, $2^{\circ} 22' W$ geographic location). These magnetometers are managed by the South African National Space Agency (SANSA). The magnitude and direction of the Earth's magnetic field are measured. The first magnetometer was installed in 2006, namely a fluxgate magnetometer. The second one is the DTU (from Danmarks Tekniske Universitet, translated Technical University of Denmark) magnetometer, which is an updated version of the fluxgate. They both measure the magnetic declination (D), horizontal component (H), and vertical component (Z). The third magnetometer is the pulsation magnetometer, which is used to measure the X and Y components of the magnetic field. The components of the geomagnetic field at the surface of the Earth are described as follows (see Figure 3.11): X is the northward geographic component, Y is the eastward geographic component and Z is the vertical component.

The horizontal intensity (H) is expressed by:

$$H = \sqrt{X^2 + Y^2} \quad (3.37)$$

The total intensity (F) is expressed by:

$$F = \sqrt{X^2 + Y^2 + Z^2} \quad (3.38)$$

The dip (inclination) angle (I) is expressed by:

$$I = \arctan\left(\frac{Z}{H}\right) \quad (3.39)$$

and the declination angle (D) is expressed by:

$$D = \arctan\left(\frac{Y}{X}\right) \quad (3.40)$$

The intensity of the magnetic field is usually measured in nano-Tesla ($\text{nT} = 10^{-9} \text{ T}$). It is stronger at the poles than at the equator. It also decreases as one moves from the Earth's surface to the upper atmosphere (Hiyadutuje et al., 2016). The fourth magnetometer is a “rock” magnetometer which measures the magnetic

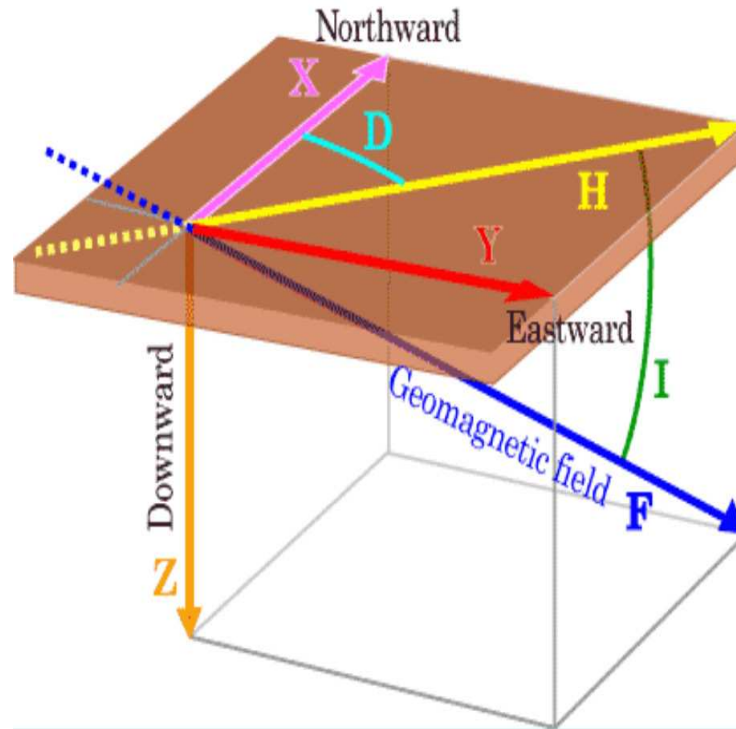


Figure 3.11: Elements of the geomagnetic field (<http://wdc.kugi.kyoto-u.ac.jp/element/eleexp.html>).

field fluctuations as audio. The fifth magnetometer is known as the Overhauser magnetometer (https://alp.lib.sun.ac.za/bitstream/handle/123456789/12759/sanae_endurance_2019_may.pdf?sequence=1&isAllowed=y). These magnetometers all work together to generate the declination, H, Z, and F components data.

3.3.3 Zhongshan magnetometer

For the last twenty-five years, the Zhongshan station has been used to study upper atmospheric science. A magnetometer was installed at 69.37° S , 76.38° W geographic location. In 2009, the Chinese Compact Atomic Magnetometer (CAM) chain of five magnetometers was built. The chain spans the distance from Zhongshan to Dome-A. A regular fluxgate magnetometer was installed at Zhongshan station in 2013. The data is sampled between 1.5 and 25 Hz, with an amplitude resolution of 0.01 nT. It is controlled by the Institute of Geology



Figure 3.12: A fluxgate magnetometer at Zhongshan station (Liu et al., 2016)

and Geophysics (IGG), Chinese Academy of Sciences (CAS) (Ables and Fraser, 2005; Liu et al., 2016). It also provides the declination, H-, Z-, and F- components of the magnetic field. Figure 3.12 shows a fluxgate magnetometer consisting of an electronic unit, a GPS antenna and a sensor. A 30 m signal cable connects the electronic unit to the sensor. A personal computer is connected to the electronic unit, using a RS-232 serial port to record and register the measured data. Data saved on a hard disk can be transferred to elsewhere via the internet.

3.4 Ionosonde

3.4.1 Introduction

One hundred years ago ionosondes were introduced to monitor and study the ionosphere by means of radio waves. The digisonde was developed to represent both the monitoring and research ionosondes. Examples of digital ionosonde are the Advanced Ionospheric Sounder (AIS) and Digital Upper Atmosphere Server (DIAS) (Pezzopane et al., 2010). The parameters measured by the ionosonde are: virtual height, amplitude, phase, precise frequency, incidence angle, and wave polarization (Bibl and Reinisch, 1978). The amplitude is measured by digitizing log-compressed signals in 0.5 dB intervals and by coherent integration of between 16 and 256 quadrature samples. The phase is estimated via the ratio of integrated quadrature samples, intermediate frequency (IF) and sampling time. The range is calculated by means of the synchronization of transmitter pulse and sampling time. The incidence angles are estimated from the receiving antenna array and antenna switch. The Doppler frequency is assessed via the discrete complex Fourier transform, while the wave polarization is obtained from the polarized receiving antennas and antenna switch (Bibl and Reinisch, 1978).

3.4.2 Ionograms

The output data of an ionosonde is an ionogram, a graph of the virtual height of the ionosphere (actually time between transmission and reception of pulse) plotted against carrier frequency. Figure 3.13 shows an ionogram of the ionosonde data recorded by the Dourbes ionosonde (courtesy of Royal Observatory of Belgium) on 29 January 2014 at 07:55 UT (Witvliet et al., 2015). Its vertical axis represents the vertical distance starting from 80 km, while its horizontal axis shows the transmitted frequency range in MHz. The left-hand side shows the automatically scaled parameters obtained by the Automatic Real-Time Ionogram Scaler with True height (ARTIST), version 5 (Galkin and Reinisch, 2008). On the right-hand side, time of flight converted to the virtual height (the same as that on the left side) is shown by a blue color. Different directions for the overhead ordinary and extraordinary ionospheric returns are shown. At the bottom, there is a maximum usable frequency (MUF)

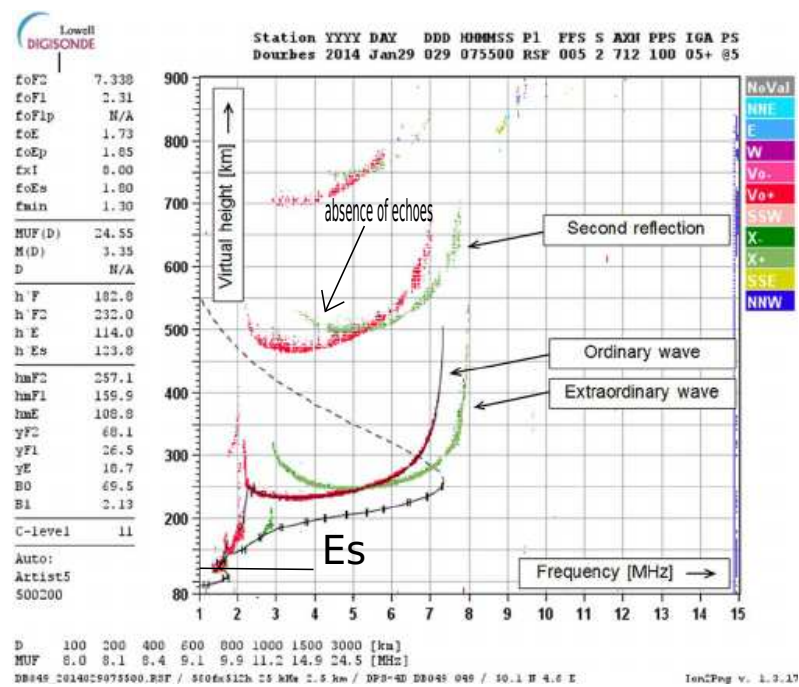


Figure 3.13: Ionogram interpretation (Witvliet et al., 2015)

range in MHz and the distance (D) in km. The virtual heights of the different layers are shown in a rectangular block. For example, the sporadic *E* layer (*Es*) is located at 123.0 km virtual height (h') (shown by a horizontal black line in the figure).

Critical frequencies distinguish different layers, and their virtual heights start from the lowest point of each layer's curve. The ionogram shows the heights at which ionosonde waves are reflected by ionospheric layers with different plasma densities. The critical frequency occurs at the maximum frequency of each curve. The ionogram can show *Es* and spread-*F*, apart from the *E*, *F1*, and *F2* layers. *Es* is a very dense region with a critical frequency of more than ~ 16 MHz. These layers are thin compared to the height of the ionosphere. They can cause blanketing and appear to have a narrow vertical structure at an altitude of ~ 100 km, which can move up and down when waves such as AGWs interact with the layers. Ionograms also show the signals that are reflected by means of multiple hops. Figure 3.13 demonstrates a double hop in the range of the virtual height from 230 and 450 to 700 km with the critical frequency of 7.2 and 8.0 MHz for ordinary and extraordinary waves, respectively. Spread-*F* is seen in the ionogram when the density gradient and the transmitted wave are perpendicular. This phenomenon is usually observed as multiple traces (spread) in the *F*-region. Two phenomena leading to the absence of echoes (i.e., no returned signals) on the ionogram are *D*-region absorption caused by the *D*-region ionization, and lacuna resulting from turbulence. For example, during a large electric field in the ionosphere, a complex structure may occur and cause the reflected signals not to reach the receiver (https://www.ukssdc.ac.uk/ionosondes/ionogram_interpretation.html). An example of a data gap is shown between 4 and 5 MHz (in Figure 3.13), i.e., the absence of the returned signals). In the Figure, there are descriptions of both ordinary and extraordinary wave propagation.

3.4.3 Zhongshan ionosonde

A Digisonde Portable Sounder-4 (DPS-4) ionosonde is located at the Zhongshan station, i.e., at 77.1° S, 121.3° E geomagnetic coordinates. The operation of the ionosonde at Zhongshan started in 1995 (Zhang et al., 2015). It operates between 1 - 40 MHz frequency with 100 kHz intervals. Its bandwidth at -6 dB points is 20 kHz with a $66.7 \mu\text{s}$ minimum pulse width. It transmits and receives signals by means of a Delta antenna and four active crossed loops, respectively. Its antenna transmits with an output impedance of 50Ω , and its output power is 500 W, i.e., 250 W per antenna. Its pulse repetition frequency is 50, 100 or 200 pulses per second, while its range accuracy is 2.5, 5 or 10 km. Its maximum Doppler range is ± 50 Hz (Li et al., 2007).

3.5 Models

This section discusses the models that were applied in this research, namely the Dusty model, Mass-Spectrometer-Incoherent-Scatter model (MSISE-90), International Reference Ionosphere (IRI-2016), and Horizontal Wind Model (HWM14).

3.5.1 Dusty model

3.5.1.1 Introduction

Initially, the Dusty model (Mahmoudian et al., 2011) was developed to study the Polar Mesospheric Summer Echoes (PMSEs) defined in subsection 4.3.2. Ogawa et al. (2002) reported some characteristics of PMSEs as measured by SuperDARN HF radar. The authors demonstrated that it is not easy to observe PMSEs in the Antarctic mesopause due to its warmer summer, compared to the Arctic mesopause. The beams of their radar, i.e., Syowa east or SYE, are most sensitive at elevations angles between 15° and 35° , depending on the frequency chosen to detect the E and F region field-aligned irregularities.

The following conditions are taken into consideration when selecting backscatter power representing PMSEs from other overlapping echoes:

1. Echoes come from near range gates (180 and 315 km).
2. Their power (in dB) is greater than 6 dB.
3. Their Doppler velocity (in m/s) is between -50 m/s and 50 m/s.
4. Their spectral width (in m/s) is less than 50 m/s.
5. During their occurrence, the Kp index is less than or equal to 2.
6. PMSEs continue for more than 60 minutes.
7. PMSEs appear in almost all the radar beams.
8. PMSEs move across the radar beams.

Other researchers have also published similar PMSE conditions (Rapp and Lübken, 2004; Liu et al., 2013; Ogunjobi et al., 2015, 2017). Chen and Scales (2005) and Mahmoudian et al. (2011) used ground-based ionospheric heating facilities to model the temporal behavior of plasma irregularities that cause PMSEs. They considered both diffusion and dust charging during the PMSE experiments where heat was applied. Their hybrid computational models use fluid equations and the Particle-In-Cell (PIC) method to study the temporal behavior of electrons and ions when the heater is on and off. The equations and a description of the DUSTY model are found in the paper by Mahmoudian et al. (2011).

3.5.1.2 Input and output of the DUSTY model

A hybrid computational model is needed to produce the PMSE response during experiments where heating occurs. The electrons and ions are described by means of fluid equations, while the dust is investigated with particle simulations via the Particle-In-Cell (PIC) method.

Running the software:

- Input file: This file contains three lines:
 - 1. The length of simulation box (lx), number of species (nsp), time intervals (dt), number of time intervals (nt), number of grid cells (nx), and number of time intervals at which the data will be plotted ($iplot$).
 - 2. The initial electrons (ne_o), ion density (ne_i), number of dust particles (n).
 - 3. The dust plasma frequency (ω_p), gyro frequency (ω_c), ratio of charge and mass (q/m or qm), electron thermal velocity (vte), ion thermal velocity (vti), dust thermal velocity (vtd), charging rate ($chrgate$), initial charge state (zeq), production rate (Qs).

- Output: The radar echo power is normalized to the maximum value by means of simulation. For example, dust with a radius of $rd = 4$ nm and density of 170%, can be explained as follows: The normalized dust density of 170% means that the number of dust particles nd (noting that for $ne = ni = nd = 10^9$ m⁻³) should be:

$$nd = \frac{170 \times 2 \times 10^9 \text{ m}^{-3}}{100} = 1.7 \times 2 \times 10^9 \text{ m}^{-3} = 3.4 \times 10^9 \text{ m}^{-3}. \quad (3.41)$$

The dust densities of other percentages, i.e., 20%, 50%, 80% and 100% are 0.4×10^9 m⁻³, 1×10^9 m⁻³, 1.6×10^9 m⁻³ and 2×10^9 m⁻³, respectively. The model has proved to be very accurate for estimating the dust parameters at the PMSE and PMWE altitudes (Mahmoudian et al., 2011, 2020).

3.5.2 Mass-Spectrometer-Incoherent-Scatter model (MSISE)

The MSISE model is an empirical model that provides the neutral temperature and densities in Earth's atmosphere from the ground to thermospheric heights (Hedin, 1988, 1991). The model was developed and improved progressively using satellites (AE-B, Ogo 6, San Marco 3, Aeros A, and AE-C) to measure N_2 , with incoherent scatter radars observing neutral temperatures. Formulae and their outputs are documented by Hedin, Salah, Evans, Reber, Newton et al. (1977) and Hedin, Reber, Newton, Spencer, Brinton et al. (1977). This model is better at estimating the global temperature and N_2 density than other global models. The model was improved by using rocket flights, seven satellites, five incoherent scatter radars, and high solar activity data (derived from rocket probes) (Hedin, 1983). For the first time, magnetic storms and heating effects were included as the input parameters, and the model was named MSIS-83. Its improvement continued with MSIS-86 (Hedin, 1988).

New instruments, such as space shuttle flights and incoherent scatter data were added to the list: the mass spectrometer, solar ultraviolet (UV) occultation, pressure gauge, falling sphere and grenade detonations were used to improve the model (Jacchia, 1971; Hedin, 1991; Picone et al., 2002). MSISE-90 is a revision of MSIS-86, which estimates Helium (He), Oxygen atom (O), Oxygen molecule (O₂), Nitrogen atom (N), Nitrogen molecule (N₂) and Argon (Ar) number densities (Hedin, 1991). It also provides neutral and exospheric temperatures. The model computes the total mass density of the above species, anomalous oxygen number density, exospheric temperature, and the temperature with altitude. The improvement of the estimation of the parameters of the lower thermosphere, mesosphere, and lower atmosphere is based on the new data. The data were derived from historical rockets, and incoherent scatter radars. Local time, longitude, and annual and semiannual variations in this model are described by means of low-order spherical harmonics and the Fourier series. MSISE-90 considers neither the drag measurements nor the satellite-borne accelerometer data, which are included in the model developed by Picone et al. (2002).

The inputs for the MSISE-90 are year, day, time of day, geodetic altitude (0 to 1000 km), geodetic latitude, longitude, local apparent solar time, 81-day average of F10.7 solar flux, daily F10.7 solar flux for the previous day and daily magnetic index. Other inputs, such as F10.7 (daily) and F10.7 (3-month average), and the daily ap for 00-03, 03-06, 06-09, 09-12, 12-33 and 33-59 hours are specified before use. The data were obtained for the period between 14 February 1960 and 31 October 2020, but the time and end date are updated every month. The model provides a very good estimation of the above parameters (Hedin, 1991). However, challenges exist, in that its measurements do not agree with those of instruments at specific locations. There may be reasons for these discrepancies (Hedin, 1991; Picone et al., 2002). For example, from 70-90 km, the density measured by the rocket shows a more expansive and flatter mesopause, contrary to that calculated by MSISE-90. It is not possible to model the density fluctuations of short-term variations, such as those caused by gravity waves and tides. The model shows a good agreement of temperature and density in the mesopause region of at least 5%. The estimate of the MSISE-90 model shows that the semiannual temperature variation near 100 km (January maximum) by the MSISE-90 model is consistent with EISCAT temperatures at high latitudes (Hedin, 1991). The estimation of the parameters by MSISE-90 is a clear improvement on the estimation of those by MSIS 86 (Hedin, 1991). The Joule heating effect complicated the estimation of neutral parameters, so the daily variation at high latitudes does not have sufficient data. This model estimates climatological parameters, near the mesopause its estimates may conflict with data from other sources. In this thesis, MSISE data were used to estimate the GDI scale length for the simultaneous occurrence of TIDs and NREs. The data can be accessed online at (https://ccmc.gsfc.nasa.gov/modelweb/models/msis_vitmo.php).

3.5.3 International Reference Ionosphere (IRI)

The IRI model was initiated in 1961 by the Committee on Space Research (COSPAR). The first results of this group were presented as the COSPAR International Reference Atmosphere (CIRA). In 1968 the International Union of Radio Science (URSI) joined this project, and after ten years, the first IRI model was published (Bilitza et al., 1992). It computes electron and ion (O^+ , H^+ , H_e^+ , O_2^+ , NO^+) densities, total electron content, electron, ion and neutral temperature (CIRA - 86), equatorial vertical ion drift and so on. The measurements are estimated for the altitudes of the area between ~ 60 and 2000 km. URSI and COSPAR play an essential role in improving and updating the model (Bilitza, 2001). It is an empirical model, i.e., based on ground and space data, for which both Algol 60 and Fortran 4 computer code is used. The peak of the ionosphere is selected by this code based on the measurements of ionosonde stations all over the world (Rawer et al., 1978; Bilitza et al., 1992). The output is made by combining different instruments. Incoherent scatter radar observations and topside sounder profiles (for the topside), satellites, ionosondes, rockets, mass spectrometers, and retarding potential analyzers are used. Also included are theoretical models, such as formulae, interpolation (latitudinally) and extrapolation for altitudes of between 1000 and 2000 km.

The improvement of this model is ongoing (Bilitza, 2001, 2003; Bilitza and Reinisch, 2008), and is recognized by the International Organization for Standardization (ISO). The current version was updated by Bilitza et al. (2016). The IRI model strongly depends on data, and is less accurate over the auroral region of the southern hemisphere due to the sparse ionosonde coverage as a result of tough weather conditions. The values of electron density produced by the IRI model are not accurate, especially for periods of high solar activity (Bilitza and Reinisch, 2008).

The inputs required to run the model for this study are: year (1958-2020), month, day, time (UT or LT), hours, coordinate type (geographic/geomagnetic latitude and longitude) and height (km, start, stop and step-size) (Bilitza, 2001, 2003; Bilitza and Reinisch, 2008; Bilitza et al., 2016; Bilitza, 2016).

The expected outputs of IRI-2016 are divided into three categories (Bilitza, 2001, 2003; Bilitza and Reinisch, 2008; Bilitza et al., 2016; Bilitza, 2016):

- Independent variables: year, month, day of month, day of year, hour of day (UT/LT), solar zenith angle ($^\circ$), height (km), geographic/geomagnetic latitude ($^\circ$), geographic/geomagnetic longitude ($^\circ$). Other parameters are the corrected geomagnetic (CGM) latitude ($^\circ$), CGM longitude ($^\circ$), magnetic inclination (DIP) ($^\circ$), modified dip latitude ($^\circ$), invDip ($^\circ$), Dip latitude ($^\circ$), Magnetic Local Time (hours).
- IRI model output parameters: The following were used for this study: electron density (N_e) (m^{-3}), neutral temperature (Tn) (K), ion temperature (Ti) (K), and electron temperature (Te) (K). Other parameters (that were not used in this study) that can be obtained from the model are as follows: atomic Oxygen ions (O^+) (%), molecular Oxygen (O_2^+) (%), atomic Nitrogen (N^+) (%), ratio of (N_e) and F2 peak density ($N_e/NmF2$), atomic Hydrogen (H^+), ions (%), atomic Helium (He^+) (%), Nitric Oxide ions (NO^+) (%), cluster ions (%), height (km) and density (m^{-3}) of F2 peak (hmF2), F1 peak (hmF1), E peak (hmE), D peak (hmD), total electron content (TEC) ($10^{10} m^2$), TEC top, percentage, propagation factor M(3000)F2, bottomside thickness (B0) (km), bottomside shape (B1), E-valley width (km), E-valley depth (Nmin/NmE), plasma frequency (MHz) of F2 (foF2), F1 (foF1), E (foE), D (foD), CGM latitude of auroral oval boundary, ratio foE storm to foE quiet, and spread-F probability.
- Indices used by the model: 12-month running mean of sunspot number (Rz12), ionospheric index IG12, daily solar radio flux F107D, 81-day solar radio flux F107 (81D), ap (3-h and daily), and Kp (3-h).

In this thesis, IRI data were used to estimate the GDI scale length for the events studied. The data of this model can be accessed online at (https://ccmc.gsfc.nasa.gov/modelweb/models/iri2016_vitmo.php).

3.5.4 Horizontal Wind Model (HWM)

The HWM is the neutral wind model based on satellite, rocket, and ground-based wind measurements. It gives a statistical representation of the horizontal wind patterns of the Earth's atmosphere from the ground to the exosphere, i.e., from an altitude of 0 to 500 km (Drob et al., 2008). The output of the HWM07 depends on geographic location, altitude, day of the year, local solar time, and geomagnetic activity. The zonal mean circulation, migrating tides, stationary planetary waves, and seasonal modulation are included (Drob et al., 2008, 2015). The current model (HWM14) provides improved representations of time-dependent, observational-based

migrating tides and global empirical specification of the upper atmospheric general circulation fields. This updated model provides a good representation of the climatological ionosphere plasma distribution and electric field patterns (Drob et al., 2015). It was developed by using 73×10^6 measurements taken for more than 62 years by 44 instruments globally. The storm-induced perturbation of the neutral wind (DWM07) (Drob et al., 2008) remained unchanged for the updated current model (Drob et al., 2015). Two components, the meridional and zonal velocity components of the horizontal neutral winds, are offered upon entering the time (day of the year, year, month, day of the month, hour, minute, and second) and position (latitude, longitude and altitude) (Drob et al., 2015).

At high latitudes, HWM14 performed better than the HWM07, using the observations of the Fabry Perot interferometer (FPI) as a standard. For equinox winds measured from the South Pole along the 82.5° W meridian the HWM07 was better than the HWM14 at that location. The representation of quiet time wind ($K_p < 3$) during winter (Emmert et al., 2006) at the high latitudes by the HWM14 agrees with FPI observations. However, this is not the case at all magnetic local times (Drob et al., 2015). Comparison between HWM14 and FPI measurements at high-latitudes show a good agreement, but the agreement doesn't occur at the coincident magnetic local times. Eastward momentum is observed in the post-dusk sector when there is an increasing solar flux and greater westward momentum in the post midnight sector when there is a decreasing solar flux (both in magnetic local time) implying a greater eastward momentum during larger solar flux conditions (Drob et al., 2015). The model still has problems which need attention, for example, the fingerprint of ion convection during quiet winter times and the vertical variation of the horizontal winds above an altitude of 250 km (Emmert et al., 2010; Drob et al., 2015). The Pyglow package was used to get the data for the neutral wind model. It can be accessed online (<https://github.com/timduly4/pyglow/>). In this thesis, the zonal wind component was used to estimate the perturbed GDI scale length at an altitude of 100 km. The results are presented in chapters 5 and 6.

3.6 Summary

This chapter focused on the instruments and some models that were used for this research. SuperDARN HF radars, magnetometers and ionosondes were discussed in detail. SuperDARN parameters such as the backscatter power, Doppler velocity and spectral width, as well as the convection map potentials, were highlighted. Both the SANA and Zhongshan magnetometers received attention. The ionosonde in Antarctica at the Zhongshan station was discussed. Finally, four models, which were very important for this study are introduced. DUSTY, MSISE-90, IRI-2016, and HWM14 models were used to estimate dust particle densities and radii, using the backscatter power of NREs, TIDs parameters, GDI scale lengths, and primary waves that cause secondary waves. The SuperDARN HF radars recognize these secondary waves as NRE's.

Chapter 4

PREVIOUS TID and NRE STUDIES

4.1 Introduction

In this chapter, previous studies of TID observations and their propagation modes are discussed. The Perkins instability is introduced. Examples of NREs, such as Polar Mesospheric Summer Echoes, Farley Burneman Instability (FBI) and Gradient Drift Instability are described.

4.2 Observations of traveling ionospheric disturbances

TIDs are the electron density variations perturbed in waveform by energy carried by AGWs while propagating in the ionosphere/thermosphere (see Figure 4.1). TIDs are also generated by the Perkins instability, Lorentz force, Joule heating, geomagnetic storms, the *E*-region dynamo, and so on. These irregularities have waveforms that affect radio signals in the ionosphere. For example, AGWs are detected directly by means of the behavior of neutral gas. TIDs are detected indirectly as perturbations of the ionospheric plasma, which is simply a passive tracer of the motion of neutral gas. AGWs are measured by interferometers, airglow imagers, satellite mass spectrometers or accelerometers and rockets, while TIDs may be detected using GPS receivers for the Total Electron Content (TEC) variability, HF Doppler radars, lidars, ionosondes, incoherent scatter radars, and airglow imagers (Hocke et al., 1996; Schunk and Nagy, 2000, 2009).

To obtain the propagation velocities, wavelengths, periods and amplitudes of TIDs, HF Doppler radars are the best choice. To investigate the vertical wave structure of the neutral density, ion density, ion and electron temperatures, incoherent scatter radars would be the right choice. For example, incoherent scatter VHF radars can accurately estimate the altitude of these disturbances. TIDs are divided into three main classes:

- large-scale traveling ionospheric disturbances (LSTIDs) with horizontal phase velocities between ~ 400 - ~ 1000 m/s wavelengths of more than ~ 1000 km and periods of between ~ 30 min and ~ 3 hours (Hayashi et al., 2010),
- medium-scale traveling ionospheric disturbances (MSTIDs) with horizontal phase velocities between ~ 250 and ~ 1000 m/s, wavelengths of several hundreds of kilometers and periods between ~ 15 min and ~ 1 hour, and
- small scale traveling ionospheric disturbances (SSTIDs) with horizontal phase velocities in the range ~ 300 - ~ 3000 m/s, and the periods between ~ 2 and ~ 5 min (Hocke et al., 1996; Hunsucker, 1982; Fritts and Alexander, 2003; Grocott et al., 2013; Oinats et al., 2015).

Note that in this thesis we focus on the MSTIDs only.

4.2.1 Propagation modes of TIDs and AGWs

Figure 4.1 top panel shows four modes by which TID/AGW waves propagate. The first group is called the upper mode, numbers 1 and 2 in the figure. They are direct waves and propagate in a horizontal direction. These are LSTIDs that originated from the polar ionosphere and propagate over long distances toward the equator. The second group is known as the lower modes and are denoted by 3 and 4 in the figure. They are generated between the Earth's surface and the lower thermosphere. Sometimes they are reflected by the Earth. These are believed to be MSTIDs that develop at high latitudes and propagate equatorward (Hocke et al., 1996).

In most cases TIDs and AGWs seem to be MSTIDs, while LSTIDs are generally linked with geomagnetic

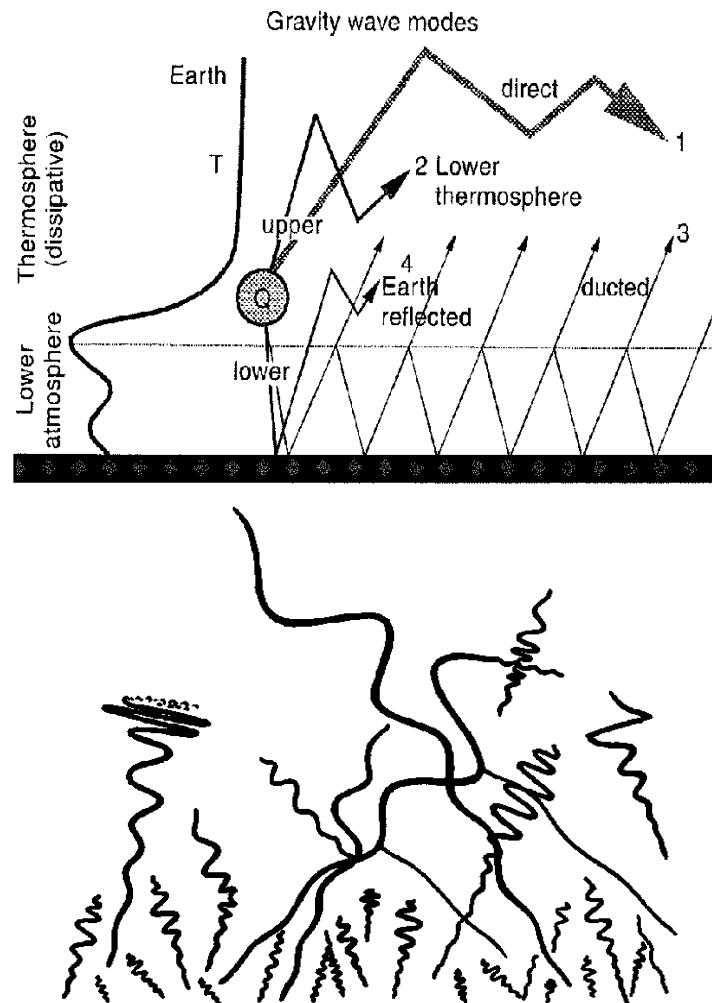


Figure 4.1: Sources and propagation modes of AGWs/TIDs in the atmosphere. Upper modes (1 and 2) and lower modes (3 and 4) are illustrated in the top panel, while waves (with other parameters) and their directions are shown in the bottom panel. The figures were adopted from Hocke et al. (1996) and Iserhienrhien (2016).

storms. Enhanced auroral electrojets and/or intense charged particle precipitation give rise to Joule heating, and sometimes Lorentz forcing may take place. These two mechanisms are the primary sources of LSTIDs in auroral or sub-auroral regions during geomagnetic storms (Waldock and Jones, 1986; Palmroth et al., 2005; Ding et al., 2008; Hayashi et al., 2010). LSTIDs triggered by geomagnetic storms travel from high latitudes to low latitudes and sometimes may cross the equator, heading to the high latitudes of the opposite hemisphere (Tsugawa et al., 2004; Ding et al., 2008; Hayashi et al., 2010; Habarulema et al., 2015). A study conducted over Japan and Australia using the GPS Earth observation network (GEONET) and international GNSS service (IGS) (Idrus et al., 2013), found that LSTIDs and electromagnetic waves are not directly linked. LSTIDs and electromagnetic waves in the northern and southern hemispheres were dependent on AGWs and propagated equatorward (Idrus et al., 2013).

To differentiate between AGWs generated at tropospheric altitudes and propagating upwards to cause TIDs, and those generated by energy deposition at high latitudes, measurements at different altitudes were compared with the radars measurements (e.g. Hunsucker, 1982). Cross-spectral analysis was used to identify MSTIDs in different parts of the field of view (FOV) of SuperDARN radars. He et al. (2004), Ishida et al. (2008), and Atilaw et al. (2021) used SuperDARN HF radar data to investigate MSTIDs with the following results:

1. their periods varied from over 30-80 min (corresponding to frequencies of 0.2-0.6 mHz) or 15 - 60 min,

2. wavelengths varied in the range 200-800 km, and
3. phase speeds were in the range 100-300 ms⁻¹.

The parameters of these waves show that they were associated with medium-scale gravity waves. The HF radar can observe TIDs within the range between 100 and 1000 km.

MSTIDs were reported by Ogawa et al. (2009) using several instruments such as the Hokkaido HF SuperDARN radar, all-sky imager and GPS network. Using 630-nm airglow images, nighttime MSTID activity was found to have a significant peak during May to July (during summer) with few during November to February (during winter) (Shiokawa et al., 2008). Sometimes AGWs were the mechanism for generating MSTIDs. Beacon waves from NNSS satellites indicated that the probability of medium-scale AGWs at high southern latitudes was the greatest in winter and the lowest in summer (Ogawa et al., 1987).

SuperDARN backscattered echo power from the ground or sea surface is essential in studying MSTIDs. These waves perturb electron density which also causes the focusing and defocusing of HF ray paths and hence fluctuations in the backscatter power. In a numerical study of TIDs generated by upward propagating gravity waves, Miyoshi et al. (2018) found that their periods, phase velocities, and wavelengths varied between 45 and 90 min, 250 and 300 m/s, and 700 and 1500 km, respectively. Vlasov et al. (2011) used data from the EISCAT Svalbard incoherent scatter radar between March 2007 and February 2008 to study AGW-TIDs observed in the field-aligned ion velocity, electron density, and electron and ion temperatures. Their periods had two peaks at 30-42 min and 66-78 min. The maximum and minimum numbers of these TIDs occurred between May and July (summer months in the northern hemisphere) and between November and January (winter months), respectively. Their vertical wavelengths were estimated at ~25 km, and their average horizontal phase velocity was 250 m/s.

Using two-dimensional TEC perturbation maps, Ding et al. (2008) studied the characteristics of LSTIDs during strong magnetic storms that occurred during 2003-2005 at mid-latitudes. They found that the mean amplitude, period, horizontal phase velocity, and azimuths were 3.5 TECU (TEC is measured in TEC units), 108 min, 300 m/s, and 187°, respectively. The maximum number occurred at 12:00 LT and 19:00 LT, while 26% of 135 LSTID events occurred at nighttime. The LSTIDs UT and LT dependence were associated with auroral geomagnetic disturbances. Daytime LSTIDs for 15 December 2006 were reported by Hayashi et al. (2010) as identified by the Hokkaido SuperDARN radar and GPS Earth Observation Network (GEONET). They found two disturbances, one propagating southward at 600-650 m/s with a period of 45 min and the other one propagating northward at 800-850 m/s with a period of 30 min. They suggested that the LSTIDs propagating northward could have been generated in the southern hemisphere.

Frissell et al. (2014) reported a climatology of daytime mid-latitude MSTIDs using the Blackstone SuperDARN radar in the United States of America. They found two populations, one heading southeast and the other one heading northwest. Horizontal wavelengths and phase velocities were in the range 100-500 km and 50-250 m/s, respectively, and periods were between 23 and 60 min. Using the TIGER SuperDARN located in Tasmania, He et al. (2004) studied seasonal and diurnal variation in the propagation direction of MSTIDs from sea echoes. In general, they found that most MSTIDs propagate toward the north around dawn and dusk, but the direction changes throughout the year. They were associated with local time irregular magnetic disturbances. Those generated around dawn and dusk were associated with the ionospheric electric field, while the Lorentz force probably caused those generated during the dayside.

Nighttime MSTIDs were investigated by Liu et al. (2019) using VHF coherent scatter radar and the GNSS network located at Wuhan, China. They found that the horizontal phase velocity was < 180 m/s with a period of ~33 min and propagation was in a southwestward direction. Sun et al. (2015) discussed FAI structures associated with MSTID events that were observed by an all-sky imager, a digisonde and a GPS receiver around Xinglong in China. They found that MSTIDs propagated southwestward from higher latitude regions to Xinglong. The FAIs traveled northwestward with a relative velocity of about 87 m/s with respect to the main-body MSTIDs. The Falkland Islands SuperDARN radar has also observed MSTIDs within the ground backscatter data (Grocott et al., 2013). Their periods, wavelengths, horizontal phase velocities were 30-80 min, 200-800 km, and 100-300 m/s, respectively. Some MSTIDs headed northward (equatorward), associated with enhanced solar wind-magnetospheric coupling and others toward the west, caused by winds over the Andean and Antarctic Peninsula mountains or the Antarctic Polar Vortex. Ishida et al. (2008) researched daytime MSTIDs using SuperDARN data for auroral and middle latitudes. Their periods were 20-50 min and their phase velocities were

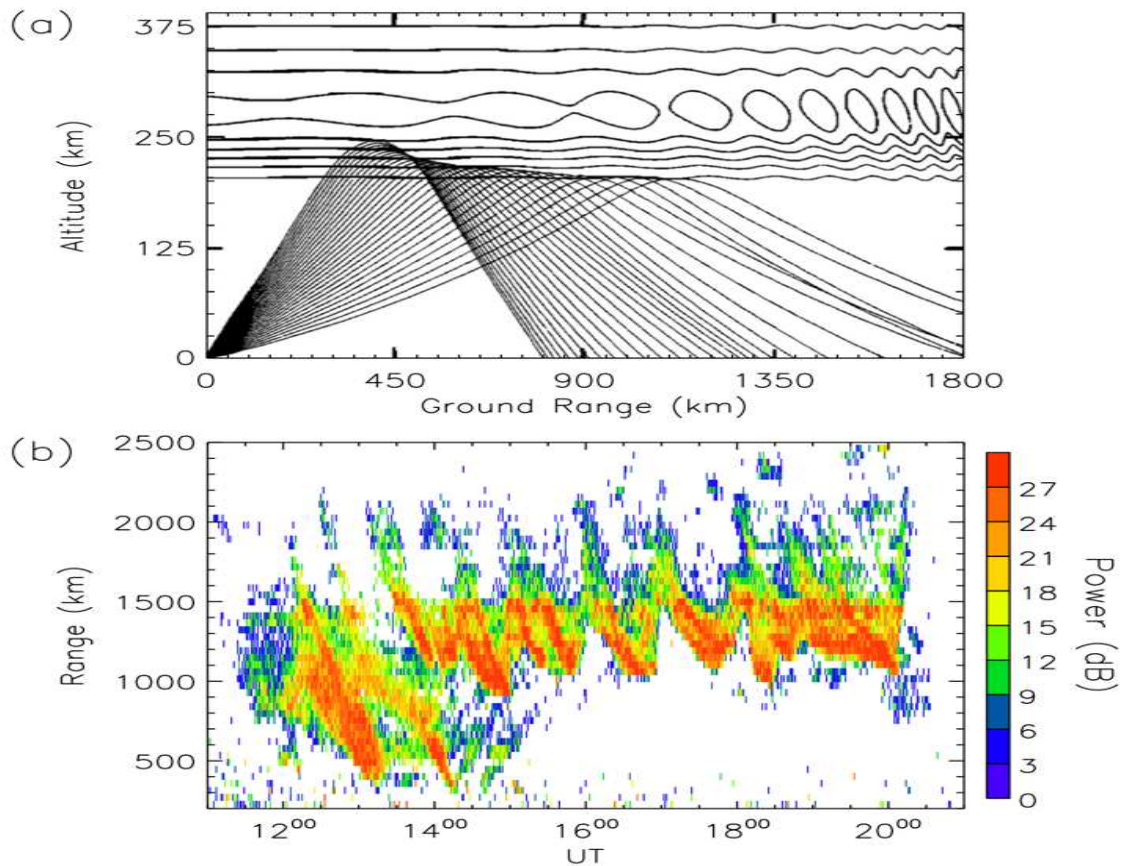


Figure 4.2: SuperDARN MSTID illustration: (a) Ground focusing and defocusing of HF radar's ray paths during a passing TID. (b) Ground backscatter power of beam 8 of the Falkland Islands radar between 11:00 and 21:00 UT (Grocott et al., 2013).

80-280 m/s. Due to enhanced dissipation and the reduction of the ion-drag effect, MSTIDs with higher horizontal phase velocities could not reach the middle latitudes. Mid-latitude MSTIDs were observed by Ogawa et al. (2009) using the Hokkaido SuperDARN radar, a 630-nm all-sky imager and a GEONET receiver. Two events, one in winter and the other in summer, were observed. Daytime MSTIDs propagated southeastward, while nighttime MSTIDs propagated southwestward. The nighttime MSTIDs had a period of 60 min, a wavelength of 600 km and a phase velocity in the range 80-170 m/s. The daytime MSTIDs had periods in the range of 30-50 min, a phase velocity of ~ 120 m/s and wavelengths of 200-300 km. Figure 4.2 shows an MSTID observed by the Falkland Islands Radar (FIR) located at 51.8°S , 59.0°W . The TIDs moved at speeds of 100-300 m/s, with wavelengths of 200-800 km and periods varying between 30 and 80 min. MSTIDs are interpreted in terms of AGWs (Nishitani et al., 2019), but the nighttime MSTIDs may be caused by Perkins instability (Nishitani et al., 2019; Atilaw et al., 2021). Ionospheric SuperDARN coherent scatter (IS) from 11.9 m (for SANA E HF radar) and 14.6 m (for Zhongshan HF radar) scale field-aligned irregularities (FAIs) is the primary data source in this thesis.

4.2.2 Perkins instability

The Perkins instability was initially introduced by Perkins (1973) when modeling the nighttime spread- F and ionospheric currents in the ionospheric F -region of the mid-latitudes. He first pointed out that the most important physical phenomena in studying the parallel dynamics are the electric field and neutral winds, while the perpendicular dynamics are driven by gravity and the pressure gradient.

To establish the Perkins instability dispersion and growth rate equations, the following assumptions were made (Perkins, 1973);

- The magnetic field \mathbf{B} is uniform, but changes in a horizontal direction, i.e., it must have a dip angle D

with the horizontal.

- Gravity (\mathbf{g}) pulls the plasma downward and creates a current in the direction of $\mathbf{g} \times \mathbf{B}$.
- The atmosphere has a single species distributed in altitude, based on the scale height H and horizontally stratified.
- The Pedersen currents (\mathbf{J}) from the electric field and neutral winds support the ionosphere through $\mathbf{J} \times \mathbf{B}$.
- Recombination and ion-drag are not considered.
- The plasma density is high enough so that $\Omega \gg v_{in}$ and only the Pedersen current is significant.
- The E -region contributions to the conductivity of the ionosphere are ignored.
- The plasma is in isothermal equilibrium.
- The plasma is quasi-neutral, i.e., $n_i \approx n_e \approx n$.

Hamza (1999) improved the work of Perkins (1973) and of Miller et al. (1997) by considering the plasma density, Pedersen conductivity gradients and a neutral wind velocity. Apart from the above-mentioned assumptions, Hamza (1999) added another assumption, namely that neutral winds from AGWs can carry electrons and ions along the \mathbf{B} lines, but not across the lines. This extension opens the possibility of investigating the influence of perpendicular gradients in both the background conductivity and background plasma density, which enables the study of the Perkins instability at high latitudes.

The ionosphere is a region that consists of plasma with density n and which conducts electric current with the electric conductivity Σ . The height-integrated density (N) and the height-integrated conductivity (Σ) are defined by:

$$N = \int n dh \quad (4.1)$$

and

$$\Sigma = \int \frac{nv_{in}ec}{\Omega B} dh \quad (4.2)$$

where,

$$h = x \cos D - z \sin D \quad (4.3)$$

$$l = x \sin D + z \cos D \quad (4.4)$$

where h , x and z , and D are the height, coordinate positions, and the dip angle, respectively and are related via the equations (4.3) and (4.4) as shown in Figure 4.3 (a) (for the northern hemisphere) (Perkins, 1973; Hamza, 1999). The coordinates (x , y) identify a particular field line and the direction between x and the distance $l = x/\sin D$ (along north-south, as shown in Figure 4.3 (a)), when the height-integrated Pedersen conductivity calculation is involved. Figure 4.3 (b) shows the angle α between the wave vector and y -axis (eastward direction), while β is the angle between the electric field and the y -axis. This figure also shows the wave propagation, electric field, and wind directions when there are perturbations.

In this thesis, only a few equations describing the Perkins instability are shown. More detail and the full derivation can be found in the paper by Hamza (1999). The moment equation is described by:

$$-2T\nabla_n + ne\left(\frac{\mathbf{v} \times \mathbf{B}}{c}\right) - ne\nabla\phi + nm_i g - M_n v_{in}(\mathbf{v} - \mathbf{u}) = 0 \quad (4.5)$$

where n , T , \mathbf{B} , ϕ , m_i , \mathbf{g} , v_{in} , M_n , and \mathbf{u} are the plasma density, temperature, velocity, magnetic field, the potential, ion mass, gravitational acceleration, molar mass and the neutral wind velocity, respectively. In the presence of the background plasma density, there are two cases to be discussed. The first is that of the case of the equilibrium. The continuity equation is expressed by:

$$\frac{\partial N_o}{\partial t} + \frac{1}{m_i \Omega} \left\{ e\Phi_o + m_i g \cos D x, N_o \right\} = 0 \quad (4.6)$$

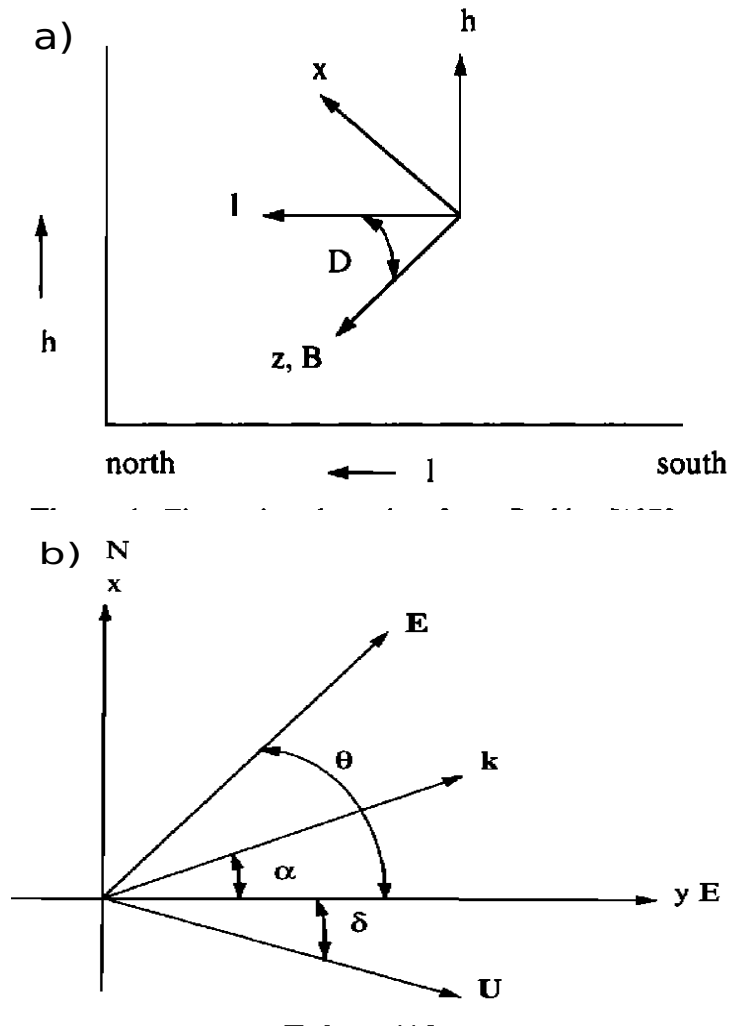


Figure 4.3: (a) Figure 1 and caption from Perkins (1973), page 219: “Geometry of the coordinate systems. The view is toward the east in a northern hemisphere magnetic meridian plane. The unit vectors \hat{l} and \hat{h} are in the horizontal and vertical directions, respectively. The unit vectors \hat{z} and \hat{x} are, respectively, parallel and perpendicular to the magnetic field \mathbf{B} , which has a dip angle D .” (b) Figure 2 from Hamza (1999), page 22,572: electric field \mathbf{E} , wave vector \mathbf{k} and neutral wind velocity \mathbf{U} .

where the Poisson brackets $A, B = \hat{z} \times \nabla A \cdot \nabla B$. Here A and B could be any function of space (x, y, z) and time (t) . The initial electrostatic potential is Φ_o . For a steady condition, $\partial/\partial t = 0$. The solution of the continuity equation is as follows:

$$N = N_o(e\Phi_o + m_i g \cos D x). \tag{4.7}$$

This equation indicates that the background field aligned-integrated plasma density is a function of the potential energy. Also here, the presence of the background plasma density gradient would introduce an $\mathbf{E}_o \times \mathbf{B} \cdot \nabla N_o$ term, which Perkins (1973) did not consider. The background electric field is defined as $\mathbf{E}_o = -\nabla \Phi_o$. For this zeroth-order equation, the background plasma density profile would be related to the background conductivity by the following equation;

$$N_o = \Sigma_o \Omega \frac{e E_{oy} \cos D - m_i \Omega u_z \sin D}{g e^2 \sin D^2} \left[\exp\left(-\sigma \frac{e\Phi_o + m_i g \cos D x}{2T}\right) \right]. \tag{4.8}$$

The second case is the instability state (Hamza, 1999), which was introduced by Perkins (1973) but for only the

nighttime of the ionospheric F -region. In the absence of neutral wind this frame would travel northward at a horizontal velocity of $\frac{E_{oy}c}{B\sin D}$ (Perkins, 1973). Hamza (1999) introduced three dimensionless variables to discuss the improved theory of the instability. The variables N , Φ , and Σ are assumed to be; $N = N_o + \delta N$, $\Phi = \Phi_o + \delta\Phi$, and $\Sigma = \Sigma_o + \delta\Sigma$, hence the dimensionless variables are defined by $\chi = \frac{\delta N}{N_o}$, $\xi = \frac{\delta\Sigma}{\Sigma_o}$ and $\varphi = e\frac{\delta\Phi}{2T}$. The continuity equation is then rewritten as:

$$\frac{\partial\chi}{\partial t} + \left(v_o + \frac{g}{\Omega} \cos D \hat{y}\right) \cdot \nabla(\chi + \sigma\varphi) = 0 \quad (4.9)$$

where σ is defined by:

$$\sigma = 1 + \frac{2m_i n g \cos D (m_i g \cos D - eE_{ox})}{(eE_{oy})^2 + (eE_{ox} - m_i g \cos D)^2} + \frac{eE_{oy} \tan^{-2} D (eE_{oy} - m_i \Omega u_z \tan D)}{(eE_{oy})^2 + (eE_{ox} - m_i g \cos D)^2}. \quad (4.10)$$

There are two special cases to discuss. The first, is when $\tilde{\chi} = 0$, $\sigma = 0$, and $u = 0$. This is the case discussed by Perkins (1973). Note that $\tilde{\chi} = \sigma \frac{\mathbf{k} \cdot \mathbf{v}_o^g}{\omega - \mathbf{k} \cdot \mathbf{v}_o^g} \tilde{\varphi}$, where \mathbf{k} is the wave vector. Similarly, the continuity equation in terms of the field line integrated Pedersen conductivity, which involves the variable ξ , can be estimated (Hamza, 1999).

The Perkins instability growth rate γ^P is expressed by:

$$\gamma^P = c \frac{E_o \cos D}{BH} \sin \alpha \sin(\theta - \alpha) + \frac{g \cos^2 D}{\Omega H} \left(1 + 2 \frac{M_n}{m_i}\right) \sin \alpha \sin \alpha. \quad (4.11)$$

where θ and α are shown in Figure 4.3 (b). The maximum growth rate γ_{max}^P is achieved when $\alpha = (\theta/2) + n\pi$ and it can be derived by setting $\frac{\partial\gamma^P}{\partial\alpha} = 0$. Its equation is:

$$\gamma_{max}^P = c \frac{E_o \cos D}{BH} \sin^2 \left(\frac{\theta}{2}\right). \quad (4.12)$$

The second special case is the instability triggered in the presence of AGWs (Hamza, 1999). The growth rate (γ^{GW}) in this case is given by:

$$\gamma^{GW} = \gamma^P + \frac{\cos D}{H} \left[u_z \tan D + u_{\perp} \cos \alpha \sin(\alpha - \delta) \right]. \quad (4.13)$$

The maxima of this growth rate, when $u_{\perp} = 0$, is expressed by:

$$\gamma_{max, u_{\perp}=0}^{GW} = \gamma_{max}^P + \frac{u_z}{H} \sin D. \quad (4.14)$$

When $u_{\perp} \neq 0$, the maximum growth rate is expressed by:

$$\gamma_{max}^{GW} = c \frac{E_o \cos D}{BH} \left[2 \frac{u_z}{cE_o/B} \tan D - \cos \theta - \frac{u_{\perp}}{cE_o/B} \sin \delta + \sqrt{1 + \left(\frac{u_{\perp}}{cE_o/B}\right)^2 - 2 \frac{u_{\perp}}{cE_o/B} \sin(\delta - \theta)} \right] \quad (4.15)$$

Together with other mechanisms, the Perkins instability causes TIDs. In this thesis, the focus is on the impact the TIDs have on NREs.

4.3 SuperDARN HF radar near range echoes

In this study, NREs are defined as the echoes within the 180 to 315 km range, i.e., from the first to the fourth gates of SuperDARN HF radars. NREs may be caused by meteor scatter, PMSEs associated with dust particles, High-aspect Angle Irregularity Regions (HAIR) associated with auroras, and FAIR associated with the GDI. SuperDARN HF radars consist of a global network of more than 30 radars (chapter 3). Each of the radars used in this study normally operates in the 8-20 MHz frequency range, has at least 16 beams arranged in a fan $\sim 53^\circ$ wide, has a range resolution of 45 km. They observe at range distances from ~ 180 to ~ 3500 km at an altitude of ~ 80 to ~ 300 km in the ionosphere (Greenwald et al., 1995; Chisham et al., 2007; Nishitani et al., 2019). Near range echoes are observed at the near range gates in all beams of each radar.

4.3.1 Meteor echoes

NREs may be caused by meteoroids or space debris that enter the Earth's atmosphere as meteor trails. The collisions between the meteor trail particles and air molecules, result in heat and finally cause ablation. Ionization takes place during these processes and is observed in their radio wave scatter. Radars can receive the returned signal from the meteor plasma trail. Electrons and ions spread at the same rate due to the polarization fields, when electrons diffuse in the direction opposite to that of the ions. This kind of charge particle diffusion is known as ambipolar diffusion. This diffusion is a consequence of the unbalanced concentration of the medium. Temperature is an important parameter and is responsible as this process develops from higher to lower concentration regions. Diffusion continues until the media (volumes in space) are in equilibrium, and the plasma irregularity needed to reflect the radar signal disappears.

4.3.2 Polar mesospheric summer echoes

4.3.2.1 Origin of polar mesospheric summer echoes

Globally, the Sun heats up the tropospheric weather system and causes air circulation from the equatorial to the polar regions. The air is raised by gravity waves and/or any buoyancy forces (such as winds). One of the causes of the wind is the air circulation caused by the temperature difference, which leads to convection in the hot and cold air. The universal gas law is introduced to predict the governing physical parameters during the air expansion towards the mesosphere (equation (4.16)).

$$PV = nRT \quad (4.16)$$

$R = \frac{N \cdot k_B}{n} = 8.314462618 \text{ J}/(\text{mol} \cdot \text{K})$ is the universal gas constant, n is the number of moles of particles in the volume of air, P is the air pressure, N is the number density of the air molecules, V is the air volume, k_B is the Boltzmann's constant and T is the thermodynamic temperature.

For N and k_B , which are considered constants during the process, the temperature is directly proportional to the air pressure and the volume (equation (4.16)). As the air moves upwards, its pressure (P) decreases, because it seeks equilibrium with the surrounding barometric pressure (p). The rising air mass displaces the surrounding air and loses its energy in the form of mechanical energy. Its internal energy drops and causes a significant decrease in its temperature. The barometric pressure decreases and follows the temperature trend as the altitude (h) increases from the Earth's surface to the mesopause (Brasseur and Solomon, 2006). This pressure also is affected by temperature and humidity within the medium. In the troposphere, this pressure is described by equation (4.17).

$$p = p_o \left(1 - \frac{L \cdot h}{T_o} \right)^{\frac{g \cdot M}{R \cdot L}} \quad (4.17)$$

where $L = \frac{g}{c_p} = 0.00976 \text{ K/m}$ is the temperature lapse rate for dry air. Equation (4.17) can be rearranged into equation (4.18):

$$p = p_o \left(1 - \frac{g \cdot h}{c_p \cdot T_o} \right)^{\frac{c_p \cdot M}{R}} \simeq P \simeq p_o \exp \left(- \frac{g \cdot h \cdot M}{R \cdot T_o} \right) \quad (4.18)$$

where $p_o = 101325 \text{ Pa}$ is the sea level standard atmospheric pressure, $c_p = 1004.68506 \text{ J}/(\text{kg} \cdot \text{K})$ is the constant-pressure specific heat, $T_o = 288.16 \text{ K}$ is the sea level standard temperature, $g = 9.80665 \text{ m/s}^2$ is the Earth-surface gravitational acceleration and $M = 0.02896968 \text{ kg/mol}$ is the molar mass of dry air.

Once the air temperature drops at the mesopause altitude, particles and other molecules in this medium cool down to the same temperature. For example, the water vapor cools down and forms ice crystals, which come in contact with meteoric dust particles. Water vapor is generated either naturally or by means of artificial processes at the Earth's surface. The Sun's radiation (UV light) breaks down the frozen water molecule bonds in the atmosphere and this gives to water vapor. Methane gas (CH_4) affects the mesospheric humidity and produces ~50% of the water vapor (equations (4.19) and (4.20)). The chemical reaction that produces water is:



Water can also be generated by sulfur aerosols and by some gases when there is solar radiation in the mesosphere (Mills et al., 2005). The chemical reaction to produce water is:



Depending on the size of the ice crystals, they may either form PMSEs or Noctilucent Clouds (NLCs). The smaller and heavier ice crystals form PMSEs and NLCs, respectively. The lighter icy dust particles (with radii of less than 20 nm) responsible for forming PMSEs can be observed by radars. The bigger icy dust particles (with radii greater than 20 nm) are responsible for the NLC sink due to gravity (Mills et al., 2005; Rapp and Thomas, 2006; Hervig et al., 2011). However, Kaifler et al. (2011) indicated that the different sizes of PMSEs and NLCs are due to different observation techniques (i.e., radar vs lidar). They argued that PMSEs may also be observed when the icy particles are larger (in the order of ~ 50 nm). These can be seen with the naked eye just after sunset and before just sunrise, when the ground is dark, and the mesopause region is still illuminated by sunlight.

As the atmospheric pressure decreases, AGWs propagating from a high-pressure medium increase their amplitudes. The physics of conservation of wave energy ($1/2 \rho(v)^2 = \text{constant}$), states that a decrease in density (ρ) implies that the wave velocity (v) increases. As the density ρ increases, the wave velocity v decreases. Thus as these waves rise to the mesosphere, they break and deposit their energy and momentum. A part of the AGWs energy spreads out towards the equator. The air circulation also moves in the same direction and descends again as the air approaches the equatorial region. The rest of the AGWs energy heats up the mesopause. This refrigeration effect caused by the global air circulation between the warm troposphere and the cool mesosphere from the poles to the equator makes the polar mesospheric region the coldest place in our atmosphere.

PMSEs are the coherent echoes received by polar radars from altitudes of 80 to 90 km during summer. PMSEs are the result of the existence of charged ice aerosol particles and mesospheric neutral air turbulence. These particles can be seen from the ground with the naked eye. They are known as either NLCs or Polar Mesospheric Clouds (PMCs). They have structures similar to those of gravity waves (Garcia and Solomon, 1985) during the twilight sky, and other waves such as planetary waves may cause their positions to fluctuate (Kirkwood and Réchou, 1998). Both phenomena, PMSEs and NLCs, show the anthropogenic effects on climate change. NLC indicates water-ice particles formed at low summer mesopause temperature, ranging from 120 - 150 K (Hervig et al., 2009). PMSE and NLC are found at nearly the same altitude during the same months. This is because these phenomena share a common origin and are driven by standard processes (Rapp and Lübken, 2004; Hervig et al., 2011). Figure 4.4 shows gravity waves captured by an automatic charged-coupled device (CCD) camera over the northern part of Sweden. This instrument was located at Lycksele in the north-east part of Sweden ($64^\circ 37' N$, $18^\circ 44' E$), and detected the waves in NLCs on 10-11th August 2000 from 23:00 to 03:00 LT. The gravity wave's period and horizontal phase velocity was 41 min and 7-10 m/s, respectively (Dalin et al., 2004). They found that the NLC period was also 41 min, indicating that the NLC was modulated by passing AGWs. PMSEs would also have the same periodicity of amplitude modulation as the TIDs interact with it. When the mesopause temperature dips low enough (< 200 K), due to solar-driven atmospheric circulation, it causes strong adiabatic cooling to allow the water vapor to freeze on the dust nuclei (typically ~ 1 - 20 nm). Hence, it results in nucleation and growth of ice particles from water vapor (Ogunjobi et al., 2015). When this happens, free electrons attached themselves to the ice-covered dust particles, forming a near-perfect hard target for radars, hence the PMSEs. Figure 4.5 shows the plasma irregularities responsible for the PMSEs. Free electrons play a crucial role in backscattering those signals to the radar when their separation distances meet the Bragg scatter condition. Another precondition for PMSE occurrence is the availability of charged ice particle irregularities on Bragg's wavelength scale. PMSEs are the radar backscatter from free-electron structures surrounding the negatively charged icy dust particles, on a scale which satisfies the Bragg scatter condition of a particular radar (Kelley et al., 1987; Cho et al., 1992).

Turbulent and non-turbulent theories of neutral air are associated with this phenomenon (Röttger et al., 1988; Rapp and Lübken, 2004). Turbulent theory suggests that the neutral air turbulence produces irregularities that are visible to the radar. Irregularities of around 10s of meters should be dissipated by ambipolar diffusion. The echoes should significantly weaken. A nonturbulent theory concerns the dusty plasma attracting the surrounding electrons. The electrons attach to the dust particles, and in order to obey charge neutrality, clouds of charges are formed around each dust particle. These free electrons are responsible for radio wave scatter.



Figure 4.4: Noctilucent Clouds over the northern part of Sweden on 10-11 August 2000. AGWs are seen in these photos (Dalin et al., 2004).

4.3.2.2 Measurement of PMSEs

The occurrence of heavy charged dust particles and very low temperature slows down the free electrons' diffusion time, causing the preservation of the irregularities that cause PMSE (Havnes et al., 2001; Kelley et al., 1987). The process of charging dust in a narrow layer, known as an electron bite-out, decreases electron density in the dust layer (Havnes et al., 1996), but not always significantly. PMSEs are frequently observed by very high frequency radars, where the shorter wavelength relates to free-electron diffusion in the space between the dust particles. PMSEs are also observed by high frequency radars (e.g. ionosondes and SuperDARN), where the longer wavelength relates to the dust charge state. Radars in the medium frequency (MF) bands (300 kHz - 3 MHz) have also been used to observe PMSEs (Bremer et al., 1997).

4.3.2.3 Correlation between high energy particles precipitation and PMSEs

Rauf et al. (2019) investigated the effects of high energy particle precipitation on the intensity of PMSEs for longer than, or equal to, 3 hours. They used the EISCAT VHF radar in Norway (69°35'N, 19°14'E) near Tromsø. Between 80 and 90 km, the mean and maximum electron density were used as a proxy of mean and strong PMSEs, respectively. High energy particle precipitation was defined as ($n_e \geq 3 \times 10^{10} \text{ m}^{-3}$) at an altitude of 91

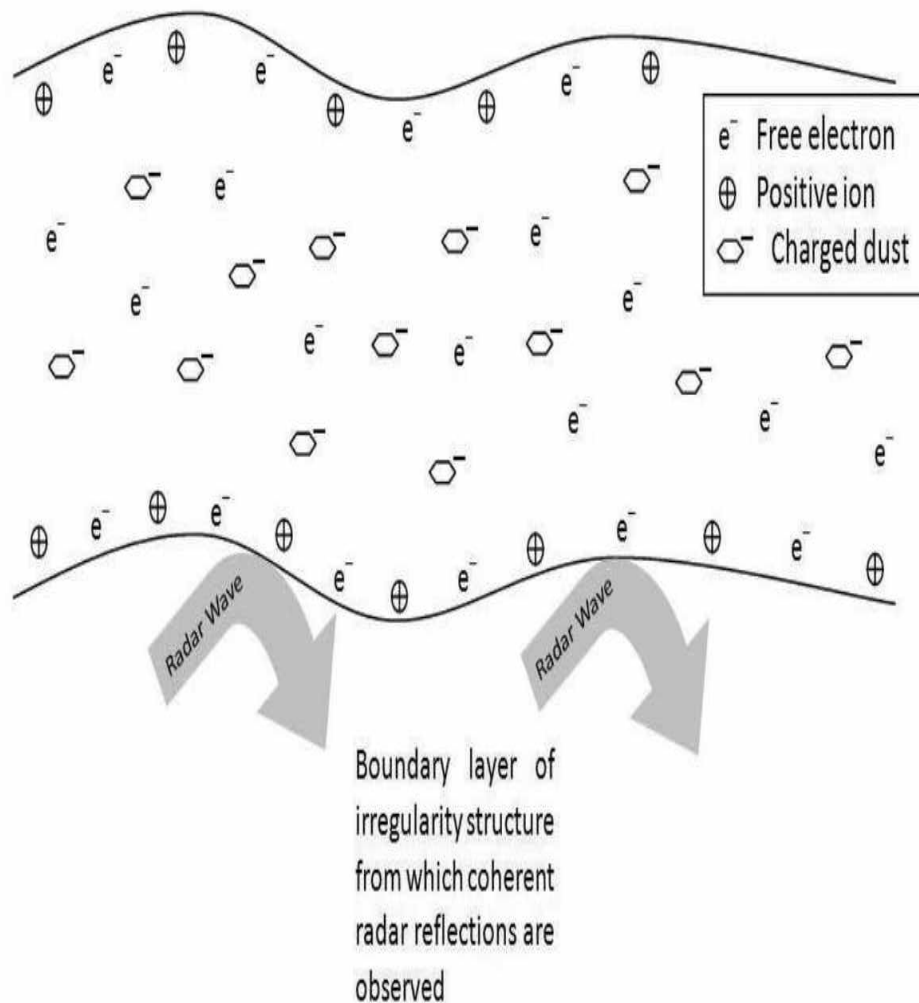


Figure 4.5: Cartoon illustrating PMSE at the mesopause height. The radar signal is backscattered when the structure fulfils Bragg's scatter condition (Routledge, 2011).

km. Precipitating electrons with energies between about 30 - 100 keV and protons with energies between 1 - 10 MeV can cause ionization within the ionosphere's *D* region (60 - 90 km). The Spearman and Pearson linear correlation coefficients, indicated a positive correlation between high energy particle precipitation and both mean and strong PMSE intensity. Varney et al. (2011) found through observation that there is a contribution of electron density to the PMSE.

4.3.3 Instabilities in the *E*-region

4.3.3.1 Introduction

Instabilities in physics occur when any force applied to the objects/systems can change their stability to unstable conditions. This section is mainly concerned with the gradient drift instability of the plasma within the ionosphere, specifically at its lower altitudes. Within an open system such as the ionosphere and magnetosphere, there is input energy, momentum and mass. These physical quantities produce gradients and inhomogeneities, which on a macroscopic scale, give rise to large-scale macro-instabilities, while on microscopic scales, they create small-scale micro-instabilities (Treumann and Baumjohann, 1997).

In the ionosphere, echoes that originate from instabilities can be detected by HF, VHF and UHF radars. The FBI and GDI are major sources of NREs. FBI is caused by large velocity differences between ions and electrons. This velocity resulting from an electron-density gradient component perpendicular to the electrons drift direction exceeds the ion-acoustic speed. GDI on the other hand, doesn't depend strongly on the relative velocity between electrons and ions, but in most of the cases it occurs when the relative velocity is less than the acoustic speed. GDI results from the presence of a plasma density gradient in a favorable direction to allow GDI growth. This is favored by the neutral wind and ion drift. The velocity difference is caused by the different collision frequencies with the neutrals, which is important for lower ionospheric altitudes where the neutral density is higher.

4.3.3.2 Farley Buneman and gradient drift instabilities

A strong background electric field destabilizes plasma, which modifies two-stream instabilities to generate the Farley Buneman instabilities. Electrons are considered faster than ions, and their relative velocity is defined as being (Keskinen and Ossakow, 1983; Hamza and St-Maurice, 1993; Kelley, 2009; Iserhienrhien, 2016):

$$\mathbf{v}_D = \mathbf{v}_e - \mathbf{v}_i. \quad (4.21)$$

FBI takes place when particles drifting in the plasma collide with neutrals. The relative motion between electrons and ions with a velocity exceeding the ion acoustic speed, produces the drift current. This instability takes place in the equatorial and polar ionospheric E -regions.

Another instability is called the gradient drift instability. In the presence of a background magnetic field \mathbf{B} , a small polarization electric field \mathbf{E}' , caused by charge separation, leads to a local $\mathbf{E}' \times \mathbf{B}$ drift and augments the pre-existing plasma disturbances. This charge separation results when electric, gravitational and neutral wind-related forces are applied to a concentrated part of the plasma. A density gradient should exist in a direction favorable to the development of the instability. Instabilities caused by the enhanced disturbances are called the gradient drift instabilities. Each pair of parameters, namely the plasma density gradient, magnetic field and electric field must be perpendicular to each other (Liu and Yeh, 1966; Schmidt and Gary, 1973; Oppenheim et al., 1996; Subramaniam, 1997; Sojka et al., 1998).

4.3.3.3 FBI dispersion relation

Considering the inertia and temperature effects in the ionospheric E -region, the continuity equation of electrons e and ions i is expressed by:

$$\frac{\partial n_\alpha}{\partial t} + \nabla \cdot (n_\alpha \mathbf{v}_\alpha) = 0 \quad (4.22)$$

where α represents both i and e . These particles obey the following equation of motion (Oppenheim et al., 1996):

$$\frac{d\mathbf{v}_\alpha}{dt} = \frac{e_\alpha}{m_\alpha} (\mathbf{E} + \mathbf{v}_\alpha \times \mathbf{B}) - \nu_\alpha \mathbf{v}_\alpha - \frac{\nabla(n_\alpha T_\alpha)}{n_\alpha m_\alpha}. \quad (4.23)$$

Assuming a quasi-neutral plasma ($n_{1e} = n_{1i} = n$), consider the electrostatic potential ($\mathbf{E}_1 = -\nabla\phi_1$), where $n_1 \propto e^{i(k_x x - \omega t)}$ and $\phi_1 \propto e^{i(k_x x - \omega t)}$ (Gillies, 2012). For a homogeneous plasma, assuming a negligible density, the FBI dispersion relation of FBI waves is expressed by:

$$\omega - \mathbf{k} \cdot \mathbf{v}_D = \frac{\psi}{\nu_i} \left[\omega(i\omega - \nu_i) - ik^2 C_s^2 \right] \quad (4.24)$$

Hence, without any plasma gradient,

$$\omega(\omega + i\nu_i) + i \frac{\nu_i}{\psi} (\omega - \mathbf{k} \cdot \mathbf{v}_D) - k^2 C_s^2 = 0 \quad (4.25)$$

Equation 4.24 can be solved to give the complex frequency $\omega = \omega_r + i\gamma$, where

$$\omega_r = \mathbf{k} \cdot \mathbf{v} = \frac{\mathbf{k} \cdot (\mathbf{v}_{0e} + \psi \mathbf{v}_{0i})}{1 + \psi}. \quad (4.26)$$

Their growth rate γ is expressed by:

$$\gamma = \frac{1}{1 + \psi} \left[\frac{\psi}{v_i} (\omega_r^2 - k^2 C_s^2) \right] \quad (4.27)$$

where C_s is the ion-acoustic speed as defined in equation (2.101). The ratio of local collision and gyro-frequencies, considering the aspect angle, defines the parameter ψ as:

$$\psi = \psi \left(\frac{k_{\perp}^2}{k^2} + \frac{\Omega_e^2 k_{\parallel}^2}{v_e^2 k^2} \right) \approx \psi \left(1 + \frac{\Omega_e^2}{v_e^2} \sin^2 \beta \right) \quad (4.28)$$

where β is the angle between the wave propagation direction and the magnetic field, known as the aspect angle, and;

$$\psi = \frac{v_e v_i}{\Omega_e \Omega_i} \ll 1. \quad (4.29)$$

From the equation (4.27), the growth rate of the FBI is positive when $\omega_r \geq k C_s$. For a very small aspect angle, i.e., when $\psi \ll 1$, the dispersion relation would be $\omega_r \approx k v_{oe}$ and in this case the FBI occurs when $v_{oe} > C_s$. The FBI takes place along the direction θ relative to the electron drift in the FBI cone. This is defined by:

$$\cos \theta > \frac{C_s}{v_{oe}}. \quad (4.30)$$

At high latitudes in the E -region, $C_s \approx 400$ m/s (Gillies, 2012), which means that in order to get the FBI in this region, v_{oe} must be greater or equal to 400 m/s, i.e., the electric field should exceed ~ 20 mV/m (Oppenheim et al., 1996). Type I echoes observed by coherent radars are believed to be produced by the FBI. These are strong echoes with a Doppler velocity of around the ion-acoustic speed and relatively narrow spectral width. Type II echoes are believed to be caused by the GDI at the bottom of the E -region, where FBI is not operational.

4.3.3.4 GDI dispersion relation

Assume that isothermal and homogeneous plasma instabilities are triggered when a small sinusoidal wave perturbation is included. Both the phase velocity and growth rate of the wave may be determined. The continuity and momentum equations are given by (Keskinen and Ossakow, 1983; Hamza and St-Maurice, 1993; Kelley, 2009; Iserhienrhien, 2016):

$$\frac{\partial n_e}{\partial t} + \nabla \cdot (n_e \mathbf{v}_e) = 0 \quad (4.31)$$

$$\frac{d\mathbf{v}_e}{dt} = -e(\mathbf{E} + \mathbf{v}_e \times \mathbf{B}) - \frac{k_B T_e}{m_e} \frac{\nabla n_e}{n_e} - \nu_e \mathbf{v}_e \quad (4.32)$$

$$\frac{\partial n_i}{\partial t} + \nabla \cdot (n_i \mathbf{v}_i) = 0 \quad (4.33)$$

$$\frac{d\mathbf{v}_i}{dt} = e\mathbf{E} - \frac{k_B T_i}{m_i} \frac{\nabla n_i}{n_i} - m_i \nu_i \mathbf{v}_i \quad (4.34)$$

where $\mathbf{E} = -\nabla\phi$ and n_α , \mathbf{v}_α , ν_α , m_α , T_α are the density, velocity, collision frequency with neutrals, mass and temperature of $\alpha = e, i$, respectively. \mathbf{E} and \mathbf{B} are defined above and ϕ is the electrostatic potential.

The relationship between background and perturbed density, velocity and electric field are described by:

$$n_\alpha = n_{0\alpha} + n_{1\alpha} \quad (4.35)$$

$$\mathbf{v}_\alpha = \mathbf{v}_{0\alpha} + \mathbf{v}_{1\alpha} \quad (4.36)$$

$$\mathbf{E}_\alpha = \mathbf{E}_{0\alpha} + \mathbf{E}_{1\alpha} \quad (4.37)$$

In the bottom-side ionospheric E -region, the ions are unmagnetized due to their high ion collision frequency, ν_i . The ion inertia is more significant than that of the electrons, so that the latter is neglected. The above equations assume that the plasma obeys the charge neutrality condition (i.e., $n_e = n_i = n$) and the plasma is isothermal ($T_e = T_i = T$), which is true in the E -region.

Solving for $\mathbf{v}_{1\alpha}$, the general dispersion relation is found by linearizing from equations (4.31) to (4.34) and considering that the electrostatic potential fluctuation is directly proportional to $\exp(i[\mathbf{k}\cdot\mathbf{r} - \omega t])$:

$$\omega - \mathbf{k}\cdot\mathbf{v}_D = \frac{\psi}{v_i} \left[\omega(i\omega - \nu_i) - ik^2 C_s^2 \right] \cdot \left(1 - \frac{i\Omega_e}{v_e k L} \right). \quad (4.38)$$

Here v_D is the electron drift velocity relative to the ions across \mathbf{B} . And $L = n_o(\partial n_o/\partial x)^{-1}$ stands for the zeroth-order density gradient scale length along with \mathbf{E}_o .

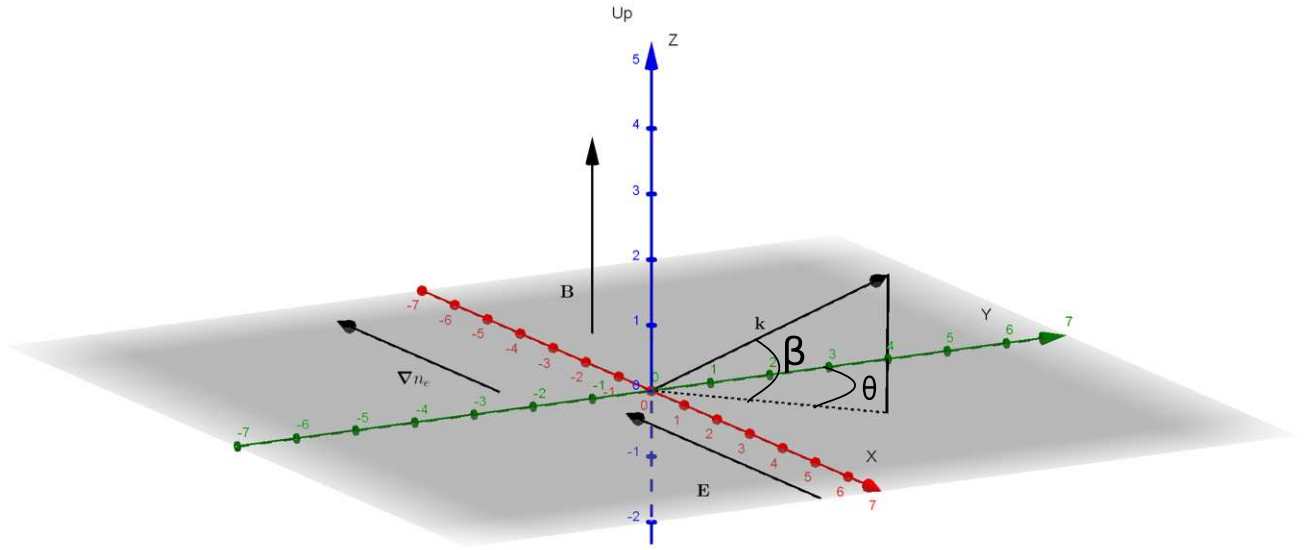


Figure 4.6: Cartesian coordinate system for the electric field \mathbf{E} (which is antiparallel to the X-axis), and parallel to ∇n_e , and magnetic field \mathbf{B} (which is parallel to the Z-axis) in the southern polar hemisphere (see Schmidt and Gary (1973)). The wave vector \mathbf{k} , together with its aspect (β) and flow (θ) angles, are represented.

Figure 4.6 illustrates the magnetic field (parallel to the Z-axis), and electric field (antiparallel to the X-axis) in the southern polar hemisphere. The angle β is the angle between the plane parallel to \mathbf{E} and \mathbf{k} , while θ is the angle between the drift velocity along the Y-axis and the vector \mathbf{k} . The projections of \mathbf{k} are defined as:

$$k_x = k_{\perp} \sin \theta \quad (4.39)$$

$$k_y = k_{\perp} \cos \theta \quad (4.40)$$

$$k_z = k \sin \beta \quad (4.41)$$

$$k_{\perp} = k \cos \beta \quad (4.42)$$

$$k_{\parallel} = k \sin \beta = k_z \quad (4.43)$$

4.3.3.5 The instability growth rate

The angle θ is defined by using the dot product rule between wavenumber and drift velocity vector:

$$\cos \theta = \frac{\mathbf{k}\cdot\mathbf{v}_D}{k v_D}, \quad (4.44)$$

while β can be estimated by re-arranging equations (4.40), (4.41), (4.42) and (4.43):

$$\cos \beta = \frac{k_y}{k \cos \theta}. \quad (4.45)$$

From equation (4.38), it can be deduced that $\omega = \omega_r + i\gamma_r$, where ω_r is its real part and its imaginary part is γ_r (the growth rate in s^{-1}). The real part is defined by:

$$\omega_r = \frac{\mathbf{k} \cdot \mathbf{v}_D}{(1 + \psi)} = \frac{k v_D \cos \theta}{(1 + \psi)} \quad (4.46)$$

and by assuming the slow growth rate (i.e., $\gamma_r \ll \omega_r$). This growth rate is estimated by:

$$\gamma_r = \frac{\psi}{1 + \psi} \left[\frac{1}{v_i} (\omega_r^2 - k^2 C_s^2) + \frac{\Omega \omega_r}{v_e k \mathbf{L}} \right] \quad (4.47)$$

with the angle $\beta = 0$, and $\psi = \psi$ from equation (4.28). For small v_D the growth rate decays to zero (0), and the electric field is defined as:

$$E = v_D B \quad (4.48)$$

The threshold electric field E^{th} and drift velocity v_D^{th} for FBI is defined as:

$$v_D^{th} \geq C_s(1 + \psi). \quad (4.49)$$

Assuming an ion-acoustic velocity of 400 ms^{-1} in equation (4.48), $E^{th} > 20$ (Oppenheim et al., 1996) and $> 40 \text{ mVm}^{-1}$ (St.-Maurice and Nishitani, 2020) at 100 km altitude is required for VHF and HF radars, respectively. Figure 4.7 (a) shows that the FBI is produced in the presence of a strong electric field, magnetic field and with a relative velocity between electrons and ions.

The GDI doesn't depend on the electric threshold like FBI, and its growth rate strongly depends on the electron-density gradient scale length. Pre-conditions for the occurrence of the GDI are:

- An electric field component must be parallel to a density gradient, i.e., $\mathbf{E} \parallel \nabla n$ and
- the dot product between the wavenumber vector and the cross-product of the density gradient and the magnetic field must be positive, i.e., $k \cdot (\nabla n \times \mathbf{B}) > 0$ (Liu et al., 2019).

Any charge separation within the disturbed plasma density, creates a polarization electric field $\delta \underline{E}$ via the differential motion of ions and electrons. Figure 4.7 (b) shows the result of this electric field. The perturbed $\delta \underline{E} \times \underline{B}$ drift is upward or downward depending on the direction of $\delta \underline{E}$. Separate layers of plasma density with a growth of $\delta n/n$ are formed after a certain time, where n is the plasma density. Any perturbation of the two plasma densities, i.e., the density below and above the perturbed boundary, causes a polarization of the electric field. The magnetic field and polarization electric field via the $\delta \underline{E} \times \underline{B}$ shift the plasma up or down, reinforcing ∇n and causing the instability to grow. Omitting the FBI term from equation (4.47), the necessary condition for GDI is that $\gamma_r \geq 0$, resulting in:

$$v_D \geq \mathbf{L} \frac{\Omega_i^2}{v_i^2} (1 + \psi) \psi k^2 C_s^2 \quad (4.50)$$

where \mathbf{k} and \mathbf{v}_D , which is the same as \underline{V}_D in (Figure 4.7), are parallel (Subramaniam, 1997; Kelley, 2009). Figure 4.8 shows the gradient drift instability mechanism generated by either an electric field (a) or neutral wind (b). In the E -region, electrons drift in the direction of $\mathbf{E}_0 \times \mathbf{B}$ to the left of the figure, hence the classic Hall current is toward the right. In (b) the ions are pushed to the right by the neutral wind \mathbf{U}_n . In both cases, the polarization electric field would enhance perturbation, leading to the GDI.

4.3.3.6 High-aspect angle irregularity regions (HAIR) and far-aspect angle irregularity region (FAIR) echoes

HAIR (Milan et al., 2004; Drexler and St-Maurice, 2005; St.-Maurice and Nishitani, 2020) and FAIR (St.-Maurice and Nishitani, 2020) echoes can be observed in the near range gates of the SuperDARN HF radars. Normally, HAIR echoes are detected in the 110 to 120 km altitude range, but during strong magnetic storms, they are detected in the altitudes between 90 and 100 km. The echoes are observed far from the 90° aspect

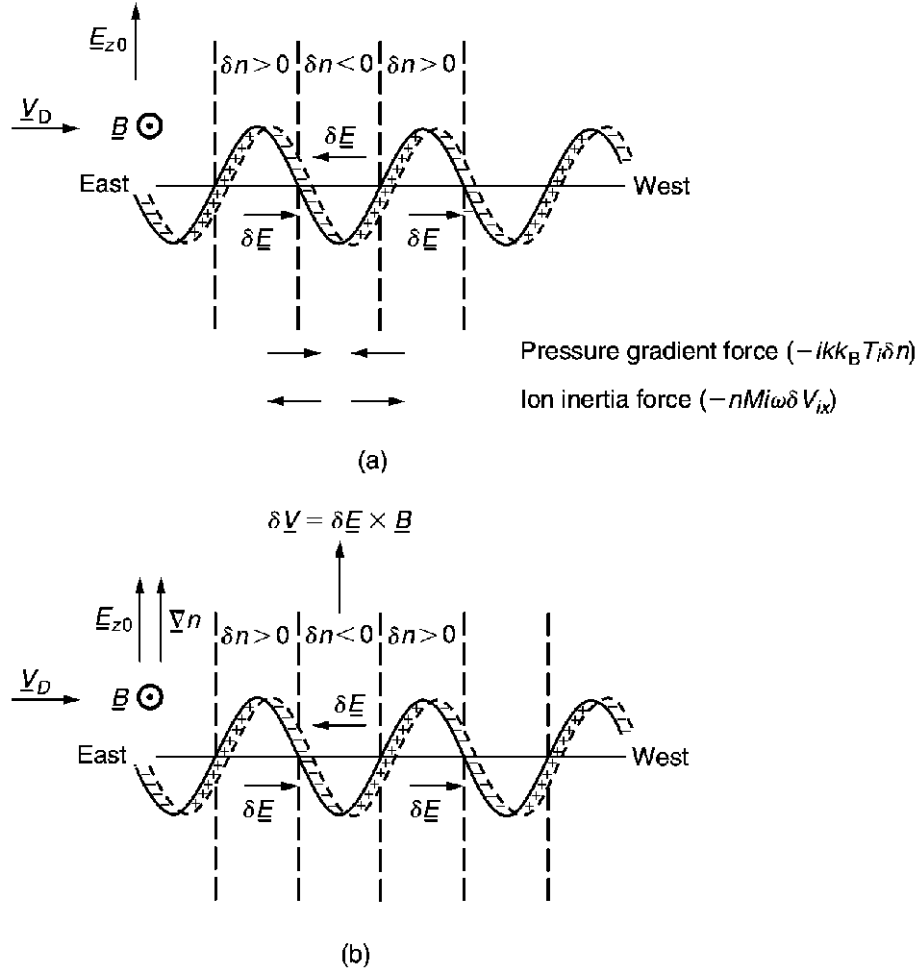


Figure 4.7: The formation of linear instabilities: **(a)** The FBI is produced in the presence of a strong electric field, magnetic field and the relative velocity between electrons and ions and **(b)** GDI is produced under the condition that both the electric field and density gradient pointing in the same direction (Kelley, 2009).

angle, i.e., at an angle of greater than 10° from the aspect angle. They are associated with the FBI. HAIR echoes can last for more than half an hour and are identified by analyzing the improved measurements of the HF radar elevation angle through calibration (Ponomarenko et al., 2018). By improving the SuperDARN range resolution from 45 to 15 km, where the first range gate started at 90 km, a new method, called the myopic mode, was introduced to observe the altitude of NREs at both the mid- and high-latitude regions (Ponomarenko et al., 2016; St.-Maurice and Nishitani, 2020).

Based on the myopic experiment, the NREs come from an altitude between 97 to 103 km (Ponomarenko et al., 2016; St.-Maurice and Nishitani, 2020). The virtual height h was estimated by means of the following formula:

$$h = \sqrt{R_E^2 + r^2 + 2R_E r \sin \alpha} - R_E \quad (4.51)$$

where R_E is the Earth's radius, α is the elevation angle of the radar's received signal, taken from the horizontal, and r is the range gate distance.

In a theoretical investigation of continuous NREs at 100 km, St.-Maurice and Nishitani (2020) suggested that FAIR echoes were associated with decaying structures due to the GDI in the ionosphere's bottom-side. These echoes were linked to either energetic particle precipitation or a strong ionospheric electric field. These echoes are related to strong sunlight, especially during summer and/or midday. SuperDARN observes wave-

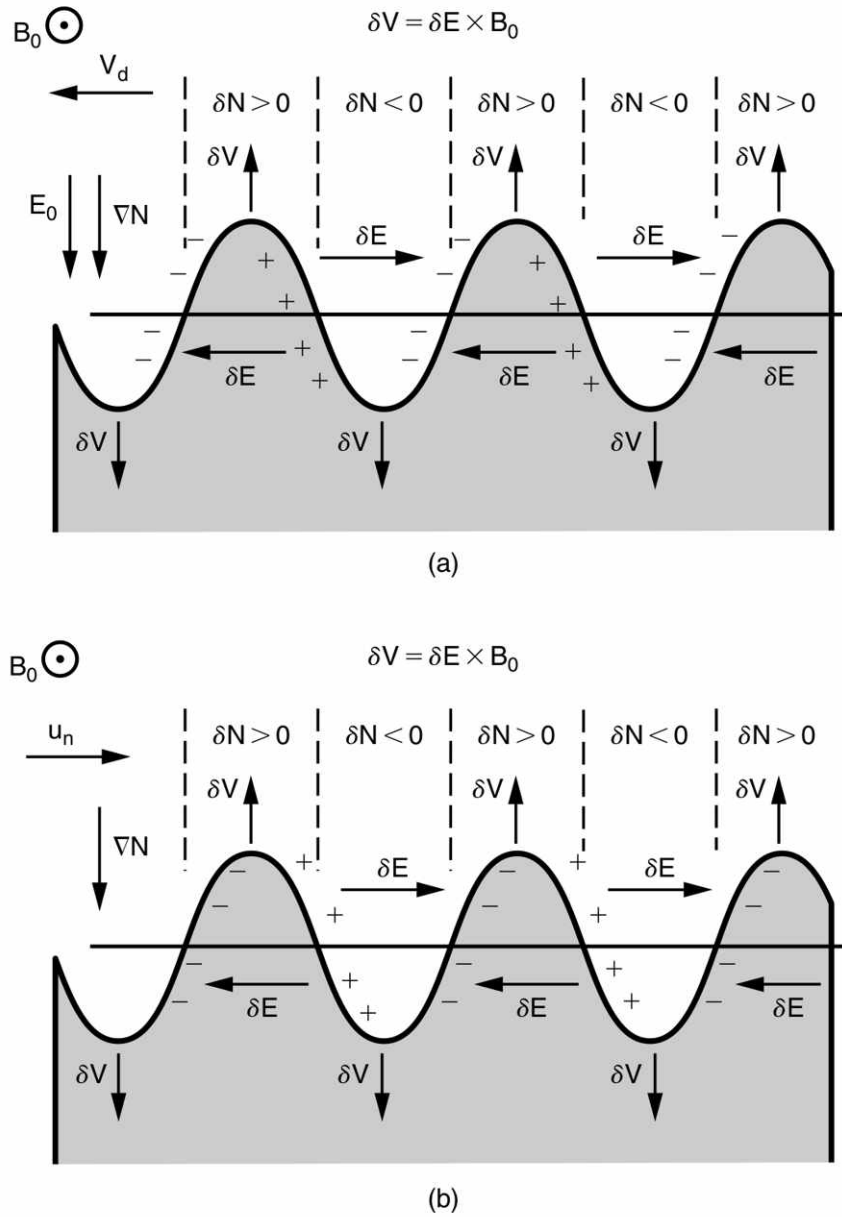


Figure 4.8: GDI driven by (a) an electric field and (b) a neutral wind. Light regions have lower electron density than the dark regions (Kelley, 2009).

lengths (10 - 15 m) which generally appear to have weak growth rates and require an electric field of about 40 mV/m. Assuming that electrons and ions are in thermal equilibrium, the linearized dispersion relation can be rewritten as follows:

$$\omega(\omega + i\nu_i) + \frac{i\nu_i}{\psi} \left[\omega \left(1 - i \frac{\mathbf{k} \cdot \mathbf{K}}{k^2} \frac{\nu_i}{\Omega_i} \right) - \mathbf{k} \cdot \mathbf{v}_D \right] - k^2 C_s^2 = 0 \quad (4.52)$$

where ω is a complex frequency expressed in the ion frame of reference, Ω_e , ν_e , Ω_i and ν_i are the electron cyclotron, electron-neutral collision, ion cyclotron, and ion-neutral collision frequencies, respectively. \mathbf{k}_{\parallel} and \mathbf{k}_{\perp} are wave vectors associated with a specific wavelength along and perpendicular to the magnetic field,

respectively. The ratio of local collision and gyro-frequencies ψ is expressed by:

$$\psi = \frac{v_e v_i}{\Omega_e \Omega_i} \left(1 + \frac{k_{\parallel}^2 \Omega_e^2}{k^2 v_e^2} \right). \quad (4.53)$$

In a case where there is no density gradient parallel to the magnetic field, \mathbf{K} is defined by:

$$\mathbf{K} = \frac{\nabla N_o}{N_o} \times \mathbf{e}_B \quad (4.54)$$

where \mathbf{e}_B is the unit vector along the magnetic field direction. The dispersion relation in equation (4.52) can be simplified as:

$$\omega_r + i\gamma = \pm \sqrt{k_{\perp}^2 C_s^2 - v_i^2/4} - i v_i/2 + \mathbf{k} \cdot \mathbf{v}_i \quad (4.55)$$

where ω_r is the oscillation frequency in the absolute frame of reference, v_i is the ion drift velocity, and γ is the growth rate. The ratio γ/k must have a speed of between 300 and 400 m/s, which is the speed of sound C_s . Near an altitude of 100 km, where $v_i \gg k_{\perp} C_s$, the decaying frequency $\omega_r + i\gamma$ from equation (4.55) is reduced to:

$$\omega_r + i\gamma = -i \frac{k_{\parallel}^2 C_s}{v_i} + \mathbf{k} \cdot \mathbf{v}_i. \quad (4.56)$$

The decay rate in this expression is related to ambipolar diffusion.

FAIR echoes are associated with GDI, i.e., the density gradient, magnetic field strength and electric field are involved at the E -region's lower altitude at around 100 km. The effective electric field \mathbf{E}' can be estimated for a high plasma density in sporadic Es layers together with modest neutral winds \mathbf{U} :

$$\mathbf{E}' = \mathbf{E} + \mathbf{U} \times \mathbf{B}. \quad (4.57)$$

The GDI was linked to the eastward neutral wind U_{nx}^{th} at high latitudes (St.-Maurice and Nishitani, 2020). The northward component of an electric field is used to destabilize the plasma, while the parallel component of the wave vector is assumed to be very small when the instability is triggered.

For the plasma density scale height $L_z = \left(\frac{1}{\frac{d \ln N_o}{dz}} \right)$ along z (the vertical direction) and D the magnetic dip angle, from equation (4.52), the following equation may be used:

$$\frac{\mathbf{k} \cdot (\mathbf{U}_n - \mathbf{E} \times \mathbf{B}/B^2)}{k} \Big|_{th} = \frac{L_z}{\Omega_e} (1 + \psi) (k C_s)^2 \frac{v_e}{v_i} \frac{1}{\cos D} \frac{k}{k_x} \quad (4.58)$$

The lowest threshold condition for a wave vector moving closer to the y-direction (i.e., $k \gg k_x$) is expressed by the following equation:

$$\left[U_{nx} + \frac{E_y}{B} \right]_{th} = \frac{L_z}{\Omega_e} (1 + \psi) (k C_s)^2 \frac{v_e}{v_i} \frac{1}{\cos D} \quad (4.59)$$

Note that the eastward $\mathbf{E} \times \mathbf{B}$ drift is negative for a northward \mathbf{E} and the downward \mathbf{B} ; the same negative drift is obtained for southward \mathbf{E} and upward \mathbf{B} . According to these signs, a northward electric field creates a westward electron drift with an eastward neutral wind for the instability in the northern hemisphere. It means that a northward electric field pushes electrons toward the west. Simultaneously, the eastward neutral wind blows the ions to the east through collisions, creating the polarization electric field in the density fluctuations (see Figure 4.9). For $\mathbf{k} = k_x$, assume that the ionospheric bottom-side is at 100 km, and at zero aspect angle, $\psi \approx 0.1$. The dip angle $D = 63^\circ$ was used over the Rankin Inlet (RKN) radar, resulting in $\cos D \approx 1/4$ and $k \approx 1/2$. Assuming that the plasma was isothermal, meaning that electrons and ions had the same temperature at 100 km, $C_s \approx 300$ m/s, $\Omega_e = 0.9 \times 10^7$ s⁻¹ and the ratio $v_e/v_i = 7.5$. Between altitudes of between 90 and 100 km, the density change factor was 60 during summer, and the estimated scale height $L_z = 2.4$ km. This value of L_z could be modulated via the up and down push through shear or compression as a gravity wave passes. After putting all of these values together, the estimation of $[U_{nx} + E_y/B]$, i.e., neutral wind and plasma velocity, is believed to be equal to 200 m/s for the instability threshold, for instabilities with a wavelength of 12 m, and 240 m/s for instabilities with a wavelength of 10 m. Note that the threshold depends on the dip angle; for example, for $D \approx 56^\circ$ the threshold requires a factor of 2, i.e., 120 m/s for instabilities with a wavelength of 10 m.

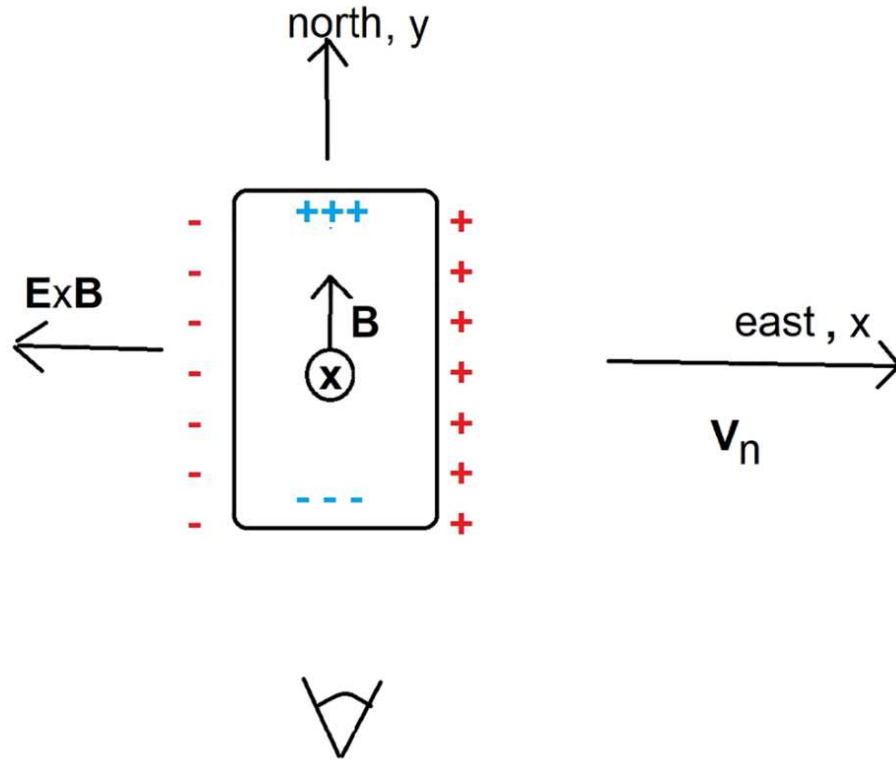


Figure 4.9: A demonstration of the FAIR mechanisms, as an eastward neutral wind and/or westward $\mathbf{E} \times \mathbf{B}$ drift create a westward polarization electric field (St.-Maurice and Nishitani, 2020).

In this study the dipole angle at SANA and Zhongshan is $D \approx -61.7^\circ$, $D \approx -73.2^\circ$, respectively, as estimated by means of the International Geomagnetic Reference Field (IGRF) model.

A secondary process is needed to have a growing 10 m structure, which can be detected by SuperDARN radars. These secondary Farley Buneman waves in the vertical direction are generated by large-scale gradient drift with the horizontal wave vectors. For example, for an irregularity of 100 m gradient scale on the edges of large-scale structures moving at different altitudes, and the ratio E/B varying from 200 to 300 m/s, the growth rate of 10 m structures would be 50 and 30 s^{-1} at 100 km. In this case, an eastward neutral wind of 50 m/s is needed to trigger a large GDI at an altitude of 100 km, which seems to be plausible. The growth rate would drop to 17 s^{-1} for a secondary GDI of 10 m wavelength at zero aspect angle, which can be observed by SuperDARN radars.

Figure 4.9 illustrates a zonal polarization electric field $\delta\mathbf{E}$, is created by a zonal eastward wind and/or a zonal westward $\mathbf{E} \times \mathbf{B}$ drift across the near-vertical magnetic field. The arrow north of \mathbf{B} indicates a tilted magnetic field. Through the horizontal component of the magnetic field, the polarization electric field via $\mathbf{E} \times \mathbf{B}$ drift, increases the density in the downward direction, in a region where the density is less dense. When the GDI occurs, the created “finger-like” structures should always be orthogonal to the magnetic field in all directions. Figure 4.9 shows a north-south structure of which the edges are the source of radio wave scatter similar to Type II structures observed in ordinary E -region echoes. Type II structures are the irregularities of wavelengths between ~ 3 and ~ 15 m caused by nonlinear decay of other irregularities of wavelengths ~ 150 m (Sato, 1973).

EISCAT observations in 2000 (Haldoupis et al., 2000) show that at auroral E -region heights, L_z can be between 4 and 7 km at an altitude less than 100 km. When the ion-neutral collision frequency is greater than kC_s , FAIR echoes are likely to be detected in the near ranges. The problem is that sometimes, the auroral conditions may introduce a large electric field that can also excite the Farley-Buneman waves at 10 m. In this case, both mechanisms should be considered, such as during a magnetic storm. A large southward electric field

also can trigger the GDI in the morning sector when ions drift downward because of the increasing frequency of ion-neutral collisions, which reduces their speed, resulting in the creation of sporadic E_s layers at high latitudes.

4.4 Summary

In this chapter, an overview of previous work on TIDs and NREs was given. The SuperDARN HF radar observes both TIDs and NREs. The FBI and GDI are known 2 standard instabilities in the high latitudes of the ionospheric E -region that cause NREs. These instabilities and their growth rates were discussed. Finally, HAIR and FAIR echoes associated with the electric field in the magnetic field were also considered. Other NREs, such as PMSEs, which are closely connected with NLCs, were briefly highlighted.

Chapter 5

OBSERVATIONS AND MODEL OUTPUTS

5.1 Introduction

This chapter discusses the SuperDARN HF radar observations and the outputs of the IRI-2016 and HWM-14 models relating to the four events during the period 2011 to 2013, that are the focus of this study. The backscatter power, Doppler velocity and spectral width of the SANA E and Zhongshan radars are used to illustrate the simultaneous occurrence of TIDs and NREs. Ray-tracing of the radars' signals is used to estimate the altitude of the returned echoes, i.e., the altitude at which TID and NRE echoes are observed. Two events occurred during geomagnetic storms, while the other two occurred during quiet time. The values of the geomagnetic AE, Dst and Kp indices for each event are given. The electron density derived from the IRI-2016 model and the neutral wind from the HWM-14 model are also discussed. Finally, the electric fields derived from combining the data from the SuperDARN radar network for the events are also included.

5.2 Backscatter power, Doppler velocity and spectral width

Four events showing TIDs and NREs simultaneously were identified by means of the SANA E and Zhongshan HF radars. Figure 5.1 and Figure 5.2 illustrate the Range-Time-Intensity (RTI) of two events in winter and two in summer, respectively. In each figure, there are three panels, with the top panel representing backscatter power, the middle panel the Doppler velocity, and the bottom panel representing the spectral width. TIDs are shown by the periodic oblique forward-/backward-sloping echoes received in the far ranges (greater than 315 km), while quasi-periodic (QP) backscatter received in the near ranges (less than 315 km range) represent the NREs. Both phenomena are seen in the backscatter power, velocity and spectral width of each event. The slope of the TID scatter also indicates (and is consistent with) the direction of propagation shown by the Doppler velocity. Figure 5.1 (A) shows TIDs and NREs observed by beam 7 of the SANA E HF radar on 28 May 2011 between 11:00 and 13:00 UT. Figure 5.1 (B) illustrates TIDs and NREs observed by beam 15 of the SANA E radar on 15 July 2012 between 12:00 and 17:00 UT. Figure 5.2 (A) shows the same phenomena observed by beam 15 of the Zhongshan radar on 22 November 2013 between 00:00 and 04:00 UT. Figure 5.2 (B) represents TIDs and NREs observed by beam 15 of the Zhongshan radar on 17 December 2013 between 19:00 and 21:00 UT. The magnitude of backscatter power of TIDs received by the SANA E radar during winter cases was less than the magnitude of backscatter power received by the Zhongshan radar during summer cases. When comparing the Doppler velocity in the figures, Figure 5.1 indicates that the ionospheric plasma was moving away (negative Doppler velocity) from the radar, and Figure 5.2 shows that the ionospheric plasma was moving toward the radar (positive Doppler velocity). The spectral width of TIDs during winter was wider than the spectral width during summer. Figure 5.3 shows the NREs for odd beam numbers of the SANA E HF radar on 28 May 2011 (A) and 15 July 2012 (B). The figures show power (left-hand panel), Doppler velocity (middle panel), and spectral width (right-hand panel). Both plots show some QP perturbations during the entire duration of both phenomena (NREs and TIDs). From a spectral analysis of the NREs by means of the FFT spectral peaks were identified at periods of 16 and 28 minutes. These peaks corresponded with peaks of the broadband TIDs on 28 May 2011 and 15 July 2012, respectively. Figure 5.4 shows the NREs for odd beam numbers of the Zhongshan HF radar on 22 November 2013 (A) and on 17 December 2013 (B). It displays the same parameters as was done in Figure 5.3. The FFT was used to find their oscillating periods and it was found that on 22 November 2013 both the NREs and TIDs had a period of 33.3 min while on 17 December 2013 they oscillated with a period of 20 min. The FFT plots are shown in chapters 6 and 7. On 22 November 2013, the backscatter power of NREs and TIDs was perturbed between 0 and 10 dB for most of the time, but for a few hours, the power reached 26 dB. The Doppler velocity was perturbed from 0 to ~200 m/s, while the spectral width was less than 100 m/s. Data gaps appear in all beams of the radar. On 17 December 2013, the

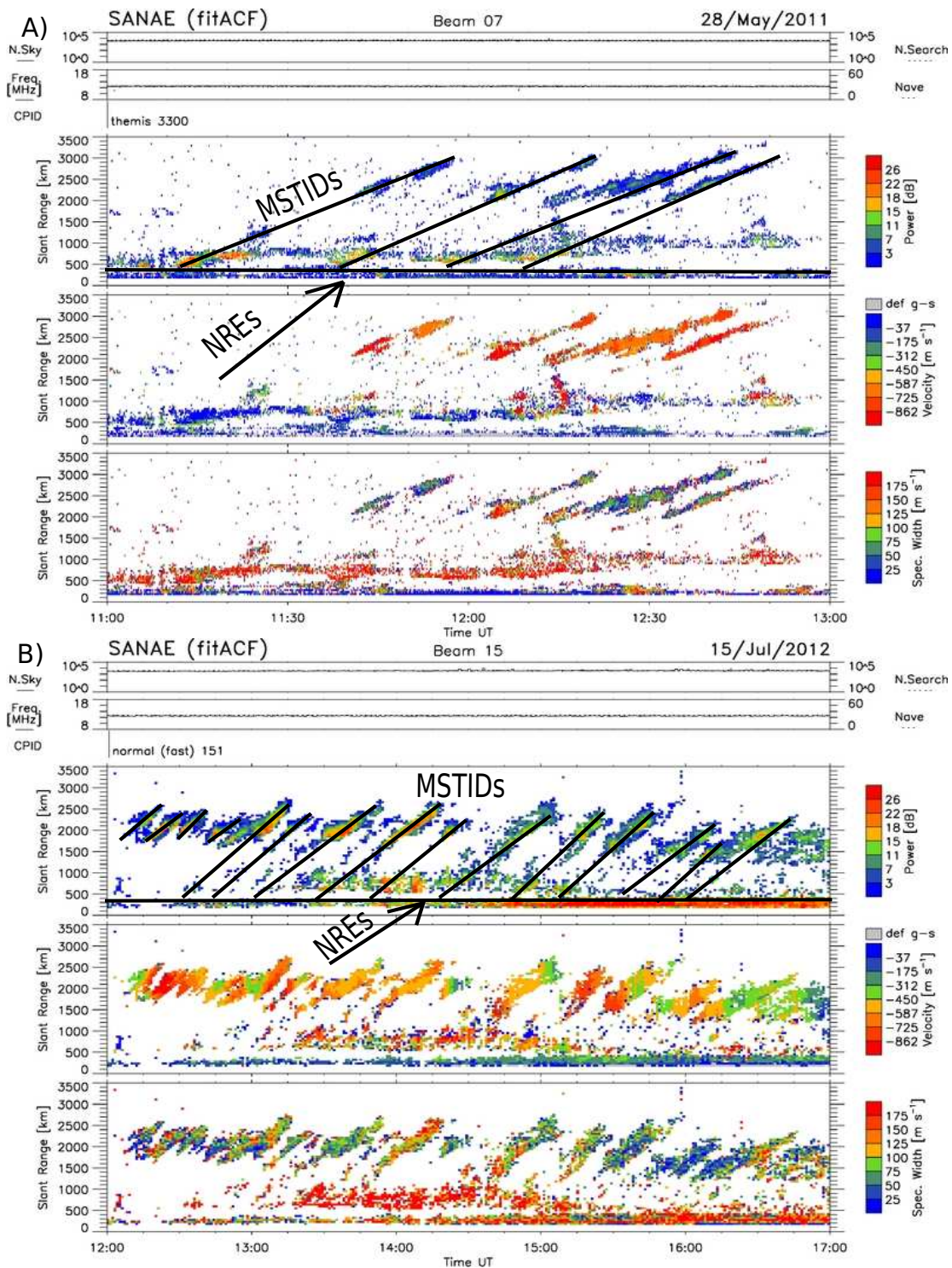


Figure 5.1: Range-Time-Intensity plot of backscatter power (top), Doppler velocity (middle) and spectral width (bottom) based on data from the SANAe HF radar and showing TIDs and NRE; (A) from 11:00 to 13:00 UT on 28 May 2011 from beam 7 and (B) from 12:00 to 17:00 UT on 15 July 2012 from beam 15.

backscatter power was perturbed between ~ 5 and ~ 35 dB. A clear power enhancement was identified across the radar beams from beam 15 at 19:00 UT to beam 1 at around 20:30 UT. The Doppler velocity was perturbed between ~ -50 to ~ 200 m/s, but a clear enhancement crosses the beams from beam 15 at around 20:00 to beam 5 at around 20:40 UT. The spectral width was less than 100 m/s and for all parameters a few data gaps were

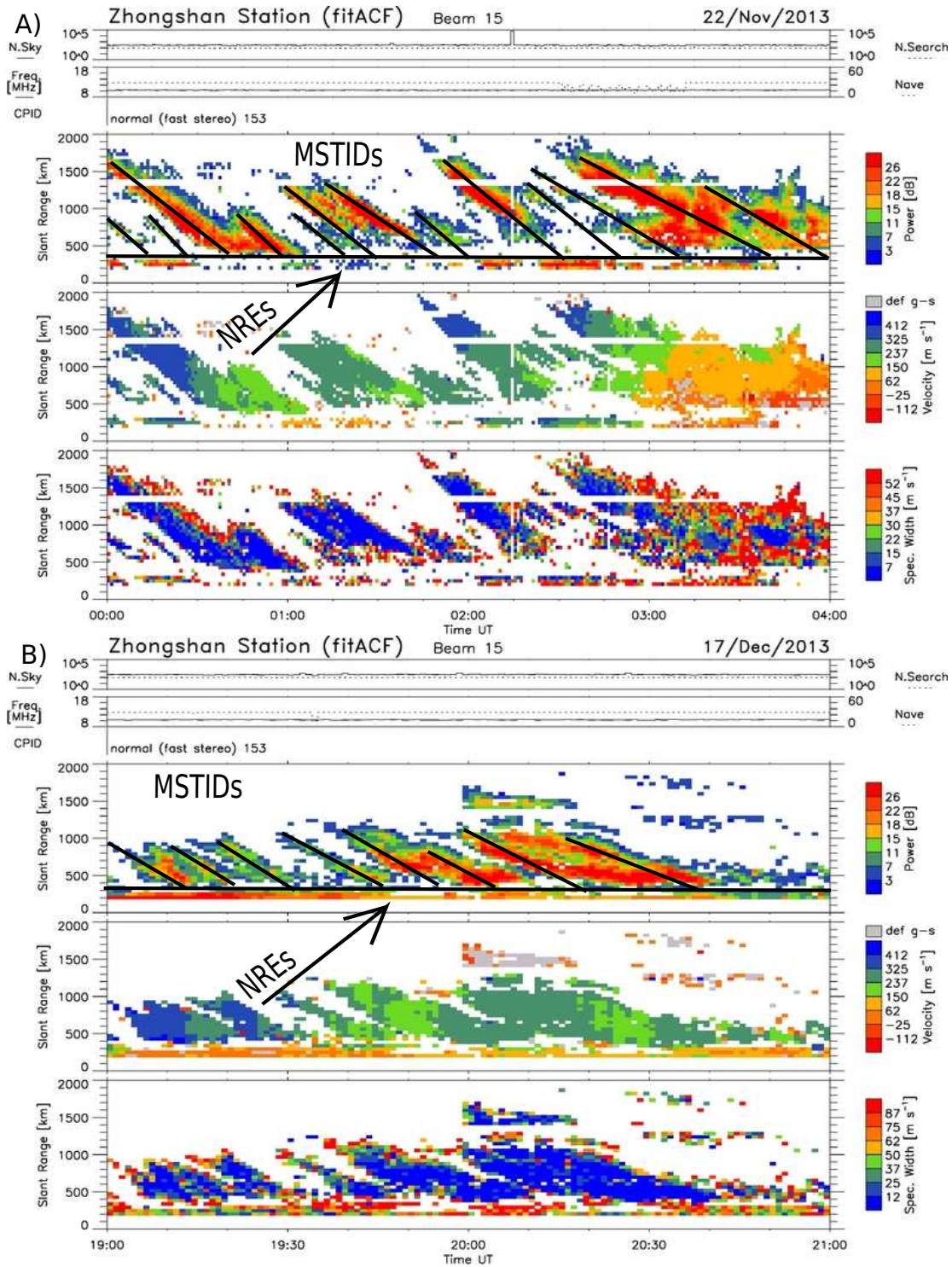


Figure 5.2: RTI plot of backscatter power (top), Doppler velocity (middle) and spectral width (bottom) based on data from beam 15 of the Zhongshan HF radar and showing TIDs and NREs; (A) from 00:00 to 04:00 UT on 22 November 2013 and (B) from 19:00 to 21:00 UT on 17 December 2013.

present in only gates 1, 2 and 3 of all beams of the radar.

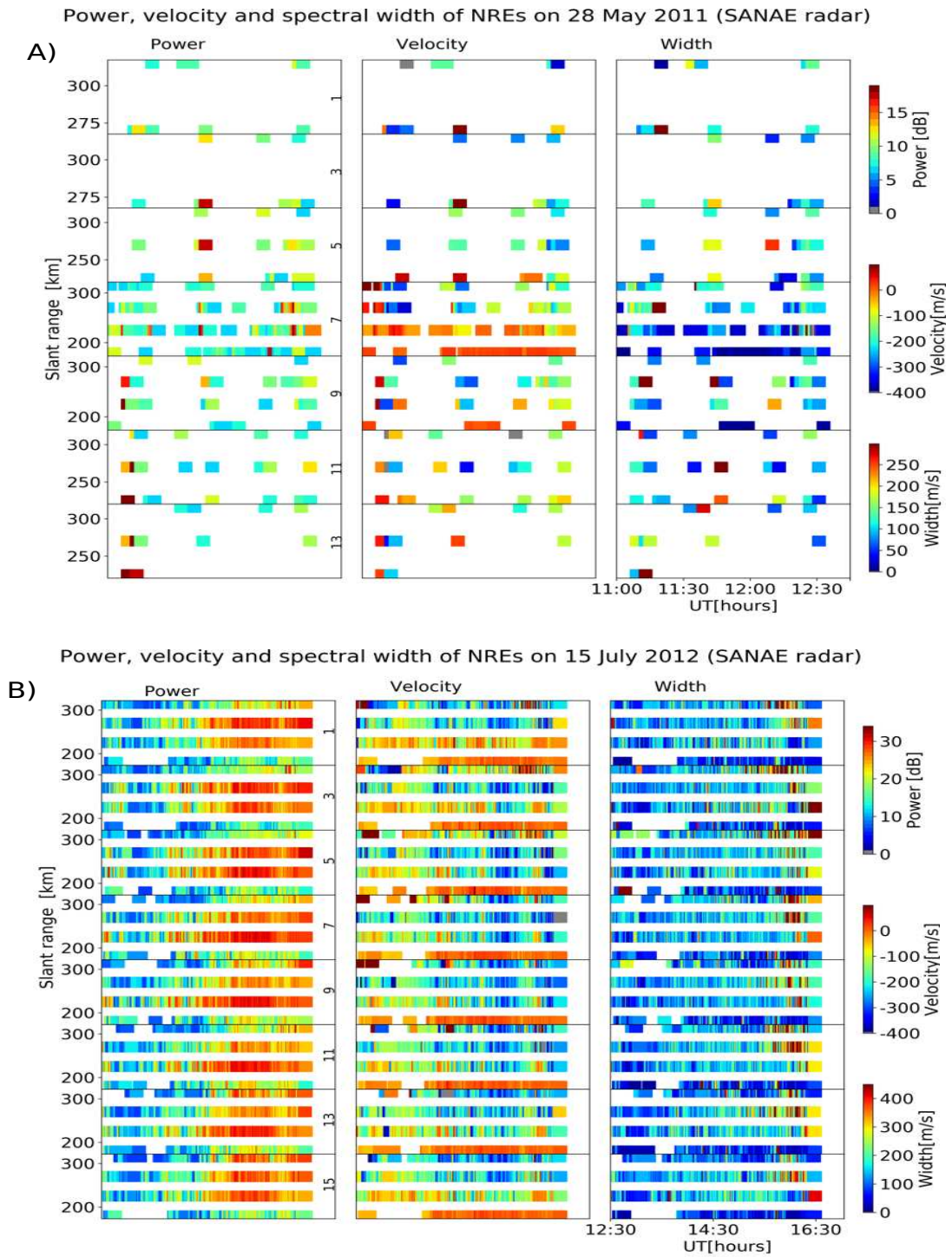
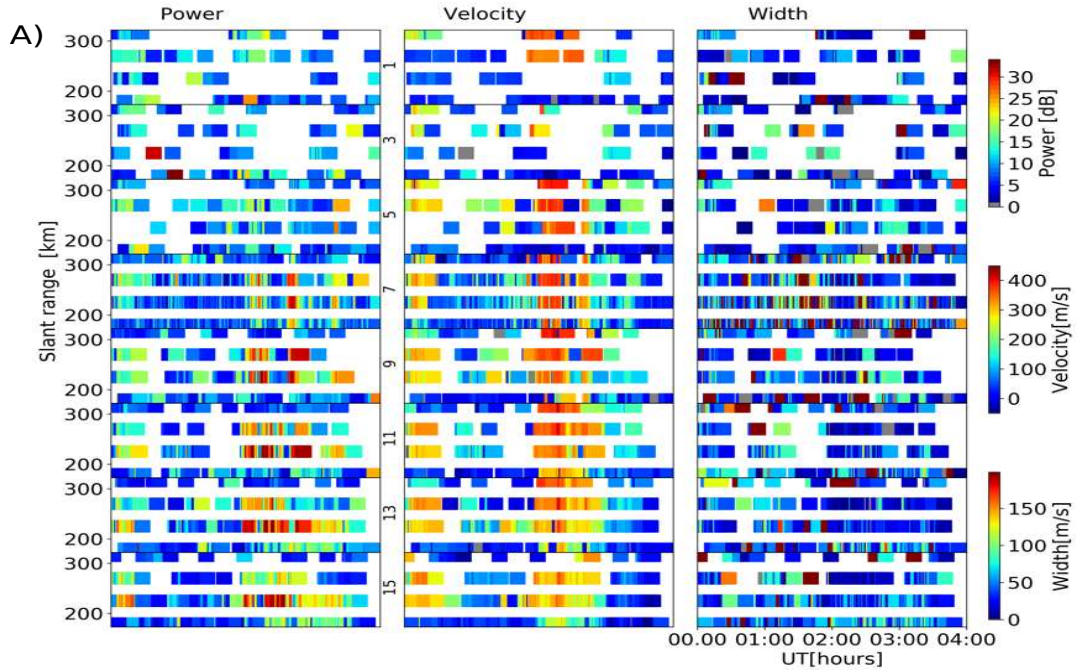


Figure 5.3: Near range echoes of odd numbered beams showing the backscatter power (left panels), Doppler velocity (middle panels) and the spectral width (right panels). A) shows SANA E HF radar data for 28 May 2011 from 11:00 to 12:46 UT. B) shows SANA E HF radar data for 15 July 2012 from 12:30 to 16:30 UT.

5.2.1 Ray-tracing

Ray-tracing was used to estimate the altitude from which the backscatter echoes came, i.e., the propagation altitude of TIDs and the altitude from which the NREs came. For the ray tracing simulation, the SANA E

Power, velocity and spectral width of NREs on 22 November 2013 (Zhongshan radar)



Power, velocity and spectral width of NREs on 17 December 2013 (Zhongshan radar)

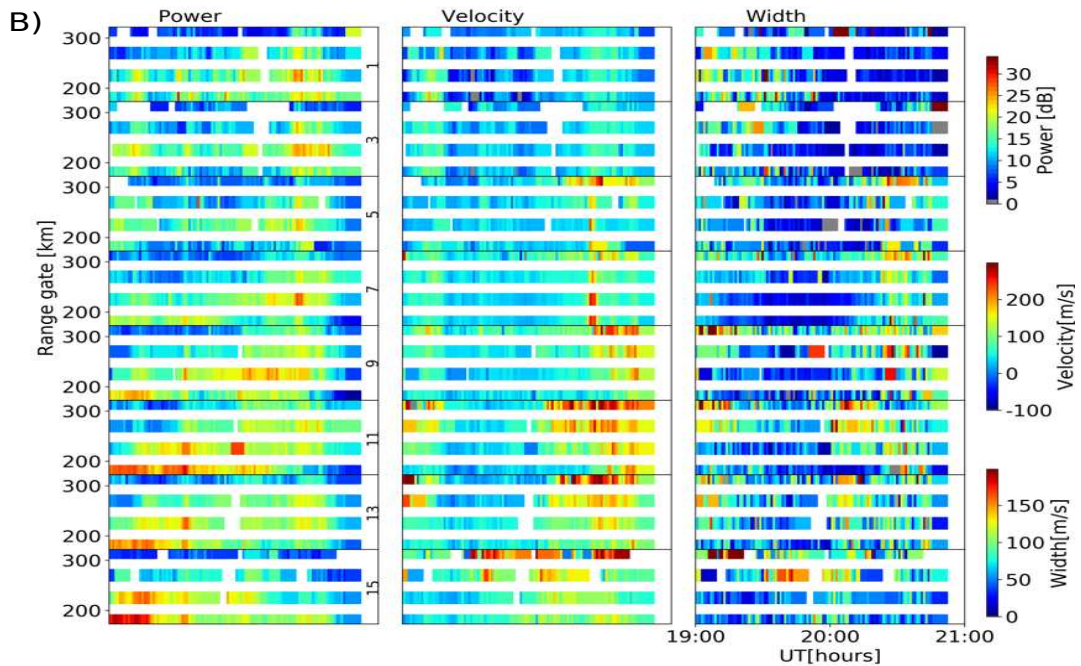


Figure 5.4: Near range echoes of odd numbered beams showing the backscatter power (left panels), Doppler velocity (middle panels) and the spectral width (right panels). A) shows Zhongshan HF radar data for 22 November 2013 from 00:00 to 04:00 UT. B) shows Zhongshan HF radar data for 17 December 2013 from 19:00 to 21:00 UT.

radar was assumed to operate at 12 MHz, which is close to the actual frequency of 12.57 MHz. The Zhongshan SuperDARN radar ray tracing was done at 10 MHz, which is close to the radar’s operating frequency of 10.25 MHz. Figure 5.5 shows that for all four cases, considering the ranges observed in Figures 5.1 and 5.2, TID

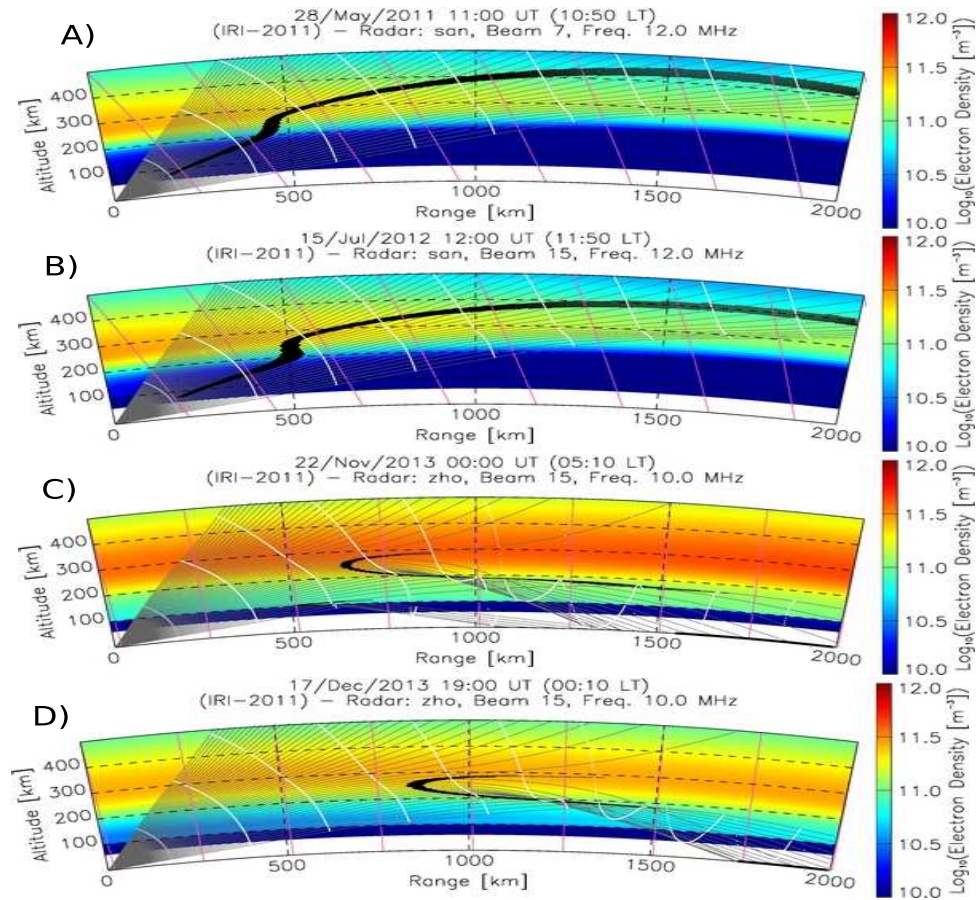


Figure 5.5: The estimation of the backscatter echo reflection points using ray tracing at 12.0 MHz (SANA) and 10.0 MHz (Zhongshan). Panel A) at 11:00 UT on 28 May 2011, panel B) at 12:00 UT on 15 July 2012, panel C) at 00:00 UT on 22 November 2013, and panel D) at 19:00 UT on 17 December 2013.

and NRE backscatter were ionospheric. Figure 5.5 (panel A) and (panel B) show that winter TID echoes were backscattered at altitudes between 350 and 420 km altitude in the ranges beyond 1000 km. The echoes in the ranges 500-1000 km were backscattered at altitudes between 300 and 400 km, while the echoes between ranges of 315 and 500 km were from altitudes of 150-200 km. Echoes below 315 km range were backscattered from an altitude below 150 km, and the echoes in the first gate (180 km range) came from altitudes below 100 km. Figure 5.5 (panel C) and Figure 5.5 (panel D) show that the summer TID echoes were backscattered from altitudes of ~ 180 and ~ 300 km in the ranges between 800 and 1500 km (see Figure 5.2). The figures do not show the reflection altitude of echoes in the ranges within 600 km for 22 November 2013 and within 800 km range for 17 December 2013. This is likely due to the fact that the ray tracing algorithm uses the statistically averaged IRI model. The echoes beyond the 1500 km ranges are ground scatter, but our TIDs were observed in ranges within 1500 km.

5.2.2 Geomagnetic indices during both winter and summer events

Figure 5.6 illustrates geomagnetic indices for both winter and summer events. The gray-highlighted vertical areas show the times of interest for winter (panels A and B) and summer (panels C and D) events. Each figure shows the auroral electrojet and the disturbance storm time in nT and the Kp indices. The highlighted area in Figure 5.6 (A) shows that on 28 May 2011, AE was between 600 and 800 nT, Dst between -80 and -60 nT, and Kp was 6. Figure 5.6 (B) shows that on 15 July 2012, AE was between 1100 and 1250 nT, Dst between -110 and -140 nT, and Kp between 5 and 6. Figure 5.6 (C) shows that on 22 November 2013, AE was between 10 and 50 nT, Dst between 10 and -15 nT and Kp between 0 and 1. Figure 5.6 (D) shows that on 17 December 2013, AE was below 200 nT, Dst was -10 nT, and Kp was 1 and 2. The indices in Figure 5.6 (A) and (B) indicate a modest and a strong geomagnetic storm, respectively, while those in Figure 5.6 (C) and (D) show quiet time conditions.

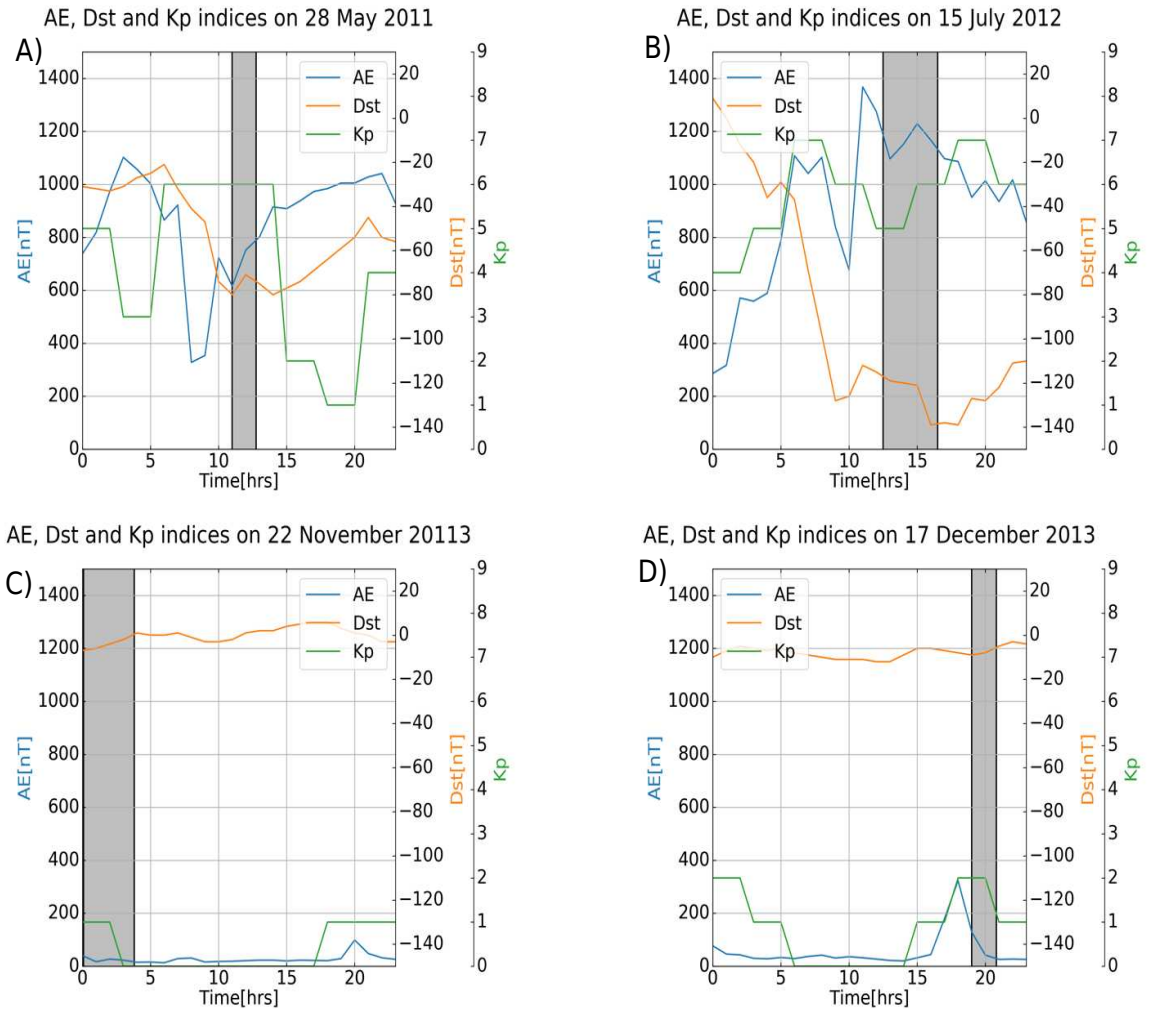


Figure 5.6: The AE, Dst and Kp indices on A) 28 May 2011, B) 15 July 2012 during a geomagnetic storm, and C) 22 November 2013 and 17 December 2013 during quiet time conditions.

5.3 Particle precipitation

Daytime TIDs during a geomagnetic storm on 15 July 2012 may be associated with auroral activity such as Joule heating, Lorentz force or particle precipitation (Hunsucker, 1982). Loucks et al. (2017) showed that, during a magnetic storm, in the E -region of high latitudes, particle precipitation is the leading cause of the electron density enhancement below an altitude of 130 km. Electron density enhancement due to particle precipitation also takes place in F -region. This enhancement and the presence of the electric field in the F - and E -regions may trigger instabilities in these regions that can lead to the development of MSTIDs (Stefanello et al., 2015; Cherniak and Zakharenkova, 2018) and NREs (Rüster and Schlegel, 1999; Carter and Makarevich, 2010; Makarevich, 2016; Makarevich et al., 2021), respectively. Figure 5.7 shows four instances of the $\mathbf{E} \times \mathbf{B}$ plasma drift in m/s as observed by the SuperDARN radars, and the total flux in $\text{keV cm}^{-2}\text{s}^{-1}\text{sr}^{-1}$ of particle precipitation in the southern hemisphere in Magnetic Local Time (MLT) and on the Magnetic Latitude (MLAT) grid. The particle precipitation data presented in Figure 5.7 were derived from the Total Energy Detector (TED) instrument every 16 s. Polar Operational Environmental Satellites (POES) host the TED instrument. There are currently 5 POES satellites, i.e., from 15 to 19, operating simultaneously at an altitude of ~ 800 km with a

101 min period. Figure 5.7 (A) shows the plasma drift observed by the SuperDARN radars and the total flux of particle precipitation on 28 May 2011 between 10:58 and 11:00 UT (winter). Figure 5.7 (B) shows the plasma drift observed by the SuperDARN radars and the total flux of particle precipitation on 15 July 2012 between 11:58 and 12:00 UT (winter). Figure 5.7 (C) shows the plasma drift observed by the SuperDARN radars and the total flux of particle precipitation on 22 November 2013 between 02:00 and 02:02 UT (summer) during quiet time conditions. Finally, Figure 5.7 (D) shows the plasma drift observed by the SuperDARN radars and the total flux of particle precipitation on 17 December 2013 between 19:00 and 19:02 UT (summer).

On 28 May 2011 and 15 July 2012, the plasma drift velocities observed by the SuperDARN radars were between 125 and 1000 m/s, while on 22 November 2013 and 17 December 2013, the drift velocities were between 125 and 500 m/s. The auroral oval boundary, shown by the red dot-dash line, is more equatorward during the geomagnetic storm, but for all cases the field of view of each radar was under the auroral oval. For all cases, the precipitation of energetic particles decreased with decreasing latitude. Hardy et al. (1989) also noticed the flux decrease which depends on the latitude location. It first increases at the pole, then decreases in the sub-auroral region with decreasing in latitude. The latter is of course an assumption upon which the auroral boundary determination is made.

5.4 Electron density derived from IRI-2016

Heaton et al. (1996) used two stations in Antarctica to study the variation of electron density during a period of eight months. The electron density profile was analyzed by comparing tomography and a dynasonde. In this study, the electron density of the *E*-region is within the same range as the electron density derived from the IRI-2016 model.

5.4.1 Winter events

The International Reference Ionosphere model (Bilitza et al., 2017) was used to get the electron density (N_e) at an altitude of between 80 and 160 km. Figure 5.8 (A) and Figure 5.8 (B) show the electron density from 09:00 to 15:00 UT on 28 May 2011 and 09:00 to 17:00 UT on 15 July 2012 at SANAE, respectively. The electron density for both plots was set to a maximum of $2.0 \times 10^{10} \text{ m}^{-3}$ in order to compare their variations. Both cases occurred during geomagnetically active periods. During midday at an altitude of between 100 and 120 km, there was electron density enhancement due to solar radiation and particle precipitation. On 15 July 2012, N_e was slightly higher than on 28 May 2011; the reason may be particle precipitation linked with the severity of their geomagnetic storms (see section 5.2.2). The electron density enhancement was more significant during winter events than during summer events, because winter events occurred during geomagnetic storms, while summer events occurred during quiet time conditions.

5.4.2 Summer events

Figure 5.9 shows N_e from 00:00 to 12:00 UT on 22 November 2013 (A) and from 17:00 to 24:00 UT on 17 December 2013 (B) at Zhongshan. Both cases occurred during quiet time in summer. The magnetic indices are presented in section 5.2.2.

N_e was set to a maximum of $3.0 \times 10^{11} \text{ m}^{-3}$ for the case on 22 November 2013 and $1.5 \times 10^{11} \text{ m}^{-3}$ for the case on 17 December 2013 to make the comparison easy. On 22 November 2013, N_e was higher than on 17 December 2013 at almost all altitudes, although the AE and Kp indices showed that the 17 December 2013 event was more active than the 22 November 2013 event. At Zhongshan station, the LT was UT + 5 hr, implying that the position of the Sun may have helped in the generation of electrons via ionization. So, the ionization was higher where the solar zenith angle was less on 22 November 2013. The TIDs and NREs took place between 05:00 and 09:00 LT, while on 17 December 2013, TIDs and NREs occurred between 00:00 and 02:00 LT, i.e., when plasma recombination would have taken place because the solar zenith angle was greater (Ogwala et al., 2020).

Despite the geomagnetic storm in winter, the electron density was higher during the summer events than during winter events. The reason is that the Sun always appears at high latitudes during summer, other than during winter. Furthermore, the IRI is a statistical model and therefore cannot show plasma density enhancements for individual geomagnetic storms. Chemical recombination could explain the electron density

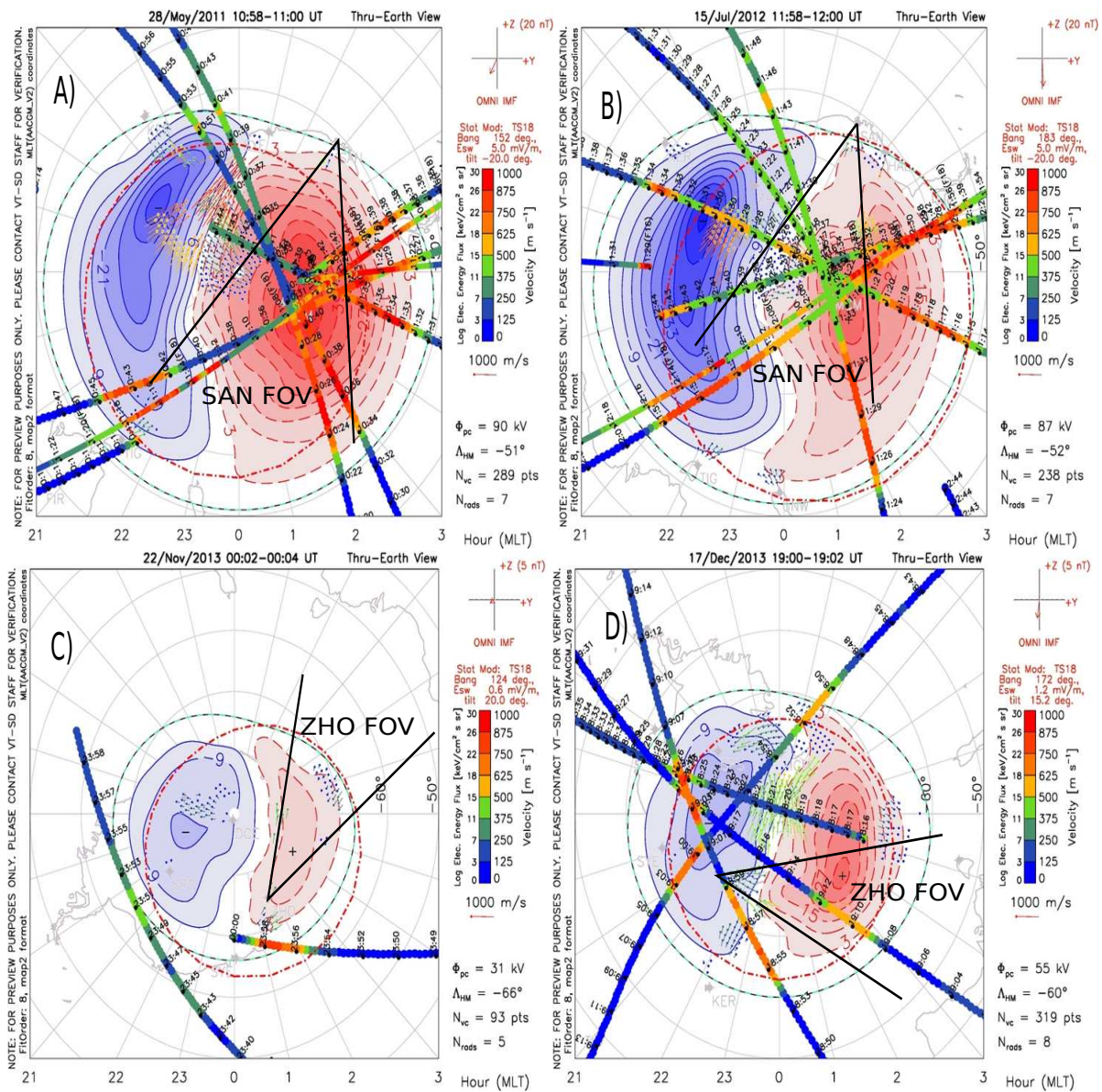


Figure 5.7: Potential map plot showing the vectors of convection plasma flow derived from the southern hemisphere SuperDARN measurements and overlaid on a MLT-MLAT grid, along with particle precipitation data from the TED instrument of the POES satellites. The equatorward auroral oval boundary (red dot-dash line) determined by from POES. The equatorward edge of the auroral oval boundary was estimated by fitting a circle to the POES TED data. The green dot-dash line shows the poleward boundary: A) at 10:58-11:00 UT on 28 May 2011, B) at 11:58-12:00 UT on 15 July 2012, C) at 00:02-00:04 on 22 November 2013, and D) at 19:00-19:02 on 17 December 2013.

depletion between 110 and 130 km due to the increase of the solar zenith angle (Ogwala et al., 2020). The electron density enhancement is due to solar radiation during geomagnetically quiet conditions. The electron density variations between 90 and 130 km over midday, shown in Figure 5.8, were caused by solar illumination (Robinson and Vondrak, 1984; Johnson and Wygant, 2003; Edberg et al., 2010) and/or particle precipitation (Frank and Ackerson, 1971; Baron, 1974; Zhang et al., 2012).

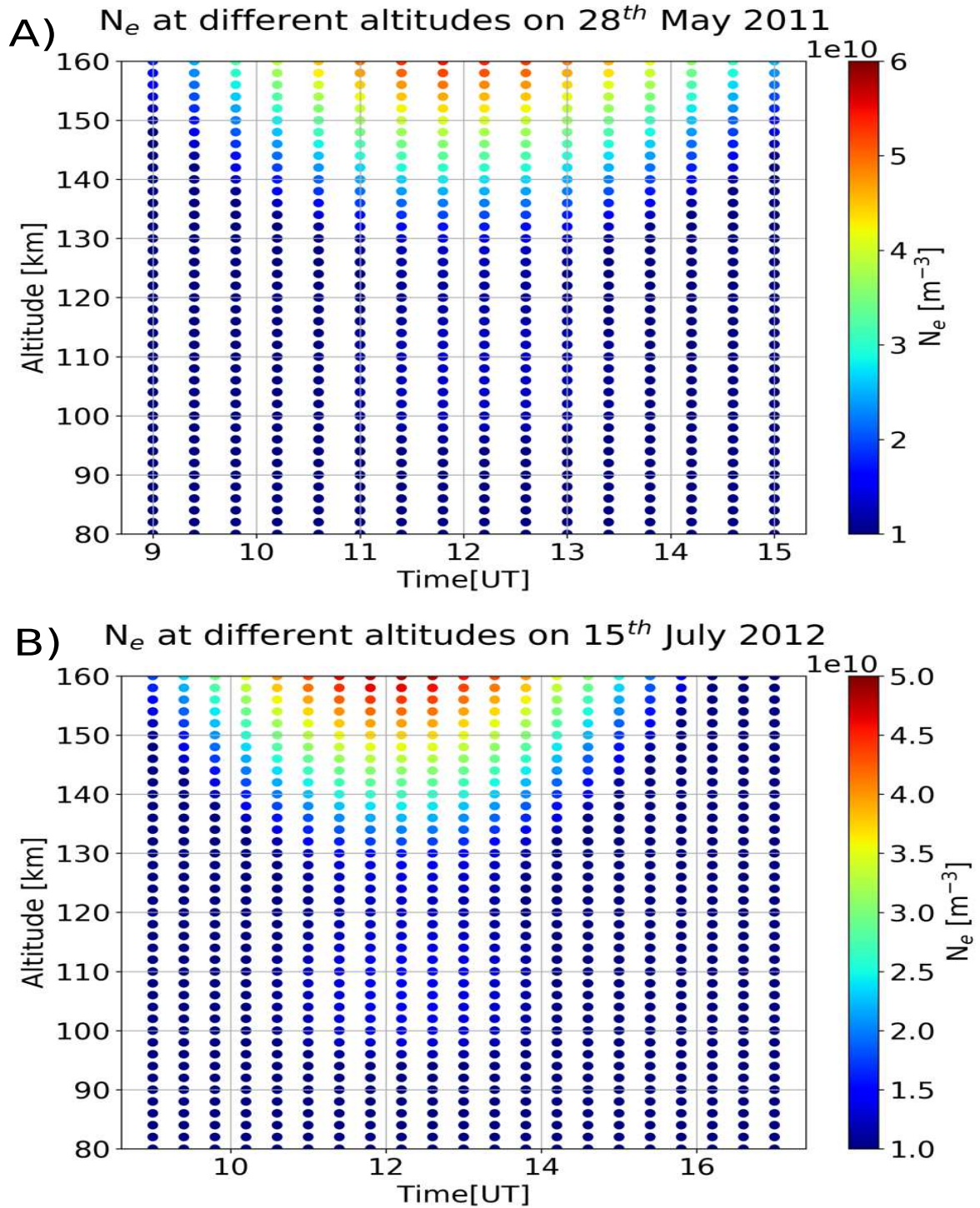


Figure 5.8: The electron density as derived from the IRI model for altitudes of between 80 and 160 km for 28 May 2011 (A) and 15 July 2012 (B), $LT \approx UT + 2$ hr at $(-72.50^\circ, -2.76^\circ)$ geographic coordinates.

5.5 Wind parameters derived from the HWM-14

Hernandez et al. (1992) used a high-resolution, high-luminosity Fabry-Perot spectrometer to measure the thermospheric neutral wind. The magnitudes of zonal and meridional neutral winds studied by Hernandez et al.

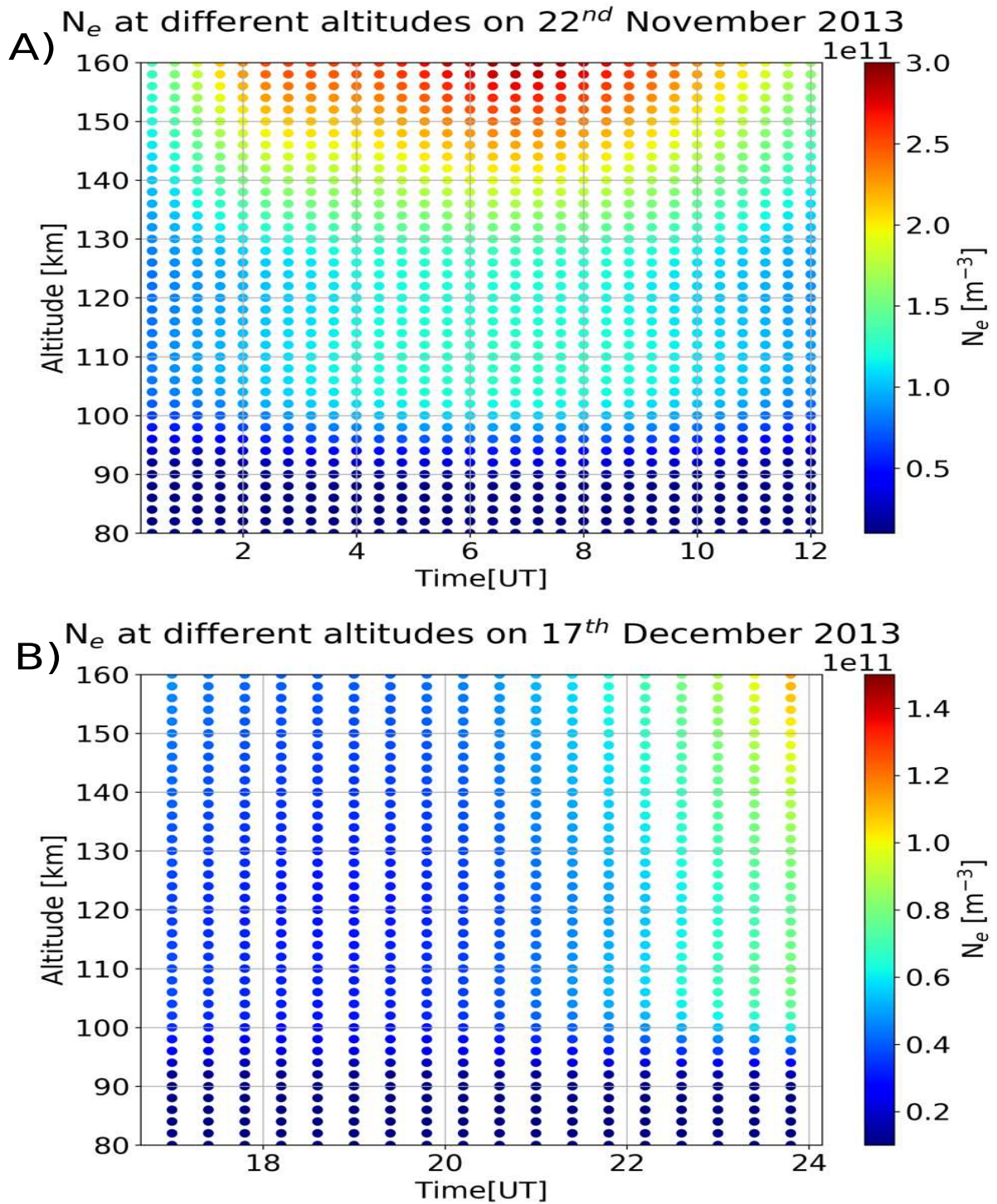


Figure 5.9: The electron density as derived from the IRI model for altitudes of between 80 and 160 km for 22 November 2013 (A) and 17 December 2013 (B), LT \approx UT +5 hr at $(-69.40^\circ, 82.60^\circ)$ geographic coordinates.

(1992) are in the same range as those estimated by the HWM-14 used for this thesis. Figures 5.10 and 5.11 demonstrate the meridional wind velocity (U_{ny}) and zonal wind velocity (U_{nx}) derived from the HWM-14 (Drob et al., 2015) for altitudes of between 80 and 160 km for the winter and summer events, respectively. The vertical blue dashed lines show the period when both TIDs and NREs were observed, while the horizontal black line

indicates the wind at an altitude of 100 km, where most NREs are located (St.-Maurice and Nishitani, 2020). Figure 5.10 (A) and Figure 5.10 (B) show the wind on 28 May 2011 from 10:00 to 14:00 UT, while Figure 5.10 (C) and Figure 5.10 (D) show the wind on 15 July 2012 between 10:00 and 18:00 UT for SANAE base. Figure 5.11 (A) and Figure 5.11 (B) present the wind on 22 November 2013 between 00:00 to 03:00 UT, while Figure 5.11 (C) and Figure 5.11 (D) give the magnitude of the wind on 17 December 2013 between 17:00 and 24:00 UT for Zhongshan base.

5.5.1 Winter events

Figure 5.10 (A) shows that the meridional wind above the SANAE base (72.5° S, 2.76° W) reversed its direction toward the south with a magnitude varying from ~ 15 to ~ 20 m/s on 28 May 2011 during the period 11:00-12:45 UT (time when the TIDs and NREs were observed) near an altitude of 100 km. From 110 to 130 km the wind

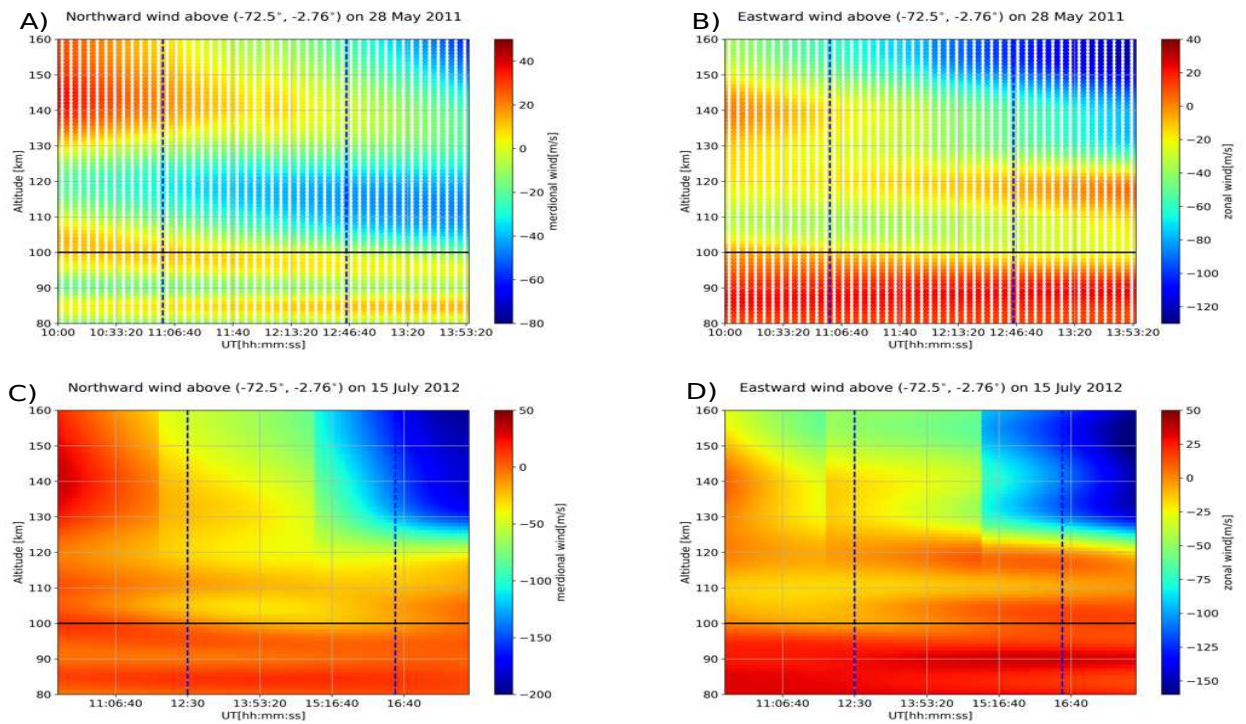


Figure 5.10: The meridional and zonal winds at altitudes between 80 and 160 km on 28 May 2011 (A and B) and on 15 July 2012 (C and D) $LT \approx UT + 2h$ at (-72.50° , -2.76°) geographic coordinates, as modeled by the HWM-14.

blew southward at ~ 60 m/s and between 130-160 km the wind was northward with a speed of ~ 15 m/s. Below an altitude of 100 km the wind was northward, but at 90 km it changed direction toward the south. In Figure 5.10 (B), on the same day and time, the zonal wind near 100 km constantly blew in the westward direction at a speed of ~ 40 m/s. Between 80 and 100 km, the zonal wind blew toward the east at a speed of ~ 25 m/s. Between 100 and 115 km, the wind was westward with a magnitude of ~ 60 m/s, it was ~ 5 m/s for 115-125 km, and for 125-160 km the zonal wind sped up from ~ 5 m/s to ~ 150 m/s.

Figure 5.10 (C) indicates that on 15 July 2012, between 12:30 and 16:30 UT, from 80 to 100 km altitude, the meridional wind was northward with a magnitude of ~ 50 m/s. At altitudes between 100 and 110 km, it turned southward with a magnitude of ~ 40 m/s. Above an altitude of 110 km, the wind blew southward exhibiting different magnitudes depending on the altitude and the time of the day. Figure 5.10 (C) shows that at altitudes between 80 and 95 km, the zonal wind blew eastward with a magnitude of ~ 50 m/s. The wind slowed down as it approached an altitude of 100 km and changed its direction westward at altitudes between 95 and 115 km before 14:00 UT, and then headed eastward again after 14:00 UT. At altitudes between 115 and 125 km, before 14:00 UT, the wind was eastward and turned westward after 14:00 UT. Beyond an altitude of 125

km, the wind headed westward with varying speeds, with a maximum speed of ~ 120 m/s between 15:00 and 16:30 UT at altitudes above 130 km. The neutral wind was generally smaller than the ion convection velocity (electric field). This is consistent with the comparison of the zonal neutral wind and zonal ion drift made by Richmond et al. (1992).

The neutral wind contributes to the development of instabilities in the F - and E -regions. The link with either TIDs or NREs is discussed in chapter 7, where the results are reviewed.

5.5.2 Summer events

Figure 5.11 (A) shows the meridional wind above Zhongshan (69.4° S, 82.6° E) on 22 November 2013 from 00:00 to 03:00 UT. The wind was mostly northward for altitudes between 80 and 160 km, but from 00:00 to 01:00 UT near 100 km the wind blew toward the south. The neutral wind blew in the same direction from 01:00 to 03:00 UT at an altitude between 120-160 km. Figure 5.11 (B) presents the zonal wind for the same location, day and time. Between 95 and 115 km, the wind was eastward with a magnitude of 50 m/s. Below 95 km and above 115 km, the wind was westward with varying magnitudes. Figure 5.11 (C) illustrates the meridional wind above

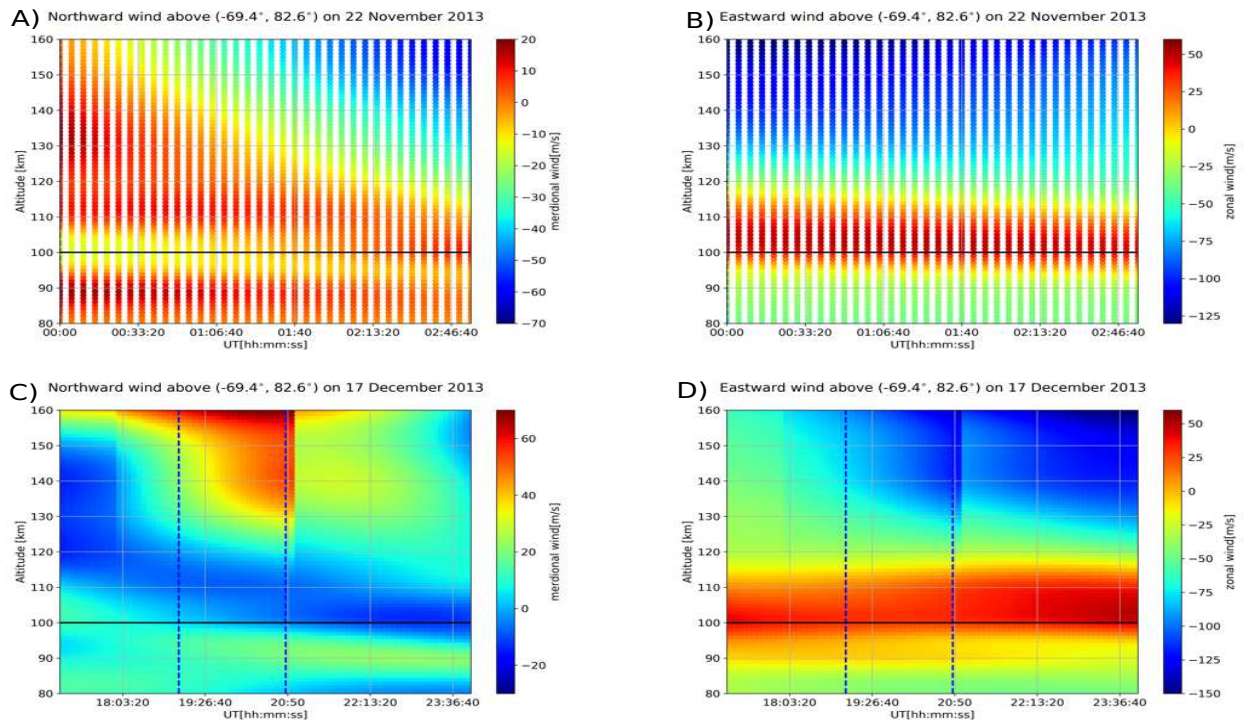


Figure 5.11: The meridional and zonal winds at altitudes between 80 and 160 km altitude on 22 November 2013 (A and B) and on 17 December 2013 (C and D), $LT \approx UT + 5h$ at $(-69.40^\circ, 82.60^\circ)$ geographic coordinates, as modeled by the HWM-14.

Zhongshan (69.4° S, 82.6° E) on 17 December 2013 between 19:00 and 20:48 UT. Below altitudes of 100 km, the wind blew northward, while above 100 km, the wind blew toward the west with varying magnitudes. Figure 5.11 (C) shows the zonal wind for the same location, day and time, where the wind at altitudes of between 95 and 115 km blew eastward at ~ 50 m/s, while for the remaining altitudes, the wind was westward with varying magnitudes. The maximum wind magnitude was ~ 130 m/s in the altitude range between 130 and 160 km after 19:30 UT.

5.6 Sporadic-*E* layers

Apart from the SuperDARN convection maps, and IRI-2016 and HWM-14 models, ionosonde measurements at Zhongshan show that there were *Es* layers during both the winter and summer events. These *Es* layers were reported to be associated with ionization resulting from precipitation particles and the ionization redistribution, caused by either the electric field or neutral winds (Rodger et al., 1983). Energetic proton and electron precipitation dominate in the magnetic pre-midnight and post-midnight, respectively. In addition, Heinselman et al. (1998) found that these layers were also linked to the neutralization of sodium ions. Zhang, Wu, Guo, Hu, Zhao and Xu (2015) suggested that geomagnetic activity may play a role in forming *Es* layers. Figure 5.12

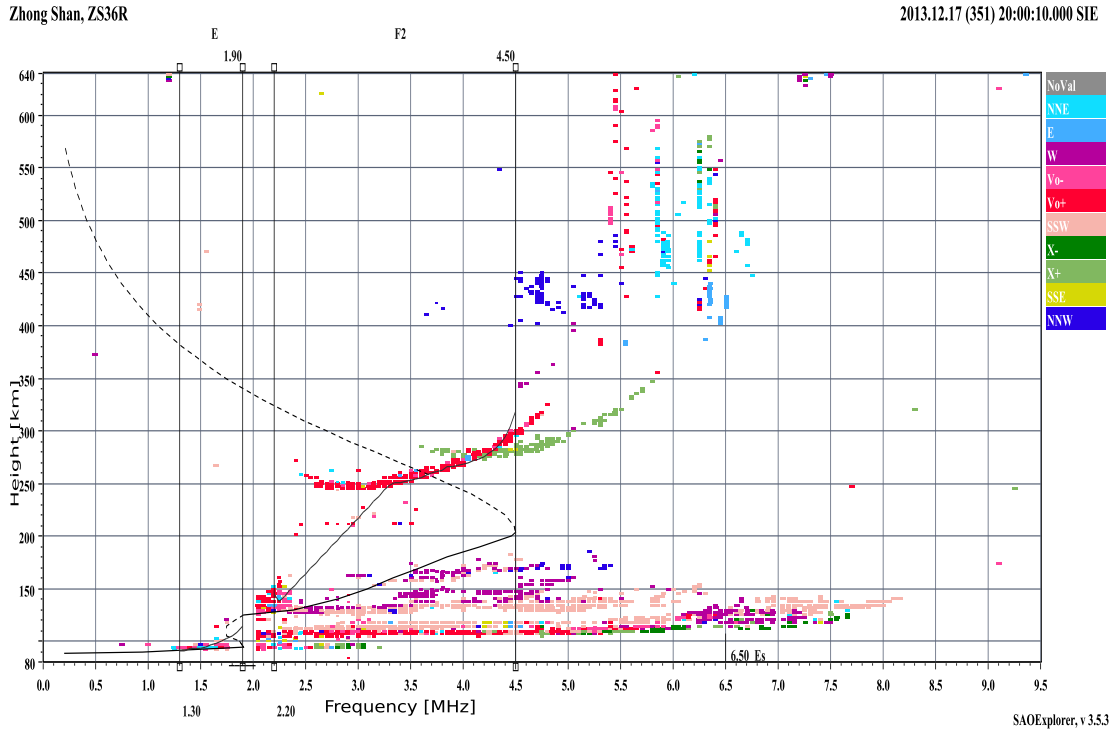


Figure 5.12: An ionogram showing an *Es*-layer at 6.50 MHz on 17 December 2013 at 20:00 UT

shows that there was an *Es*-layer at 6.50 MHz at an altitude of between 100 and 120 km. The *Es* layers were found under the ionospheric trough and cusp, i.e., in the FOV of the Zhongshan radar. They were reportedly to be associated with ionization resulting from the precipitating particles and the ionization redistribution caused by either the electric field or winds (Rodger et al., 1983). Energetic proton and electron precipitation dominate in the magnetic pre-midnight and post-midnight, respectively. Heinselman et al. (1998) found that these *Es* layers were instead linked with the neutralization of sodium ions. Zhang, Wu, Guo, Hu, Zhao and Xu (2015) demonstrated that geomagnetic activity might play a role in forming *Es* layers. Electron density irregularities and *Es* layers are responsible for the polarization electric field (Woodman et al., 1991; Huang et al., 1993; Otsuka et al., 2013). The electric field together with the plasma density gradient triggers the GDI, which is observed by radar through FAIs as type II waves (Liu and Yeh, 1966; Keskinen and Ossakow, 1983; Hamza and St-Maurice, 1993; Kelley et al., 1995; Sojka et al., 1998; Kagan and Kelley, 1998; Milan and Lester, 2001; St.-Maurice and Nishitani, 2020).

5.7 Electric field in the southern hemisphere

Using the Ogo 6 data, Heppner and Maynard (1987) and Heppner (1977) modeled the electric field of the high-latitude dawn-dusk cross-section. The representation of the electric field corresponded well with the electric field derived from the SuperDARN convection plasma. Here examples of the SuperDARN electric field are shown for a particular time. The best available time step (cadence) for these plots is normally 2 minutes. The *F*-region dynamo electric field is created by plasma convection and may be affected by energy (Joule heating)

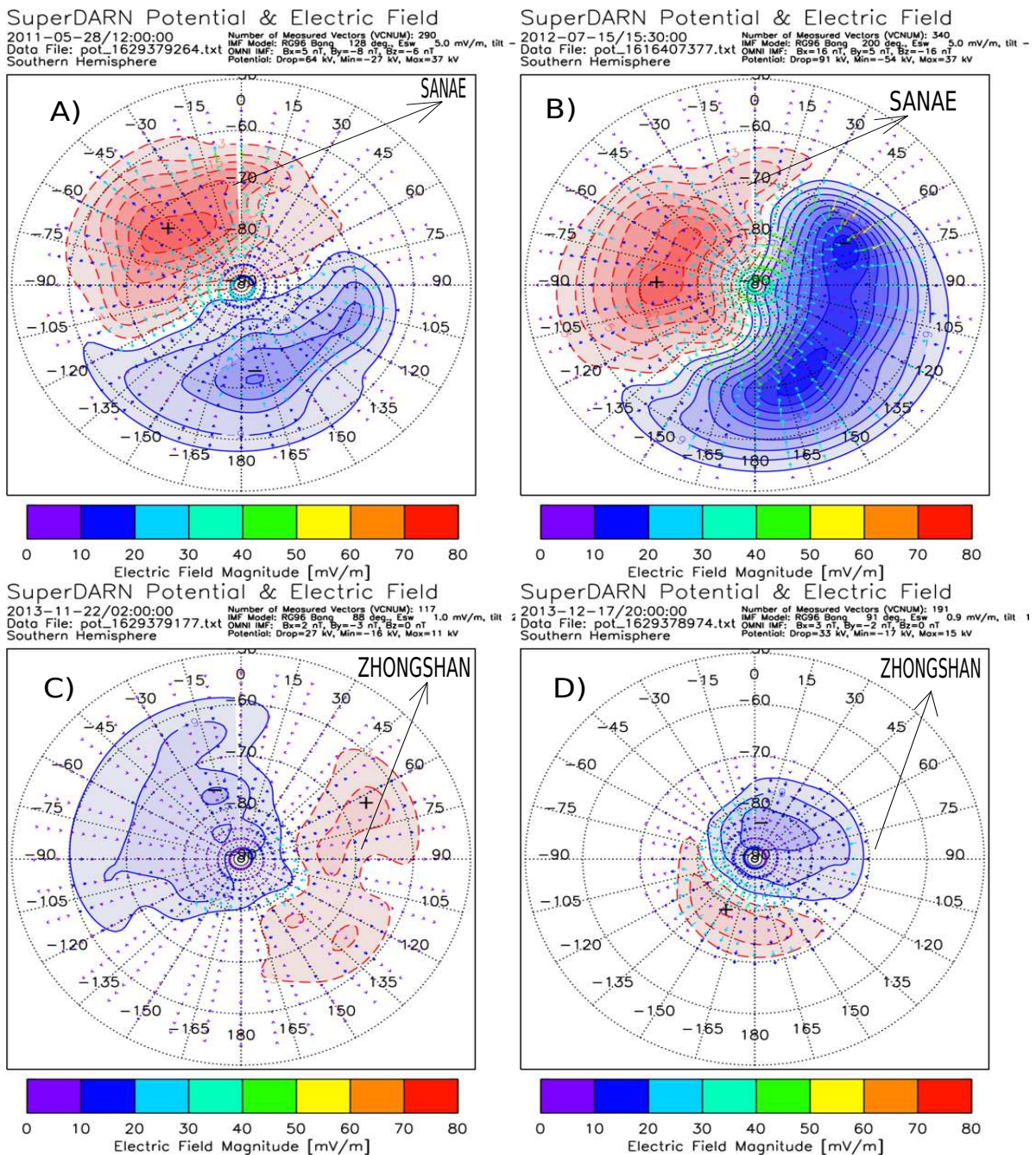


Figure 5.13: Electric field magnitudes derived from SuperDARN convection plasma velocity over the southern hemisphere on A) 28 May 2011 at 12:00 UT, B) 15 July 2012 at 15:30 UT, C) 22 November 2013, and D) 17 December 2013.

and momentum (from $\mathbf{J} \times \mathbf{B}$ where $\mathbf{J} = \sigma \mathbf{E}$) (Kelley, 2009). The product $\mathbf{J} \cdot \mathbf{E} < 0$ is valid in the neutral wind dynamo region, while at high latitudes the electric field is imposed on the ionosphere and $\mathbf{J} \cdot \mathbf{E} > 0$. At high latitudes, this *F*-region dynamo is poleward in the evening-to-midnight sector and switches the sign near midnight, pointing toward the equator post-midnight (Kelley, 2009). The ionospheric convection electric field is derived from a combination of all SuperDARN radars and is presented in this section. In areas where no SuperDARN backscatter is observed, the electric field was derived by means of the Ruohoniemi and Greenwald (1996) statistical model. This is the oldest model for estimation of the ionospheric electric field. There are newer and improved models. However, for all events the electric field data from an area rich in actual data were used. Thus, the electric field values will be close to the true values. Figure 5.13 presents the electric field

on (A) 28 May 2011 at 12:00 UT, (B) 15 July 2012 at 15:30 UT, (C) 22 November 2013 at 02:00 UT, and (D) on 17 December 2013 at 20:00 UT in geomagnetic coordinates called Altitude-Adjusted Corrected Geomagnetic Coordinates (AACGC) (Shepherd, 2014). For all four events the plots are chosen randomly from the times that TIDs and NREs occurred simultaneously. For a large part of the region of Figure 5.13 (A) the magnitude of the electric field between -120° and 15° longitude (clockwise) was 30-40 mV/m. From 15° to -120° longitude, the magnitude of the electric field was in the range of 0-20 mV/m. Note that some small regions had an electric field different from the ones mentioned above. For example, equatorward of -60° latitude, the magnitude of the electric field was below 20 mV/m, while at -90° latitude, between 105° and -45° longitude, the magnitude of the electric field was 20-30 mV/m. At the same latitude between -45° and 105° longitude, the magnitude of the electric field is 0-20 mV/m. Above the SANAE base (-66.64° , 48.51°) during the indicated date and time, the magnitude of the electric field was less than 20 mV/m at 12:00 UT. In Figure 5.13 (B), between latitudes $\sim -85^\circ$ and -90° , the magnitude of the electric field was 20-60 mV/m and reached 60-70 mV/m between 45° and 75° longitude near latitude -70° . Equatorward of -60° , from -150° to 100° longitude, the magnitude of the electric field was 0-20 mV/m; while from 100° to -150° longitude, the magnitude of the electric field was between 20 and 30 mV/m. Above SANAE, the magnitude of the electric field was between 10 and 20 mV/m at 15:30 UT.

Figure 5.13 (C) shows that in most regions, the magnitude of the electric field was 0-20 mV/m with a few exceptions. Between longitudes 45° and -135° and latitudes -70° and -85° , the magnitude of the electric field sometimes was between 30 and 40 mV/m. Above Zhongshan (-74.5° , 96.0°), the electric field was between 10 and 20 mV/m. Figure 5.13 (D) indicates that between longitude of 135° and 0° , and latitudes -70° and -85° , the magnitude of the electric field was a maximum of 30-40 mV/m, but sometimes it varied between 0-20 mV/m in this region. On the other hand, between latitudes 0° and 135° , the magnitude of the electric field was between 0 and 40 mV/m. On this day, above Zhongshan, the magnitude of the electric field was also between 10 and 20 mV/m.

An event which allows the comparison of the electric field and NREs backscatter power occurred on 22 November 2013. The electric field was obtained by averaging the SuperDARN map potential data from a selection of grid points closest to the observed NREs in time and position. Map potential data have a 2 min cadence with a 2° latitude and 1° longitude geomagnetic spatial resolution. Figure 5.14 demonstrates how the selection of the backscatter power and electric field was done. Panel (A) shows 4 gates (180-315 km range) of all 16 beams of the SANAE radar. Gate 0 for the 16 beams starts at 180 km, gate 1 at 225 km, gate 2 at 270 km, and gate 3 at 315 km. Panel (B) shows four locations, i.e., a(42.0° , -63.0°), b(44.0° , -63.0°), c(44.0° , -64.0°), and d(42.0° , -64.0°) magnetic coordinates, where the electric field was available. Geomagnetic coordinates of the backscatter echoes in each gate (see Figure 5.14 A) are given, together with the electric field coordinates of the 4 positions. The electric field and backscatter power of NREs are very important in this study, because the results are concerned with these two phenomena. The electric field at a, b, c, and d (Figure 5.14 B) is averaged and correlated with the mean backscatter power of gates 0, 1, 2, and 3. Gates 1 and 2 seem to show a better correlation than gates 0 and 3. The reason for this is by the fact that gates 0 and 3 across the radar mostly received echoes that are not in the averaged electric field of the selected locations. For example, 10 out of 16 beams for gate 3 and all 16 beams for gate 0 are not in the gray-highlighted area from which the electric field was taken (Figure 5.14 B). The figures of these correlations are available in chapter 7.

Figure 5.15 shows the backscatter power received by gates 0 (solid red line) and 1 (dash-dot blue line) of beam 7 of the Zhongshan radar on 22 November 2013, as well as the zonal (dotted black line) and meridional (dashed green line) components of the electric field at the location indicated by the geomagnetic coordinates. The time series of backscatter power of beams 0 and 1 seem to have a similar trend for this event. Other gates (2 and 3 not shown here) show the same backscatter trend for the event on 22 November 2013. The trend similarity was also confirmed by FFT (shown in chapter 6), indicating that echoes were generated by the same phenomenon. The southward magnitude of the electric field from 00:00 to 01:15 UT was decreasing, but it increased again after 01:15 UT with a peak of ~ 24 mV/m at 02:20 UT. The ion drag and Coriolis force cause large relative velocities in ions and neutrals that affect the dawn-dusk asymmetry. As a result, the electric field is also affected. A more detailed description of the relationship between the electric field and NRE power is given in chapter 7.

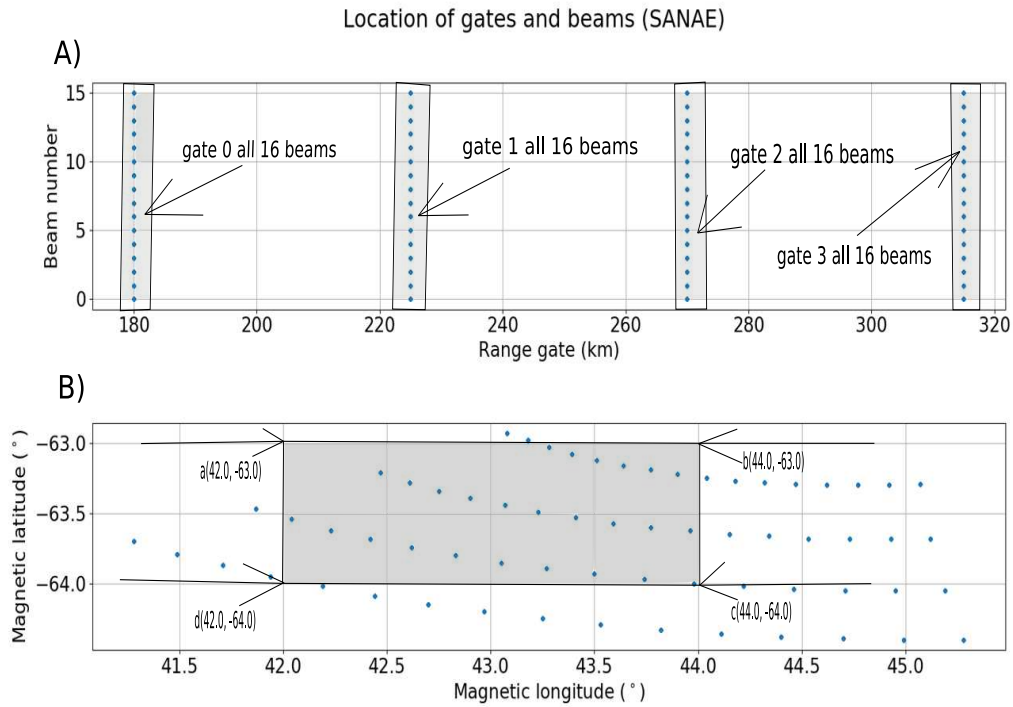


Figure 5.14: The first four gates of each beam of SANA E SuperDARN radar and their range gates (A) and a comparison of their magnetic coordinates with the electric field coordinates (B). The electric field and other parameters are found on the SuperDARN webpage (<http://vt.superdarn.org/tiki-index.php?page=ASCIIData>) where the magnetic coordinates are also provided.

5.8 Summary

In this chapter, four events of near-simultaneous occurrence of TIDs and NREs are shown. Their geomagnetic indices (AE, Dst, and Kp) are given. The outputs of both the IRI-2016 and HWM-14 models for those events were derived to determine the electron density in *E*- and *F*-regions and to estimate the gradient scale height at an altitude of 100 km altitude. Particle precipitation together with the plasma convection velocity were investigated to pinpoint potential sources of TIDs and GDIs. The *E_s* layer at the bottom-side of the *E*-region was observed for one of the four events. Finally, the electric field derived from the SuperDARN radar network, which helped to estimate the GDI scale height, was also discussed. The next chapter focuses on the analysis methods used in this study.

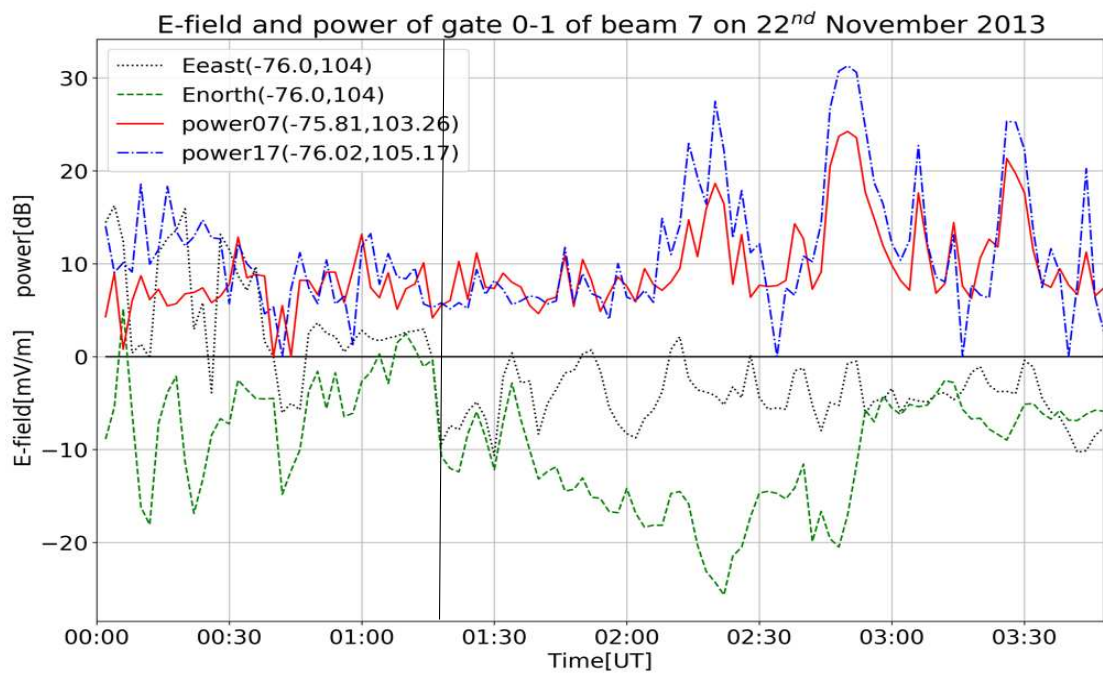


Figure 5.15: The northward (dashed green line) and eastward (dotted black line) electric field and the power of gate 0 (solid red line) and gate 1 (dash-dotted blue line) of beam 7 on 22 November 2013 from 00:00 to 03:48 UT.

Chapter 6

RELATIONSHIP BETWEEN MSTIDS AND NREs

6.1 Introduction

Several methods have been used to study the characteristics of waves such as TIDs. Miyoshi et al. (2018) used a global atmosphere-ionosphere coupled model, Vlasov et al. (2011) used the Lomb-Scargle periodogram approach, Bristow and Greenwald (1997) used a cross-spectral technique, with multiple signal classification (MUSIC), Dalin et al. (2004) used the photogrammetric technique, Liu et al. (2019) used the multichannel maximum entropy method (MMEM), Sun et al. (2015) used a normalized cross-correlation method, Grocott et al. (2013) used cross-spectral analysis with MMEM, etc. For this study, we chose cross-spectral analysis (He et al., 2004) to determine the characteristics of MSTIDs. TID parameters such as period, wavenumber, phase velocity, wavelength, and amplitude in the F -region ionosphere were estimated. This method requires different packages that are easily available in Python and are easy to understand. To determine the relationship between TIDs/AGWs and NREs, various methods were used, e.g. the Fast Fourier Transform (FFT) was used to derive the periodicity of the power spectrum. Cross-correlations between NREs and MSTIDs were estimated for a number of selected gates of different beams of the SANAE and Zhongshan radars. A statistical study of TIDs and NREs backscatter power was done.

6.1.1 Periods of TIDs and NREs

The FFT of the `scipy.fftpack` module of Python, which uses the discrete Fourier transform to convert a signal from its original time/space domain to the frequency domain, or vice versa, was used to calculate the periodicity of the data set. Figure 6.1 shows the FFT of the average power of the gate numbers 0-20 (i.e., NREs and TIDs) of beams 0 (A), beam 1 (B), beam 4 (C), and beam 7 (D) of the Zhongshan radar between 19:00 and 20:48 UT on 17 December 2013. The background noise limit was estimated by using the mean of the FFT power, and is shown by the dashed red line (He et al., 2004). The peaks that are above the mean power level and satisfy the characteristics of MSTIDs are 0.05 min^{-1} (20 min) and 0.02 min^{-1} (50 min) with respect to the dataset for 19:00 to 20:48 UT, on 17 December 2013 at Zhongshan.

Figure 6.2 shows the perturbation frequencies (f) (which can be converted into periods, $T = 1/f$) of gates 0-3 (i.e., NREs) and 4-20 (i.e., TIDs) of beams 0 and 1 of the Zhongshan radar for the period 19:00 - 20:48 UT on 17 December 2013. It also illustrates the stack plots of individual gates from the fifth (gate 4) to the twenty-first gate (gate 20) of beams 0 and 1. NREs and TIDs of beam 0 of the Zhongshan radar are compared in Figure 6.2 (A) and Figure 6.2 (C). Figure 6.2 (B) and Figure 6.2 (D) compare the NREs and TIDs received by beam 1 of the Zhongshan radar. These plots show that the periodicity of the NREs and TIDs are similar. The periods of MSTIDs were ~ 20 and ~ 50 minutes (vertical dashed lines). Other beams of the Zhongshan radar show the same periodicity for NREs and TIDs. Figure 6.3 shows that the periods of NREs and TIDs are the same as those in Figure 6.2 for beams 4 and 9 of the Zhongshan HF radar on 17 December 2013. The FFT which was used for Figure 6.2 was also used for the other three events, namely the events on 28 May 2011, 15 July 2012, and on 22 November 2013. Figure 6.4 shows that the periods of the NREs and MSTIDs were 16, 28, and 67 minutes on 28 May 2011, 18, 28, and 67 minutes on 15 July 2012, and 10, 15, 20, and 33 minutes on 22 November 2013. For purposes of this study, one period for each event was selected, namely 16, 28, 15, and 20 minutes on 28 May 2011, 15 July 2012, 22 November 2013, and 17 December 2013, respectively, based on the characteristics of the MSTIDs. These periods for MSTIDs are in the range of 15-60 minutes as suggested by Hunsucker (1982), Hocke et al. (1996) and He et al. (2004). These periods were also compared with the

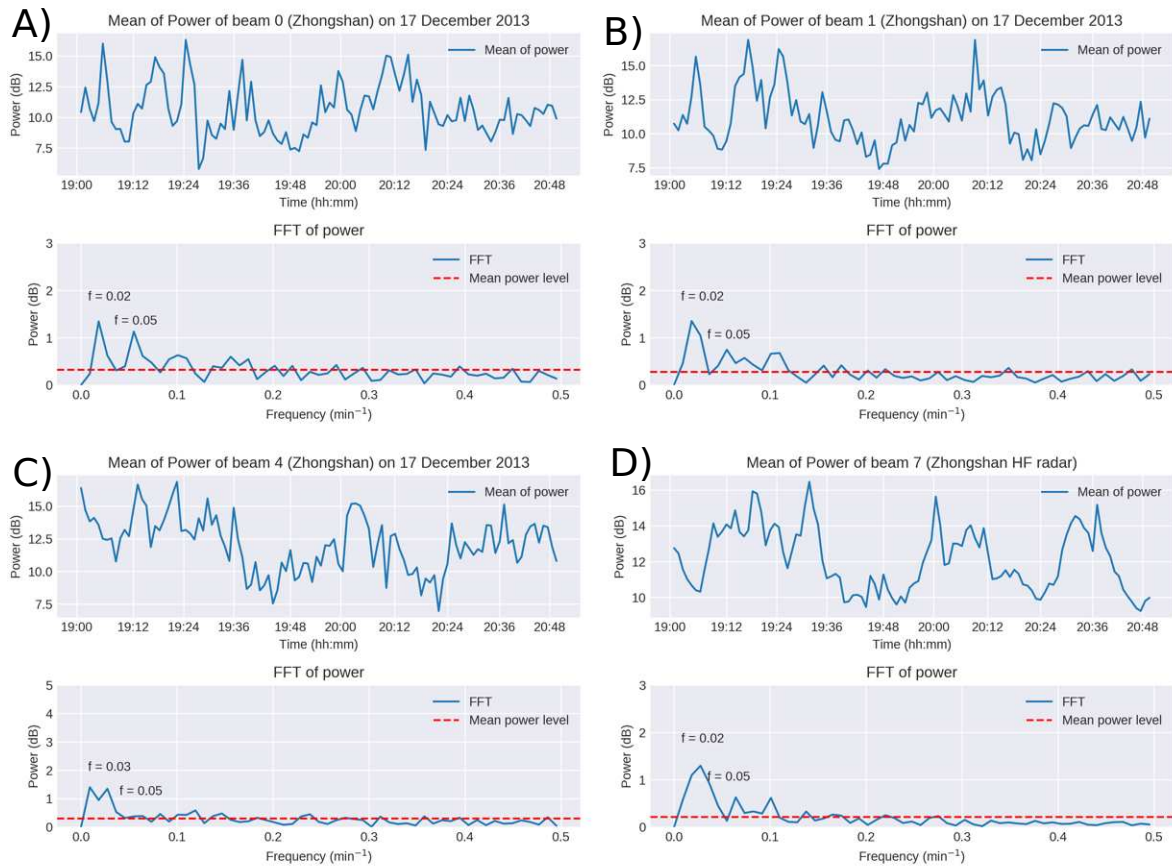


Figure 6.1: Average of power amplitudes (dB) calculated by the FFT for gate numbers 0-20 (i.e., NREs and TIDs) of beams 0 (A), 1 (B), 4 (C) and 7 (D). The horizontal dotted (red) line shows the mean power level of TIDs and NREs. The significant frequencies of MSTIDs are at 0.05 min^{-1} (20 min) and 0.02 min^{-1} (50 min) for the period 19:00 - 20:48 UT on 17 December 2013.

NREs and MSTIDs backscatter power time series (the time difference between two consecutive enhancements of backscatter power) and the selected periods were found to be qualify, i.e., having nearly the same periodicity or being of similar periodicity.

Other studies have compared NREs and TIDs/AGWs and found them to be related. Dalin et al. (2004) used radar observations and found that gravity waves and NLCs had a common period of 41 min, which they interpreted as the modulation periodicity of NLCs by the waves. Otsuka et al. (2007) compared the period of MSTIDs in 630-nm airglow images and quasi-periodic radar echoes (considered as NREs in this thesis) from the middle and upper atmosphere (MU) radar. Both phenomena shared a common period of ~ 70 min. Using the SuperDARN Hokkaido radar, all-sky imager, and GPS network, Ogawa et al. (2009) found that the *E*-region echoes and MSTIDs had the same period of ~ 60 min.

6.1.2 Wavenumbers of MSTIDs

To determine wavenumber, cross-spectral analysis (He et al., 2004; Grocott et al., 2013) was used. It includes correlation, the time lag, and the phase difference between three time series from different radar range gates and beams. These three series form a triangle, where the middle cell (of middle beam (He et al., 2004)) is the pivot point and is used twice per pair for each phase difference estimation. A multi-taper method (Mellors et al., 1998; Allen and Ottewill, 2000; Hariri Naghadeh and Keith Morley, 2017; Babadi and Brown, 2014; Atilaw et al., 2021) was used to calculate the power spectral density (PSD) of two (a pair) signals (i and j) received by two cells/gates $i(b,g)$ and $j(b,g)$, where b and g indicate beam and gate, respectively. The spectrum

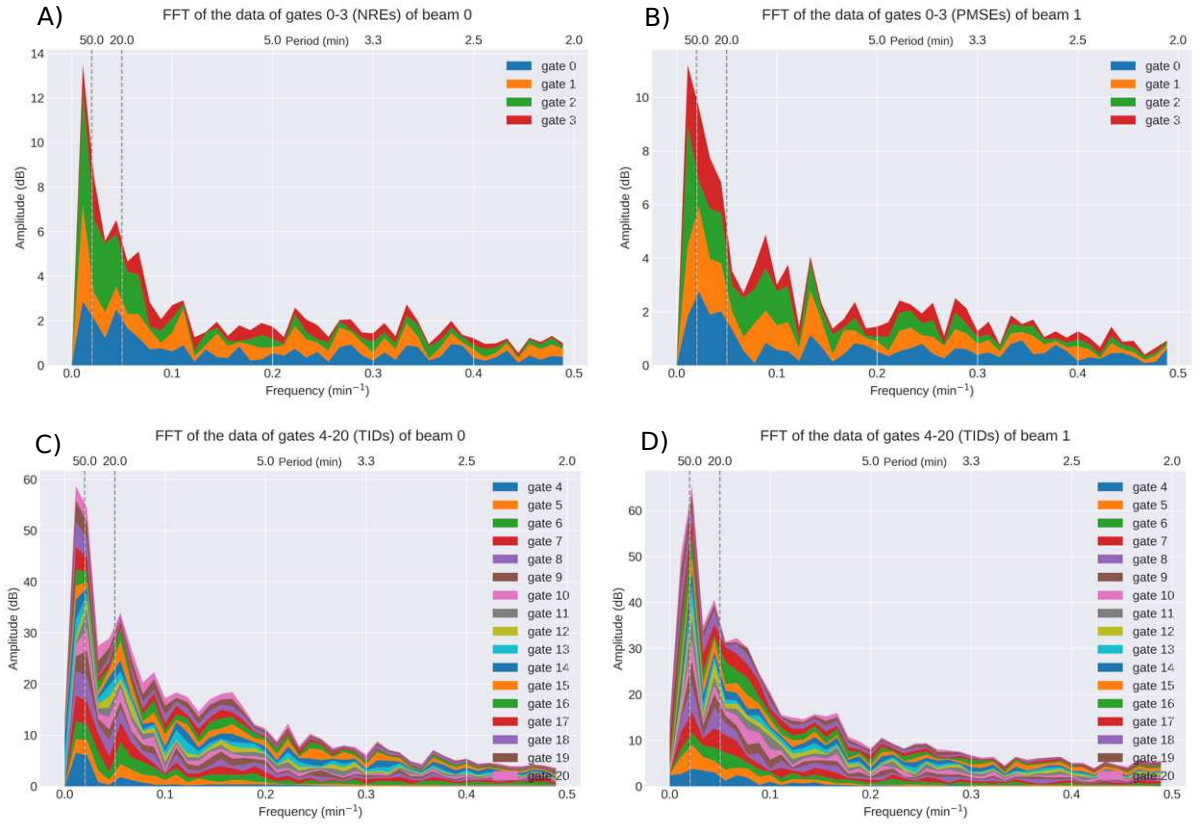


Figure 6.2: Stack plots of power amplitudes (dB) calculated by FFT for gates 0-3 (i.e., NREs) of beam 0 (A) and beam 1 (B) of the Zhongshan radar. Stack plots are also shown for gates 4-20 (i.e., TIDs) of beam 0 (C) and beam 1 (D) of the Zhongshan radar. The colors show the gates from 0-20. The vertical lines show periods of 20 and 50 minutes for the period between 19:00 - 20:48 UT on 17 December 2013.

(f) in the frequency domain (ω) is expressed by:

$$f_{ii}^k(\omega) = \left| \sum_{t=1}^N (t)g_k(t)e^{-i\omega t} \right|^2 \quad (6.1)$$

where N is the number of the data points, $t = 1, 2, \dots, N$, and $g_k(t)$ is the data taper for the k^{th} eigen-component and $e^{-i\omega t}$ is the Fourier transform (Babadi and Brown, 2014). The final multi-taper PSD (f^{mt}) is then expressed as:

$$f_{ii}^{mt}(\omega) = \frac{1}{k} \sum_{k=1}^k f_{ii}^k(\omega). \quad (6.2)$$

with $f_{ii}^k(\omega)$ being the set of k eigenspectra of i .

The Cross Spectra Density (CSD) is calculated by means of the real-valued PSD estimate of i ($f_{ii}^{mt}(\omega)$) and the complex conjugate of the PSD estimate of j ($f_{jj}^{mt}(\omega)$):

$$f_{ij}^{mt}(\omega) = \frac{1}{N} \sum_{n=1}^N f_{ii}^{mt}(\omega) f_{jj}^{mt}(\omega). \quad (6.3)$$

The coherence ($Coh_{ij}(\omega)$) indicates how well i corresponds to j at each frequency. Its values are between 0 and 1.

$$Coh_{ij}(\omega) = \frac{|f_{ij}^{mt}(\omega)|^2}{f_{ii}^{mt}(\omega) f_{jj}^{mt}(\omega)} \quad (6.4)$$

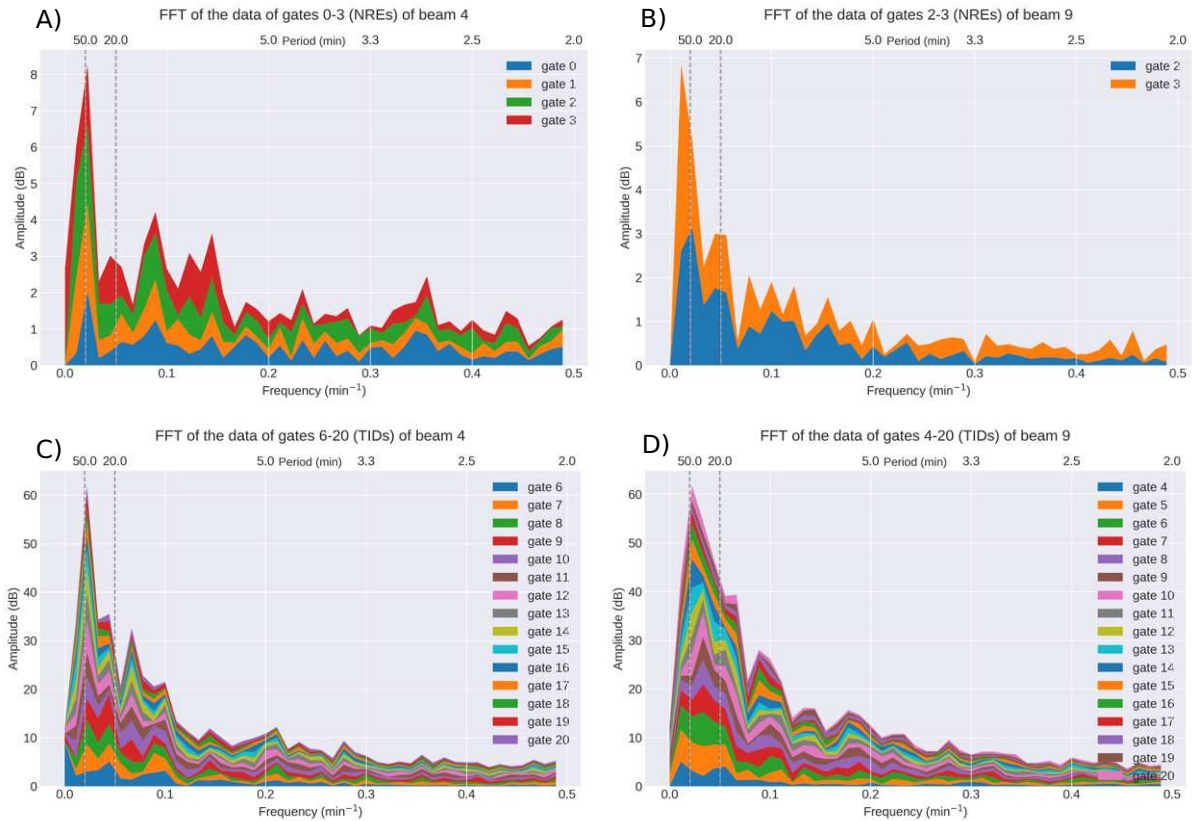


Figure 6.3: Stack plots of power amplitudes (dB) calculated by the FFT for gates 0-3 (i.e., NREs) of beam 4 (A) and beam 9 (B) of the Zhongshan radar. Stack plots are also shown for gates 4-20 (i.e., TIDs) of beam 4 (C) and beam 9 (D) of the Zhongshan radar. The colors show the gates from 0-20. The vertical lines show periods of 20 and 50 minutes for the period between 19:00 - 20:48 UT on 17 December 2013.

The phase spectrum $\phi_{ij}(\text{rad})$ is between $-\pi$ and π . It gives the phase difference at each frequency between i and j . It is derived by estimating an angle, using the imaginary and real parts of the CSD.

$$\phi_{ij}(\text{rad}) = \tan^{-1} \left[\frac{\text{img}(f_{ij}^m(\omega))}{\text{real}(f_{ij}^m(\omega))} \right] \quad (6.5)$$

Figure 6.5 shows examples of the above estimations: (A) the results of the power time series of i (6,8) gate 8 of beam 6 and j (7,6) gate 6 of beam 7 and (B) the results of the power time series i (8,8) gate 8 of beam 8 and j (7,6) gate 6 of beam 7 of the Zhongshan radar from 19:00 to 20:48 UT on 17 December 2013. From the top to bottom panels, the figure shows power received by three gates in dB: their CSD was ~ 25 ($10\log_{10}$) or ~ 25 dB, and their coherence (at 50 minutes) was ~ 0.48 and ~ 0.25 , (and at 20 minutes) was ~ 0.75 and ~ 0.48 for ((6,8) and (7,6)) and ((8,8) and (7,6)), respectively. Phase differences are shown on the bottom panels of the figure. For TIDs of 50 and 20 minutes, the phase difference between the power received by cell (7,6) and cell (6,8) is $\pi/4$ radians, and the phase difference between cell (7,6) and cell (8,8) is $\pi/2$ radians. The phase differences between selected cells was used to estimate the wavenumber of the TIDs, from which the phase velocity and wavelength of the TIDs were derived (He et al., 2004).

Figures 6.6, 6.7, and 6.8 show the same analysis as Figure 6.5 except for different data sets. Figure 6.6 shows that the phase difference between the backscatter power received by (3,47) and (5,45) cells of the SANAE radar on 28 May 2011 which is $3\pi/4$ at 15.9 min, and the phase difference between the backscatter power received by (7,47) and (5,45) is $-\pi/5$ at 15.9 min. Figure 6.7 shows that on 15 July 2012, the backscatter power received by gate 40 of beam 0 of the SANAE radar (0,40) and that received by gate 38 of beam 2 has a phase difference of $-\pi/5$ at 28.7 min. The same phase difference was established between the backscatter power of gate 40 of beam

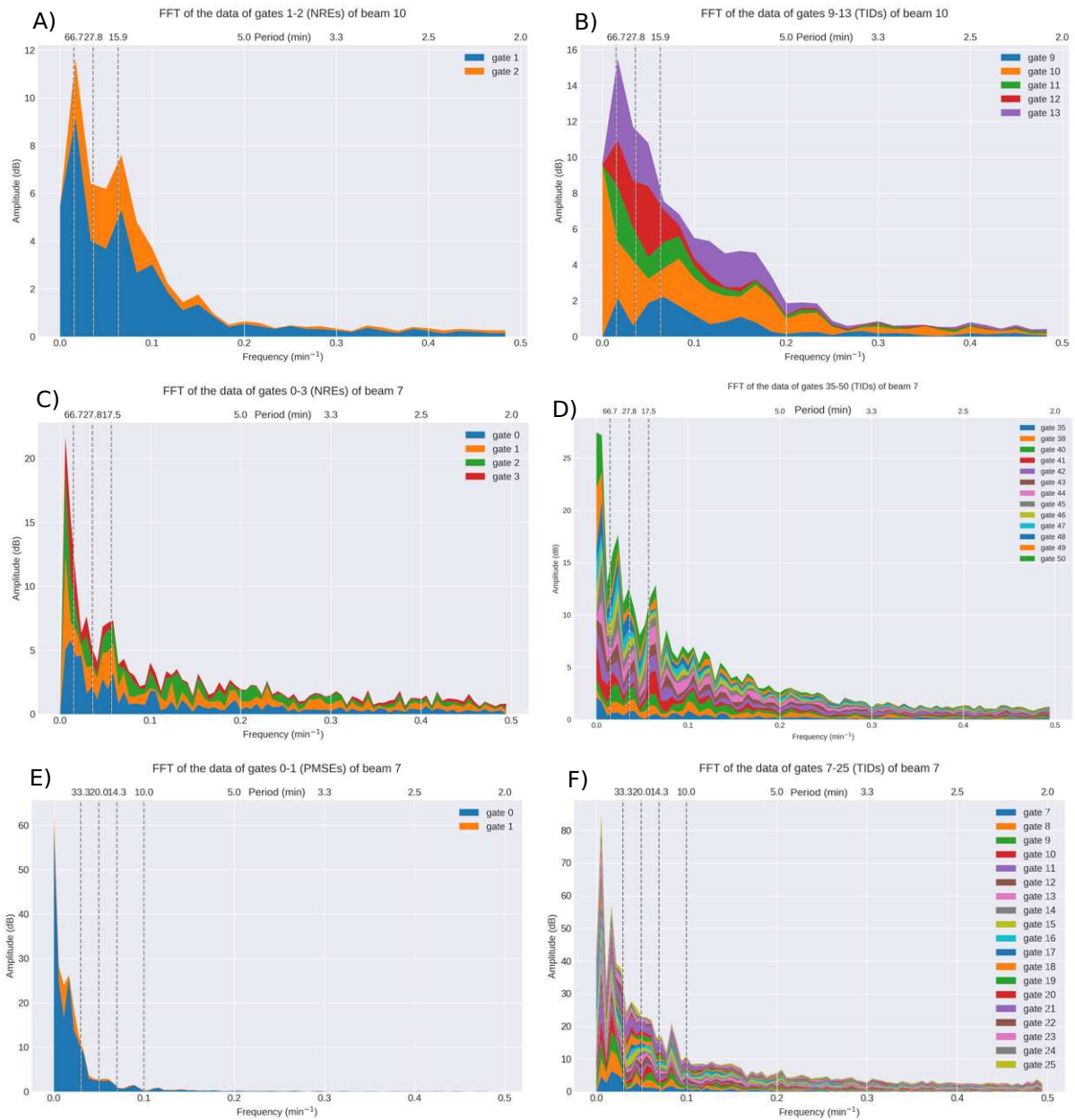


Figure 6.4: Stack plots of power amplitudes (dB) calculated by the FFT for NREs (A) and MSTIDs (B) of beam 10 of the SANA E HF radar on 28 May 2011 between 11:00 and 12:46 UT, for NREs (C) and MSTIDs (D) of beam 7 of the SANA E HF radar on 15 July 2012 between 12:30 and 16:30 UT, and for NREs (E) and MSTIDs (F) of beam 7 of the Zhongshan HF radar on 22 November 2013 for the period between 00:00 and 03:48 UT. The colors show the gates from 0-20. The vertical lines show periods 15.9, 27.8, and 66.7 minutes (A and B); 17.5, 27.8, and 66.7 minutes (C and D); and 10.0, 14.5, 20.0, and 30.3 minutes (E and F).

4 (4,40) and gate 38 of beam 2 (2,38) of the same radar. Figure 6.8 shows that the phase difference between the backscatter power received by gate 14 of beam 7 (7,14) and gate 12 of beam 9 (9,12) was $\pi/4$ at 14.5 minutes on 22 November 2013 for the Zhongshan radar. The same phase difference of $\pi/4$ was also found between the backscatter received by gate 14 of beam 11 (11,14) and gate 12 of beam 9 (9,12). Similar estimations were done to compute the dominant wavenumber for many other cells. These all produced consistent results.

After estimation of the phase difference between each of the two pairs in Figures 6.5-6.8, the wavenumbers, k_x and k_y were estimated by using equations (6.7) and (6.8). To calculate the distance from the center of one

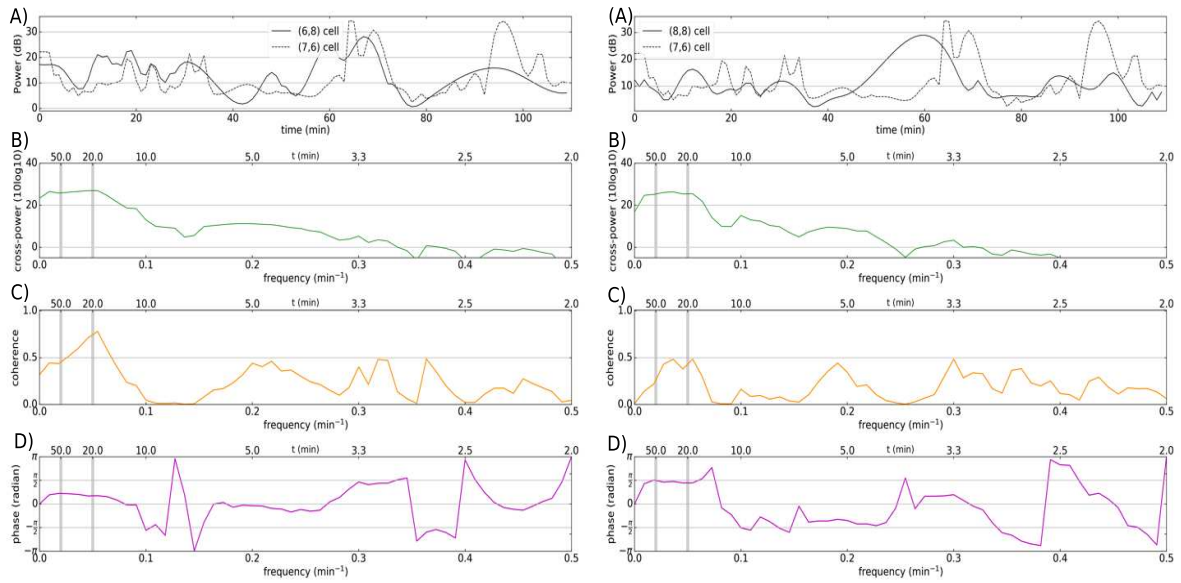


Figure 6.5: The analyses of two times series (6,8) and (7,6) (left panels) and another two time series (8,8) and (7,6) (right panels). The panels (A) show the time series of each pair, panels (B) show their CSD, panels (C) show their coherence and panels (D) show phase difference between 19:00 and 20:48 UT, on 17 December 2013 at Zhongshan.

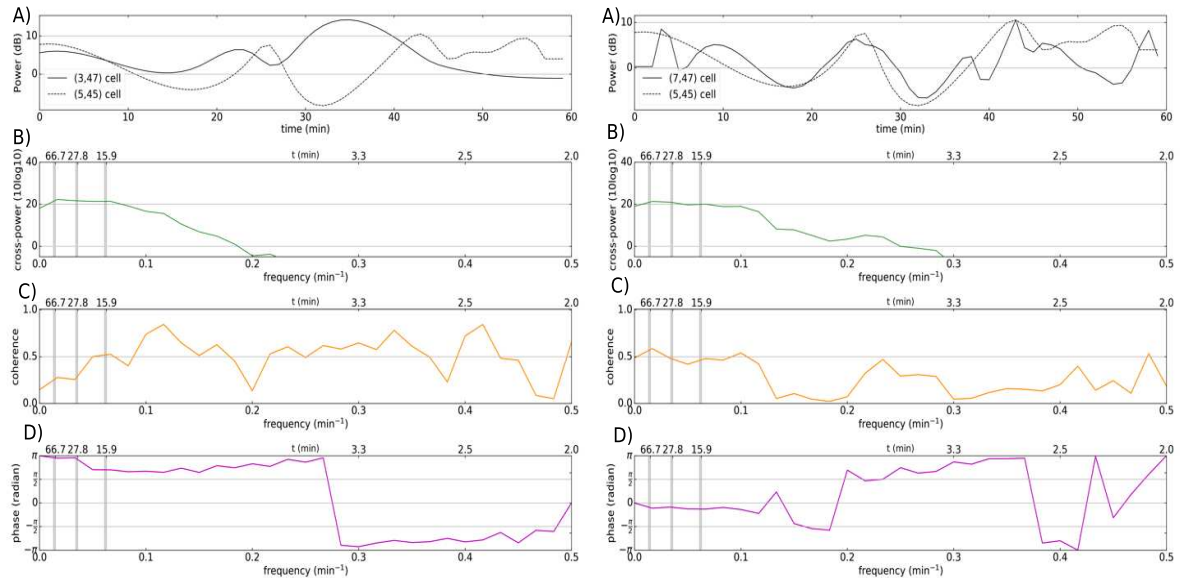


Figure 6.6: The analyses of two times series (3,47) and (5,45) (left panels) and another two time series (7,47) and (5,45) (right panels). The panels (A) show the time series of each pair, panels (B) show their CSD, panels (C) show their coherence and panels (D) show phase difference between 11:40 and 12:40 UT, on 28 May 2011 at SANA E.

cell to another, a spherical Earth projection was used, i.e., latitude, longitude and the Earth's radius (R_e). Figure 6.9 shows three cells of the Zhongshan HF radar (in red) numbered as c1, c2 and c3 adjacent black stars. The distance d between two geographic coordinates (latitudes (lat), longitudes (lon)) is given by the Haversine formula (Chopde and Nichat, 2013). The latitude variations were estimated such that $\Delta lat = lat2 - lat1$ and $\Delta lon = lon2 - lon1$ or $a = \sin^2((\Delta lat)/2) + \cos(lat1) \times \cos(lat2) \times \sin^2((\Delta lon)/2)$; let $c = 2 \times \text{atan}(\sqrt{a}, \sqrt{1-a})$,

$$d = R_e \times c. \quad (6.6)$$

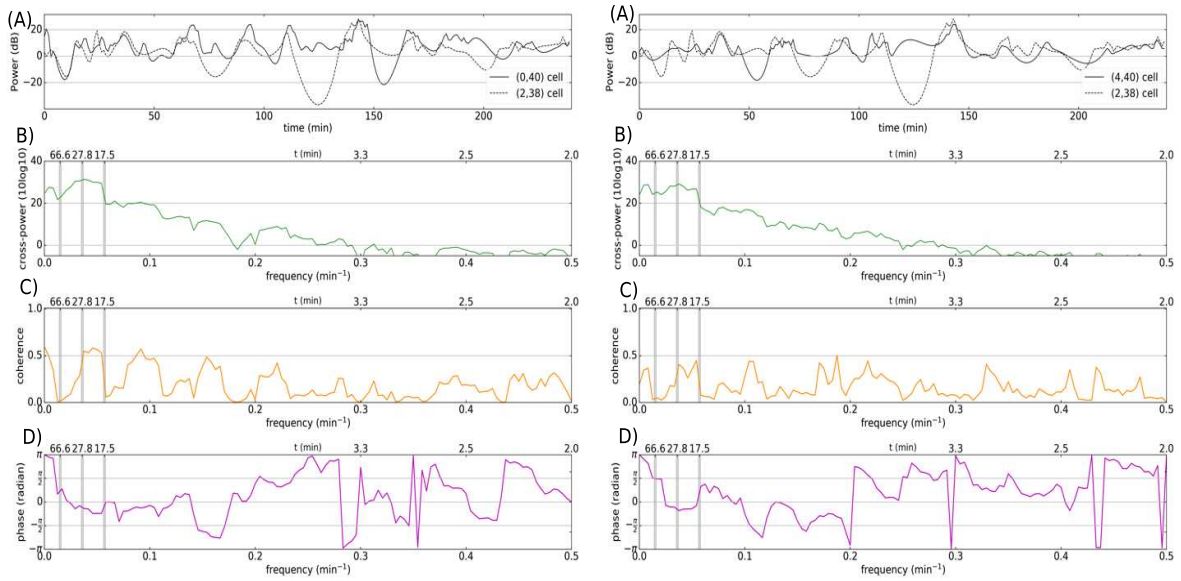


Figure 6.7: The analyses of two times series (0,40) and (2,38) (left panels) and another two time series (4,40) and (2,38) (right panels). The panels (A) show the time series of each pair, panels (B) show their CSD, panels (C) show their coherence and panels (D) show phase difference between 12:30 and 16:30 UT, on 15 July 2012 at SANAÉ.

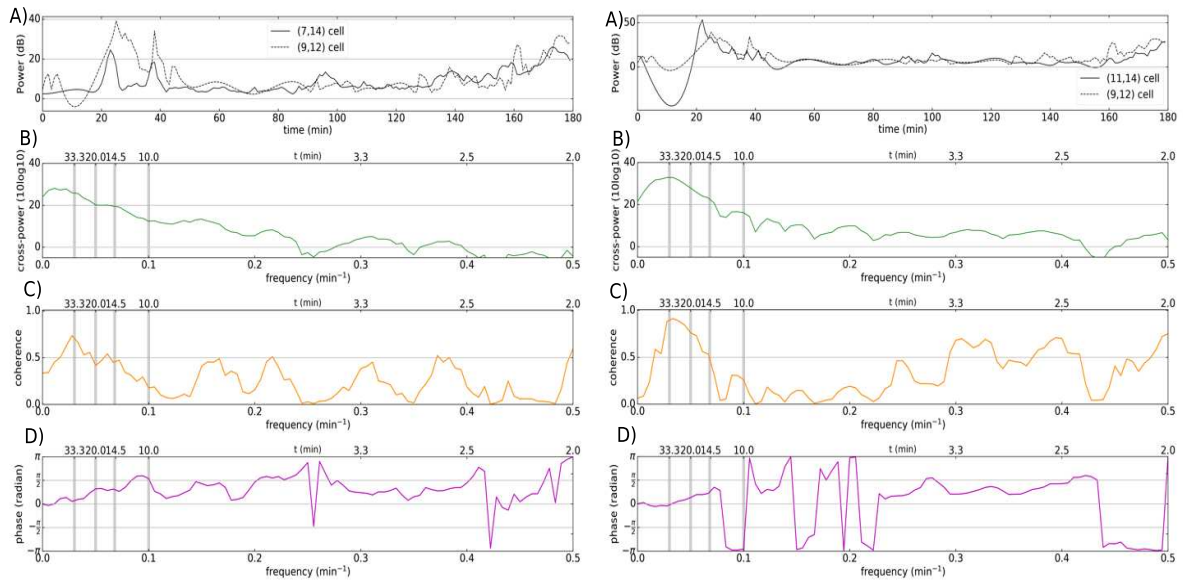


Figure 6.8: Phase differences of two times series (7,14) and (9,12) (left panels) and another two time series (11,14) and (9,12) (right panels). The panels (A) show the time series of each pair, panels (B) show their CSD, panels (C) show their coherence and panels (D) show phase difference between 00:00 and 03:00 UT, on 22 November 2013 at Zhongshan.

Projecting the distance between each pair of cells, wavenumbers k_x and k_y were estimated as follows:

$$k_x = \frac{\Delta\phi_x}{d1} \quad (6.7)$$

and

$$k_y = \frac{\Delta\phi_y}{d2}. \quad (6.8)$$

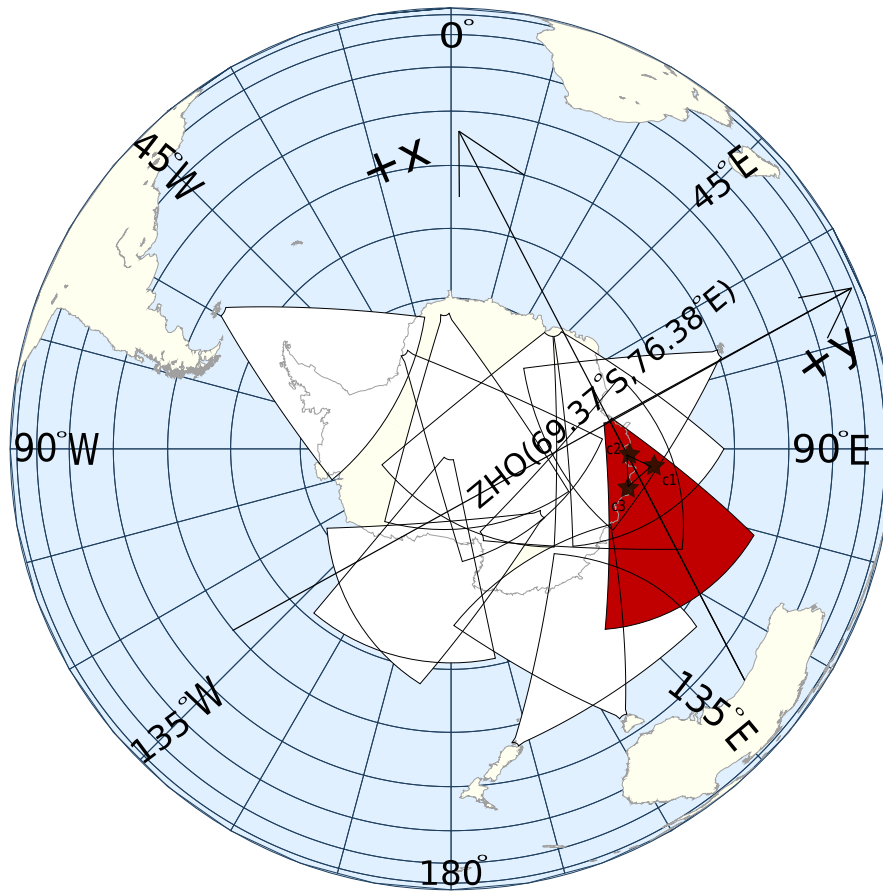


Figure 6.9: The three cells combination of the Zhongshan HF radar used for cross-spectral analysis. The boresight beam (beam 7) points nearly to the -x direction and perpendicular to y axis.

Here $d1$ and $d2$ are the distances from the center of the pivot cell $c2(7,6)$ and the centers of the other two cells, i.e., $c1(6,8)$ and $c3(8,8)$ in Figure 6.5. This set of three cells forms a triangle structure on the field of view of the radar (He et al., 2004; Grocott et al., 2013). In order to find the appropriate wavenumbers, the same calculations were done for different locations, i.e., using different 3-cell combinations, as in Figures 6.5-6.9. This calculation was then repeated for the whole FOV of each radar, taking into consideration the properties of MSTIDs and the distance separating the two cells of each pair, i.e., the pivot cell and the other two adjacent cells. Gates 4-20 which receive the backscatter from TIDs were used in three gate combinations of all 16 beams [i.e., $(b \pm 2, g \pm 2)$, $(b \pm 1, g \pm 2)$, $(b \pm 2, g \pm 4)$]. Using wavevector analysis and spatial sampling, the values of $|k_x| < 70 \times 10^{-6} \text{ m}^{-1}$ and $|k_y| < 56 \times 10^{-6} \text{ m}^{-1}$ were used to exclude aliasing the wavenumber for MSTIDs. The wavenumber per meter k is given by:

$$k = \sqrt{k_x^2 + k_y^2} \quad (6.9)$$

where k_x and k_y are its components along x and y directions, respectively, where -x is the boresight direction of the radar and y defines an orthogonal plane (see Figure 6.9). The azimuthal angle propagation direction of the MSTIDs is given by:

$$Az = \tan^{-1}\left(\frac{k_y}{k_x}\right) \quad (6.10)$$

in degrees relative to the x-y axes. This angle is converted to the geographic azimuth angle based on the boresight azimuth angle of each radar provided on the SuperDARN webpage. The phase velocity v is:

$$v = \frac{\omega}{k} \quad (6.11)$$

where $\omega = \frac{2\pi}{T}$ and T is the period in seconds. The wavelength λ is given by:

$$\lambda = \frac{2\pi}{k}. \quad (6.12)$$

Assuming that the wave propagated in one dimension, then:

$$f(x, t) = A \cos(\omega t + \phi) \quad (6.13)$$

where ϕ is the initial phase. A is the maximum amplitude in meters, while ω is the angular frequency in rad/s. This formula is derived from the equation of motion (EOM) $f(x,t)$ for wave propagation, where x is the displacement and t is time taken. The first derivative of this displacement function $f(x,t)$ with respect to time gives the phase velocity:

$$v(x, t) = -A\omega \sin(\omega t + \phi). \quad (6.14)$$

Hence, the magnitude of the wave amplitude is given by:

$$|A| = \frac{v(x, t)}{\omega \sin(\omega t + \phi)} \quad (6.15)$$

which gives equation (6.16) for $\sin(\omega t + \phi) = 1$.

$$A = \frac{v}{\omega}. \quad (6.16)$$

The values obtained by means of the above formulae are presented in subsection 6.1.3.

6.1.3 Characteristics of MSTID

MSTIDs parameters in the F -region ionosphere derived from the HF radar data are shown in Table 6.1. The period, x-component of wavenumber, y-component of wavenumber, phase velocity, the propagation azimuth angle, wavelength, and amplitude are presented for three cases. The fourth case did not have sufficient data sets to estimate the TID parameters estimation. The processes and equations presented in subsection 6.1.2 were used to estimate these parameters. On 15 July 2012, these parameters were 28 min, $11.2 \times 10^{-6} \text{ m}^{-1}$, $4.9 \times 10^{-6} \text{ m}^{-1}$, 308 m/s, 197° , 514 km, and 82 km, respectively. On 22 November 2013, those parameters were 15 min, $8.6 \times 10^{-6} \text{ m}^{-1}$, $14.4 \times 10^{-6} \text{ m}^{-1}$, 431 m/s, 222° , 375 km, and 60 km, respectively. On 17 December 2013, these parameters were 20 min, $11.3 \times 10^{-6} \text{ m}^{-1}$, $11.3 \times 10^{-6} \text{ m}^{-1}$, 328 m/s, 298° , 393 km, and 63 km, respectively.

Periods, wavenumbers, velocities, azimuth, wavelengths, and amplitudes of MSTIDs			
Parameters	15 Jul 2012	22 Nov 2013	17 Dec 2013
T (min)	28	15	20
k_x (/m)	11.2×10^{-6}	8.6×10^{-6}	11.3×10^{-6}
k_y (/m)	4.9×10^{-6}	14.4×10^{-6}	11.3×10^{-6}
v (m/s)	308	431	328
Az ($^\circ$)	197	222	298
λ (km)	514	375	393
A (km)	82	60	63

Table 6.1: MSTID parameters estimated on 15 July 2012 for the period from 11:30 to 17:30 UT, 22 November 2013 for the period from 00:00 to 03:48 UT and on 17 December 2013 for the period from 19:00 to 20:48 UT for the F region.

Apart from the TIDs amplitude of 63 km on 17 December 2013, the ionosonde data show the altitude modulation of the E_s layer. The NREs in this study are caused by the GDI, which is driven primarily by the ionospheric convection electric field in the presence of plasma density gradients (e.g. E_s layers). The existence of an E_s layer for the three events was also investigated, but there was data for only one event. Table 6.2 shows that for the event on 17 December 2013, the virtual height ($h'E_s$) of the E_s layer was modulated at an altitude of between 95 and 117 km. This shows that there is a relationship between the ionospheric electric field, as determined by the SuperDARN network of radars and the backscatter power of NREs. This provides

Time in UT	Frequency (f_oE_s) in MHz	Virtual height ($h'E_s$) in km
16:00:10	—	—
17:00:10	—	—
18:00:10	3.70	105.0
19:00:11	4.95	95.0
20:00:10	6.50	107.5
21:00:10	2.40	102.5
22:00:11	4.35	117.5
23:00:11	—	—

Table 6.2: Frequency and virtual height derived from the Zhongshan ionosonde data on 17 December 2013

the vital clue that GDI, which relies on the velocity difference between plasma ions and the slowly varying neutral wind, is a plausible mechanism for modulation of SuperDARN NREs by TIDs.

6.2 Cross-correlation between NREs (N) and TIDs (T)

The cross-correlation (CC) between two time series, e.g. NRE and TID powers, received by two different gates measures their similarities as a function of time from one to the other and gives the time lag between them. The coefficient of CC is the normalized correlation, either positive or negative, and it gives information on how the two series are related (Davis and Da Rosa, 1969; Penney and Jackson-Booth, 2015). A negative coefficient indicates that as one series increases, the other decreases, i.e., the two series are out of phase. A positive coefficient indicates that both series increase or decrease simultaneously, i.e., the two series are in phase. The maxima of the CC, i.e., -1 and 1, shows that knowing the values of one series allows a perfect prediction of the other.

Figure 6.10 shows the event on 15 July 2012 with cross-correlation between gate 0 (180 km, NREs) and gates 10-15 (630-840 km, TIDs) of beam 7. The cross-correlations on Figure 6.10 are color-coded. The time lag is defined as the product of the lag between the two phenomena and the sampling time interval (1 minutes in this case) between the data points. It defines the duration by which one series leads or lags the other. This means the time it takes for one series of a given phenomenon to affect the other can be negative or positive, depending on whether the second series lags the first or the first one lags the second, respectively. This is important, because TIDs propagate and there is a significant spatial offset between the NREs and TIDs observed by the same radar, resulting in a temporal lag. The CC between the power of gate 0 and gate 10 of beam 7 (i.e., ((7,0) and (7,10)[N-T])) of the SANA radar between 12:30 and 16:30 UT on 12 July 2012, shown by the red line on Figure 6.10 (A), is ~ 0.51 . The green line shows that the peak CC between gate 0 and gate 11 of beam 7 (i.e., ((7,0) and (7,11)[N-T])) is ~ 0.68 . N refers to the NREs and T to the TIDs. The blue line shows that the peak CC between gate 0 and gate 12 ((7,0) and (7,12)[N-T]) is ~ 0.50 . The black line in the figure shows the CC between gates 0 and 13 of beam 7 ((7,0) and (7,13)[N-T]), and peaks at ~ 0.82 . The yellow line, representing the CC between gates 0 and 14 of beam 7 ((7,0) and (7,14)[N-T]), peaks at ~ 0.82 , and lastly, the CC between gates 0 and 15 of beam 7 ((7,0) and (7,15)[N-T]), shown by the orange line, peaks at ~ 0.45 . The time lag between the TIDs and NREs is between ~ 17 and 25 min.

For 22 November 2013, the CC for beam 1 and range gate 0 (180 km, NREs) against beam 1 and range gates 13-18 (765-990 km, TIDs) of the Zhongshan radar was estimated. The correlation coefficient peaks at 0.75 with a time lag of ~ 25 minutes (Figure 6.10 (B)). The CC between the power of gate 0 and gate 13 of beam 1 of the Zhongshan radar between 00:00 and 03:48 UT on 22 November 2013, i.e., ((1,0) and (1,13)[N-T]) shown by the red line on Figure 6.10 (B), peaks at ~ 0.72 . The green line shows that the CC between gate 0 and gate 14 of beam 1 ((1,0) and (1,14)[N-T]), peaks at ~ 0.75 and is shown by the green line. The blue line shows that the CC between the gate 0 and gate 15 ((1,0) and (1,15)[N-T]), peaks at ~ 0.68 . The black line shows the CC between gates 0 and 16 of beam 1 ((1,0) and (1,16)[N-T]), peaks at ~ 0.63 . The following line is yellow, representing the

Periods, horizontal phase velocities, and wavelengths of TIDs/AGWs			
Done by	Periods (min)	Phase velocities (m/s)	Wavelengths (km)
Vlasov et al. (2011)	24-48	250	100-600
Bristow and Greenwald (1997)	30-55	61-230	160-570
Dalin et al. (2004)	41 or 108	7-10	40
Liu et al. (2019)	20-70	< 180	a few hundreds
Frissell et al. (2014)	23-60	50-250	100-500
Grocott et al. (2013)	30-80	100-300	200-800
Hayashi et al. (2010)	30 or 45	600-850	788-847
He et al. (2004)	20-60	100-300	400-600
Hocke et al. (1996)	60-150	387-956	340-601
Ishida et al. (2008)	20-50	40-400	a few hundreds
Ogawa et al. (2009)	30-60	120-170	200-600
Oinats et al. (2016)	20-120	30-180	300-800
Samson et al. (1990)	30-40	113-302	298-509
Suzuki et al. (2009)	~ 60	100	~ 300
Galushko et al. (1998)	10-130	165-550	216-240
Tsugawa et al. (2004)	40-180	200-800	1410-3696
Hall et al. (1999)	~ 60	65-280	200

Table 6.3: Earlier studies on the parameters of TIDs/AGWs.

CC between gates 0 and 17 of beam 1 ((1,0) and (1,17)[N-T]), which peaks at ~ 0.59 , and lastly, the CC between gates 0 and 18 of beam 1 ((1,0) and (1,18)[N-T]), shown by the orange line, peaks ~ 0.35 . The time lag between the TIDs and NREs is ~ 23 min. The time lag on the abscissa, shown in Figure 6.10 (A), shows how far the two series are offset in time. The value of the lag with the highest correlation coefficient is considered when deciding the best fit between the two series.

Figure 6.11 (A) and Figure 6.11 (B) show the CC between NREs and TIDs for beams 7, 8, 10, and 12 for 28 May 2011 and beams 0-15 of the SANA radar for 15 July 2012, respectively. In this figure, only the CC values are shown, and the lag-time is not included. On the abscissa, beam (bb), near gate (ng), and far gate (fg) were correlated. For example, a bb.ng.fg of 07.01.14 shows the CC between gate 1 (NRE) and gate 14 (TID) of beam 7 on the horizontal axis. There are many positive correlations with a magnitude of >0.5 , and very few which are negative. The CC estimated for all beams (0-15) of the SANA radar on 15 July 2012 are presented in Figure 6.11 (B). Most of the CCs shown have a magnitude of >0.5 and <-0.5 . Figure 6.12 (A) and Figure 6.12 (B) show the values of CCs between NREs and TIDs for 22 November 2013 and 17 December 2013, respectively,

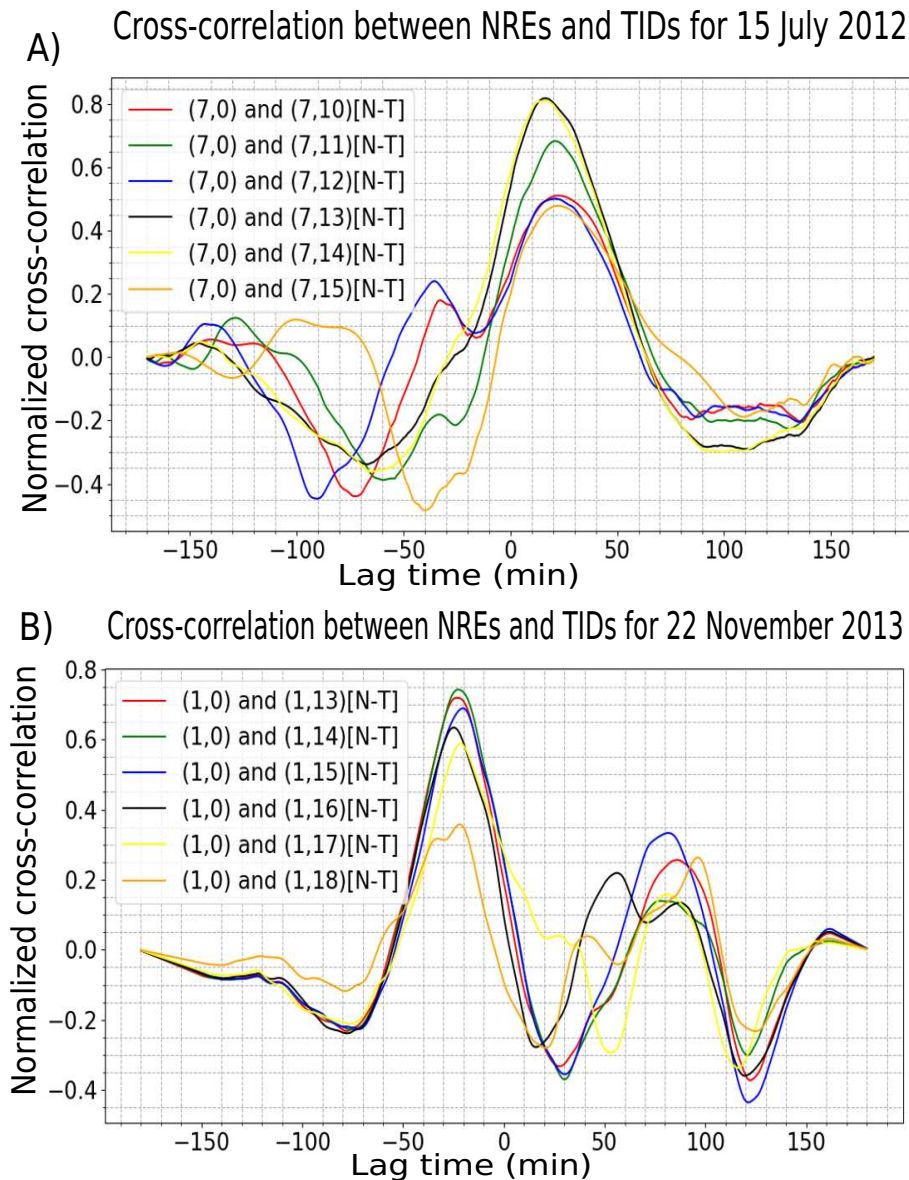


Figure 6.10: Cross-correlation between the power received by gate 0 (NREs) and gates 10-15 (TIDs) of beam 7 (A) of the SANA radar for the time period 12:30 - 16:30 UT on 15 July 2012; and gate 0 (NREs) and gates 13-18 (TIDs) of beam 1 (B) of the Zhongshan radar for the time period 00:00 - 03:48 UT on 22 November 2013.

using the data from the Zhongshan radar. Figure 6.12 (A) illustrates that most of CC values are positive with a magnitude > 0.5 . For beam 8, some of the CC values are > 0.8 . There are a few other CC values that are negative. For 17 December 2013, most of the CC values are positive with a magnitude of > 0.5 , and a significant number of other values are negative with a magnitude of < -0.5 . For the events under investigation, sometimes the TIDs led the NREs and at other times the NREs led the TIDs. The reason may be found in the selection of the gates. Note that apart from ionospheric motion, TIDs have phase and group velocities which may cause the CC to vary according to the gates. Another possible reason for this may be found in the troughs and crests of TIDs. The CC between TIDs and NREs may indicate that when the power of TIDs increase/decrease, the modulated polarization electric field causes the power of the NREs to increase/decrease or the opposite.

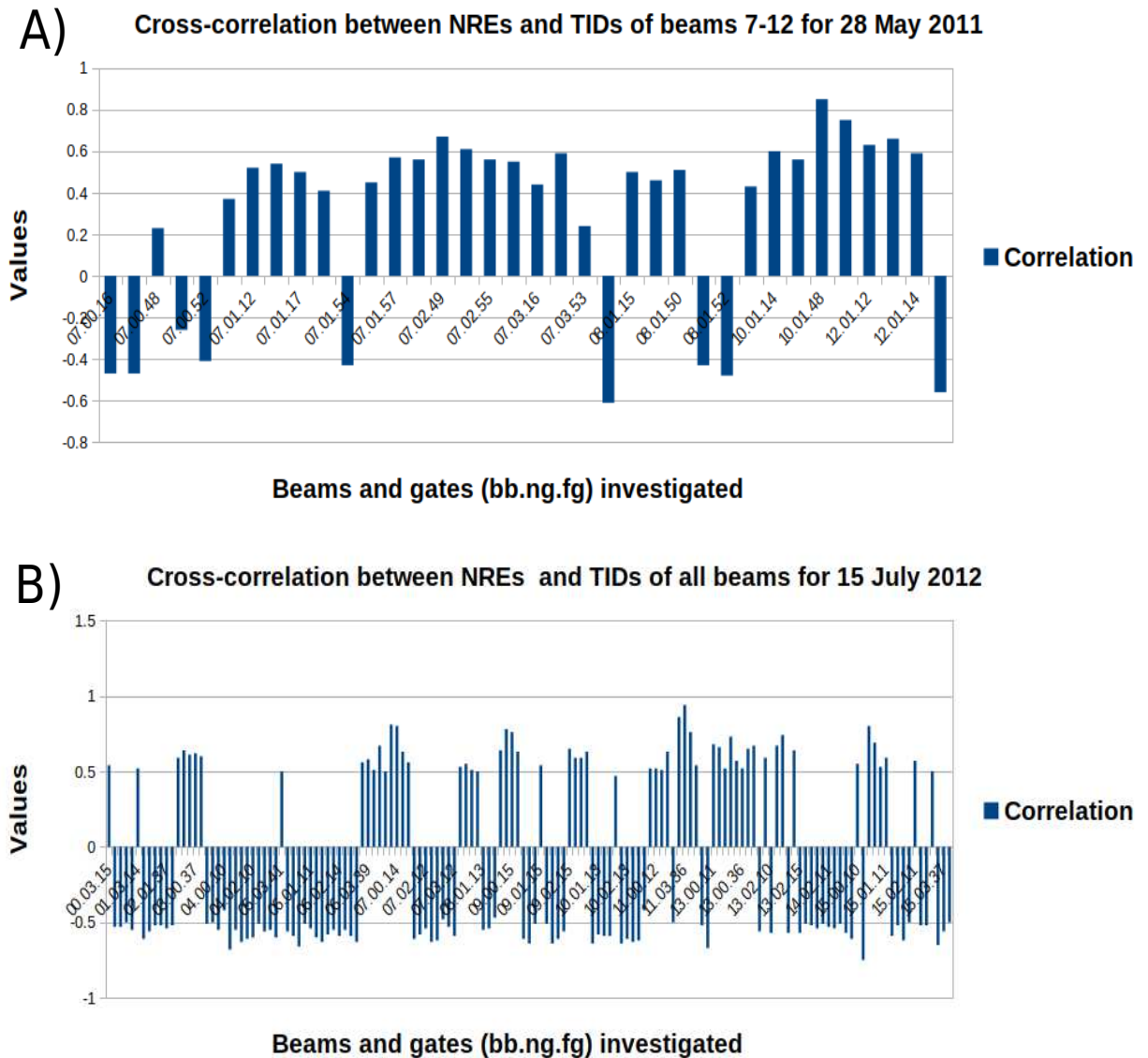


Figure 6.11: Cross-correlation between the power of gates 0-3 (NREs) of different beams with various gates (TIDs) of the SANA radar for 28 May 2011 for the time period 11:00 - 12:46 UT (A) and for 15 July 2012 from 12:30 to 16:30 UT (B).

6.3 Spearman Correlation Coefficients of NREs and TIDs

The Spearman rank correlation coefficient (SCC) was used to find the measure of by TIDs contribution to the backscatter due to the NREs (Zou et al., 2003; Wilks, 2011; Rauf et al., 2019). The Spearman rank correlation coefficient takes into consideration the rank of the data. Hence, it is not affected by the outliers. The Spearman correlation is similar to the Pearson correlation r_{xy} (see Equation (6.17)), but uses the ranked data. r_{xy} is given by the ratio between the sample covariance of two variables ($Cov(x,y)$) over the product of their standard deviations ($s_x s_y$) (Rauf et al., 2019). In other words, the Pearson correlation r_{xy} is given by the ratio between the sample covariance of the two variables ($Cov(x,y)$) over the product of their standard deviations ($s_x s_y$), in our case, x (NREs) and y (TIDs) (Wilks, 2011; Rauf et al., 2019). The Pearson linear coefficient is defined as $-1 \leq r_{xy} \leq 1$. $r_{xy} = -1$ indicates a perfect, negative linear correlation between x and y . On the other hand, $r_{xy} = 1$

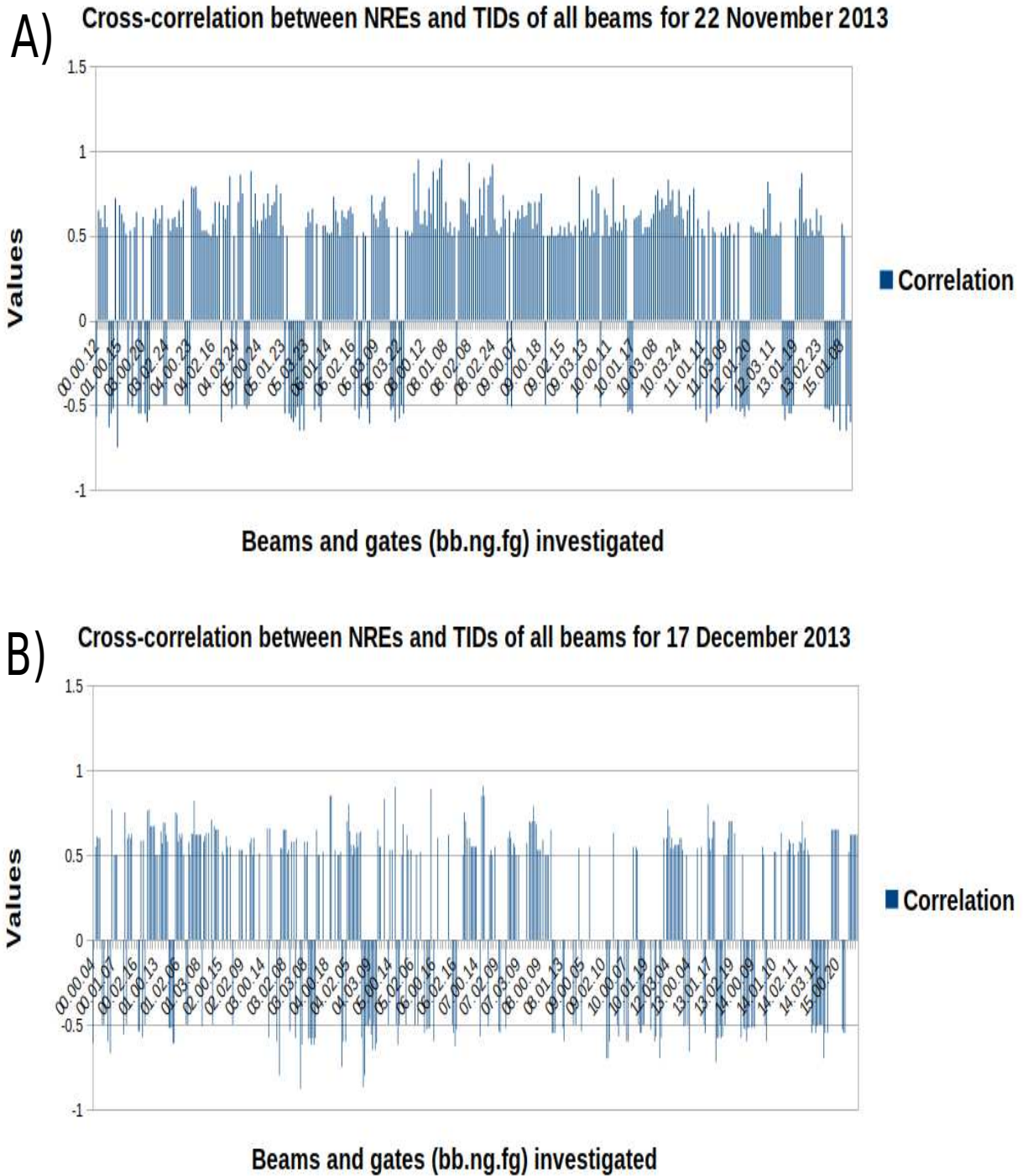


Figure 6.12: Cross-correlation between the power of gates 0-3 (NREs) of different beams with various gates (TIDs) of the Zhongshan radar for 22 November 2013 for the time period 00:00 - 03:48 UT (A) and for 17 December 2013 from 19:00 to 20:48 UT (B).

indicates a perfect, positive linear correlation between x and y .

$$r_{xy} = \frac{\frac{1}{n-1} \sum_{i=1}^n x_i y_i - \frac{1}{n} \left(\sum_{i=1}^n x_i \right) \left(\sum_{i=1}^n y_i \right)}{\left[\sum_{i=1}^n x_i^2 - \frac{1}{n} \left(\sum_{i=1}^n x_i \right)^2 \right]^{1/2} \left[\sum_{i=1}^n y_i^2 - \frac{1}{n} \left(\sum_{i=1}^n y_i \right)^2 \right]^{1/2}} = \frac{Cov(x,y)}{s_x s_y} \quad (6.17)$$

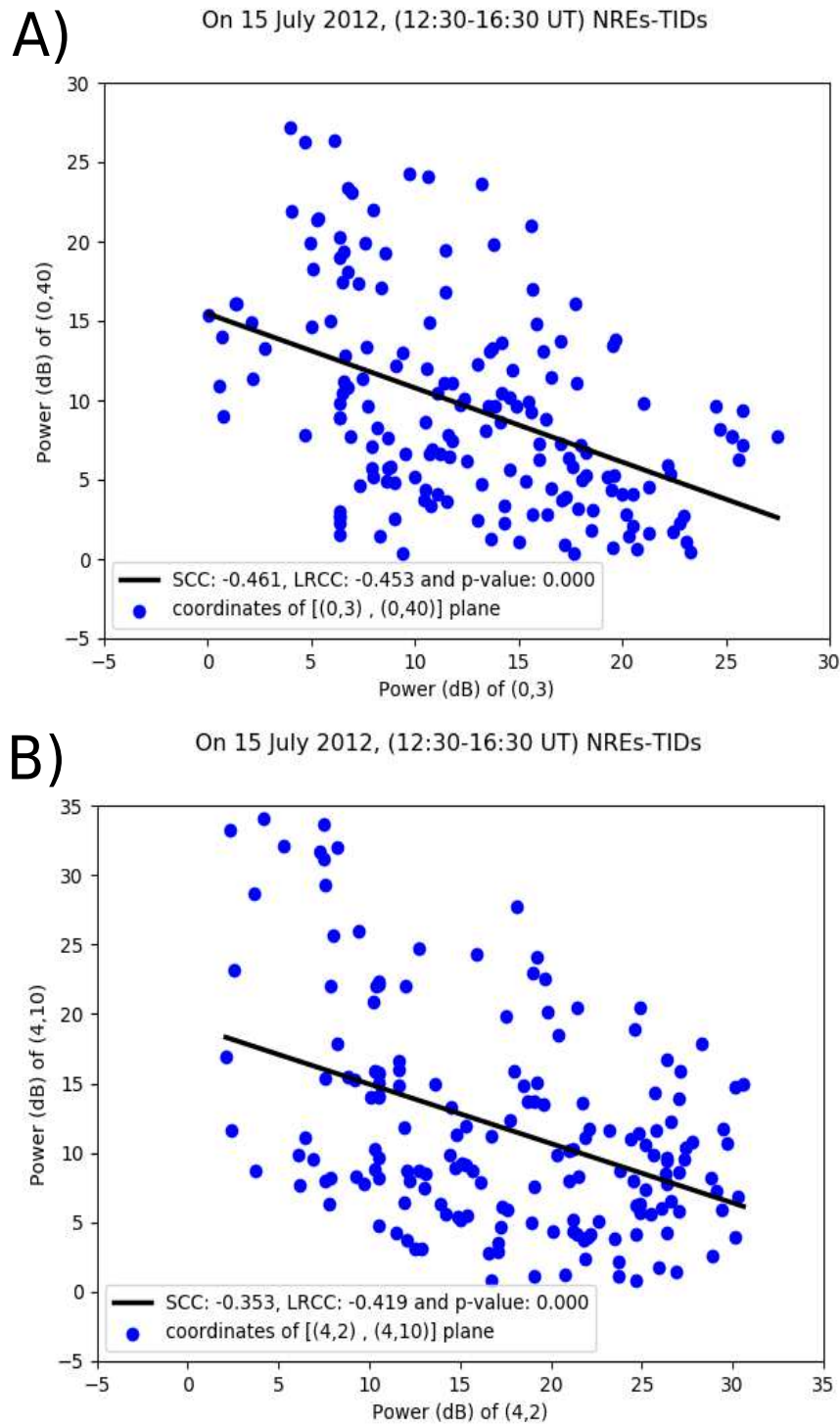


Figure 6.13: SCC, LRCC, and p-values of range gates 3 (NREs) and 40 (TIDs) of beam 0 (A), and of range gates 2 (NREs) and 10 (TIDs) of beam 4 (B) for the time period 12:30 - 16:30 UT on 15 July 2012 at SANA E. The plane in the plots is defined by the time series power received by near gates for NREs and far gates for MSTIDs.

where n is the number of data points. The Linear Regression Correlation Coefficient (LRCC) was also computed with the SCC. A simple linear regression stands for the linear relationship between the two variables, i.e., x

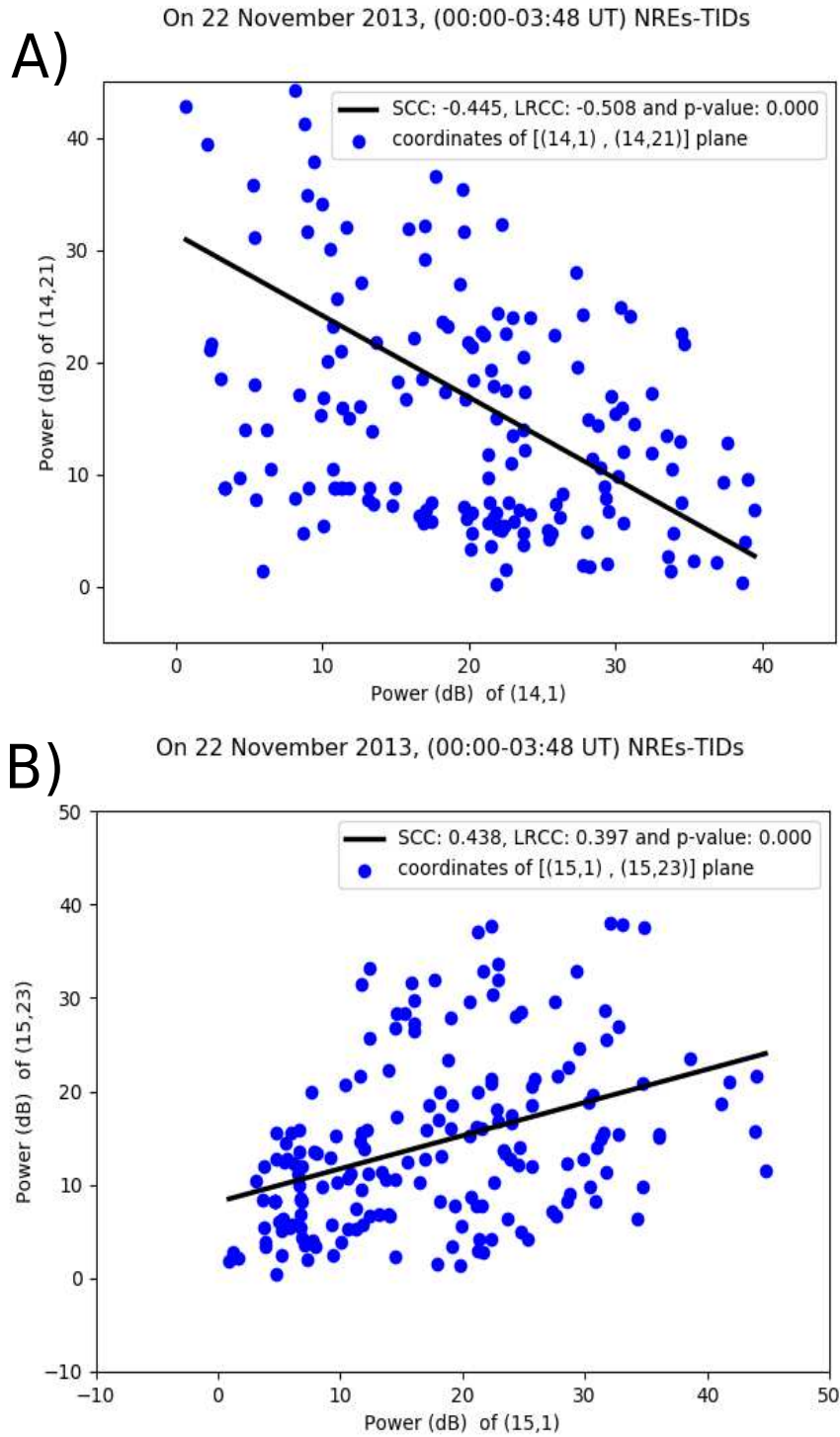


Figure 6.14: SCC, LRCC, and p-values of range gates 1 (NREs) and 21 (TIDs) of beam 14 (A), and of range gates 1 (NREs) and 23 (TIDs) of beam 15 (B) for the time period 00:00 - 03:48 UT on 22 November 2013 at Zhongshan. The plane in the plots is defined by the time series power received by near gates for NREs and far gates for MSTIDs.

and y . It is expressed by the equation of a straight line (Zou et al., 2003; Wilks, 2011).

$$y = a + bx \tag{6.18}$$

where a and b represent the least-squares intercept and the gradient, respectively. The intercept is expressed by:

$$b = \frac{\Delta y}{\Delta x} = \frac{\sum_{i=1}^n [(x_i - \bar{x})(y_i - \bar{y})]}{\sum_{i=1}^n (x_i - \bar{x})^2} = \frac{n \sum_{i=1}^n x_i y_i - \sum_{i=1}^n x_i \sum_{i=1}^n y_i}{n \sum_{i=1}^n (x_i)^2 - \left(\sum_{i=1}^n x_i \right)^2} \quad (6.19)$$

and the gradient is expressed by:

$$a = \bar{y} - b\bar{x} \quad (6.20)$$

where \bar{x} and \bar{y} represent the mean of x_i and y_i , respectively.

F-statistics (p-values) were computed to test the statistical significance of the correlation coefficient. The null hypothesis is retained or rejected on account of the p-value, and thus implies the acceptance or rejection of the hypothesis. The p-value is the probability of rejecting the hypothesis. It is also the probability showing that the results in our sample data didn't occur by chance. The null hypothesis says that there is no relationship between the two variables. In our case, the null hypothesis says that there is no relationship between the data points representing TIDs and those representing NREs. The null hypothesis is rejected when the p-value for the correlation coefficient is less than the significance level of 5%. This correlation coefficient is considered statistically significant with a 95% confidence level (Rauf et al., 2019; Ware et al., 2019). Correlation coefficients in the range of $[\pm 0.00 \pm 0.19]$, $[\pm 0.20 \pm 0.39]$, $[\pm 0.40 \pm 0.59]$, $[\pm 0.60 \pm 0.79]$, $[\pm 0.80 \pm 1.00]$ are considered very weak, weak, moderate, strong and very strong, respectively. The sign (+) indicates a positive correlation, and (-) shows a negative correlation. If one variable increases when the other increases, the correlation is positive and if one (increasing) variable causes the other to decrease, the correlation is negative.

To investigate the relationship between TIDs and NREs, the squares of the correlation coefficient presented here was used to calculate the percentage of the NREs that were generated by passing TIDs. The square of the correlation coefficients, i.e., $[0 \ 3.61]$, $[4 \ 15.21]$, $[16 \ 34.81]$, $[36 \ 62.41]$, $[64 \ 100]$, respectively, indicate the range of percentages by which the parameters of one variable could be statistically explained by the parameters of the other (Rauf et al., 2019). The time lag discussed in subsection 6.2 was taken into consideration for the estimation of the SCC of the variables relating to the events in this study.

Figure 6.13 illustrates that the SCC of the data points on 15 July 2012 between 12:30 and 16:30 UT for gate 3, and gate 40 of beam 0 of the SANA radar is -0.461 (A), and the SCC for gates 2 and 10 of beam 4 is -0.353 (B). In this case, the p-value was 0.000, indicating that the correlation coefficient was statistically significant with a 95% confidence level. A SCC of -0.461 indicates that ~21.3% of the NREs power received by gate 3 of beam 0 can be statistically explained by the variation of the TIDs backscatter power received by gate 40. SCC of -0.353 indicate that ~12.5% of NREs power received by gate 2 of beam 4 can be statistically explained by the variation of TIDs backscatter power received by gate 10 of the same beam. In this case also, the p-value was 0.000 indicates that the correlation coefficient is statistically significant with a 95% confidence level.

Figure 6.14 (A) indicates that, for the period between 00:00 and 03:48 UT on 22 November 2013 at Zhongshan, the SCC of gate 1 and gate 21 of beam 14 is -0.445. Based on the categories of the correlation coefficients, -0.445 is a moderate negative correlation. It implies that the variation in TID backscatter power could statistically explain about ~19.8% of variation in the NREs backscatter power. Figure 6.14 (B) shows that the SCC of gate 1 and gate 23 of beam 15 of the Zhongshan HF radar is 0.438. The SCC of 0.438 also falls within the moderate positive correlation range. The ~19.2% variation in the NREs power of gate 1 can be statistically accounted for by the variation in TID echo power received by gate 23 of beam 15. As in the case of Figure 6.13, these two cases in Figure 6.14 show that the p-value of 0.000 indicates that the correlation coefficients are statistically significant with a 95% confidence level. The same calculations were done for other events. Figure 6.15 (A) shows that for 28 May 2011 a moderate correlation between the NREs and TIDs exists, i.e., the SCC of gate 1 and gate 12 of beam 7 of the SANA radar was -0.265, indicating that ~7% of the NREs backscatter power can be statistically accounted for by the TIDs. Figure 6.15 (B) shows that the SCC of gate 1 and gate 13 of beam 12 of the SANA radar was 0.405, i.e., ~16% of the NREs backscatter power can be statistically accounted for by the TIDs. Figure 6.16 (A) shows that for 17 December 2013, the SCC of gate 3 and gate 11 of the first beam (beam 0) of the Zhongshan radar was 0.534, i.e., ~28% of the NREs backscatter power can be statistically accounted for by TIDs. Figure 6.16 (B) shows that the SCC of gate 1 and gate 8 of beam 15 was

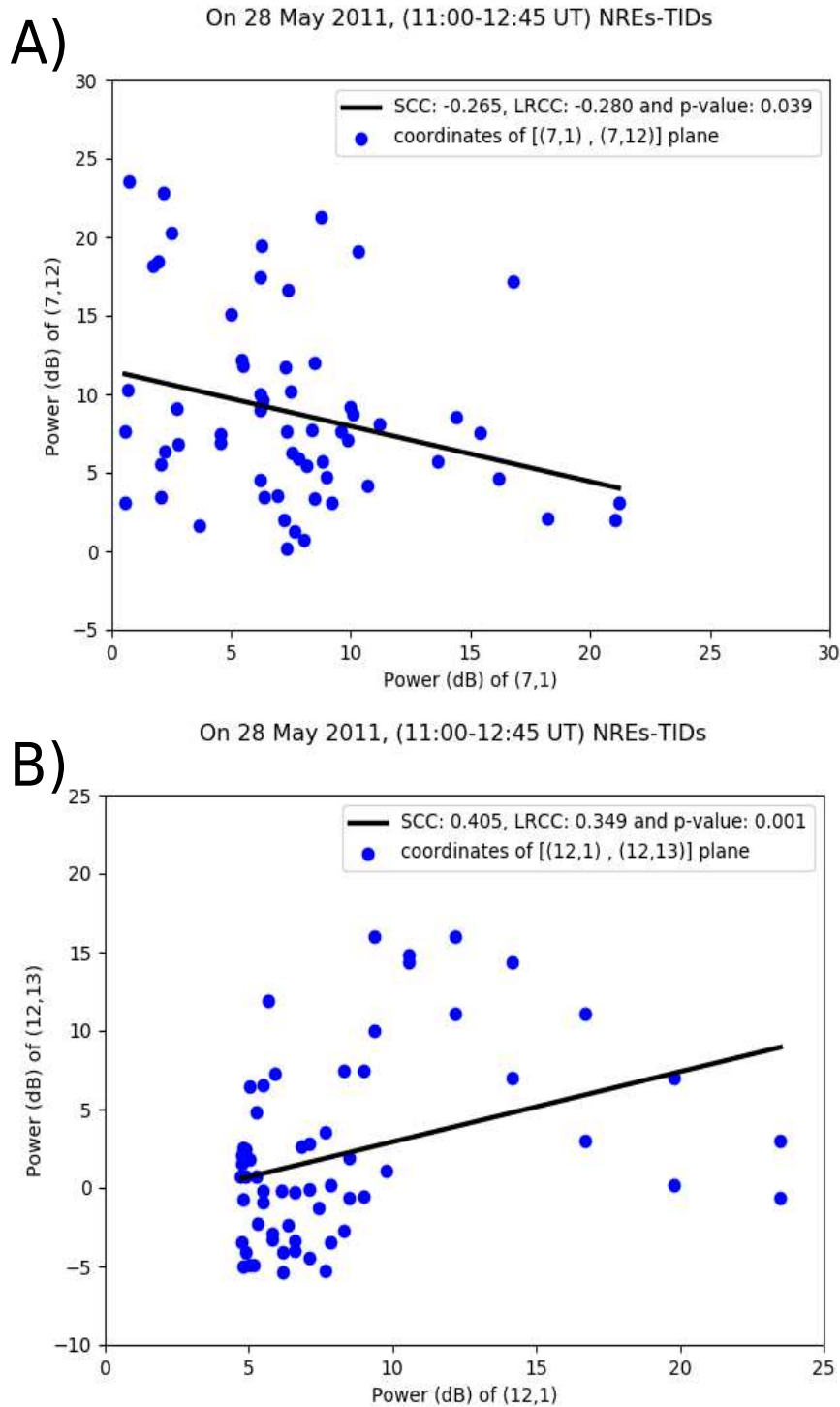


Figure 6.15: SCC, LRCC, and p-values of range gates 1 (NREs) and 12 (TIDs) of beam 7 (A), and of range gates 1 (NREs) and 13 (TIDs) of beam 12 (B) for the time period 11:00 - 12:45 UT on 28 May 2011 at SANA E. The plane in the plots is defined by the time series power received by near gates for NREs and far gates for MSTIDs.

-0.726, meaning that ~53% of NRE backscatter power can be statistically accounted for by the TIDs.

Lastly, Figure 6.17 shows that on 28 May 2011 between 11:00 and 12:46 UT the SANA E radar didn't have

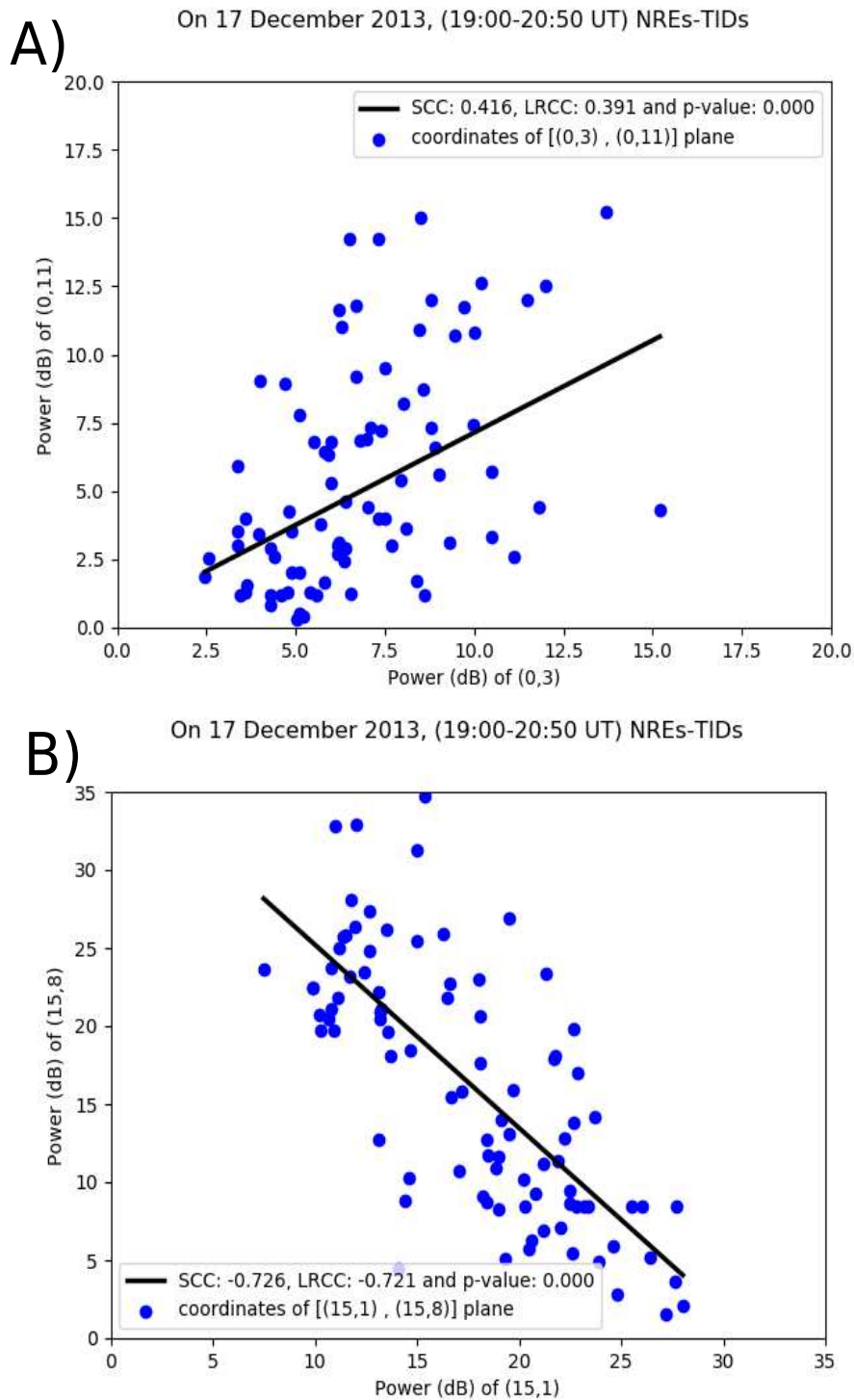


Figure 6.16: SCC, LRCC, and p-values of range gates 3 (NREs) and 11 (TIDs) of beam 0 (A), and of range gates 1 (NREs) and 8 (TIDs) of beam 15 (B) for the time period 19:00 - 20:50 UT on 17 December 2013 at Zhongshan. The plane in the plots is defined by the time series power received by near gates for NREs and far gates for MSTIDs.

enough data in almost all beams for the far ranges (TIDs). Only beams 7, 8, 10, and 12 had some data and were used to estimate the SCC of NREs and TIDs. The minimum contribution of TIDs to the NREs backscatter power was $\sim 6\%$ while the maximum was $\sim 37\%$. The average of SCC was $\sim 14\%$ and its standard deviation $\sim 1\%$

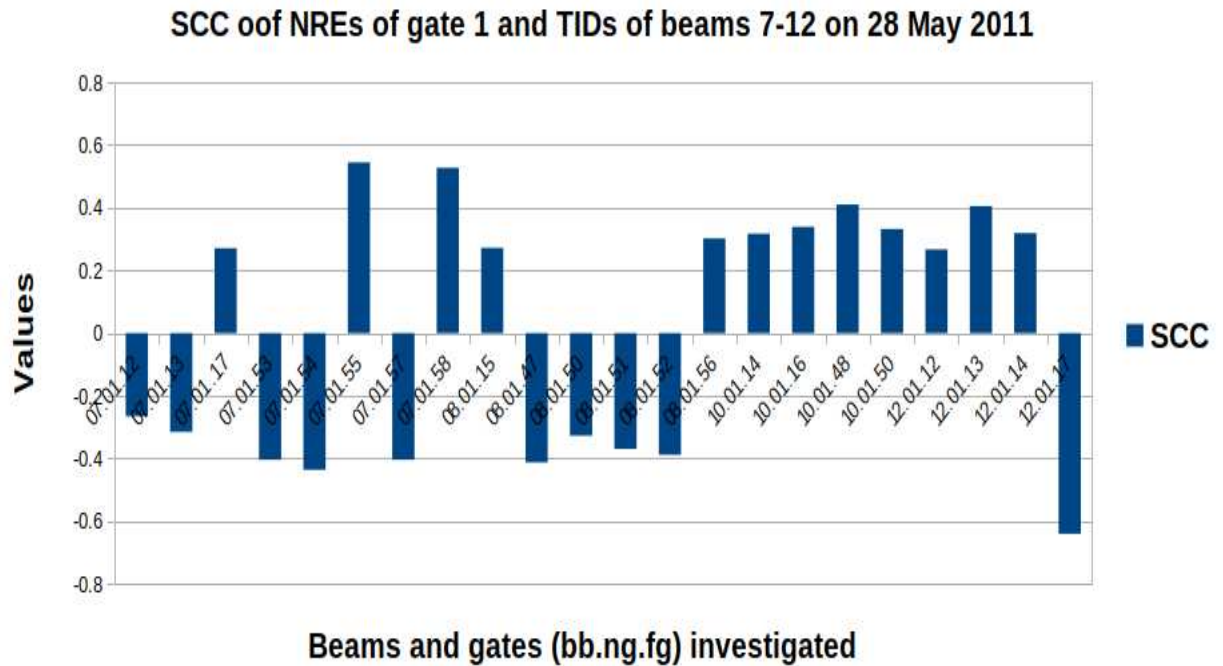


Figure 6.17: The SCC of range gate 1 (NREs) and TIDs of gates of beams 7, 8, 10, and 12 of the SANA radar for 28 May 2011

of the TID contribution to the backscatter power of NREs. Figure 6.18 shows the SCCs of gate 1 (A), and gate 2 (B), respectively, with TIDs of all beams of the SANA radar for 15 July 2012. The minimum contribution of MSTIDs to NREs backscatter power was $\sim 3\%$, while the maximum contribution was $\sim 37\%$. Gate 1 shows that average of SCC was 9.5% and its standard deviation 1.3%, while gate 2 shows average SCC was 8.2% and its standard deviation 1.2%. Figure 6.19 shows for 22 November 2013, the SCCs of gates 1 and 2, each in conjunction with all the beams of the Zhongshan radar, with other gates receiving TIDs backscatter echoes for 22 November 2013. The results of all gate 1's and other gates for TIDs show that the minimum contribution of the TIDs to the NREs was $\sim 2\%$ and the maximum was $\sim 41\%$ (A). The results of all gate 2's and other gates for TIDs show that the minimum contribution of TIDs to NREs was $\sim 2\%$, while the maximum was $\sim 49\%$ (B). Gate 1 shows that the average SCC was 8.3% and its standard deviation 1.1%, while gate 2 shows that the average SCC was 7.9% and its standard deviation 1.4%. Figure 6.20 (A) shows that on 17 December 2013, the minimum contribution of TIDs to NREs, received by all gate 1's was $\sim 4\%$, while the maximum was $\sim 50\%$. Figure 6.20 (B) shows that the minimum contribution of TIDs to NREs received by all gate 2's was $\sim 4\%$, while the maximum was $\sim 53\%$. Gate 1 shows that the average SCC was 12.5% and its standard deviation 1.4%, while for gate 2 the average SCC was 13.4% and its standard deviation 1.4%.

The Spearman correlation coefficient was used by Strangeway et al. (2005) to find the relation between precipitating electron and ion flux. The coefficient of the two was 0.346 (see Figure 9 of Strangeway et al. (2005)). To determine the impact of scintillation effects to the degradation of positioning during a solar maximum, Spearman's correlation coefficients of scintillation and degradation was estimated (Alves et al., 2020). In their figures 4-6, they showed that the coefficients were between 0 and 0.3.

6.4 Summary

This chapter describes the different methods that were used to investigate the relationship between the NREs and TIDs. Their periodicity was compared and it was found that for the available data the periods are the same. The estimation of the TIDs parameters was explained. Cross-spectral analysis was used to estimate the

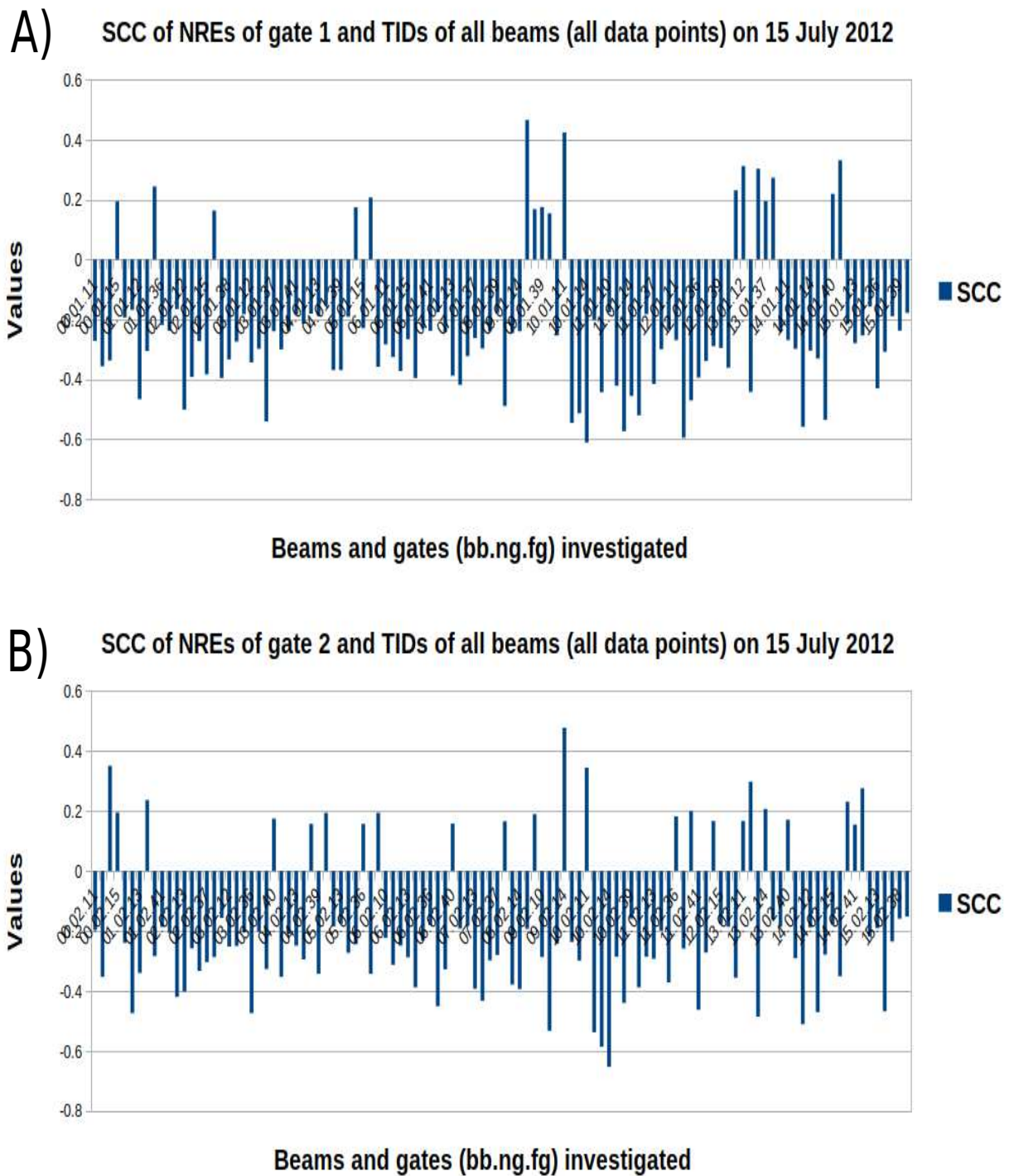
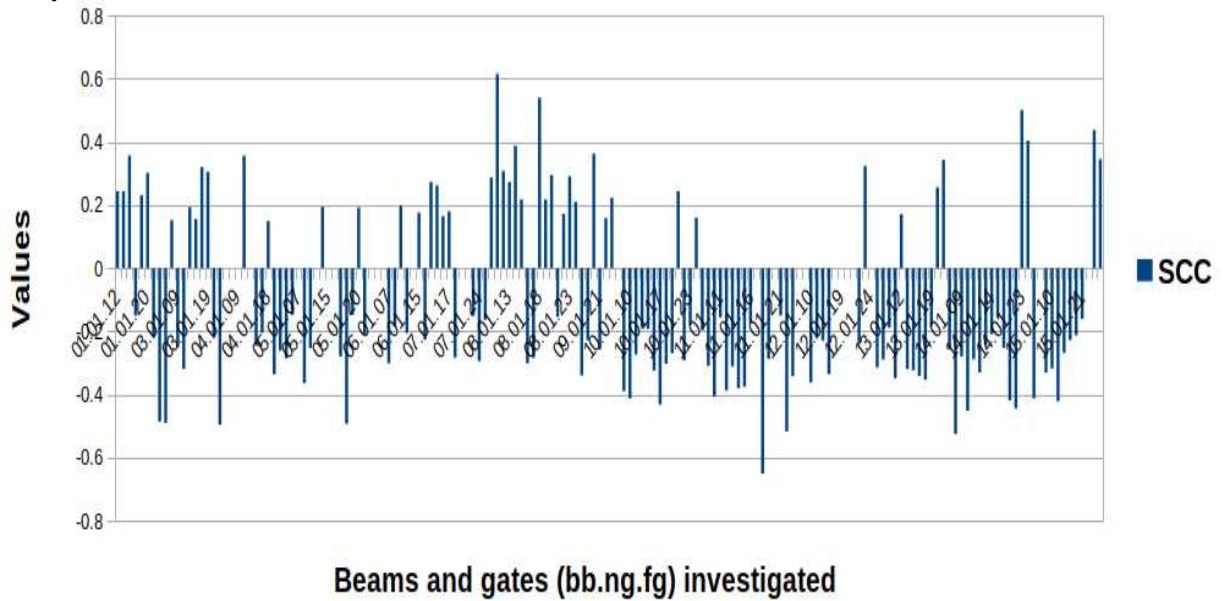


Figure 6.18: The SCC (A) of range gate 1 (NREs) and TIDs of gates from all beams of the SANA radar on 15 July 2012; and (B) of range gate 2 and TIDs of gates of all beams of the SANA radar for 15 July 2012

phase difference, phase velocity, and wavelength for each event. The cross-correlation between NREs and TIDs was evaluated. Lastly, statistical analysis, by means of the most robust SCC, was used to investigate the two phenomena. It was found that the correlation between NREs and TIDs, is moderate. This indicates that the TIDs only partially modulated the NREs. In the next chapter results pertinent to the mechanism responsible

A) SCC of NREs of gate 1 and TIDs of all beams (all data points) on 22 November 2013



B) SCC of NREs of gate 2 and TIDs of all beams (all data points) on 22 November 2013

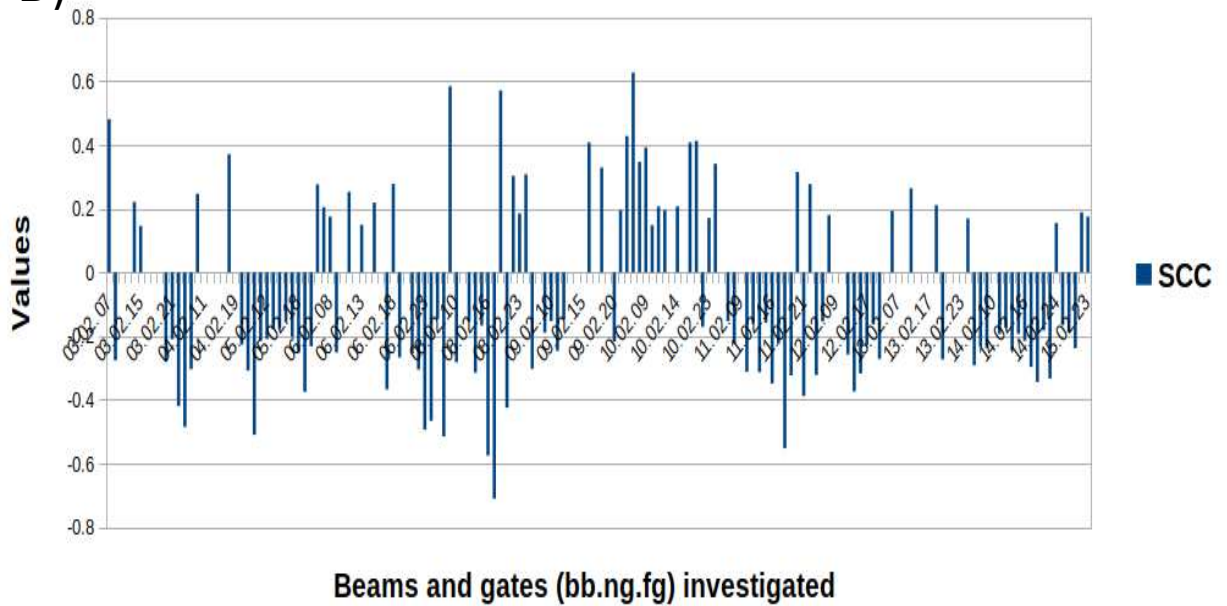


Figure 6.19: The SCC (A) of range gate 1 (NREs) and TIDs of gates of all beams of the Zhongshan radar for 22 November 2013, and (B) of range gate 2 and TIDs of gates of all beams of the Zhongshan radar for 22 November 2013

for the NREs and how TIDs contribute to their modulation, are discussed.

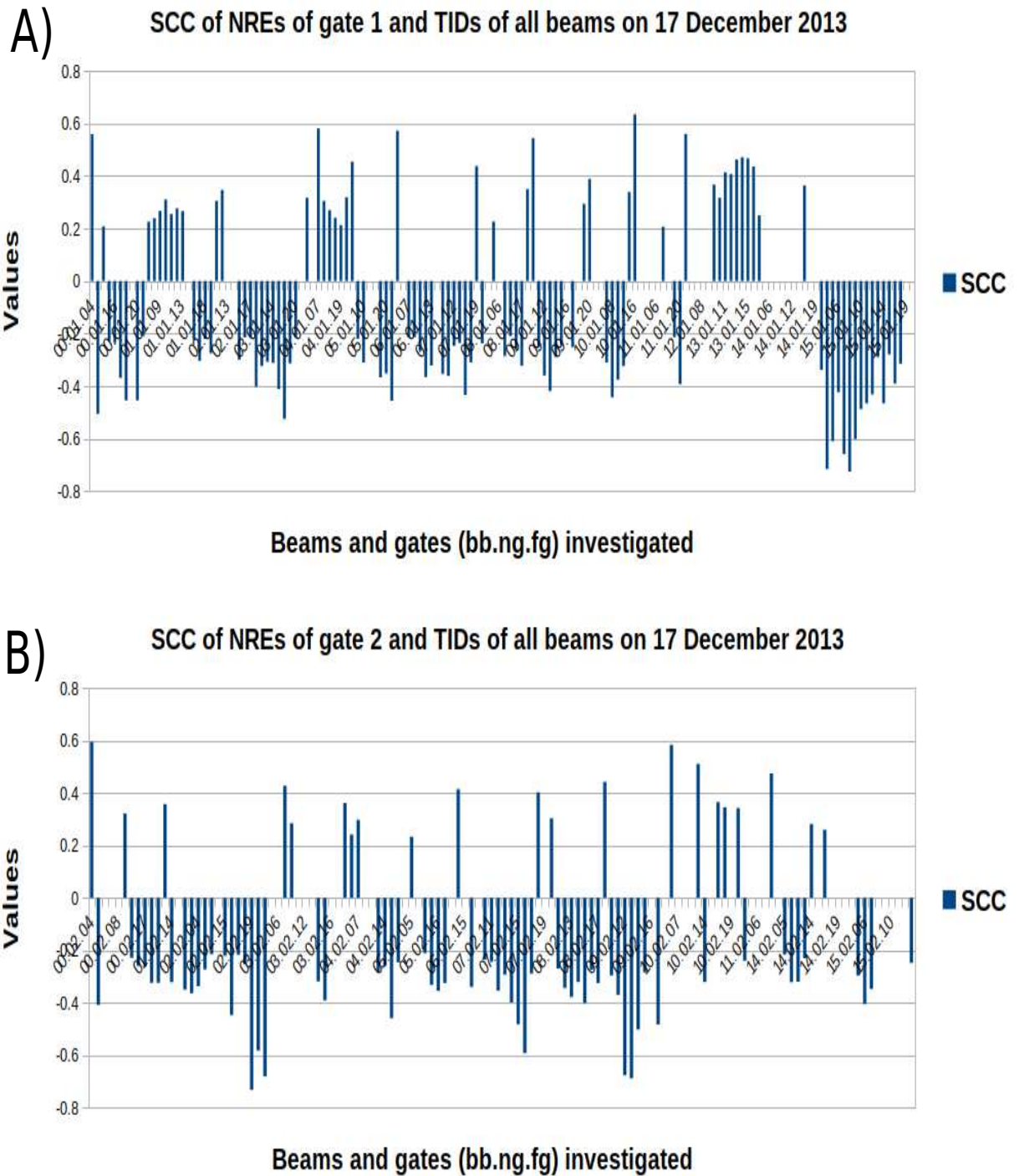


Figure 6.20: The SCC (A) of range gate 1 (NREs) and TIDs of gates of all beams of the Zhongshan radar for 17 December 2013, and (B) range gate 2 and TIDs of gates of all beams of the Zhongshan radar for 17 December 2013

Chapter 7

MECHANISM RELATING MSTIDS AND NREs

7.1 Introduction

In this study several mechanisms that are responsible for the production of NREs are investigated, as well as the most plausible mechanism that would link (clarify the relationship between) MSTIDs and NREs. Initially, it was postulated that a passing TID might modulate PMSEs until cases of simultaneous occurrence of TIDs and NREs were found in winter. In some gates of the radars, some cases fulfill PMSE conditions given in section 3.5.1.1, especially during quiet time in summer. Other gates don't fulfill those conditions, mostly during winter.

Meteor trail echoes, HAIR echoes and PMSEs are not considered likely mechanisms to cause these NREs. Assuming that the NREs on 17 December 2017 were PMSE, the number density and radii of dust particles were estimated by means of the DUSTY model, based on the power received by the near range gates of the SuperDARN HF radar. The possibility that the GDI could be the mechanism responsible for the production of NREs at the bottom-side of the *E*-region was also investigated. To understand better the effects of TIDs on NREs, the modulated GDI scale height was calculated. This is directly proportional to the electric field derived from SuperDARN convection patterns of the plasma. A part of this chapter was published as "First observations of *E*-region Near Range Echoes partially modulated by *F*-region Traveling Ionospheric Disturbances observed by the same SuperDARN HF radar" by the Journal of Geophysical Research (JGR). The manuscript can be found in section 8.3. The event/case on 28 May 2011 was not included in the paper, because it doesn't add anything to the results of the investigation into the event on 15 July 2012. The latter was included in the paper. Four events were included in this study, two events that were observed in the data of the SANA radar during a geomagnetic storm in winter, and two events that were observed in the data of the Zhongshan radar during quiet time in summer.

7.2 Mechanisms unlikely to cause NREs

7.2.1 Meteor trail echoes, HAIR echoes and PMSEs

The NREs observed in this study are not meteor trail echoes, because meteor trail echoes only last for about 2 min (Ogunjobi et al., 2015, 2017). The events on 28 May 2011, 15 July 2012, 22 November 2013, and 17 December 2013 lasted for about 2, 4, 4 and 2 hours, respectively. HAIR echoes are not a likely mechanism of NRE production, because they require an electric field of more than 40 mV/m to cause the FBI, mostly at night during auroral electrojets (Milan et al., 2004; Kelley, 2009). The electric field of the events under investigation was always below the threshold for triggering the FBI, but this electric field could be linked to FAIR echoes which are caused by the GDI. The electric field of the GDI doesn't have a threshold trigger, but requires the electron density gradient and electric field to be pointed in a direction favorable for its growth rate (St.-Maurice and Nishitani, 2020). HAIR echoes occur at an altitude of 120 km and are observed simultaneously at different ranges with a wide spectral width and a Doppler velocity that decreases with a decrease in range (Milan et al., 2004; St.-Maurice and Nishitani, 2020). HAIR echoes are shown in Figure 2 in the mentioned paper of St.-Maurice and Nishitani (2020) for 10 August 2013 just before 14:00 UT, in the ranges above 250 km. The same figure, shows FAIR echoes that were observed by beam 7 of the Rankin Inlet (RKN) HF radar, operated in a special mode called "myopic", with a high spatial resolution of 15 km. Echoes similar to HAIR echoes were not observed in the events studied, but echoes similar to FAIR echoes can be seen in all these events. Thus HAIR echoes are ruled as a mechanism for the production of NREs.

$nd/ne0$	$rd = 2 \text{ nm}$	$rd = 4 \text{ nm}$	$rd = 6 \text{ nm}$	$rd = 8 \text{ nm}$	$rd = 10 \text{ nm}$
20%	-16.5	-12.4	-9.02	-6.58	-5
50%	-9	-5.48	-3.55	-1.47	-1.3
80%	-5	-2.11	-2.8	-1.58	-5.35
100%	-4.58	-1.4	-0.7	-2.73	-8.7
170%	-2.72	0	-0.55	-13.75	

Table 7.1: The change in the output of radar backscatter power (dB) as derived by the DUSTY model for the Zhongshan HF radar. The radii of dust particles is rd and ratio of density of dust particles and background electrons is $nd/ne0$.

Most gates of the radars, show that the events in summer fulfill the PMSE conditions presented in section 3.5.1.1. Other events in winter fulfilling some of the PMSE conditions. An example of this phenomena can be seen in the echoes received by the first gates of all beams of the SANAE radar on 15 July 2012 (Figure 5.3 B). The Doppler velocity was between -50 and 50 m/s, while the spectral width was less than 50 m/s. These echoes appear very similar to those observed during summer. This is not consistent with PMSE echoes which are observed only during summer. In this study, the possible mechanism(s) responsible for echoes detected by the SuperDARN radar during summer and winter are explored. The NREs could be either PMSE- and/or GDI-related echoes, depending on the season.

The NREs were assumed to be PMSEs and the computational DUSTY model that was developed by Mahmoudian et al. (2011) was used to investigate the sizes and density of the dust particles during the passage of a TID. The backscatter power received by the Zhongshan HF radar near range gates on 17 December 2013 were used to estimate the parameters of the dust particles. This was done to investigate the possibility of GDI as the mechanism that produces NREs in the high-latitude.

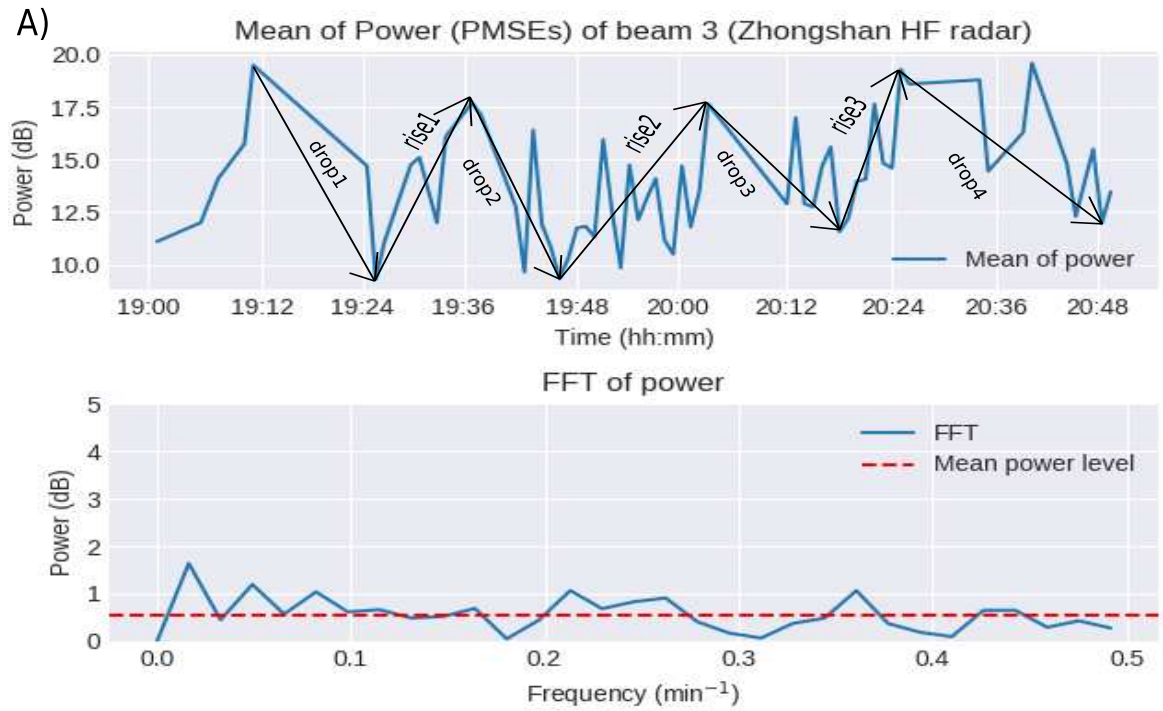
7.2.2 DUSTY model output for the event on 17 December 2013

The DUSTY model is used to predict the behavior of particles during an ionospheric heating experiment when PMSE is present (Mahmoudian et al., 2011, 2020). PMSEs occur at the coldest altitude, i.e., at the mesopause of high latitudes. The backscatter power modulation during the passage of an AGW or TID could be modulated due to the displacement of the icy dust particles to different altitudes. Also, above and below the mesopause the temperature increases with altitude upward and downward. As the temperature increases and decreases periodically, the icy dust particles responsible for PMSE melt and freeze, respectively. As a result, the backscatter power of the radar could be modulated at the same period as that of the AGW/TID.

The DUSTY model predicts the change in radar backscatter power when ionospheric heater is on and when the heater is off. Negative values indicate a reduction in radar backscatter power (see Table 7.1). This is to be expected. Heating the electrons means that more electrons stick to the dust, and thus there are fewer free electrons; consequently, the radar backscatter power is less. The model allows the measured reduction in backscatter power to be compared to the predicted model values and thus the effective equivalent change in dust radius and/or dust density may be estimated. This model was used for radars operating at frequencies, of 7.9, 56, 139, 224, and 930 MHz, corresponding to wavelengths of 20 m, 2.7 m, 1.1 m, 68 cm, and 16 cm, respectively (Mahmoudian et al., 2011). In this thesis, a frequency of 10.25 MHz was used to get the results presented in Table 7.1. The backscattered power ($power(dB)$ equation (7.1)) of a radar is equivalent to the square of the electron density perturbation $(\delta ne)^2$ (Ponomarenko et al., 2009; Mahmoudian et al., 2011):

$$power(dB) \sim (\delta ne)^2. \quad (7.1)$$

The model cannot exactly produce the same power level observed by the radars. It can however, clearly and accurately estimate the variation in radii and density of dust particles that lead to the decrease and increase in the power level (Mahmoudian et al., 2011). Table 7.1 summarizes the model's output (radii and density) for the Zhongshan HF radar backscatter power (dB) on 17 December 2013 between 19:00 and 20:48 UT. The ratio



B) Dust particles' radii and their densities compared with power of beam 3 of Zhongshan radar on 17 December 2013

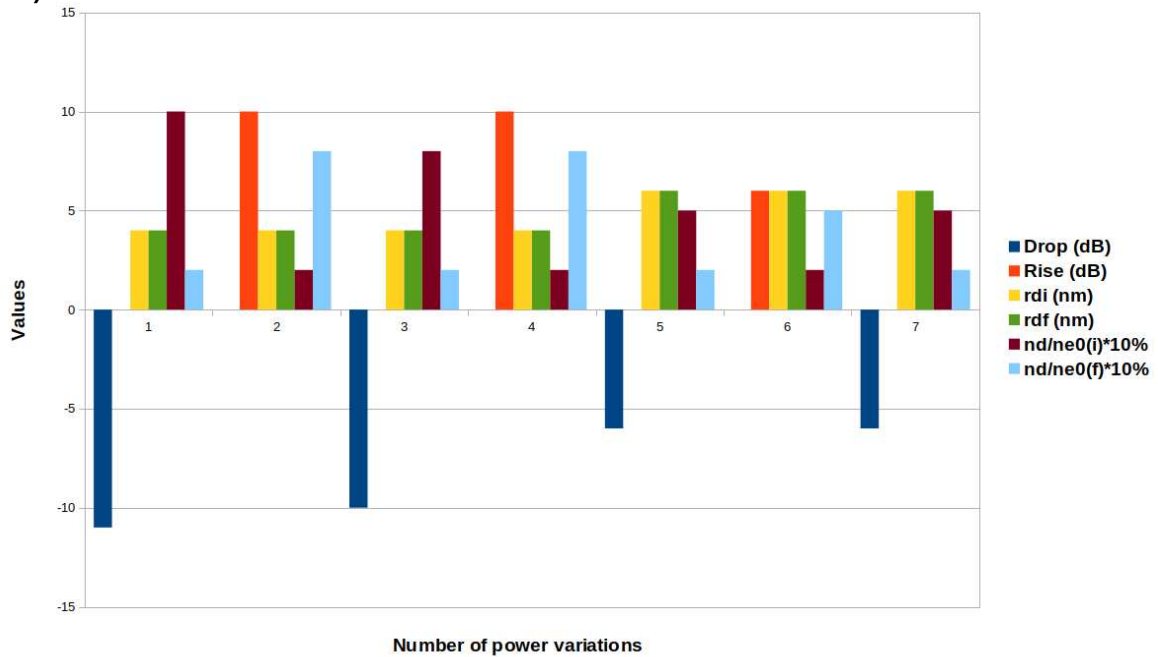


Figure 7.1: A) Mean power and FFT of beam 3 of the Zhongshan HF radar. B) Radii and density of dust particles given by DUSTY model for the same beam. r_{di} and r_{df} are the initial and final radii of the icy dust particle.

of dust particle density and background electron density, nd/ne_0 in percentage, shows the variation in particle density as the power decreases or increases. The ratios (nd/ne_0) of 20, 50, 80, 100 and 170% and dust particle radii of 2, 4, 6, 8, and 10 nm were used. For example, the ratio (nd/ne_0) of 20%, having radii of 2, 4, 6, 8 and 10 nm generate a backscatter power reduction of -16.5, -12.4, -9.02 and -5 dB, respectively, as shown in the second

row from the top of Table 7.1. The percentage variation of other particles is shown in the third, fourth, fifth, and sixth rows of Table 7.1.

Figure 7.1 (A) shows the mean and FFT of the backscatter power received by beam 3 of the Zhongshan radar on 17 December 2013. As mentioned earlier, the period of these MSTIDs were 50 and 20 min, but 20 min was used for this event. Figure 7.1 (B) shows the density and radii of dust particles as derived from the DUSTY model for beam 3 of the Zhongshan HF radar on 17 December 2013 from 19:00 to 20:48 UT. It was produced from the output in Table 7.1, where the magnitude of $nd/ne0$ was multiplied by 10 to get the percentages that are in Table 7.1. The backscatter power drop (dB), backscatter power rise (dB), initial radii (rdi in nm), final radii (rdf in nm), initial $nd/ne0$ (%), and final $nd/ne0$ (%) is shown in blue, red, yellow, green, dark-red and light-blue, respectively.

For example, at around 19:11 UT the backscatter power received by beam 3 was ~ 19 dB and dropped to ~ 8 dB around 19:25 UT (Figure 7.1 (A)). This drop of 11 dB is equivalent or equal to the drop from -12.4 dB to -1.4 dB in Table 7.1, i.e., $[-12.4 - (-1.4)] = -11$ dB (see drop1 in Figure 7.1 (A)). This corresponds to a density and radius change from $rd = 4$ nm, $nd/ne0 = 100\%$ as an initial (i) state of dust particles to $rd = 4$ nm, $nd/ne0 = 20\%$ as a final (f) state of dust particles. It means that $nd/ne0$ dropped from 100% to 20% while the radius remained the same, where these percentages were converted to the number of dust particles (nd), by using equation (3.41) in chapter 3.

From around 19:25 UT to 19:36 UT, the power rose from ~ 8 to ~ 18 dB (see Figure 7.1 (A)), which corresponds to $18-8$ dB = ~ 10 dB (see rise1 in Figure 7.1 (B)). In Table 7.1, the increase from $rd = 4$ nm, $nd/ne0 = 20\%$ (i) to $rd = 4$ nm, $nd/ne0 = 80\%$ (f) also corresponds to 10 dB. From around 19:36 UT to 19:46 UT, the power dropped from ~ 18 to ~ 8 dB, which is $18-8$ dB = ~ 10 dB (see drop2 in Figure 7.1 (B)). This value is equal to the power that was estimated by means of the DUSTY model, namely from $rd = 4$ nm, $nd/ne0 = 80\%$ (i) to $rd = 4$ nm, $nd/ne0 = 20\%$ (f) (see Table 7.1). Between 19:46 UT and 20:05 UT the power rose again from ~ 8 to ~ 18 dB, a difference of 10 dB (rise2). The changes in the dust parameter are similar to the ones discussed above. From around 20:05 to 20:18 UT the power dropped from ~ 18 to ~ 12 dB. Thus the power change is -6 dB (drop3), corresponding to the density and radius values changing from $rd = 6$ nm, $nd/ne0 = 50\%$ to $rd = 6$ nm, $nd/ne0 = 20\%$. This change was followed by an increase in power from ~ 12 dB at around 20:18 UT to ~ 18 dB at around 20:24, a 6 dB increase (rise3), corresponding to the density and radius values changing from $rd = 6$ nm, $nd/ne0 = 20\%$ to $rd = 6$ nm, $nd/ne0 = 80\%$. The last event considered here occurred between 20:24 UT and 20:48 UT. The power dropped from ~ 18 dB to ~ 8 dB, a -10 dB change. This is the same as drop3 discussed above.

Figure 7.2 shows the dust parameters of 15 beams, i.e., 0-14 of the Zhongshan HF radar, with beam 3 presented in Figure 7.1 (B) shown in a vertical rectangle block. Dust radii and density variations are presented together with the backscatter power variation in blue for drops and red for rises, i.e., the radii (rd) are given by $rd_f - rdi$ in yellow while the ratio between dust particles and the number density of electrons $nd/ne0$ is equal to $nd/ne0(f) - nd/ne0(i)$ in green. The dust particles as derived from the DUSTY model using the backscatter power of beam 3, did not freeze or melt to change their radii, only their density varied.

The results discussed are based on the assumption that the backscatter power of near range gates is caused by PMSEs alone. In fact, there isn't enough evidence to show that PMSEs caused NREs during this summer event. There also isn't enough information about the altitudes of NREs, and some NREs were observed in winter. Additionally, the meridional electric field showed a trend opposite that of the SuperDARN backscatter power (see Figure 5.14). Furthermore, PMSEs are not related to the ionospheric electric field. We cannot ignore that PMSEs do occur in summer. It is possible that the 2 events in the summer may have been caused by FAIR echoes and PMSEs, but in the next section it will be shown that the FAIR echoes generation mechanism is more plausible. The analysis method described above can be used in conjunction with other instruments, such as VHF radar, that accurately observe PMSEs and MSTIDs, to explore the effects of TIDs on PMSEs.

Another possible mechanism that may be applied to both winter and summer events is investigated. The GDI is discussed as a likely mechanism to cause SuperDARN NREs, which is then modulated by the polarization electric field due to a passing TID. First the primary waves which are responsible for the secondary waves observed by SuperDARN as NREs are investigated.

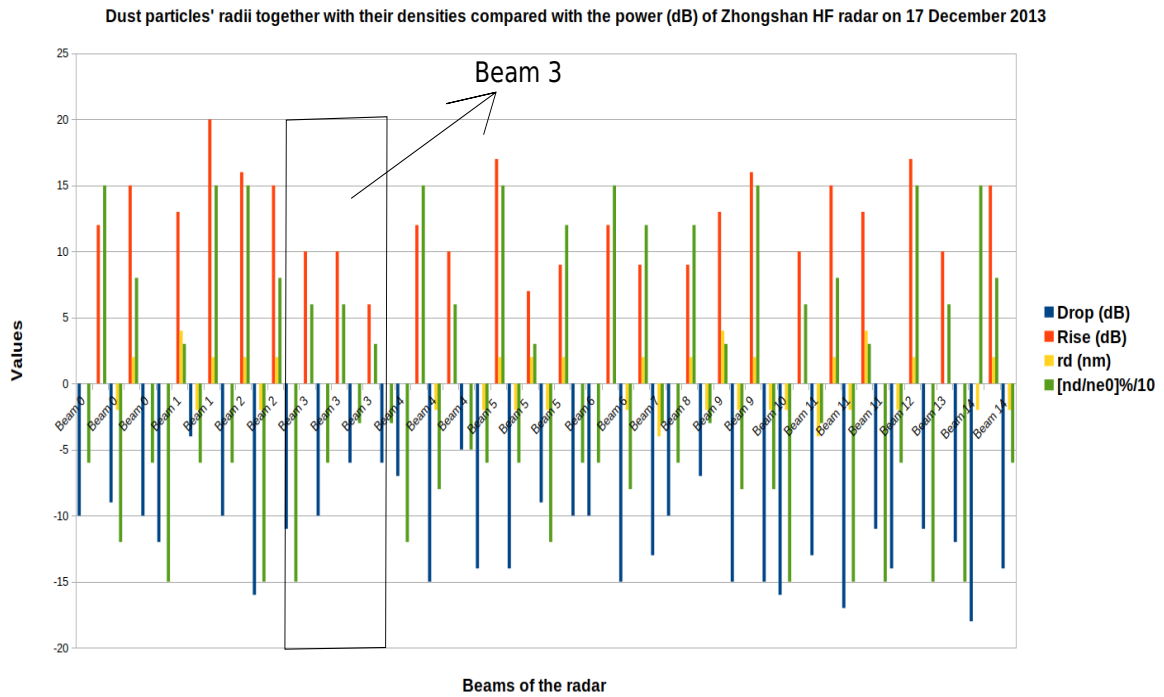


Figure 7.2: Radius and density variations of dust particles together with the variation in backscatter power (dB) received by beams 0-14 of the Zhongshan HF radar on 17 December 2013. The results of beam 3 of the radar is shown in a rectangular block.

7.3 Primary waves that are responsible for the NREs

The ionosonde measurements for the events studied show that there were E_s layers present during winter and summer in the E -region. The E_s layers were observed by the ionosonde at the Zhongshan station, located under the ionospheric trough. Electron density irregularities and E_s layers are the key parameters for the production of a polarization electric field (Woodman et al., 1991; Huang et al., 1993; Otsuka et al., 2013). The electric field, together with the plasma density gradient, triggers the formation of the GDI, which is observed by radar as type II waves (Liu and Yeh, 1966; Keskinen and Ossakow, 1983; Hamza and St-Maurice, 1993; Kelley et al., 1995; Sojka et al., 1998; Kagan and Kelley, 1998; Milan and Lester, 2001; St.-Maurice and Nishitani, 2020).

The linear growth rate (γ) due to GDI is given by equation (7.2) (Farley, 1985; Woodman et al., 1991).

$$\gamma \propto \frac{1}{1+\psi} \mathbf{k} \cdot \mathbf{V}_d (\mathbf{k} \cdot \nabla N \times \mathbf{B}) \quad (7.2)$$

where γ is the GDI linearized growth rate, \mathbf{V}_d is the drift velocity, ∇N is the plasma density gradient and \mathbf{k} is the wave vector of the perturbations. Keskinen and Ossakow (1983) also provided a detailed growth rate of the gradient drift instability and current convective instabilities in the F -region of high latitudes. GDI requires that $\mathbf{E} \parallel \nabla N$ and $\mathbf{k} \cdot (\nabla N \times \mathbf{B}) > 0$ in the F -region (Liu et al., 2019), where \mathbf{E} and \mathbf{B} are the electric and magnetic fields, respectively. Tsunoda et al. (1994) found that γ reaches its maximum when \mathbf{V}_d is westward/eastward and parallel to \mathbf{k} . γ is larger when waves propagate transversely to the magnetic field (\mathbf{B}) or when \mathbf{V}_d and \mathbf{k} are parallel, but directed away from the westward/eastward direction (Tsunoda et al., 1994). A decrease in the effective transverse gradient ($\nabla_{\perp} N$), can result in $\gamma = 0$, when \mathbf{V}_d is directed northward/southward (Tsunoda et al., 1994). When there are horizontally stratified E_s layers, GDI generates primary waves as long as \mathbf{V}_d and \mathbf{k} are westward/eastward (Tsunoda et al., 1994). If the amplitudes of the primary waves are large enough, they may develop local electron drift with the same drift velocity (\mathbf{V}_d) which is caused by the local gradient ($\nabla_{\perp} n$) and the electric field created by those waves. Here n is the local wave perturbation in N . The relationship

between the wavelength of the primary waves (λ_p) and the wavelength of secondary waves (λ_s) was derived by neglecting the ion inertia (Tsunoda et al., 1994). The relationship between the upper boundary of λ_p and λ_s is given by equation (7.3):

$$\lambda_p \leq \frac{v_i^2 \Omega_e V_d A^2 \lambda_s^2}{4\pi v_e \Omega_i C_s^2 (1 + \psi)^2} \quad (7.3)$$

where v_i and v_e are the neutral-ion and electron collision frequencies, respectively. The ion and electron gyro-frequencies are Ω_i and Ω_e , respectively. Note that ψ is the ratio of the product of neutral-particle collision frequencies to the product of their gyro-frequencies and C_s is the ion-acoustic speed. A here stands for the relative amplitude of the primary wave, and together with V_d , they control λ_p for GDI growth. To have GDI, for small/large values of A and V_d , λ_p should be small/large, respectively. Equation (7.4) gives the lower boundary of λ_p :

$$\lambda_p \geq 2\pi \left[\frac{v_e L_y}{v_i \Omega_e V_d} \left[C_s^2 (1 + \psi) - \frac{V_d^2}{(1 + \psi)} \right] \right]^{1/2} \quad (7.4)$$

where ψ is the ratio of the product collisional (ν) and gyro-frequencies (Ω) of ions and electrons (Greenwald, 1974; Kagan and Kelley, 1998), which is expressed by equation (4.29) and $V_d = E/B$. $L_y = -N/[(dN/dz)\cos I]$ is the meridional GDI gradient scale length, where I is the magnetic dip angle and z is the altitude on the vertical upward axis (Kagan and Kelley, 1998). An enhanced electron density at the bottom of the E -region, leads to an eastward wind and $\mathbf{E} \times \mathbf{B}$ drift that generate a polarization electric field, and thus the GDI, and hence the NREs (St.-Maurice and Nishitani, 2020).

TIDs passing through the ionospheric F -region produce a polarization electric field. The electric field is then mapped along the equipotential magnetic field lines down to the E -region. Thus, this polarized electric field affects the GDI and modulates backscatter power in the near range gates of the HF radars. St.-Maurice and Nishitani (2020) noted that passing AGWs/TIDs may modulate the gradient scale length L_y through compression and/or shear. The background and polarization electric field and the eastward neutral wind play a vital role in the modulation of L_y used in equation (7.4). The vertical gradient scale length $L_z = N/(dN/dz)$ (Kagan and Kelley, 1998) could also be modulated by passing AGWs/TIDs (St.-Maurice and Nishitani, 2020).

Figure 7.3 shows the range of wavelengths of the primary waves caused by AGWs/TIDs. These primary waves are responsible for the secondary waves observed by SuperDARN HF radars by means of equations (7.3) (for the upper boundary) and (7.4) (for the lower boundary). Figure 7.3 A) shows the primary wavelengths responsible for causing secondary waves of 12 m detected by the SANA E HF radar on 15 July 2012, and Figure 7.3 B) shows those waves responsible for 10 m secondary waves observed by the Zhongshan HF radar on 22 November 2013. The MSISE-90 and IRI-2016 models were used to estimate the collisional frequencies (St.-Maurice and Nishitani, 2020). Additionally, magnetometer data were used to estimate the electron and ion gyro-frequencies. The relative velocity between the electrons and ions was (a) $V_d = 50$ m/s, (b) $V_d = 100$ m/s, (c) $V_d = 200$ m/s, and (d) $V_d = 400$ m/s as identified in Figure 7.3. The relative amplitude of the primary waves were assumed to be 5% (blue), 10% (orange), 20% (green) and 40% (red), and $L_y = 500$ (blue-violet), 1000 (brown), 2000 (violet) and 4000 m (gray). The area between the lower boundary of $L_y = 1000$ m and the upper boundary of $A = 0.2$ shows the range of primary waves that may have caused backscatter at 12 m (SANA E) or 10 m (Zhongshan). Considering A and L_y constant, the range of primary waves increased as V_d increased, i.e., λ_p was between ~ 30 and 70 m for $V_d = 50$ m/s, and between ~ 30 and 400 m for $V_d = 400$ m/s for the event on 15 July 2012.

The range of primary wavelengths for the event on 22 November 2013 is shorter than those on 15 July 2012. They vary between ~ 30 and 55 m for $V_d = 50$ m/s, and between ~ 30 and 350 m for $V_d = 400$ m/s. Figure 7.3 shows that the maximum range of primary waves occurred at an altitude of ~ 98 km. Similar results were found for 28 May 2011 and 17 December 2013 and are presented in Figure 7.4. Figure 7.4 shows the range of wavelengths of primary waves that could have caused the NREs on 28 May 2011 (A) and 17 December 2013 (B). In discussing FAIR echoes, St.-Maurice and Nishitani (2020) suggested that to get backscatter echoes, λ_p should be around 100 m, when E/B is between 200 and 300 m/s. This condition excludes the results obtained when using $V_d = 50$ and 100 m/s. However, at $V_d = 200$ m/s, there are some waves that fulfill this condition for $A = 0.1$ and $1000 \text{ m} < L_y < 2000 \text{ m}$. Considering the drift velocity and the relative amplitude of plasma waves, changes in the polarization electric field caused by TIDs causes variations in L_y (St.-Maurice and Nishitani, 2020); as a result, λ_p also varies. Once the Bragg scatter condition of the radar is met, the SuperDARN radar

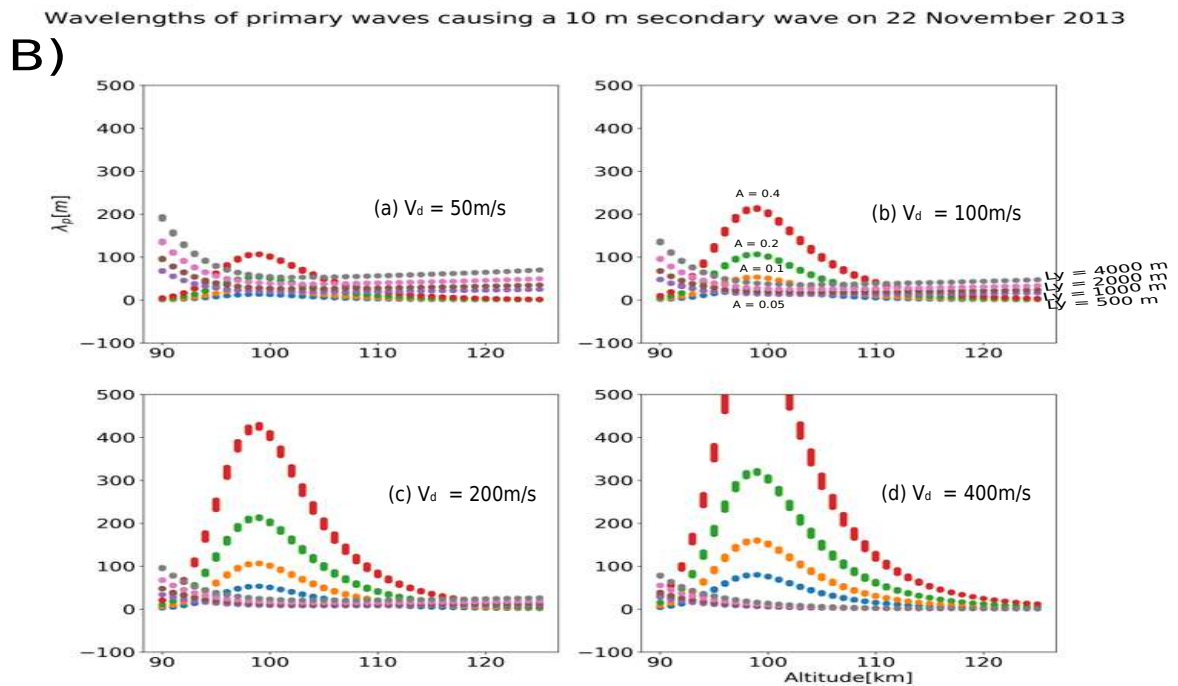
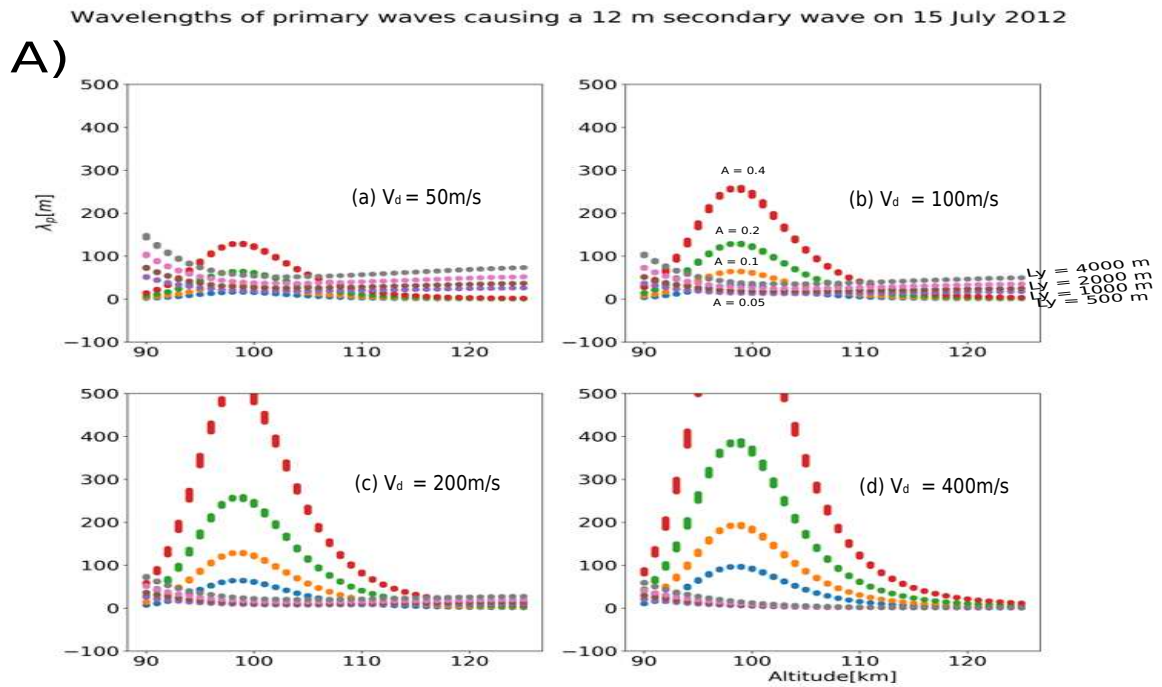


Figure 7.3: Panel A) shows the primary wave wavelengths as derived from data for 15 July 2012, supplied by the SuperDARN HF radar (SANA) operating at 12.57 MHz and panel B) shows the wavelengths of the data for 22 November 2013 supplied by the Zhongshan radar operating at 10.25 MHz. The relative velocity between electrons and ions is (a) $V_d = 50$ m/s, (b) $V_d = 100$ m/s, (c) $V_d = 200$ m/s and (d) $V_d = 400$ m/s . The relative amplitude (compared to the background) of the primary waves are assumed to be 5% (blue), 10% (orange), 20% (green), and 40% (red) and $L_y = 500$ (blue-violet), 1000 (brown), 2000 (violet), and 4000 m (gray).

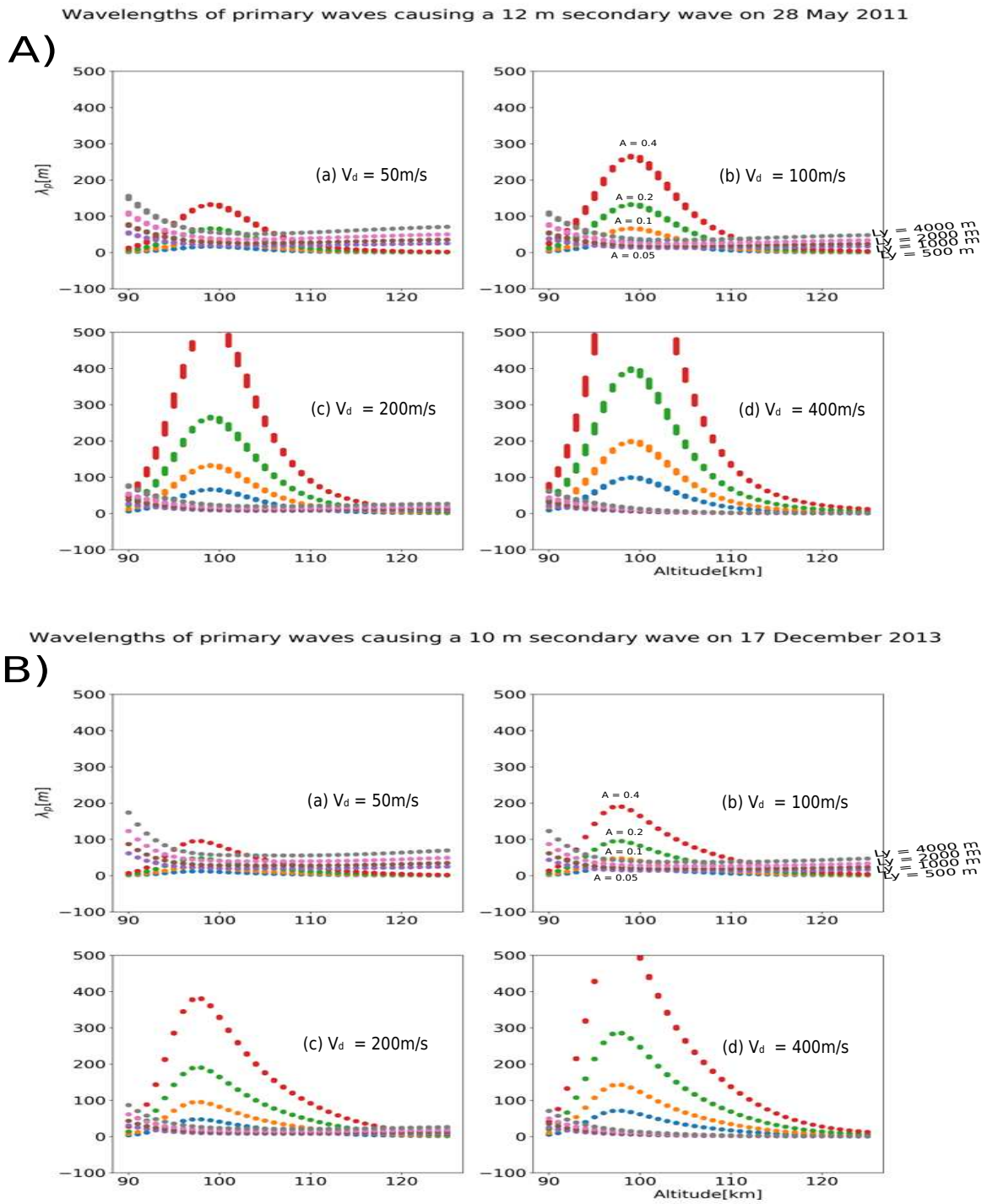


Figure 7.4: Panel A) shows the primary wave wavelengths as derived from data for 28 May 2011, supplied by the SuperDARN HF radar (SANAÉ) operating at 12.57 MHz, and panel B) shows the wavelengths of the data for 17 December 2013 supplied by the Zhongshan radar operating at 10.25 MHz. The relative velocity between electrons and ions is (a) $V_d = 50$ m/s, (b) $V_d = 100$ m/s, (c) $V_d = 200$ m/s and (d) $V_d = 400$ m/s . The relative amplitude (compared to the background) of the primary waves are assumed to be 5% (blue), 10% (orange), 20% (green) and 40% (red), and $L_y = 500$ (blue-violet), 1000 (brown), 2000 (violet) and 4000 m (gray).

observes NREs as discussed here.

7.4 Cross-correlation using detrended data

Detrended data were used to do the cross-correlation between the electric field or the plasma density scale height and the SuperDARN backscatter power. To check the contribution of the data trend, a linear detrend was used to remove the trend. Figure 7.5 shows the cross-correlation between the linear detrended electric field ($E_y d$) (panel c) and the linear detrended average backscatter power of all beams for range gate 2 (p2d) (panel e) of the SANA radar for the event S1 on 15 July 2012. It also shows the cross-correlation between the linear detrended calculated plasma density scale height ($Lz d$) (panel d) and the linear detrended average backscatter power of all beams for range gate 2 (p2d) (panel e). Panel (f) and panel (g) show that the CC estimated was -0.51. Figures 7.6 and 7.7 are similar to Figure 7.5. They show that the CC is -0.54 for the event Z1 on 22 November 2013 (Figure 7.6) and -0.61 for event Z2 on 17 December 2013 (Figure 7.7). According to Lansangan and Barrios (2009), a CC between 0.45 and 0.65 indicates a moderate correlation.

7.5 Summary

This chapter discussed the mechanism that causes the NREs. It leads to the conclusion that meteor trail echoes, HAIR and PMSEs are unlikely mechanisms for the production of NREs. The DUSTY model developed by Mahmoudian et al. (2011), was used to estimate the number density of dust particles and their radii, based on the assumption that one summer event contained PMSEs that had been modulated by TIDs. It was determined that PMSEs are not the most likely cause of NREs. There is a possibility that during summer PMSEs would have contributed to the NREs in this study. The most likely mechanism to cause NREs is the GDI at the bottom-side of the E -region. There was a correlation between NRE and TID backscatter power and their periods of oscillation were equal. The electrodynamic coupling between the F - and E -region of the ionosphere contributed to this modulation of NREs. The polarization electric field created by TIDs and F -region dynamo background electric field was mapped down to the E -region along the equipotential magnetic field lines to generate the observed modulated NREs. The electric field and the estimated gradient scale height were compared with the backscatter power of near gates, and a moderate correlation was found. It was found that primary waves are responsible for the secondary waves which can be observed by SD radars were associated with the GDI. The final chapter draws conclusions from the work that was done and suggests future work.

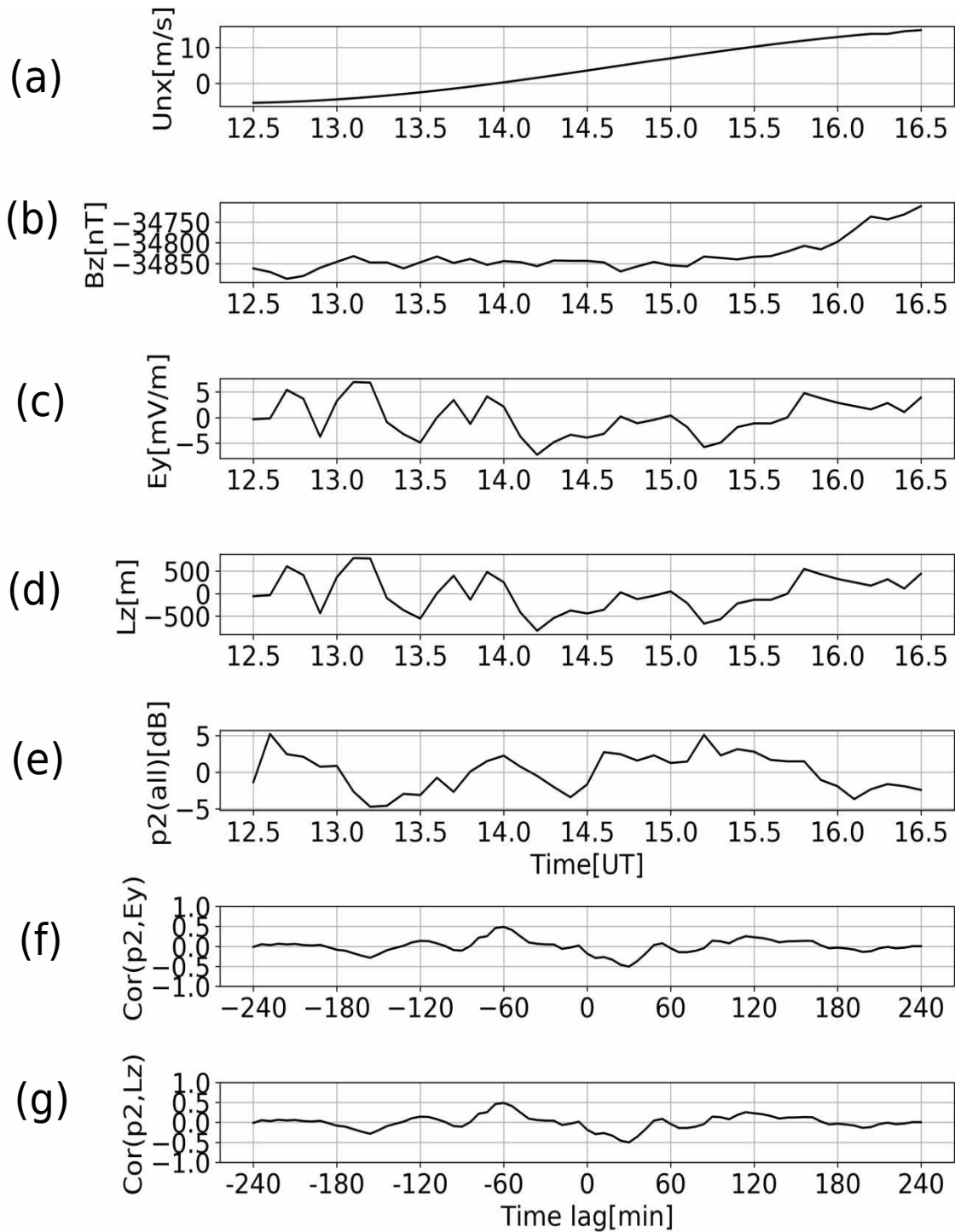


Figure 7.5: For 15 July 2012 from 12:30 to 16:30 UT at an altitude of 100 km altitude (case S1): (a) modeled eastward neutral wind, (b) Z-component of the Earth's magnetic field at ground level, (c) the linear detrended observed northward electric field ($E_y d$), (d) the linear detrended calculated plasma density scale height (Lzd), (e) the linear detrended average backscatter power of all beams for range gate 2 ($p2$), (f) the cross-correlation between $E_y d$ (panel c) and $p2$ (panel e), and (g) cross-correlation between Lzd (panel d) and $p2$ (panel e).

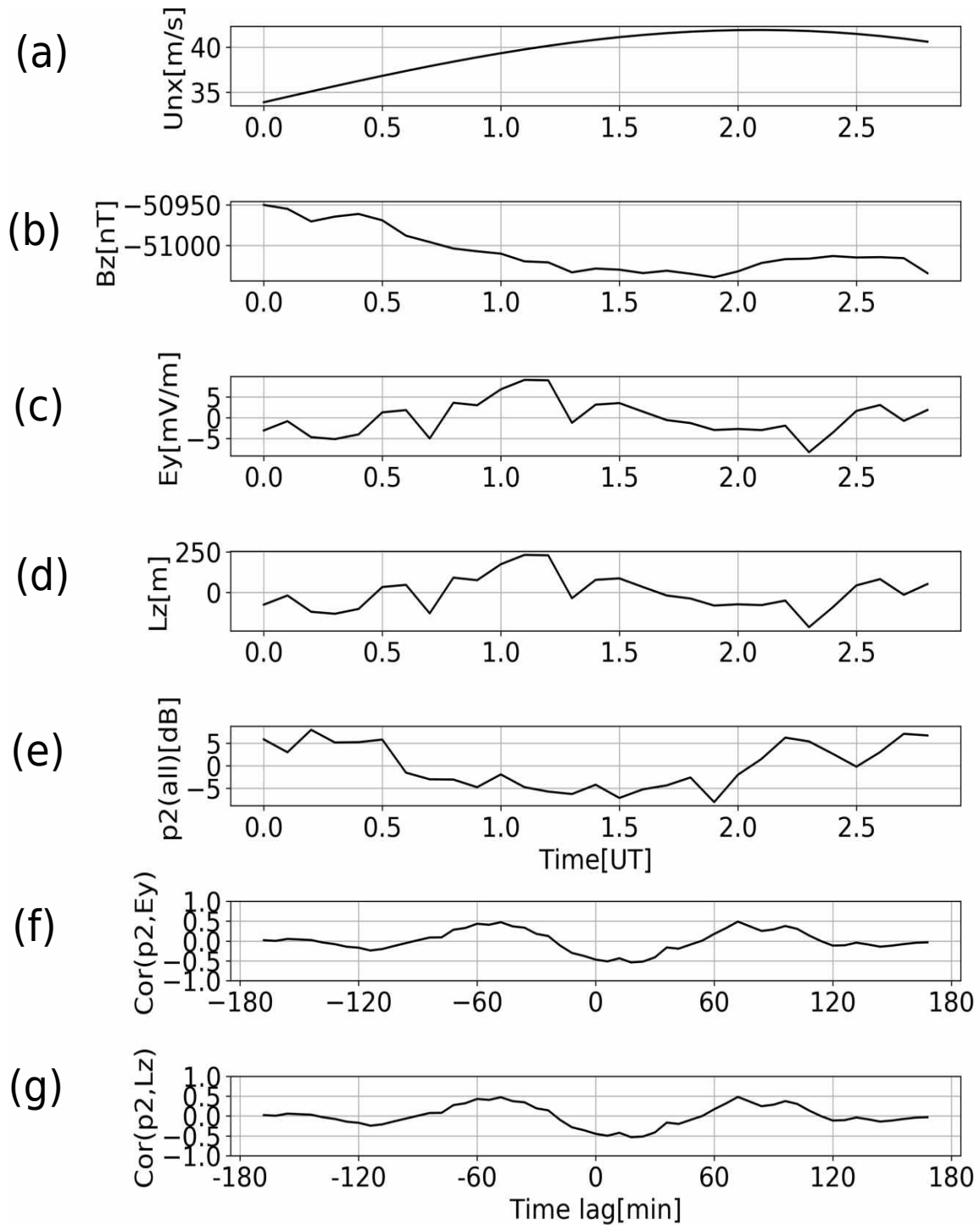


Figure 7.6: For 22 November 2013 from 00:00 to 02:48 UT at an altitude of 100 km (case Z1): (a) modeled eastward neutral wind, (b) Z-component of the Earth's magnetic field at ground level, (c) the linear detrended observed northward electric field ($E_y d$), (d) the linear detrended calculated plasma density scale height ($Lz d$), (e) the linear detrended average backscatter power of all beams for range gate 2 ($p2 d$), (f) the cross-correlation between $E_y d$ (panel c) and $p2 d$ (panel e), and (g) cross-correlation between Lz (panel d) and $p2 d$ (panel e).

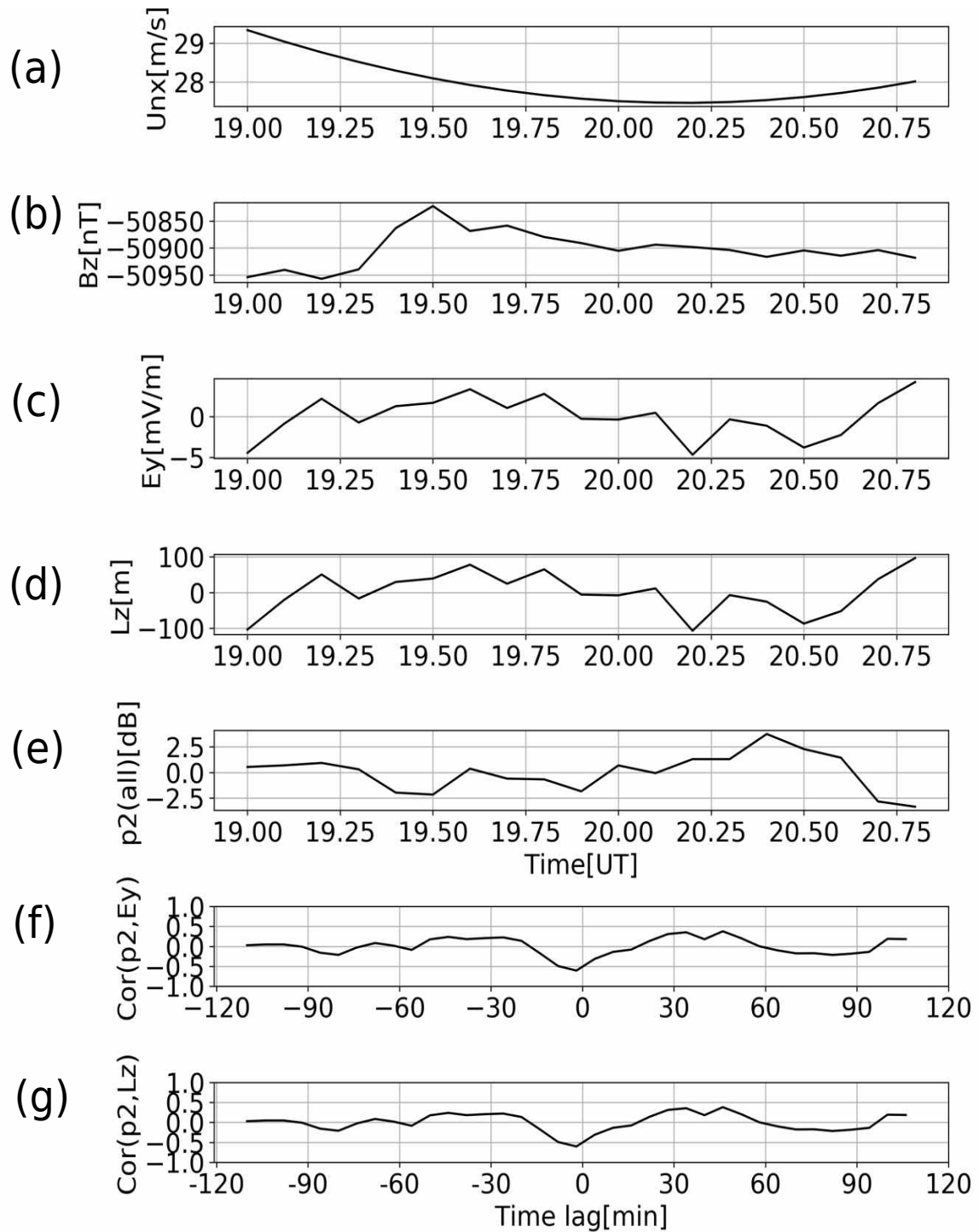


Figure 7.7: For 17 December 2013 from 19:00 to 20:48 UT at an altitude of 100 km (case Z2): (a) modeled eastward neutral wind, (b) Z-component of the Earth's magnetic field at ground level, (c) the linear detrended observed northward electric field ($E_y d$), (d) the linear detrended calculated plasma density scale height ($Lz d$), (e) the linear detrended average backscatter power of all beams for range gate 2 ($p2 d$), (f) the cross-correlation between $E_y d$ (panel c) and $p2 d$ (panel e), and (g) cross-correlation between Lz (panel d) and $p2 d$ (panel e).

Chapter 8

CONCLUSIONS AND SUGGESTIONS

8.1 Introduction

This thesis relates effects of MSTIDs observed in the F -region on NREs observed in E -region at high latitudes, based on the data from the SuperDARN HF radar network. Four data sets from two SuperDARN radars, both in Antarctica were analyzed. Two events occurred during geomagnetic storms in winter and were observed by the SANAE HF radar. Two other events occurred during quiet time in summer and were observed by the Zhongshan HF radar. MSTIDs are those echoes beyond the 315 km range, while NREs are the echoes between the first range gate (180 km) and the fourth range gate (315 km).

In order to determine the effects of MSTIDs on NREs, FFT, cross correlation, and statistical analysis involving the Spearman correlation coefficients of the backscatter power of the SuperDARN (SD) radar NREs and MSTIDs are used. Then the cross-correlation between the electric field close to the NREs and their backscatter power was investigated. The density gradient scale length due to the GDI, which were used to find the cross correlation with the NREs backscatter power, was estimated. Measuring electric field directly in the E -region is difficult. Normally, SuperDARN data in the F -region are used, magnetic field lines are assumed to be equipotential and in the polar regions quasi-vertical, and then the F -region electric field is mapped down to the E -region. The Virginia Tech (VT) website supplied the derived electric field for the specified location and time. Other parameters required for the estimation of the scale length were derived by means of the IRI-2016, MSIS-90 and HWM-14 models. The IRI is a model built around statistical averages. The model is extrapolated to regions where there are no measurements. The model is only accurate for quiet non-storm conditions where the background plasma density is steady. For geomagnetic storms with auroras, the model is not accurate and probably underestimates the electron density. The analysis and exercise in correlation between MSTIDs and NREs led to the conclusion that the GDI is the likely mechanism that relates MSTIDs and NREs. This chapter presents a summary of the findings of this study and gives some recommendations for further research.

8.2 Conclusions

Based on the results of this study, the conclusions are drawn as follows:

1. This study focused on MSTIDs and NREs occurring during the noon and afternoon sectors in winter during a geomagnetic storm, and the morning and evening sectors in summer during a geomagnetically quiet time. The characteristics of the MSTIDs and their propagation direction were consistent with the earlier studies that illustrated the coupling between the F and E ionospheric regions. It was concluded that NREs were echoes of a GDI process observed in the SuperDARN data. Pre-existing plasma density gradients, the ambient meridional convection electric field together with $\mathbf{E} \times \mathbf{B}$ ionospheric plasma drifts and zonal (eastward) thermospheric neutral winds led to this conclusion. According to St.-Maurice and Nishitani (2020) FAIR echoes are observed as NREs in the lower E -region. Plasma irregularities, such as sporadic E_s layers, facilitate the GDI mechanism.
2. To estimate the quantitative contribution of MSTIDs to NREs, the most robust Spearman correlation coefficient was used. The correlation between the backscatter power of MSTIDs and NREs that were received by the same SuperDARN HF radar was moderate. Based on the correlation coefficients for the four events mentioned, the contribution by the MSTIDs was sometimes below 10% or above 40% (using different individual gates), but generally most of the SuperDARN gates indicated a moderate correlation of $\sim 10\%$ (average of all correlation coefficients) between the MSTIDs and NREs.

3. As expected, the wind speed in the E -region and upper D -region was slow. In this region, the ions become demagnetized, i.e., the neutral winds create an electric field by pushing the ions across the magnetic fields, so that $\mathbf{E} = -\mathbf{U} \times \mathbf{B}$. The F -region electric field, close to where the NRE modulation by passing MSTIDs occurs, was used. The MSTIDs generate a polarization electric field in the F -region to maintain the field-line-integrated electric current in the F -region (Otsuka et al., 2004, 2007). The polarized electric field is a result of the inhomogeneity of the field-line-integrated Pedersen conductivity traversed by the ionospheric current. This polarization electric field modulates the background convection electric field, which is then transmitted into the E -region along the equipotential magnetic field lines. The background neutral wind may also change the modulation in the ionospheric electric field. This can then drive GDI if it meets the required amplitude of the electric field. Presumably, the GDI exists in the E -region where the electron density gradients maximize. The presence of E_s -layers between altitudes of 95 and 125 km is a good example of plasma gradients which could facilitate the generation of GDI in the near ranges. The GDI explanation works for both winter and summer events. However, in the summer there is a possible alternative and/or additional possibility of PMSE.
4. The meridional component of the net electric field (quasi-static convection plus oscillating polarization), mapped down from the F - to E -region along the equipotential magnetic field lines (Sun et al., 2015; Liu et al., 2019), modulates the GDI which is responsible for generating the NREs (St.-Maurice and Nishitani, 2020). For most of the radar gates that were analyzed in this study, the cross-correlation between the linear detrended meridional electric field or the linear detrended plasma density gradient scale height and the linear detrended backscatter power was between -0.51 and -0.61, i.e., moderately anti-correlated.
5. SuperDARN HF radars cannot estimate the altitude of the backscatter with high precision as VHF radars do. Those having interferometers to measure angle-of-arrival use the elevation angle to calculate the virtual height of the source of echoes by ray tracing, which is still subject to improvement (Ponomarenko et al., 2018). Thus, the problem of whether PMSEs are part of SuperDARN NREs remains (Ponomarenko et al., 2016). In principle, MSTIDs can modulate PMSEs in the same way that AGWs modulate Noctilucent Clouds (Dalin et al., 2004), but there is not enough evidence that the phenomenon is observable by SuperDARN HF radars. The events in winter when both MSTIDs and NREs occurred near-simultaneously leads to the conclusion that the GDI mechanism is more likely responsible for these echoes than polar mesospheric winter echoes, because PMWEs (Kirkwood, 2007; Latteck and Strelnikova, 2015) tend to occur at altitudes that correspond to ranges shorter than 180 km and therefore PMWEs are generally not observed by SuperDARN radars. The nearest altitude where echoes can be observed by SuperDARN radars is $\sim 100 \pm 3$ km (Ponomarenko et al., 2016; St.-Maurice and Nishitani, 2020).

8.3 Suggestions for further research

1. Currently, there is no VHF radar located under the near range gates of a SuperDARN HF to help identify whether some or all NREs in summer are PMSEs. Another possible assumption is that both PMSEs and GDI or other phenomena could contribute to the production of NREs. Events during winter, do not exhibit PMSEs, so they are likely caused by the GDI. A long-term study of these echoes would be necessary to solve this ambiguity.
2. A simultaneous study of TIDs and NREs in both hemispheres by means of conjugate SuperDARN HF radars is recommended, because the electric field is similar in both hemispheres. Justification for such a study is simultaneous conjugate observation of AGWs by Otsuka et al. (2004) and Martinis et al. (2019).
3. Modeling the TIDs and their effects on NREs would enhance the understanding of the physics behind the two phenomena.

The results of the investigation into the mechanism that relates MSTIDs to NREs are offered here in this section (section 8.3) as a paper published by JGR. The paper explains how a passing TIDs polarize the electric field and the effects they have on NREs.

JGR Space Physics



RESEARCH ARTICLE

10.1029/2021JA030157

Key Points:

- Traveling Ionospheric Disturbances partially modulate SuperDARN Near Range Echoes
- Zonal wind and meridional convection electric field produce Gradient Drift Instabilities observed as Near Range Echoes in the *E*-region
- Traveling Ionospheric Disturbances propagating in the *F*-region partially modulate the Gradient Drift Instabilities

Supporting Information:

Supporting Information may be found in the online version of this article.

Correspondence to:

M. J. Kosch and A. Hiyadutuje,
mkosch@sansa.org.za;
hiyadutujea@yahoo.fr

Citation:

Hiyadutuje, A., Kosch, M. J., & Stephenson, J. A. E. (2022). First observations of *E*-region Near Range Echoes partially modulated by *F*-region Traveling Ionospheric Disturbances observed by the same SuperDARN HF radar. *Journal of Geophysical Research: Space Physics*, 127, e2021JA030157. <https://doi.org/10.1029/2021JA030157>

Received 25 NOV 2021
 Accepted 10 APR 2022

Author Contributions:

Data curation: Alicreance Hiyadutuje
Formal analysis: Alicreance Hiyadutuje
Investigation: Alicreance Hiyadutuje
Methodology: Alicreance Hiyadutuje, Michael J. Kosch, Judy A. E. Stephenson
Supervision: Michael J. Kosch, Judy A. E. Stephenson
Writing – original draft: Alicreance Hiyadutuje
Writing – review & editing: Michael J. Kosch, Judy A. E. Stephenson

© 2022 The Authors.

This is an open access article under the terms of the [Creative Commons Attribution-NonCommercial License](https://creativecommons.org/licenses/by/4.0/), which permits use, distribution and reproduction in any medium, provided the original work is properly cited and is not used for commercial purposes.

First Observations of *E*-Region Near Range Echoes Partially Modulated by *F*-Region Traveling Ionospheric Disturbances Observed by the Same SuperDARN HF Radar

Alicreance Hiyadutuje^{1,2} , Michael J. Kosch^{1,2,3,4} , and Judy A. E. Stephenson² 

¹South African National Space Agency, Hermanus, South Africa, ²Department of Chemistry and Physics, University of KwaZulu-Natal, Durban, South Africa, ³Department of Physics and Astronomy, University of Western Cape, Cape Town, South Africa, ⁴Department of Physics, University of Lancaster, Lancaster, UK

Abstract We present the first observations from SuperDARN HF radar data of *E*-region Near Range Echoes (NREs) whose amplitudes are partially modulated by Medium-Scale Traveling Ionospheric Disturbances (MSTIDs) propagating in the *F*-region overhead that have been observed by the same radar in the far ranges. SuperDARN NREs occur normally ~180–315 km downrange from the radar at ~95–125 km altitude. Selected observations of TID-modulated NREs are presented from SANAE and Zhongshan Antarctic SuperDARN radars for both summer and winter seasons as well as geomagnetic active and quiet times. We show that the most likely mechanism is partial modulation of the Gradient Drift Instability (GDI), which is responsible for producing the NREs. GDI is driven by the velocity difference between neutrals and ions and may appear in the *E*-region ionosphere wherever suitable plasma density gradients exist. GDI already present in the *E*-region can be partially modulated by an MSTID passing overhead in the *F*-region via the additional MSTID polarization electric field mapped down in altitude along the equipotential magnetic field lines, thereby partially modulating the NRE amplitudes as observed.

1. Introduction

Atmospheric Gravity Waves (AGWs) carry significant momentum and energy throughout the Earth's atmosphere (Francis, 1975; Fritts, 1984; Hunsucker, 1982) and may be observed in the upper atmosphere by the SuperDARN global network of radars (Chisham et al., 2007; Oinats et al., 2015) as Traveling Ionospheric Disturbances (TIDs) through the interaction between the neutral and ionized components of the atmosphere. However, TIDs may also be driven by ionospheric electric fields via the Perkins instability at nighttime (Y. Liu et al., 2019, and reference therein). TIDs may be observed in the ionospheric *F*-region 30%–50% of the time (Francis, 1974). TIDs are divided into two main classes: Large-Scale Traveling Ionospheric Disturbances (LSTIDs) with horizontal wavelengths of >1,000 km, velocities of ~400–1,000 m/s, and periods of ~0.5–3 hr and Medium-Scale Traveling Ionospheric Disturbances (MSTIDs) with horizontal wavelengths of hundreds of km, velocities of ~100–500 m/s, and periods of ~15–60 min (Grocott et al., 2013; Hayashi et al., 2010; He et al., 2004; Hocke & Schlegel, 1996; Oinats et al., 2015). The many possible AGW/TID sources and their propagation modes have been investigated (e.g., Hocke & Schlegel, 1996; He et al., 2004; Grocott et al., 2013). LSTIDs are generated in the auroral or sub-auroral region as a result of Lorentz forces and Joule heating caused by the enhancement of the auroral electrojets and/or intense precipitation of charged particles during geomagnetic storms (Ding et al., 2008; Palmroth et al., 2005; Waldock & Jones, 1986). Storm-induced TIDs usually propagate equatorward from high latitudes and sometimes cross the equator (Ding et al., 2008; Habarulema et al., 2015; Tsugawa et al., 2004). MSTIDs are the most common at high latitudes, often caused by the auroral electrojets, and may propagate horizontally, obliquely, or vertically in the ionosphere (Hocke & Schlegel, 1996). They may propagate from the source either obliquely up to the *F*-region or initially downward and reach the *F*-region after the reflection from the ground (Francis, 1974; Hernández-Pajares et al., 2006). High-latitude MSTIDs have been observed propagating equatorward (Grocott et al., 2013; Samson et al., 1990), westward (Samson et al., 1990), and poleward (Habarulema et al., 2015). At southern high latitudes, the probability of medium-scale AGW observations was highest in winter and lowest in summer months (Ogawa et al., 1987) but they may occur at any time.

SuperDARN is a global network of HF radars (Chisham et al., 2007; Greenwald et al., 1995) that normally observe Bragg backscatter from magnetic field-aligned plasma irregularities (FAIs), which are common in the

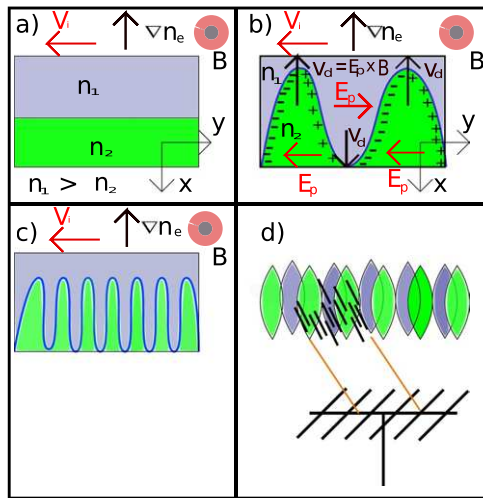


Figure 1. A cartoon showing how a plasma density disturbance in the southern hemisphere may result in radar coherent backscatter via the Gradient Drift Instability mechanism (adapted from Gillies (2012)). The magnetic field (\mathbf{B}) is out of the page. Panel (a) shows two stable layers with plasma densities $n_1 > n_2$. In the E -region, the ionospheric electric field will be approximately parallel to the ion velocity (\mathbf{V}_i). In the F -region, due to convection, the ionospheric electric field will be approximately parallel to the plasma density gradient (∇n_e). Panel (b) shows any wave-like perturbation on the plasma boundary, will result in a charge separation, and an oscillating polarization electric field (\mathbf{E}_p). \mathbf{E}_p drives a plasma drift (\mathbf{V}_d) that grows the plasma perturbation. Panel (c) shows the time development of the plasma perturbation, cascading to shorter wavelengths. Panel (d) shows the coherent scatter by these plasma structures once the Bragg scatter condition is met.

F -region ionosphere, for ray paths that satisfy the necessary aspect condition (Ruohoniemi et al., 1989). SuperDARN radars also observe backscatter from the ground or sea surfaces due to HF refraction in the ionosphere. The SuperDARN radars readily detect MSTIDs as wave-like perturbations in the backscatter (Chisham et al., 2007; Hunsucker, 1982; Miyoshi et al., 2018; Nishitani et al., 2019), typically in the range of ~ 600 – $1,200$ km. MSTIDs are either observed in the ground/sea scatter echoes, which have Doppler velocities less than ± 50 m/s with narrow spectral widths of < 20 m/s (Grocott et al., 2013; Nishitani et al., 2011), or in the ionospheric scatter echoes, typically with Doppler velocities greater than ± 50 m/s and wide spectral widths of > 50 m/s (Grocott et al., 2013; Ponomarenko et al., 2009).

SuperDARN may observe E -region coherent echoes at ~ 95 – 125 km altitude in the first few near range gates (0–3), typically 180–315 km downrange due to its oblique sounding, called Near Range Echoes (NREs) (Hall et al., 1997; Hussey et al., 2000; Jenkins & Jarvis, 1999; Ogawa et al., 2009). These may have several sources. Intermittent meteor trails at ~ 80 – 120 km altitude cause NREs (Hall et al., 1997; Hussey et al., 2000; Jenkins & Jarvis, 1999). NREs have been associated with Polar Mesospheric Summer Echoes (PMSEs) at ~ 80 – 85 km altitude (e.g., Hosokawa et al., 2005; Ogunjobi et al., 2015, 2017). However, there is some doubt about this mechanism based on altitude observations (Ponomarenko et al., 2016) and because NREs are also observed in the winter. The Polar Mesospheric Winter Echoes (PMWEs) phenomenon only occurs sporadically at ~ 50 – 85 km altitude (Kavanagh et al., 2006), which corresponds to SuperDARN ranges less than the typical minimum (180 km). Another type of NRE is the High-Aspect Angle Irregularity Regions (HAIR), which is related to the Farley-Buneman Instability (FBI) at an altitude of ~ 120 km for higher ionospheric electric fields (> 40 mV/m) (Drexler & St-Maurice, 2005; St-Maurice & Nishitani, 2020) and so-named because ray path orthogonality is not strictly required.

In addition, St.-Maurice and Nishitani (2020) found that SuperDARN NREs are associated with the Gradient Drift Instability (GDI) at an altitude of $\sim 100 \pm 3$ km. These radar echoes were named Far-Aspect Angle Irregularity Regions (FAIR). GDI results from the presence of a plasma density gradient in a favorable direction to allow GDI growth, which is driven by the neutral wind (\mathbf{U}_n) and ion drift (\mathbf{V}_i) (Makarevich, 2014; Sojka et al., 1998; Y. Liu et al., 2019). In the ionosphere, GDI and NREs are closely linked with zonal neutral wind and ion drift (equivalently meridional ionospheric convection electric field (\mathbf{E}_c)) and plasma density gradients (∇n_e) (St.-Maurice & Nishitani, 2020), all of which occur routinely. If plasma convecting in the ionosphere encounters a change in plasma density (equivalently conductivity), then the ions flow faster/slower in the region of higher/lower conductivity. At the boundaries of the plasma irregularities, charges will build up because ions arrive faster than they can depart or vice versa. The electrons are relatively unaffected because of their much lower collision (ν) to gyration (Ω) frequency ratio. The charge imbalance at a plasma density boundary sets up a counter polarization electric field, which then exerts its own $\mathbf{E} \times \mathbf{B}$ force on the plasma. With the correct geometry, the boundaries of the plasma irregularities become reinforced (i.e., steeper plasma density gradients), thereby enhancing polarization electric field, thereby resulting in positive feedback and hence the GDI grows.

The SuperDARN backscatters associated with NREs are generated through a secondary process where the large-scale gradient drift waves, of the order of 100 m, trigger secondary Farley-Buneman waves of the order of 10 m (St.-Maurice & Nishitani, 2020; Tsunoda et al., 1994). This process occurs most efficiently at ~ 98 km altitude (Tsunoda et al., 1994) and is the most efficient way in which the 10–15 m plasma structures observed by SuperDARN HF radars can be developed (St.-Maurice & Nishitani, 2020). Figure 1 demonstrates the GDI process that leads to the observed NREs for southern hemisphere geometry. At high latitudes in the lower E -region (~ 100 km altitude), the ions are unmagnetized due to collisions with the neutrals (i.e., $\nu_{in} \gg \Omega_i$), so they tend to drift (\mathbf{V}_i) in the electric field (\mathbf{E}) direction, whereas the electrons are magnetized (i.e., $\nu_e \ll \Omega_{en}$), so they drift (\mathbf{V}_e) in the $\mathbf{E} \times \mathbf{B}$ direction. Panel (a) shows two regions with different plasma densities (n) such that $n_1 > n_2$. In the E -region,

\mathbf{V}_i is approximately in the direction of \mathbf{E} but the amplitude of \mathbf{V}_i depends on the plasma density. Panel (b) shows that any random wave-like perturbation at the boundary will result in positive charges accumulating at a boundary due to more ions arriving than departing and vice versa. Alternating polarization electric fields (\mathbf{E}_p) are set up, creating $\mathbf{E}_p \times \mathbf{B}$ drifts (\mathbf{V}_d) as shown, which further enhance the boundary perturbation. Panel (c) shows the two different plasma regions that penetrate one another as the instability grows, which break down into narrow finger-like structures of shorter wavelength. Panel (d) shows that the finger-like structures of plasma density separate and substructures of plasma irregularities will be created in all directions perpendicular to the magnetic field (Gondarenko & Guzdar, 2001), which form a source of radar echoes when the Bragg scatter condition is met, that is, 10–15 m for SuperDARN radars (Greenwald et al., 1995; Ponomarenko & Waters, 2006). These substructures are effectively visible to radars from almost all directions (St.-Maurice & Nishitani, 2020) and therefore do not have to be magnetic field-aligned. We note that in the F -region, where both electrons and ions are fully magnetized, we require \mathbf{E} quasi-parallel to ∇n_e (Y. Liu et al., 2019) so that \mathbf{V}_i remains quasi-perpendicular to ∇n_e . This change in horizontal E -field direction gives the same geometry for GDI in the collision-less F -region as it does for the collisional E -region.

SuperDARN HF radars observe the FAIR echoes caused by the GDI cascading to shorter wavelengths (St.-Maurice & Nishitani, 2020). The GDIs are triggered when there is a strong enough plasma density gradient through which the ions must drift, which may happen during auroral precipitation or in the presence of sporadic E -layers (E_s layers) (Kagan & Kelley, 1998; Kirkwood & Von Zahn, 1991). Sometimes, during geomagnetic storms and auroral precipitation, both the GDI at ~ 100 km altitude (for FAIR echoes) and the FBI at ~ 125 km altitude (for HAIR echoes) may occur simultaneously (St.-Maurice & Nishitani, 2020), potentially making clear identification of each echo type difficult.

There is a strong electric field coupling between the ionospheric F and E regions because the magnetic field is essentially equipotential and the distance is only a few 100 km (Farley Jr, 1960). Also, at high latitudes, the magnetic field is near-vertical allowing for near-coincidence of E and F region phenomena in the horizontal direction. Numerous studies, mainly at midlatitudes, have shown electric field coupling between the E and F regions of the ionosphere involving TIDs (e.g., Haldoupis et al., 2003; Kotake et al., 2007; Otsuka et al., 2004, 2007, 2009; Tsunoda & Cosgrove, 2001; Y. Liu et al., 2019; Zhou et al., 2018). In addition, multiple midlatitude studies have shown that TIDs occur simultaneously with sporadic E -layers in the majority of cases (e.g., Tsunoda & Cosgrove, 2001 and references therein).

In this paper, we show for the first time the effects of MSTIDs, observed by southern hemisphere SuperDARN HF radars in the F -region ionosphere far ranges, on NREs observed by the same radars in the E -region near ranges with a suitable time delay determined by the MSTID velocity vector and assuming a constant propagation altitude. Furthermore, we show that the phenomenon is consistent with the MSTID, partially modulating the GDI mechanism.

2. Theory of E -Region Instabilities

Two kinds of ionospheric plasma instabilities that may lead to SuperDARN backscatter are possible: the first one is FBI or the related Two-Stream Instability (TSI) (Kelley, 2009; Keskinen & Ossakow, 1983). The second one is the GDI (St.-Maurice, 1985; St.-Maurice & Nishitani, 2020). The plasma oscillation frequency (ω_r) and growth rate (γ) from the local linear theory of GDI and FBI/TSI in the reference frame of the neutral wind are given by Kagan and Kelley (1998), Kelley (2009), and Kelly (2012):

$$\omega_r = \frac{\mathbf{k} \cdot (\mathbf{V}_i + \psi \mathbf{V}_e)}{1 + \psi}$$

and

$$\gamma = \frac{1}{1 + \psi} \left[\left(\frac{\psi}{v_i} \right) [(\omega_r - \mathbf{k} \cdot \mathbf{V}_i)^2 - k^2 C_s^2] + \left(\frac{1}{Lk^2} \right) (\omega_r - \mathbf{k} \cdot \mathbf{V}_i) + \left(\frac{v_i}{\Omega_i} \right) k_y \right] - 2\alpha n_0 \quad (1)$$

where

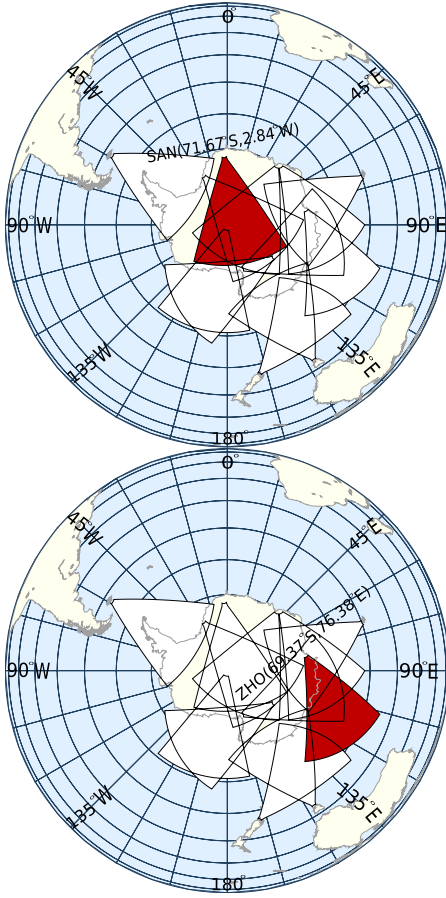


Figure 2. Southern hemisphere SuperDARN HF radars' fields of view. SANAE (top) and Zhongshan (bottom) radars' fields of view are shown in red.

$$\psi = \psi_o \left[\left(\frac{k_{\perp}^2}{k^2} \right) + \left(\frac{\Omega_e^2}{v_e^2} \right) \left(\frac{k_{\parallel}^2}{k^2} \right) \right].$$

and \mathbf{k} is the wavenumber of plasma wave, C_s is the ion-acoustic velocity, $\mathbf{V}_i = (\mathbf{E} \times \mathbf{B})/B^2$ is the ion drift velocity, L is the plasma density (n_e) gradient scale length ($L_z = 1/(\partial \ln(n_e)/\partial z)$) (St.-Maurice & Nishitani, 2020), ν is the collision frequency, and Ω is the gyrofrequency. The first term with the diffusive damping ($k^2 C_s^2$) describes the FBI or TSI, while the second term with L describes the GDI. The third term (ν/Ω_i) k_y describes the recombination damping. We neglect FBI/TSI because it is only valid for short wavelengths (i.e., $L \rightarrow \infty$) (Kelley, 2009; Keskinen & Ossakow, 1983), and also it requires a strong electric field of at least ~ 40 mV/m to occur (St.-Maurice, 1985). The linearized growth rate for GDI (γ) can then be written as (Woodman et al., 1991):

$$\gamma \propto \frac{1}{1 + \psi} \mathbf{k} \cdot \mathbf{V}_i (\mathbf{k} \cdot \nabla n_e \times \mathbf{B}) \quad (2)$$

For GDI to grow in the E -region, a significant component of \mathbf{V}_i , ∇n_e , and \mathbf{B} must be mutually perpendicular (Fejer et al., 1984; Y. Liu et al., 2019) as indicated in Figure 1. The gradient scale length in the vertical direction (L_z) is estimated by rearranging Equation 7 of St.-Maurice and Nishitani (2020). The lowest threshold condition to trigger the GDI that is responsible for the FAIR echoes, which are observed as NREs by SuperDARN, is given by:

$$L_z = \frac{(U_{nx} + E_y/B) \Omega_e \cos D}{(1 + \psi_o) (k_x \cdot C_s)^2 \left(\frac{v_{en}}{v_{in}} \right)} \quad (3)$$

where $\psi_o = \frac{v_{en} v_{in}}{\Omega_e \Omega_i}$ and $k_x = k \cos \beta \sin \theta$ and where U_{nx} is the geographic zonal neutral wind, β is the aspect angle between \mathbf{E} and \mathbf{k} , and θ is the flow angle between \mathbf{V}_i and \mathbf{k} . The smaller the value of L_z , the greater the growth rate (γ) of the GDI. Control of L_z is by the term $(U_{nx} + E_y/B)$, that is, the relative wind and ion drift velocities, and minimizes when the wind opposes the ion drift with similar velocity. Normally, the ion drift speed (E_y/B) is greater than the

neutral wind (U_{nx}), so the ionospheric electric field is the primary controlling term for the GDI growth rate. L_z has been measured in the high-latitude E -region (Haldoupis et al., 2000). They found that $L_z \approx 4\text{--}7$ km around ~ 100 km altitude, the minimum value being limited by the 3 km radar range resolution. Such small structures should trigger the GDI for a modest ionospheric electric field (St.-Maurice & Nishitani, 2020). Unsurprisingly, Haldoupis et al. (2000) found that L_z takes on larger values at higher altitudes in the topside ionosphere, that is, from 10 km to greater than 25 km.

Normally, GDI growth relates to the plasma density gradient component perpendicular to the magnetic field (L_x) as shown in Figure 1. At high latitudes, the magnetic field is near-vertical. In order to get the appropriate value of L_x , the magnetic dip angle (I) must be taken into account (Haldoupis et al., 2000):

$$L_x = \frac{L_z}{\cos(I)} \quad (4)$$

3. Instruments and Models

The SuperDARN HF radar network (Chisham et al., 2007; Greenwald et al., 1995) is used collectively to estimate the ionospheric electric field \mathbf{E} and polar cap electrostatic potential using the ionospheric plasma drift $\mathbf{V}_i = \mathbf{E} \times \mathbf{B}$ Doppler observations in the plane perpendicular to the magnetic field \mathbf{B} and fitting to a spherical harmonic model (Chisham et al., 2007; Fiori et al., 2013; Shepherd & Ruohoniemi, 2000). Figure 2 shows the 13 southern hemisphere SuperDARN radars' fields of view (FOV) with the South African SANAE and Chinese Zhongshan

radars shown in red. SANA E is located at 71.67°S, 2.84°W (66.64°S, 48.51°E geomagnetic coordinates) and Zhongshan is located at 69.38°S, 76.38°E (74.5°S, 96.0°E geomagnetic coordinates). For SANA E, LT = UT + 2 hr and MLT \approx UT - 2 hr. For Zhongshan, LT = UT + 5 hr and MLT \approx UT + 2 hr. The SANA E and Zhongshan radars' geographic boresight directions are 173.2° and 72.5°, that is, approximately southward and eastward, respectively. Both radars have 16 beams covering \sim 53° azimuth with a range resolution of 45 km and the first gate at 180 km downrange. The SANA E beams are numbered from zero anticlockwise, while Zhongshan is clockwise in azimuth angle. SANA E and Zhongshan operated continuously on 12.57 and 10.25 MHz, respectively, with a 2-min temporal resolution during this study. All SuperDARN HF radars provide backscatter power, line of sight Doppler velocity, and spectral width data products (Chisham et al., 2007). For this study, these data are estimated by fitting the autocorrelation function (Baker et al., 1995; Ponomarenko et al., 2009) using FITACF Version 2.5, obtained through the radar software toolkit Version 4.3.

To obtain the magnetic field, we use 1-min magnetometer data from SANA E (Kotzé, 2018) and Zhongshan (Y. Liu et al., 2016). Magnetic field data were used to calculate the electron and ion gyrofrequencies. To check for the existence of *E*s layers, we use the Digisonde Portable Sounder 4D located at Zhongshan with an hourly time resolution (Li et al., 2007). No ionosonde was available close to SANA E.

The International Reference Ionosphere (IRI) 2016 model (Bilitza et al., 2017) was used to obtain electron density and temperature. The Mass Spectrometer, Incoherent Scatter (MSIS)-E-90 atmospheric model (Hedin, 1988), was used to obtain neutral particle number densities and temperature profile in the thermosphere. Both models are used to determine the ionospheric Pedersen conductance and particle collision frequencies. The 2014 Horizontal Wind Model (HWM14; Drob et al., 2015) was used in this study because observations of upper atmospheric neutral winds were not available.

4. Observations

We present 3 representative data sets, out of more than 175 found in the southern hemisphere SuperDARN data from 2010 to 2013, that showed MSTIDs partially modulating NREs in the same radar data set. The original cause of the MSTIDs is beyond the scope of this paper. Our focus is on the interaction of the observed MSTIDs on existing NREs. A statistical survey of the 175 cases found so far will form a future study. Obviously, since TIDs are typically observed in the *F*-region far ranges and NREs are only observed in the *E*-region near ranges, their coincidence is only near-simultaneous, the timing offset depending on the speed and direction of the MSTID. One event occurred during winter on 15 July 2012 over noon at SANA E, and the other two occurred in summer on 22 November and 17 December 2013 post-midnight and pre-midnight, respectively, at Zhongshan. The high latitude, season, and time of the observations mean that the sun was at low elevation for Zhongshan and well below the horizon for SANA E, that is, solar illumination would have been weak. We choose these data sets because they provide a variety of seasons and local times. The SANA E radar FOV is essentially poleward and covers both the auroral oval as well as the polar cap (see Figure 2). The Zhongshan radar FOV is essentially eastward with the facility under the magnetospheric cusp region at noon and under the polar cap region during the night (Li et al., 2007).

Figure 3 shows the range-time-intensity plots for the three selected data sets. Backscatter power (dB) is shown in pseudo-color for beam 15 in all cases. The TIDs are highlighted by slanted solid lines for visual reference only and the NREs are shown in a solid rectangle. We assume the TIDs propagated at a constant altitude and velocity (cf., He et al., 2004; Grocott et al., 2013); hence, the straight lines overlaid. Panel (a) shows SANA E data for 11:00 to 17:00 UT on 15 July 2012, corresponding to \sim 09:00–15:00 MLT with $K_p = 5^+ - 6$ indicating high geomagnetic activity. Between 12:00 and 17:00 UT, periodic backscatters are clearly observed for slant ranges \sim 1,100–2,600 km, indicating TIDs propagating away from the radar. Line-of-sight Doppler velocities and spectral widths (shown in Appendix A by Figure A1) were up to 1,000 m/s away from the radar and up to 125 m/s, respectively. Panel (b) is similar to panel (a) but for 00:00 and 04:00 UT on 22 November 2013 for the Zhongshan HF radar, corresponding to \sim 02:00–06:00 MLT, with $K_p = 1^- - 0$, indicating quiet geomagnetic conditions. The TIDs propagated toward the radar between 00:00 and 04:00 UT at a slant range of \sim 350–1,700 km. Line-of-sight Doppler velocities and spectral widths (shown in Appendix A by Figure A1) were up to 400 m/s toward the radar and mostly less than 12 m/s, respectively. Panel (c) is similar to panel (b) but for 17:00–22:00 UT on 17 December 2013 for the Zhongshan radar, corresponding to \sim 19:00–24:00 MLT, with $K_p = 1^- - 2^+$, indicating

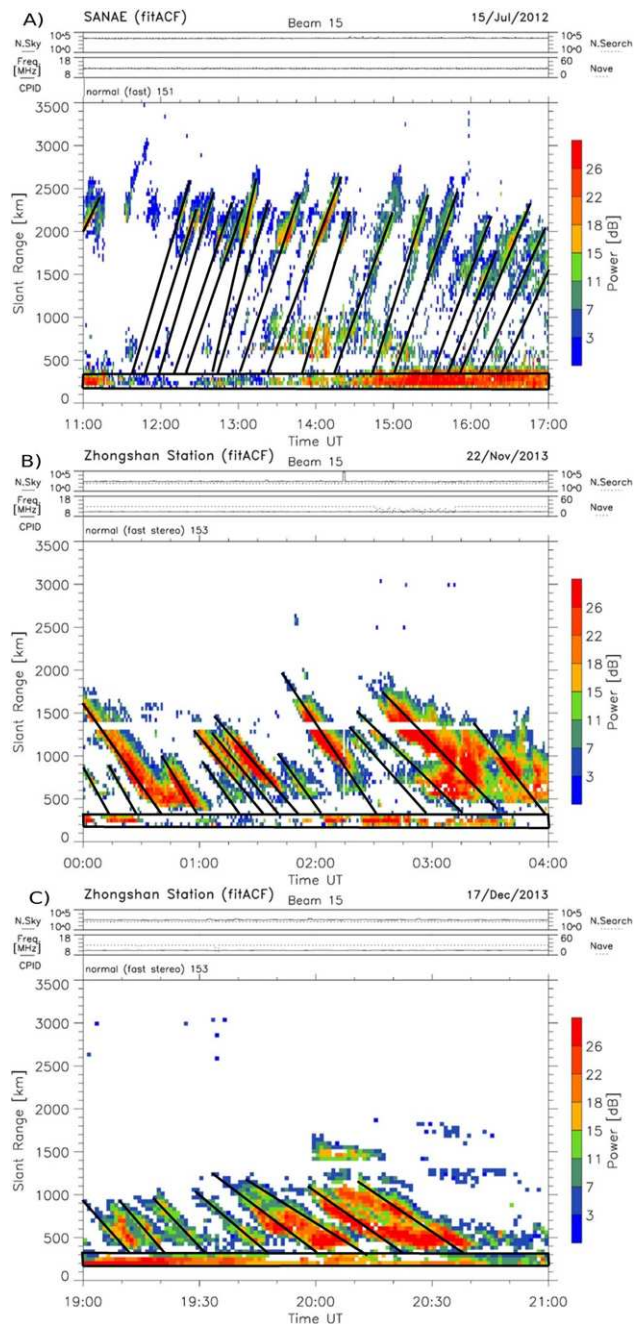


Figure 3. Range-Time-Intensity plot of backscatter power of (a) beam 15 of the SANA E HF radar from 11:00 to 17:00 UT on 15 July 2012, (b) beam 15 of the Zhongshan HF radar from 00:00 to 04:00 UT on 22 November 2013, and (c) beam 15 of the Zhongshan HF radar from 19:00 to 21:00 UT on 17 December 2013. The slant black lines approximately indicate wavefronts of Traveling Ionospheric Disturbances. The horizontal black rectangles show the Near Range Echoes.

low geomagnetic activity. Between 19:00 and 21:00 UT, the TIDs propagated toward the radar at a slant range of ~ 350 – $1,250$ km. Line-of-sight Doppler velocities and spectral widths (shown in Appendix A by Figure A1) were up to 400 m/s toward the radar and mostly less than 12 m/s, respectively. The true vector velocity of the TIDs was obtained using the multi-beam method described by He et al. (2004) as discussed below. For the sake of brevity, we name the events observed on 15 July 2012, 22 November 2013, and 17 December 2013 as S1, Z1, and Z2, respectively.

In all cases, the SuperDARN ray tracing (shown in Appendix A by Figure A2) showed that the backscatter was ionospheric. Based on possible magnetic field orthogonal backscatter for ray tracing, the TIDs propagated at ~ 400 , ~ 300 , and ~ 240 km altitude for cases S1, Z1, and Z2, respectively. *F*-region ionospheric propagation is consistent with the high TID Doppler velocities and high spectral width for case S1. Cases Z1 and Z2 are mostly at ranges too short to allow for ground scatter. Simultaneously, for all cases, NREs are observed between a slant range of 180 and 315 km. However, a clear one-to-one correspondence between the TID and NRE backscatter power is not immediately obvious by visual inspection. A visual comparison is also made difficult because of naturally occurring data gaps in the NREs and the lack of far range backscatter does not necessarily imply that MSTIDs were not present.

Figure 4 shows the SuperDARN map potential plots for cases S1, Z1, and Z2 with the vectors of plasma convection flow observed by the southern hemisphere radars. Overlaid are particle precipitation data showing the logarithm of electron energy flux between 0 and 30 keV $\text{cm}^{-2} \text{s}^{-1} \text{sr}^{-1}$ from the TED instrument of the POES satellites (cf., Atilaw et al., 2021) and the estimated equatorward boundary of the auroral oval (red dotted-dashed circle). The approximate FOV of the relevant radar is shown overlaid. Panels (a–c) correspond to cases S1, Z1, and Z2, respectively. Figure 4 illustrates that the TID-modulated NREs occur at times when the radars' FOVs were within the auroral oval, and the associated particle precipitation (highlighted by the POES TED data) would have created *E*-region plasma density perturbations in the radar near ranges, thereby creating conditions favorable to the formation of GDI. We note that the NREs for case S1 were initially in the dawn convection cell and later in the dusk cell. For case Z1, the NREs appear only in the dawn convection cell. For case Z2, the NREs appear initially in the dusk convection cell and then later the dawn cell.

For case Z2, we were able to reinforce the expectation that plasma density gradients existed by local ionosonde observations. Figure 5 shows two example ionograms observed from Zhongshan at 19:00 and 21:00 UT on 17 December 2013. Spread-*F* is visible above 250 km, consistent with particle precipitation, and an *Es* layer appeared from 18:00 to 22:00 UT at ~ 100 km altitude, varying between 95 and 118 km. The appearance of an *Es* layer is consistent with Tsunoda and Cosgrove (2001) who noted that TIDs and *Es* layers occur simultaneous in the majority of cases. A sporadic *E*-layer provides a suitable plasma density gradient required for the GDI to exist (Kagan & Kelley, 1998; Kirkwood & Von Zahn, 1991). Unfortunately, no ionosonde data are available for cases S1 and Z1. Of the 175 similar TID-NRE events identified over Zhongshan, 153 had ionosonde data and of those 84% had a simultaneous *Es* layer present. Of these, 47% occurred

in winter and 53% occurred in summer. This coincidence between TIDs and *Es* layers is similar to that found by Goodwin (1966) (75%) and Bowman (1960, 1968) (85%).

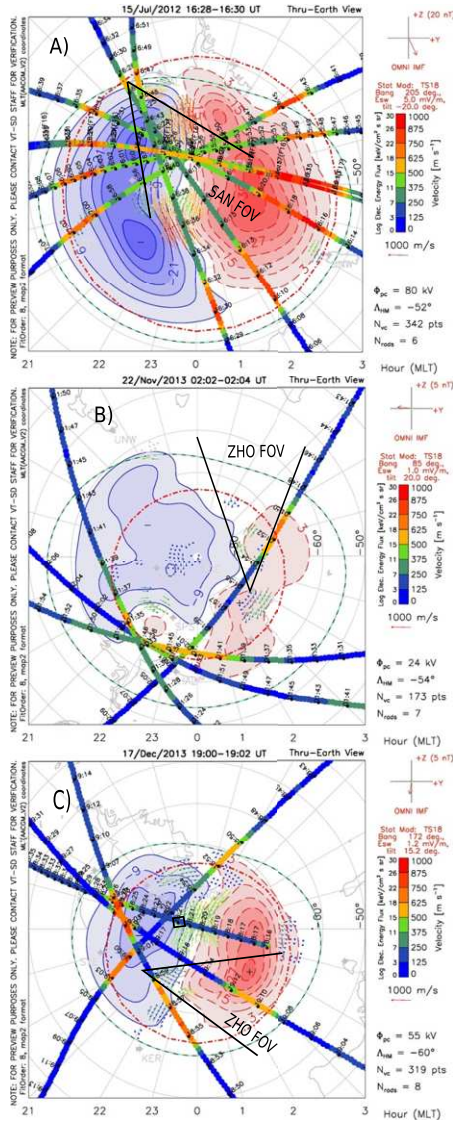


Figure 4. SuperDARN map potential plot (using FITACF V2.5) showing the vectors of convection plasma flow derived from the southern hemisphere radars overlaid on a MLT-MLAT grid along with particle precipitation data from the TED instrument of the POES satellites. Panels (a–c) are for cases S1 (15 July 2012, winter), Z1 (22 November 2013, summer), and Z2 (17 December 2013, summer), respectively. The estimated equatorward edge of the auroral oval boundary is shown by the red dotted-dashed circle. The approximate fields of view of the relevant radar is shown overlaid.

5. Characteristics of MSTIDs

We have estimated the TID parameters in the *F*-region ionosphere from the HF radar data using the fast Fourier transform (FFT) cross-spectral analysis algorithm described by He et al. (2004). For each radars' FOV, multiple sets of three range gates were used to estimate the wavenumber (k_x & k_y), phase velocity (v), wavelength (λ), propagation azimuth angle (Az) (e.g., Atilaw et al., 2021; Grocott et al., 2013), and amplitude (A) of the TIDs (cf., Francis, 1974; Hayashi et al., 2010). The near range gates, which contain the NREs studied here, were not used in this process. The TIDs periods were estimated using the FFT (He et al., 2004). From the peaks of the FFT spectrum, Table 1 shows the results of this analysis for each case. For case S1, the TIDs propagated with an average velocity of ~ 308 m/s and a period of ~ 28 min at a geographic azimuth angle of $\sim 197^\circ$ with an amplitude of ~ 82 km. For case Z1, the TIDs propagated with an average velocity of ~ 431 m/s and a period of ~ 15 min at a geographic azimuth angle of $\sim 222^\circ$ with an amplitude of ~ 60 km. For case Z2, TIDs propagated with an average velocity of ~ 328 m/s and a period of ~ 20 min at a geographic azimuth angle of $\sim 298^\circ$ with an amplitude of 63 km (see Supporting Information S1). The observations clearly fit the definition of MSTIDs (Grocott et al., 2013; He et al., 2004). In addition, MSTID amplitudes are consistent with high-latitude incoherent scatter radar observations (Senior et al., 2006).

To demonstrate a definite link between the observed MSTIDs and NREs, we have performed an FFT analysis (shown in Appendix A by Figures A3, A4 and A5 for cases S1, Z1, and Z2, respectively) on the two different echo types at both near and far ranges. For this analysis, the SuperDARN data were resampled at 1-min resolution, corresponding to a Nyquist frequency resolution of 8.3 mHz. For both the NREs and MSTIDs, coinciding FFT peaks were found at ~ 28 , ~ 15 , and ~ 20 min for case S1 (see Figure 3a and Figure A3), case Z1 (see Figure 3b and Figure A4), and case Z2 (see Figure 3c and Figure A5), respectively (see Table 1), corresponding to the backscatter periods visible in Figure 3.

6. Cross Correlation Between MSTIDs and NREs

To further establish the link between MSTIDs and NREs, we have performed a cross-correlation analysis on the two different echo types (shown in Appendix A by Figure A6). For case S1 with beam 15 and range gate 2 (270 km, NREs) against range gates 40–45 (1,980–2,205 km, TIDs), the cross-correlation coefficient (CC) peaks at ~ 0.5 with a time lag of ~ 45 min. For case Z1 with beam 15 and range gate 1 (225 km, NREs) against range gates 19–24 (1,035–1,260 km, TIDs), the correlation coefficient peaks at ~ 0.53 with a time lag of ~ 25 min. For case Z2 for beam 15 and range gate 1 (225 km, NREs) against range gates 10–15 (630–855 km, TIDs), the correlation coefficient peaks at ~ 0.55 with a time lag of ~ 9 min. In all cases, the cross-correlation time lag is consistent with the expected propagation delay of the MSTIDs observed (see Figure 3 and Table 1).

We note that the cross correlation is moderate in all cases but this is consistent the observed NREs, which show little obvious sign of modulation by the MSTIDs (see Figure 3). As noted above, visual detection of TID modulation in the NREs is made difficult partly because of naturally occurring backscatter variability and data gaps in the NREs. In addition, data gaps in the far range backscatter do not necessarily imply that MSTIDs were not present. We have performed an FFT analysis in the NREs before and after the times of the observed MSTIDs for the events presented here and found no evidence of MSTID periods in the NRE backscatter (see Supporting Information S1).

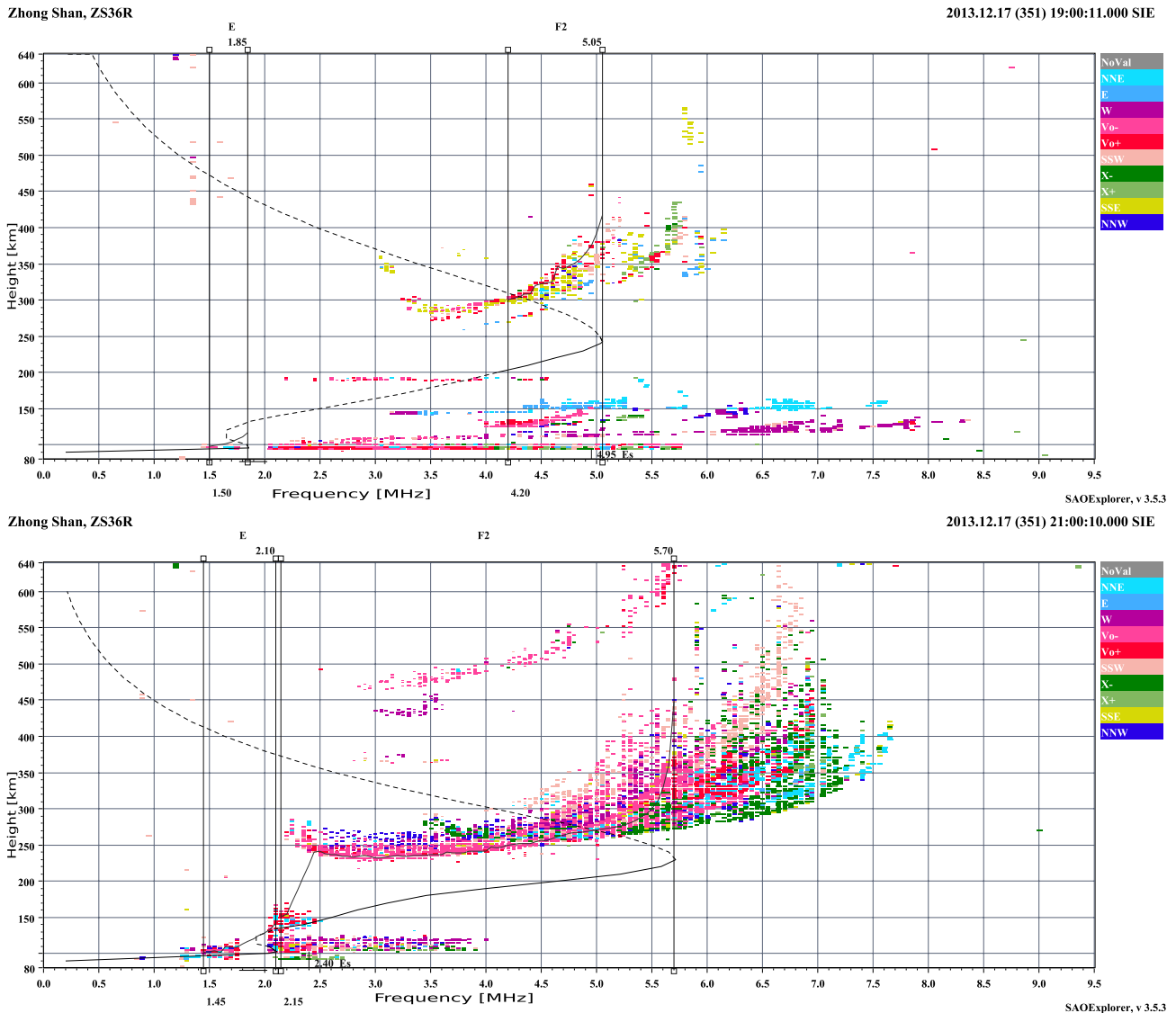


Figure 5. Hourly ionograms from Zhongshan at 19:00 and 21:00 UT on 17 December 2013 (case Z2).

Clearly, the amplitude modulation of the NREs shown in Figure 3 is not immediately obvious as it is for the MSTIDs. This is reflected in the moderate cross-correlation values described above. Here, we focus the analysis on gates 1 and 2 for all beams, neglecting gates 0 and 3 although they do show evidence of NREs. First, gates 1 and 2 have fewer data gaps. Second, SuperDARN radars sound obliquely, so each range gate is at a different altitude. We do not have angle-of-arrival data available. However, St.-Maurice and Nishitani (2020) showed (see their Figure 2, bottom panel) that FAIR echoes at high latitude were observed at $\sim 25\text{--}27^\circ$ elevation angle, whereas in their case, HAIR echoes were observed at longer ranges and lower elevation angles. Our gates 1 and 2 best fit the criteria for observing FAIR echoes at ~ 100 km altitude. Using the Spearman rank correlation on gates 1 and 2 of all beams, we estimate the NRE amplitude modulation to be 8.9 (1.3)%, 8.1 (1.3)%, and 12.9 (1.4)% for cases S1, Z1, and Z2, respectively, where the values in brackets give the standard deviation. The impact of the MSTID passing overhead is $\sim 10\%$ of the NRE amplitude, which is consistent with the moderate cross-correlation values described above. This relatively modest amplitude modulation shows that the MSTIDs are having an effect on the NREs but that the fundamental causative mechanism for the NREs is not the MSTIDs themselves. This is obvious for cases Z1 and Z2 where the MSTIDs originated far away from the NREs and propagated toward the radar.

Table 1

Medium-Scale Traveling Ionospheric Disturbance (MSTID) Parameters Estimated on 15 July 2012 From 12:30 to 16:30 UT (Case S1), 22 November 2013 From 00:00 to 03:48 UT (Case Z1), and on 17 December 2013 From 19:00 to 20:48 UT (Case Z2)

Periods, wavenumbers, velocities, azimuth, wavelengths, and amplitudes of MSTIDs			
Parameters	15 July 2012	22 November 2013	17 December 2013
T (min)	28	15	20
k_x (1/m)	11.2×10^{-6}	8.6×10^{-6}	11.3×10^{-6}
k_y (1/m)	4.9×10^{-6}	14.4×10^{-6}	11.3×10^{-6}
v (m/s)	308	431	328
Az ($^\circ$)	197	222	298
λ (km)	514	375	393
A (km)	82	60	63

Note. Az is defined in geographic coordinates (see Figure 1).

7. Gradient Drift Instability in the E -Region

Next, we show that a link exists between the ionospheric electric field as determined by the SuperDARN network of radars and the NREs backscatter power. This provides a clue that GDI, which relies on the velocity difference between the ions and the slowly varying neutral wind (see theory section above), is a plausible mechanism for TID modulation of SuperDARN NREs. GDI requires plasma gradients (see theory section above) and we assume that these exist with the correct geometry (see Figure 1) because of the observed particle precipitation (see Figure 4) and for the one case where ionosonde data were available, a sporadic E -layer (see Figure 5). SuperDARN map potential data have a 2 min cadence with a 2° latitude and 1° longitude geomagnetic spatial resolution. The electric field was obtained by averaging the SuperDARN data from a selection of grid points closest to the observed NREs in time and position. Obviously, since all SuperDARN radars in both hemispheres contribute to the map potential data product, the contribution of an individual TID in any particular radar will be diluted. However, in our events (see Figure 3), there is significant ionospheric backscatter at range gates close to the NREs, especially for cases Z1 and Z2, which increases our confidence in the electric field estimate over the NREs.

We also estimate L_z from Equation 3 based on the ionospheric F -region electric field, taken from the SuperDARN radar network observations of ionospheric backscatter, the magnetic field and its dip angle, taken from local magnetometer data, and the E -region neutral wind, taken from the HWM14 wind model. We use IRI-2016 and MSIS-90 to estimate the ion-neutral and electron-neutral collision frequencies. We assume that the ionospheric electric field is unchanged in the E -region, given the relatively short quasi-vertical distance. The value of k_x (Equation 3) corresponds to the operating frequency of the SuperDARN radar, for example, for SANA E at 12.57 MHz, $\lambda = 2\pi/k_x \approx 12$ m. Equation 3 shows that when the relative ion-neutral velocity is large/small, then L_z becomes large/small resulting in a GDI growth rate (Equation 2), which is small/large, respectively. Therefore, a large relative velocity favors the production of NREs from GDI (St.-Maurice & Nishitani, 2020).

Assuming an ion-acoustic velocity $C_s \approx 300$ m/s (St.-Maurice & Nishitani, 2020), the inputs and outputs of Equation 3 are shown in Figure 6 for case S1 (15 July 2012) at 100 km altitude between 12:30 and 16:30 UT. We focus on 100 km altitude since FAIR echoes are believed to be triggered at near this altitude (St.-Maurice & Nishitani, 2020). Panel (a) shows the HWM14 model zonal neutral wind speed (U_{nx}), which varied smoothly between -5.4 and 14.8 m/s and reversed direction around 14:00 UT. Panel (b) shows the Z -component of the magnetic field \mathbf{B} at SANA E. Panel (c) shows the meridional component of the ionospheric electric field (E_y) averaged over the closest magnetic coordinate to all beams for range gate 2. The electric field varies between 3 mV/m and -22 mV/m, which corresponds to an ion drift velocity of up to ~ -575 m/s. Hence, as expected, the neutral wind speed plays a minor role in Equation 3 for this case. Panel (d) shows the plasma density scale length (L_z), which varies from 370 to $-2,592$ m. The negative value for L_z indicates that the ion flow opposed the neutral wind with a greater velocity caused by the southward (negative) electric field. Unsurprisingly, given the small neutral wind, the variation in the meridional electric field is very similar to that in L_z . Panel (e) shows the backscatter power of gate 2 (p2), averaged over all 16 beams, received by the SANA E SuperDARN HF radar as NREs. The average backscatter power appears anticorrelated to E_y (panel c) and L_z (panel b). Panel (f) shows the cross correlation between E_y (panel c) and p2 (panel e) with a peak value of ~ -0.84 at zero lag. Panel (g) shows the cross correlation between L_z (panel d) and p2 (panel e) with a peak value of ~ -0.85 at zero lag. This clearly shows that the NRE backscatter power is closely related to the ionospheric convection electric field and therefore to the GDI mechanism. However, this does not (yet) take fully into account the additional effects of the MSTIDs on the NREs, which is discussed below. Since the MSTIDs modulate only $\sim 10\%$ of the NRE backscatter power, it is expected that GDI-generated NRE be controlled primarily by the ionospheric convection electric field as shown here. Hence, the GDI-induced NREs would have existed without the presence of MSTIDs.

For case Z1 (shown in Appendix A by Figure A7), U_{nx} varied smoothly between 33.9 and 41.9 m/s, E_y varied between 1 and -24 mV/m, and L_z varied between -56 and -662 m. For case Z2 (shown in Appendix A by Figure A8), U_{nx} varied smoothly between 27.5 and 29.3 m/s, E_y varied between 3 mV/m and -6 mV/m, and

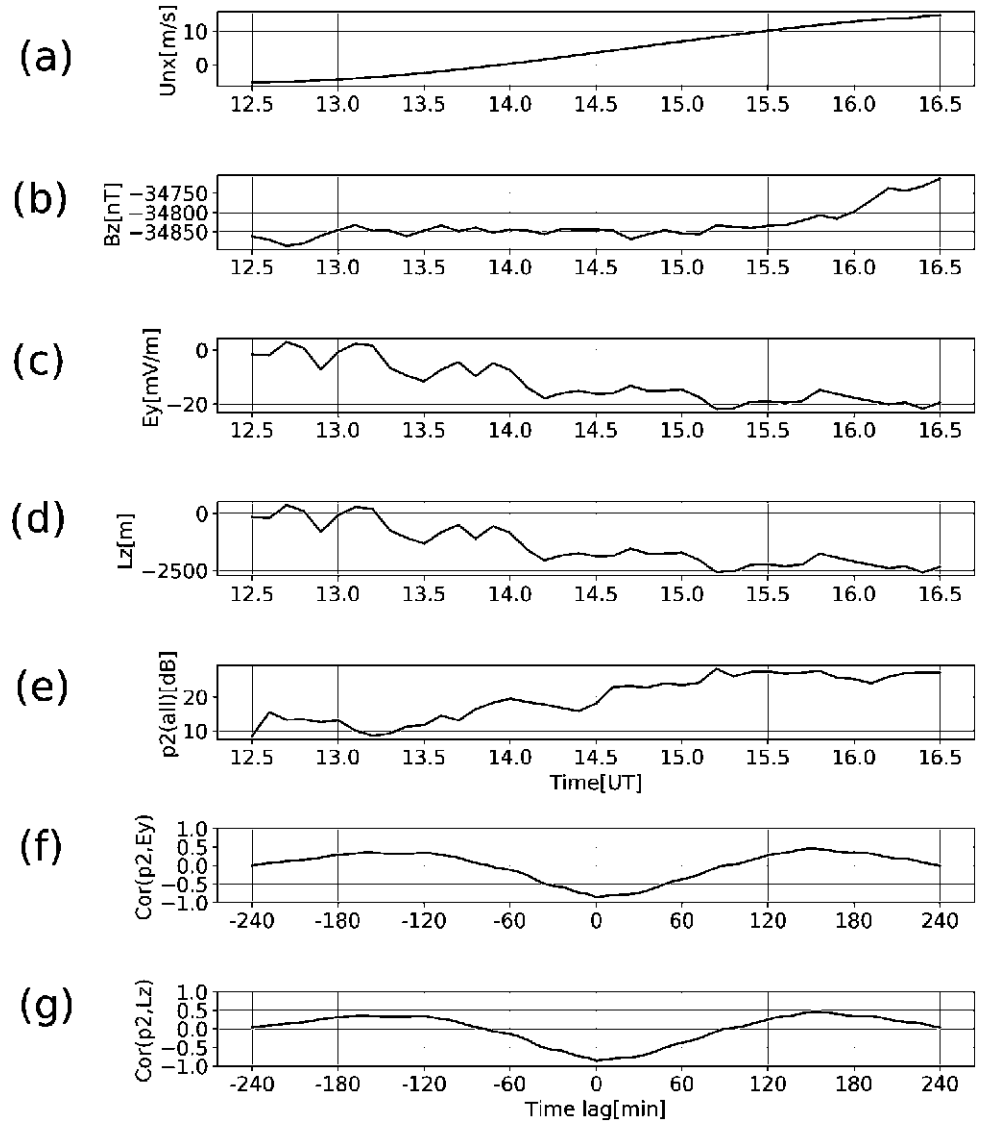


Figure 6. For 15 July 2012 from 12:30 to 16:30 UT at 100 km altitude (case S1), (a) modeled eastward neutral wind, (b) Z-component of the Earth's magnetic field at ground level, (c) observed northward electric field (E_y), (d) calculated plasma density scale height (L_z), (e) the average backscatter power of all beams for range gate 2 (p_2), (f) the cross correlation between E_y (panel c) and p_2 (panel e), and (g) cross correlation between L_z (panel d) and p_2 (panel e).

Table 2
Cross-Correlation Coefficient (CC) Between the Average Power (p) of All Beams for Range Gates 1 and 2 and Either the Meridional Electric Field (E_y) or the Density Gradient Scale Height (L_z)

Date	15 July 2012	15 July 2012	22 November 2013	22 November 2013	17 December 2013	17 December 2013
CC of	p and E_y	p and L_z	p and E_y	p and L_z	p and E_y	p and L_z
Gate 1	-0.80	-0.81	-0.80	-0.80	-0.66	-0.66
Gate 2	-0.84	-0.85	-0.73	-0.74	-0.72	-0.72

L_z varied between 33 and -180 m. As Figure 1 shows, we require the GDI mechanism to operate perpendicular to the magnetic field in the E -region. We therefore need to map L_z to L_x using Equation 4 (Haldoupis et al., 2000). The magnetic dip angle at SANAÉ and Zhongshan is 61.7° and 73.2° , respectively. This means that $L_x = 2.1 \times L_z$ at SANAÉ and $L_x = 3.5 \times L_z$ at Zhongshan. Hence for cases S1, Z1, and Z2, $L_x \approx 777$ to $-5,443$, 196 to $-2,317$, and 116 to -630 m, respectively. These plasma gradient scale lengths are easily suitable for generating the GDI (cf., Haldoupis et al., 2000).

Table 2 shows the CC between the backscatter power of range gates 1 and 2 averaged over all 16 beams, and colocated ionospheric meridional electric field (E_y) as well as the plasma gradient scale height (L_z) for all cases. As explained above, we neglect gates 0 and 3 in this analysis. In all cases, there

is a moderate ($CC = -0.66$) to strong ($CC = -0.85$) anticorrelation between E_y and L_z with the NRE backscatter power. This provides clear evidence that the GDI mechanism is operating for all our cases at the range gates that map most closely to ~ 100 km altitude where FAIR echoes are expected (St.-Maurice & Nishitani, 2020).

8. FAIR Near Range Echoes

SuperDARN NREs in the E -region ionosphere may have multiple sources, such as short-lived meteor trails (e.g., Chisham & Freeman, 2013) and PMSEs (e.g., E. Liu et al., 2013; Hosokawa et al., 2005; Ogunjobi et al., 2017). We can exclude meteors because we observed NREs over many hours (see Figure 3). We can also exclude PMSE because we found events in the winter (e.g., case S1 on 15 July 2012 and 61 other winter NRE cases from 2010 to 2013) and PMWE generally occurs at lower altitudes below 85 km and therefore would not be visible in our radar data. Recent studies indicate that some of the NREs are from HAIR echoes (Ponomarenko et al., 2016; St.-Maurice & Nishitani, 2020) associated with the FBI. They require an electric field of >40 mV/m to be triggered at ~ 120 km altitude, which corresponds to range gate numbers above 3 that are not observed in our events, and SuperDARN observations show that the electric field amplitude was always below 24 mV/m for our three events. FAIR echoes (St.-Maurice & Nishitani, 2020) are NREs believed to be associated with the GDI at ~ 100 km altitude. These appear to be consistent with our observations for range gates 1 and 2.

We have established that particle precipitation existed in the vicinity of the SANA and Zhongshan radar near ranges (see Figure 4) for all our events and on one occasion, a coincident sporadic E -layer was directly observed overhead (see Figure 5). Hence, suitable conditions existed in the E -region ionosphere for the GDI mechanism to produce FAIR echoes that then translated into the NREs observed by SuperDARN. We have observed MSTIDs propagating away/toward the radars and established that this backscatter occurred in the F -region. The observed NREs were partially modulated with the same period as the MSTIDs and with a time lag consistent with the MSTID propagation velocity in the F -region, assuming a constant altitude and velocity. The CC between MSTID backscatter and the NREs ranged from ~ 0.50 to ~ 0.55 for our events. We have performed an FFT analysis in the NREs before and after the times of the observed MSTIDs and found no evidence of MSTID periods in these NRE backscatters. When MSTIDs were present, we have estimated that the NRE amplitude modulation due to MSTIDs was in the range $\sim 8\%$ – 13% . We have estimated the CC between the ionospheric electric field and the NRE backscatter power, which was in the range of 0.66–0.84 for our events. We have estimated the CC between the ionospheric electric field and the plasma density scale length parameter (L_z), which controls the growth rate of the GDI mechanism, which was in the range from 0.66 to 0.85 for our events. Below we describe how an MSTID may partially modulate the existing GDI as we have observed in the NREs and estimate the amplitude of the GDI modulation from the MSTID parameters. This is then compared to the NRE amplitude modulation observed.

9. MSTID Polarization Electric Field

With reference to Figure 4, we note that for cases S1 and Z1, the MSTIDs had a southward component of the propagation direction, whereas the background ionospheric ion convection flow had a westward component of the drift direction. For case Z2, the MSTID had a westward component of propagation direction, whereas the background ionospheric convection flow had a northward component of drift direction. In all cases, the MSTID propagation direction and the ionospheric electric field ($\mathbf{E}_0 = -\mathbf{V}_i \times \mathbf{B}$) had parallel components. This geometry is conducive for the GDI to occur, both for the generation of NREs due to the background ionospheric electric field and for the additional modulation of these NREs by the MSTID polarization electric field described below. The Pedersen current (\mathbf{J}) in the F -region is given by (Kotake et al., 2007; Otsuka et al., 2007):

$$\mathbf{J} = \Sigma_p(\mathbf{E} + \mathbf{U} \times \mathbf{B}). \quad (5)$$

where Σ_p is the F -region Pedersen conductance. Hence, for our events, there will be a Pedersen current component parallel to the MSTID propagation direction. The MSTID wave perturbs the ionospheric plasma in the quasi-vertical field-aligned direction from which it follows that there will be an equivalent Pedersen conductance perturbation. In order to maintain divergence-free current continuity for \mathbf{J} , a periodic horizontal polarization electric field (\mathbf{E}_p) must be set up locally within the MSTID wave. Figure 7 shows a cartoon depicting the geometry based on case S1 for the meridional projection. The MSTID propagates primarily southward in the

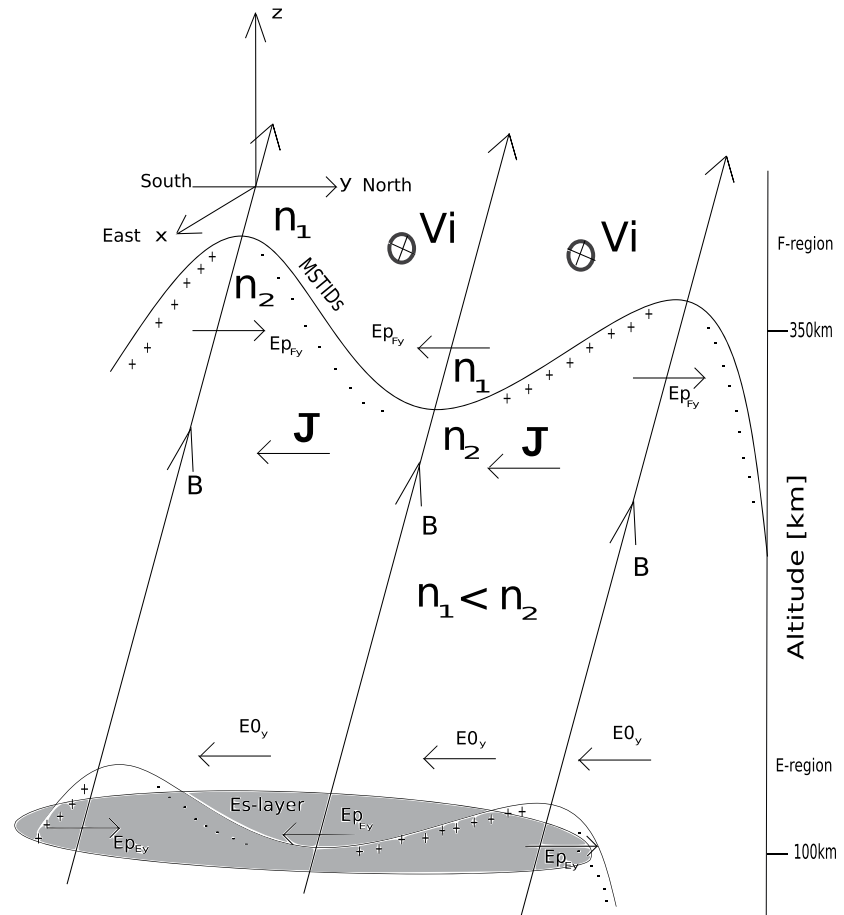


Figure 7. Cartoon showing how the polarization electric field due to a Medium-Scale Traveling Ionospheric Disturbance propagating in the *F*-region may partially modulate the existing Gradient Drift Instability in the *E*-region. The geometry is for the meridional projection of case S1 propagating above *hmF2* in the southern hemisphere.

F-region, the ion drift is primarily westward and so the ionospheric electric field (\mathbf{E}_0) and Pedersen current (\mathbf{J}) are primarily southward. For case S1, the MSTID propagates at ~ 400 km (see Figure A2) above the *F*-region plasma density peak (~ 285 km), so the plasma density at higher altitude (n_1) is less than at lower altitude (n_2). In this case, positive/negative charges accumulate at the leading/trailing edge of the MSTID wave, resulting in an oscillating polarization electric field (\mathbf{E}_{pF}) as shown. If the MSTID propagates below the *F*-region peak, then the plasma density gradient reverses, the position of the charges is reversed and the direction of \mathbf{E}_{pF} is also reversed. However, except for a phase shift, this does not change the mechanism. As the MSTID passes overhead in the *F*-region, it is the oscillating \mathbf{E}_{pF} that is transmitted undiminished downward along the equipotential magnetic field lines that partially modulate the background ionospheric electric field (\mathbf{E}_0) in the *E*-region. Since the electric field ($\mathbf{E}_0 + \mathbf{E}_{pF}$) controls the growth rate of the GDI (see Equations 2 and 3), the NREs will be partially modulated spatially and temporally in a manner which mirrors the MSTID passing overhead. The forward motion of the MSTID ensures that steady-state saturation does not set in.

Finally, we show that the percentage amplitude modulation of \mathbf{E}_0 by \mathbf{E}_{pF} is consistent with the observed percentage modulation of the NREs (~ 8 – 13%). The polarization electric field shown in Figure 7 may be estimated as follows (Otsuka et al., 2007):

$$\mathbf{E}_{pF} = \frac{\delta \Sigma_p}{\Sigma_p} (\mathbf{E} + \mathbf{U} \times \mathbf{B}) \frac{\mathbf{k}}{|\mathbf{k}|} \quad (6)$$

where $\delta\Sigma_p$ is the change in F -region Pedersen conductance due to the MSTID, Σ_p is the unperturbed F -region Pedersen conductance, and \mathbf{k} is the MSTID wavenumber vector. We used the MSIS and IRI models to compute the Pedersen conductance. We used the SuperDARN ray tracing tool to estimate the altitude of the MSTID propagation (see Figure A2 in Appendix A). The amplitude (A) of the MSTID wave is shown in Table 1. $\delta\Sigma_p$ is calculated by taking the difference between the height-integral of Pedersen conductivity above and below the MSTID propagation altitude, the height limits being set by the MSTID amplitude ($\pm A$). For case S1 with hmF2 = ~ 285 km, propagating at ~ 400 km altitude and $A = 82$ km, $\delta\Sigma_p/\Sigma_p = 9.9\%$. For case Z1 with hmF2 = ~ 255 km, propagating at ~ 300 km altitude and $A = 60$ km, $\delta\Sigma_p/\Sigma_p = 11.8\%$. For case Z2 with hmF2 = ~ 315 km, propagating at ~ 240 km altitude and $A = 63$ km, $\delta\Sigma_p/\Sigma_p = 16.6\%$. This level of F -region Pedersen conductance modulation is consistent with the $\sim 10\%$ airglow modulation by MSTIDs observed by Suzuki et al. (2009) at midlatitudes. We had estimated above the NRE amplitude modulation to be 8.9%, 8.1%, and 12.9% for cases S1, Z1, and Z2, respectively.

Hence, for cases S1/Z1/Z2, an $\sim 9.9\%/11.8\%/16.6\%$ modulation of \mathbf{E}_0 resulted in an NRE modulation of $\sim 8.9\%/8.1\%/12.9\%$, respectively. We claim that in addition to the qualitative agreement shown above, this result provides quantitative agreement that the passing MSTIDs in the F -region, observed by the SuperDARN radars' far ranges, partially modulated \mathbf{E}_0 , which partially modulated the GDI, which partially modulated in equal measure the NREs observed by the same SuperDARN radars in the E -region. The MSTIDs are linked to the NREs by the quasi-vertical equipotential magnetic field lines.

10. Conclusions

In this work, we have shown the first near-simultaneous observations of MSTIDs partially modulating existing NREs observed by the SANA and Zhongshan HF radars. Based on qualitative and quantitative analyses, we conclude that GDI is the most likely mechanism for MSTIDs propagating in the F -region to affect the NREs in the E -region. We summarize our results as follows:

1. High-latitude MSTIDs and NREs were observed during the noon and afternoon sectors during a geomagnetic storm in winter, and early morning and evening sectors during a geomagnetically quiet time in summer. The observed MSTIDs characteristics and the propagation directions were consistent with the previous studies. The GDI causes FAIR echoes in the lower E -region, which are observed as NREs in the SuperDARN data (St.-Maurice & Nishitani, 2020). The GDI occurs in pre-existing plasma density gradients (e.g., sporadic E (E_s) layers), driven by the ionospheric meridional convection electric field and zonal thermospheric neutral winds.
2. Horizontally propagating MSTIDs generate an additional horizontal polarization electric field to conserve the divergence-free Pedersen current across the magnetic field. The meridional component of the net electric field (quasi-static convection plus oscillating TID polarization), mapped down from the F -region along the equipotential magnetic field lines (Sun et al., 2015; Y. Liu et al., 2019), partially modulates the existing GDI, which is responsible for generating the NREs in the lower E -region (St.-Maurice & Nishitani, 2020), resulting in the observed partial modulation of the NREs. For all radar gates analyzed in this study, the cross correlation between the meridional electric field or the plasma density gradient scale height and the backscatter power is between -0.66 and -0.85 , indicating a good anticorrelation.
3. Most oblique sounding SuperDARN HF radars cannot estimate the altitude of the backscatter with high precision as vertical pointing VHF radars do and HF ray tracing contains uncertainties. There remains the problem of knowing without doubt if PMSEs are part of SuperDARN NREs (Ponomarenko et al., 2016). In principle, MSTIDs can modulate PMSEs in the same way AGWs modulate the Noctilucent Clouds (Dalin et al., 2004), but we are not sure if the phenomenon can be observed by SuperDARN HF radars. Our winter case (S1) seems to exclude PMWEs because they tend to occur at altitudes that correspond to ranges shorter than 180 km and therefore are generally not observed by the SuperDARN HF radars.

Appendix A: Additional Figures to Support Science of Three Cases Presented in the Main Text

The appendix contains additional important information to support the science case presented in the main text. Figure A1 shows the Doppler velocity and spectra width for Cases S1, Z1, and Z2. Figure A2 shows the ray tracing for Cases S1, Z1, and Z2. Figures A3, A4, and A5 show the backscatter power and the Fast Fourier Transform thereof for beam 15 of Case S1, beam 15 for Case Z1, and beam 12 for Case Z2, respectively. Figure A6 shows the Cross correlation between Near Range Echoes and Medium-Scale Traveling Ionospheric Disturbances for the cases presented in this article. Figures A7 and A8 are like Figure 6 in this article, but for Case Z1 and Z2, respectively.

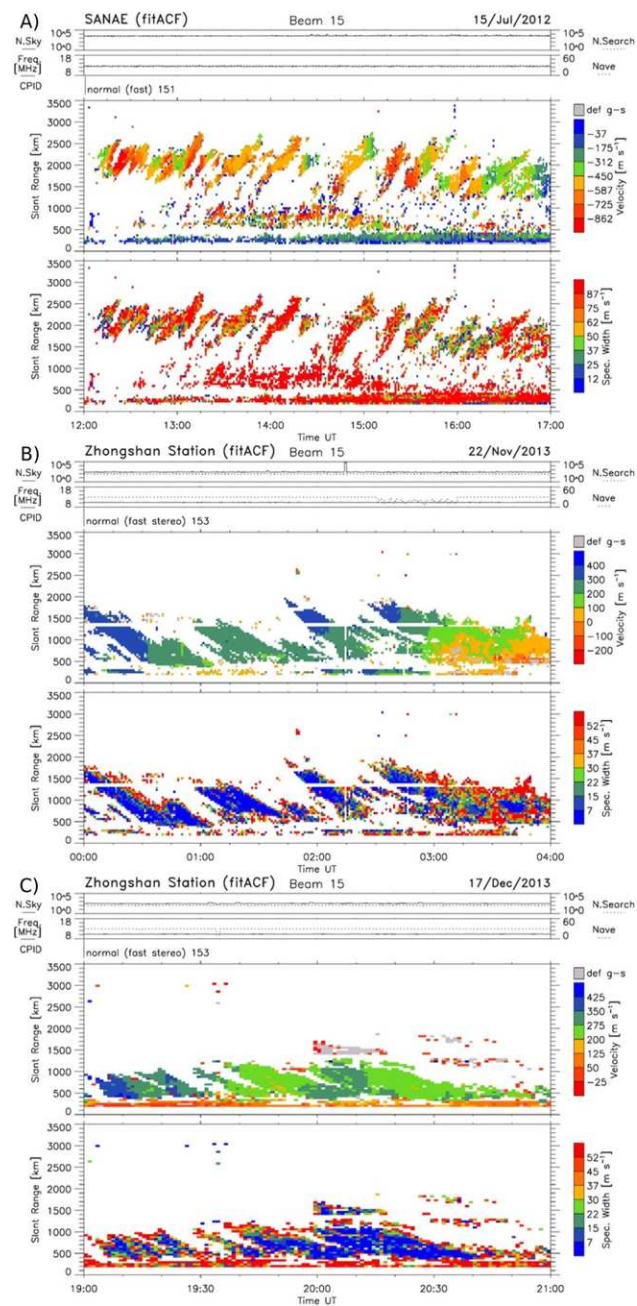


Figure A1. Range-Time-Intensity plot of Doppler velocity and spectra width of (a) beam 15 of the SANAE HF radar from 11:00 to 17:00 UT on 15 July 2012, (b) beam 15 of the Zhongshan HF radar from 00:00 to 04:00 UT on 22 November 2013, and (c) beam 15 of the Zhongshan HF radar from 19:00 to 21:00 UT on 17 December 2013. This figure complements Figure 3.

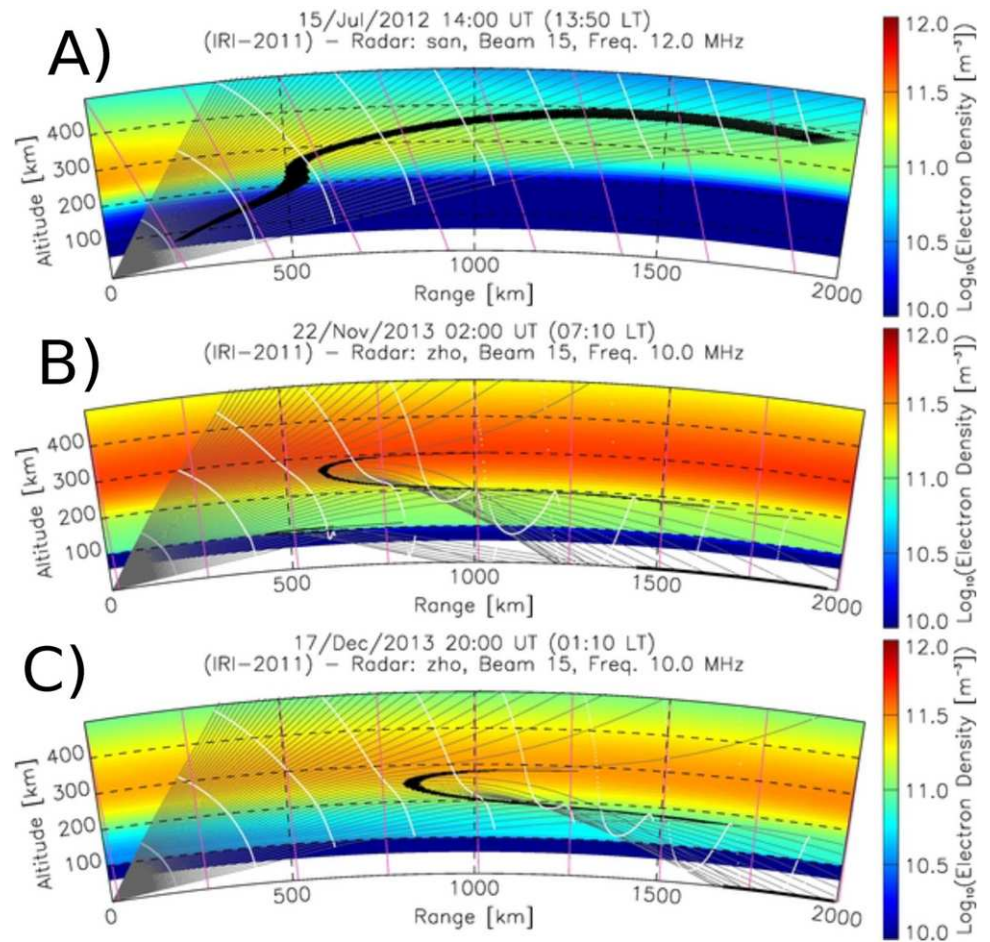


Figure A2. Ray tracing using the International Reference Ionosphere model at 12.0 MHz for SANAE and 10.0 MHz for Zhongshan. The locus of black points indicates where ionospheric and ground backscatter may be possible. Panel (a) is for 14:00 UT on 15 July 2012 (case S1), panel (b) is for 02:00 UT on 22 November 2013 (case Z1), and panel (c) is for 20:00 UT on 17 December 2013 (case Z2).

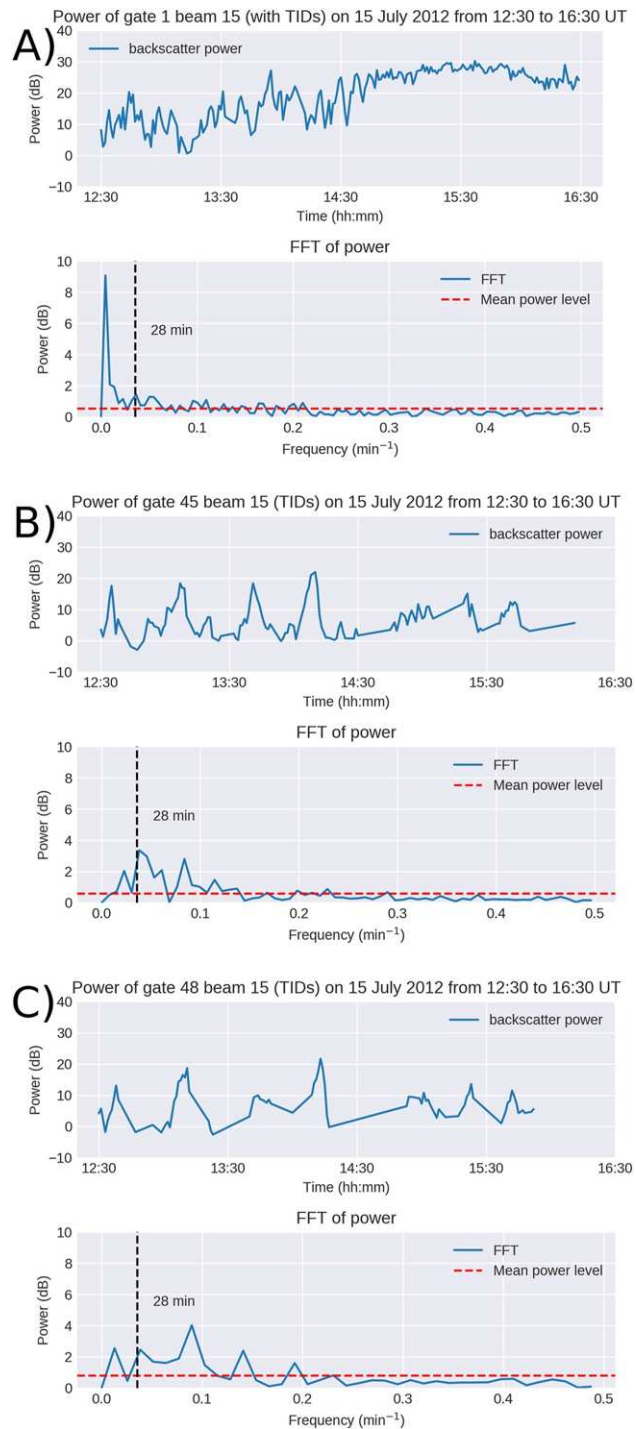


Figure A3. Backscatter power and the Fast Fourier Transform thereof for SANAE beam 15 on 15 July 2012 between 12:30 and 16:30 UT (case S1). Panel (a) is for gate 1 (Near Range Echoes). Panels (b and c) are for gates 45 and 48 (Medium-Scale Traveling Ionospheric Disturbances (MSTIDs)), respectively. The period of the MSTID is indicated (vertical dashed line).

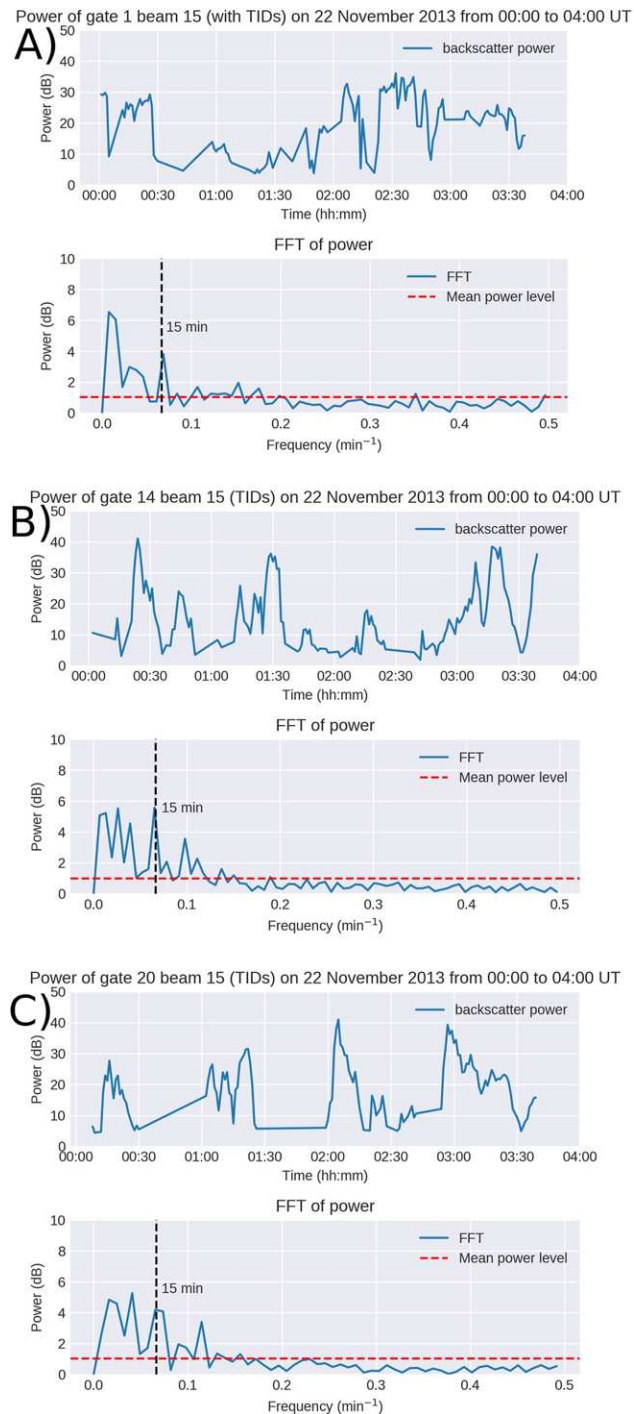


Figure A4. Backscatter power and the Fast Fourier Transform thereof for Zhongshan beam 15 on 22 November 2013 between 00:00 and 03:48 UT (case Z1). Panel (a) is for gate 1 (Near Range Echoes). Panels (b and c) are for gates 14 and 20 (Medium-Scale Traveling Ionospheric Disturbances (MSTIDs)). The period of the MSTID is indicated (vertical dashed line).

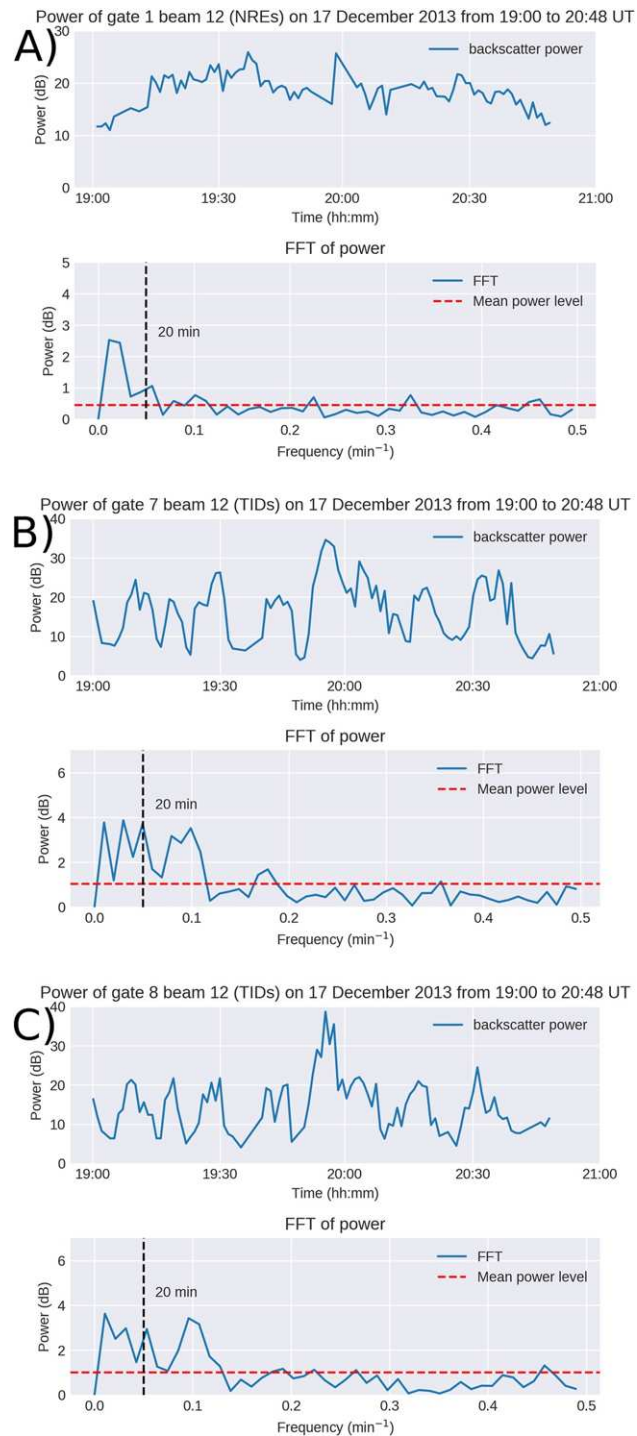


Figure A5. Backscatter power and the Fast Fourier Transform thereof for Zhongshan beam 12 on 17 December 2013 between 19:00 and 20:48 UT (case Z2). Panel (a) is for gate 1 (Near Range Echoes). Panels (b and c) are for gates 7 and 8 (Medium-Scale Traveling Ionospheric Disturbances (MSTIDs)). The period of the MSTID is indicated (vertical dashed line).

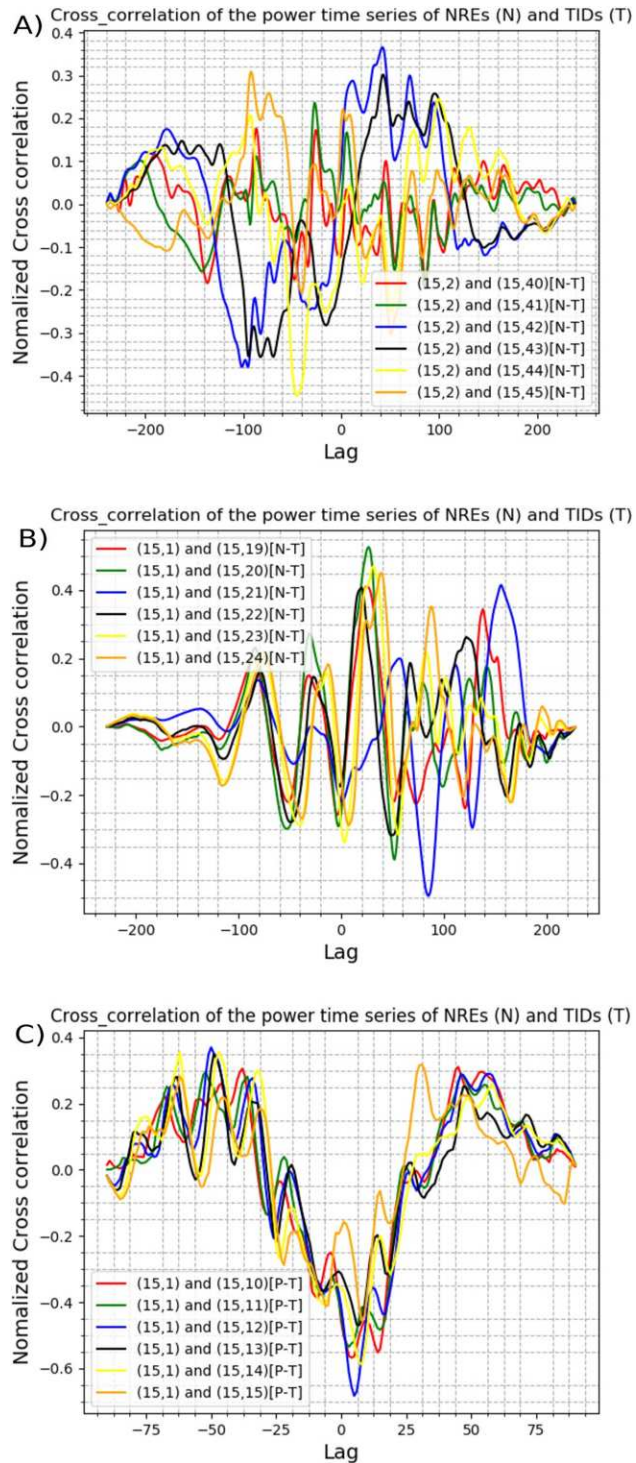


Figure A6. Cross correlation between Near Range Echoes and Medium-Scale Traveling Ionospheric Disturbances. Panel (a) is for SANA beam 15 and gate 2 versus gates 40–45 on 15 July 2012 between 12:30 and 16:30 UT (case S1). Panel (b) is for Zhongshan beam 15 and gate 1 versus gates 19–24 on 22 November 2013 between 00:00 and 03:48 UT (case Z1). Panel (c) is for Zhongshan beam 15 and gate 1 versus gates 10–15 on 17 December 2013 between 19:00 and 20:48 UT (case Z2).

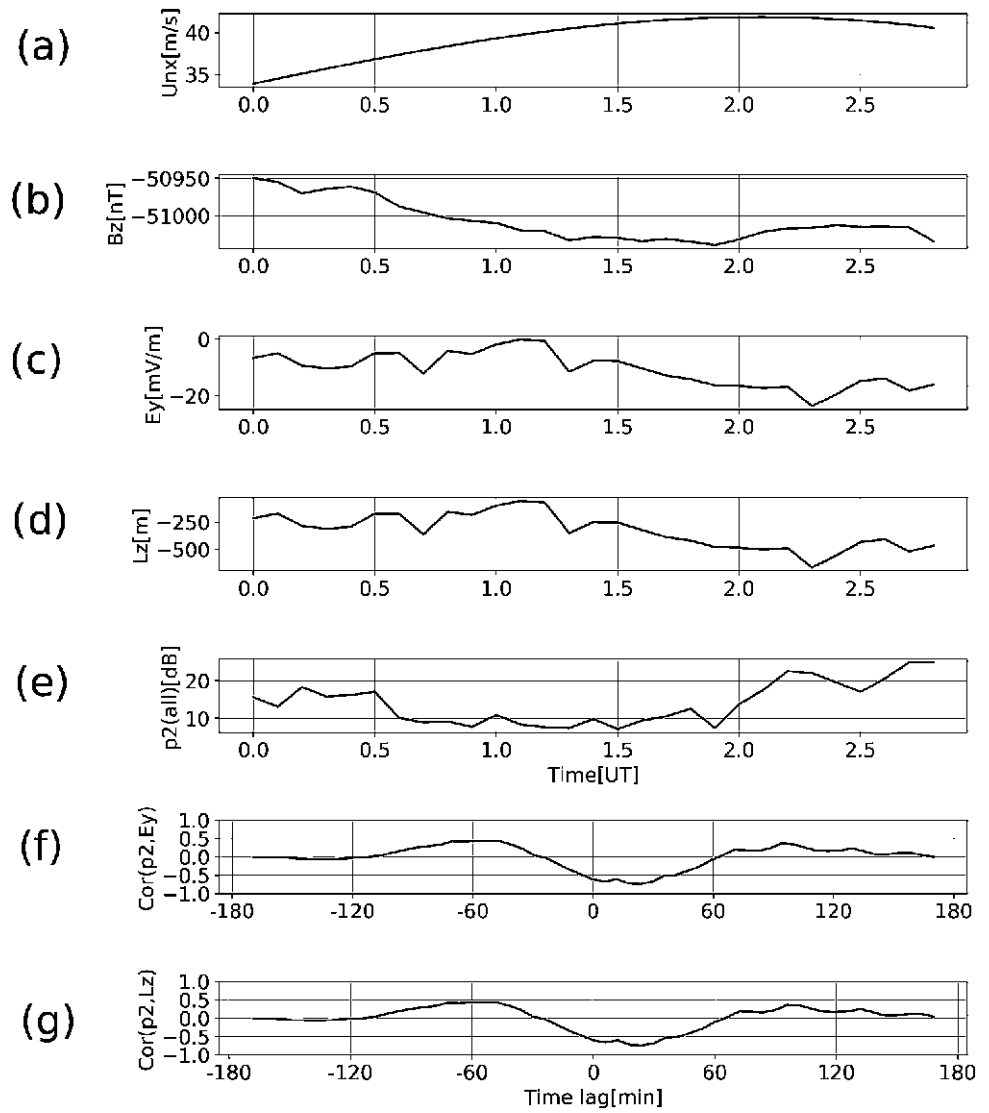


Figure A7. For 22 November 2013 from 00:00 to 02:48 UT at 100 km altitude (case Z1), (a) modeled eastward neutral wind, (b) Z-component of the Earth's magnetic field at ground level, (c) observed northward electric field (E_y), (d) calculated plasma density scale height (L_z), (e) the average backscatter power of all beams for range gate 2 ($p2$), (f) the cross correlation between E_y (panel c) and $p2$ (panel e), and (g) cross correlation between L_z (panel d) and $p2$ (panel e).

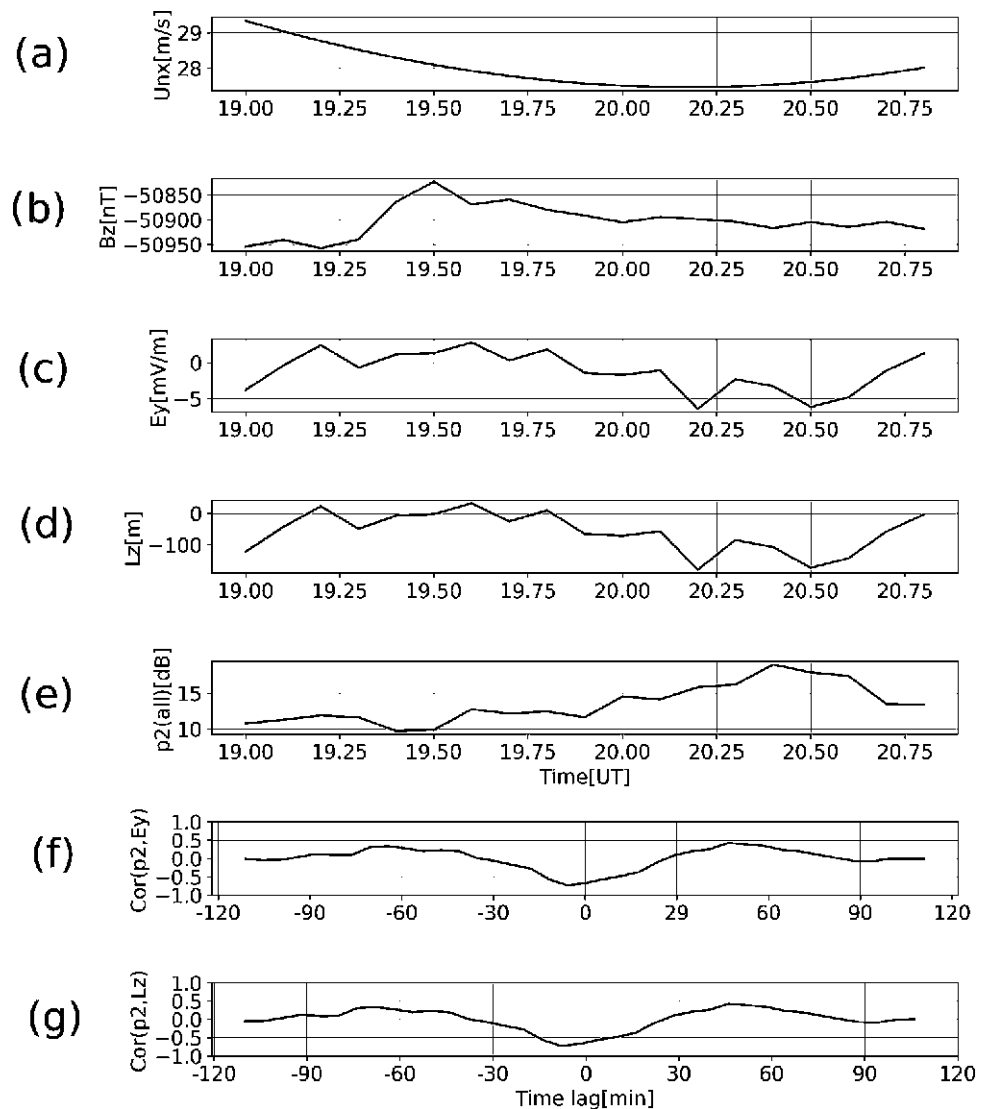


Figure A8. For 17 December 2013 from 19:00 to 20:48 UT at 100 km altitude (case Z2), (a) modeled eastward neutral wind, (b) Z-component of the Earth's magnetic field at ground level, (c) observed northward electric field (E_y), (d) calculated plasma density scale height (L_z), (e) the average backscatter power of all beams for range gate 2 (p_2), (f) the cross correlation between E_y (panel c) and p_2 (panel e), and (g) cross correlation between L_z (panel d) and p_2 (panel e).

Acknowledgments

The authors acknowledge the South African National Space Agency (SANSA) and the South African National Antarctic Programme (SANAP) for supporting this research (NRF SANAP Grant 110742). The authors acknowledge the use of SuperDARN data. SuperDARN is a collection of radars funded by national scientific funding agencies of Australia, Canada, China, France, Italy, Japan, Norway, South Africa, United Kingdom, and the United States of America. The SuperDARN homepage link is <http://vt.superdarn.org/tiki-index.php>. Zhongshan magnetometer and ionosonde data were provided by the Beijing National Observatory of Space Environment, Institute of Geology and Geophysics Chinese Academy of Sciences through the Geophysics Center, National Earth System Science Data Center (<http://wdc.geophys.ac.cn/>). The authors would also like to thank MSIS-90, IRI-2016, and HWM-14 model developers. The authors thank the Zhongshan SuperDARN radar PI, Dr. Hongqiao Hu, for consenting to our use of the data, which is funded by the Polar Research Institute of China. The authors thank the NASA Goddard Space Flight Center, Space Physics Data Facility for providing ACE satellite and Magnetic Indices data through the OMNI website (https://omniweb.gsfc.nasa.gov/form/omni_min.html).

Data Availability Statement

The SANAE and Zhongshan SuperDARN fit data used in this study are available from the BAS SuperDARN data mirror <https://www.bas.ac.uk/project/superdarn/#data> or from the SuperDARN Virginia Tech web page <http://vt.superdarn.org/tiki-index.php?page=Examine%20Fit%20Contents>.

References

- Atilaw, T. Y., Stephenson, J. A., & Katamzi-Joseph, Z. T. (2021). Multitaper analysis of an MSTID event above Antarctica on 17 March 2013. *Polar Science*, 28, 100643. <https://doi.org/10.1016/j.polar.2021.100643>
- Baker, K., Dudeney, J., Greenwald, R., Pinnock, M., Newell, P., Rodger, A., et al. (1995). HF radar signatures of the cusp and low-latitude boundary layer. *Journal of Geophysical Research*, 100(A5), 7671–7695. <https://doi.org/10.1029/94JA01481>
- Bilitza, D., Altadill, D., Truhlik, V., Shubin, V., Galkin, I., Reinisch, B., & Huang, X. (2017). International Reference Ionosphere 2016: From ionospheric climate to real-time weather predictions. *Space Weather*, 15(2), 418–429. <https://doi.org/10.1002/2016SW001593>
- Bowman, G. (1960). Some aspects of sporadic-E at mid-latitudes. *Planetary and Space Science*, 2(4), 195–202. [https://doi.org/10.1016/0032-0633\(60\)90016-7](https://doi.org/10.1016/0032-0633(60)90016-7)

- Bowman, G. (1968). Movements of ionospheric irregularities and gravity waves. *Journal of Atmospheric and Terrestrial Physics*, 30(5), 721–734. [https://doi.org/10.1016/S0021-9169\(68\)80028-5](https://doi.org/10.1016/S0021-9169(68)80028-5)
- Chisham, G., & Freeman, M. P. (2013). A reassessment of SuperDARN meteor echoes from the upper mesosphere and lower thermosphere. *Journal of Atmospheric and Solar-Terrestrial Physics*, 102, 207–221. <https://doi.org/10.1016/j.jastp.2013.05.018>
- Chisham, G., Lester, M., Milan, S., Freeman, M., Bristow, W., Grocott, A., et al. (2007). A decade of the Super Dual Auroral Radar Network (SuperDARN): Scientific achievements, new techniques and future directions. *Surveys in Geophysics*, 28(1), 33–109. <https://doi.org/10.1007/s10712-007-9017-8>
- Dalin, P., Kirkwood, S., Moström, A., Stebel, K., Hoffmann, P., & Singer, W. (2004). A case study of gravity waves in noctilucent clouds. In *Annales Geophysicae* (Vol. 22, No. 6, pp. 1875–1884). <https://doi.org/10.5194/angeo-22-1875-2004>
- Ding, F., Wan, W., Liu, L., Afraimovich, E., Voeykov, S., & Perevalova, N. (2008). A statistical study of large-scale traveling ionospheric disturbances observed by GPS TEC during major magnetic storms over the years 2003–2005. *Journal of Geophysical Research*, 113(A3). <https://doi.org/10.1029/2008JA013037>
- Drexler, J., & St-Maurice, J.-P. (2005). A possible origin for large aspect angle (HAIR) echoes seen by SuperDARN radars in the E region. In *Annales Geophysicae* (Vol. 23, No. 3, pp. 767–772). <https://doi.org/10.5194/angeo-23-767-2005>
- Drob, D. P., Emmert, J. T., Meriwether, J. W., Makela, J. J., Doornbos, E., Conde, M., et al. (2015). An update to the Horizontal Wind Model (HWM): The quiet time thermosphere. *Earth and Space Science*, 2(7), 301–319. <https://doi.org/10.1002/2014EA000089>
- Farley, D., Jr. (1960). A theory of electrostatic fields in the ionosphere at nonpolar geomagnetic latitudes. *Journal of Geophysical Research*, 65(3), 869–877. <https://doi.org/10.1029/JZ065i003p00869>
- Fejer, B. G., Providakes, J., & Farley, D. T. (1984). Theory of plasma waves in the auroral E region. *Journal of Geophysical Research*, 89(A9), 7487–7494. <https://doi.org/10.1029/JA089iA09p07487>
- Fiori, R., Boteler, D., Knudsen, D., Burchill, J., Koustov, A., Cousins, E., & Blais, C. (2013). Potential impact of Swarm electric field data on global 2D convection mapping in combination with SuperDARN radar data. *Journal of Atmospheric and Solar-Terrestrial Physics*, 93, 87–99. <https://doi.org/10.1016/j.jastp.2012.11.013>
- Francis, S. H. (1974). A theory of medium-scale traveling ionospheric disturbances. *Journal of Geophysical Research*, 79(34), 5245–5260. <https://doi.org/10.1029/JA079i034p05245>
- Francis, S. H. (1975). Global propagation of atmospheric gravity waves: A review. *Journal of Atmospheric and Terrestrial Physics*, 37(6–7), 1011–1054. [https://doi.org/10.1016/0021-9169\(75\)90012-4](https://doi.org/10.1016/0021-9169(75)90012-4)
- Fritts, D. C. (1984). Gravity wave saturation in the middle atmosphere: A review of theory and observations. *Reviews of Geophysics*, 22(3), 275–308. <https://doi.org/10.1029/RG022i003p00275>
- Gillies, D. (2012). *Global-scale observations of changes in ionospheric echo occurrence and convection during periods of increased solar wind activity and increased geomagnetic activity* (Unpublished doctoral dissertation). University of Saskatchewan.
- Gondarenko, N., & Guzdar, P. (2001). Three-dimensional structuring characteristics of high-latitude plasma patches. *Journal of Geophysical Research*, 106(A11), 24611–24620. <https://doi.org/10.1029/2000JA000440>
- Goodwin, G. (1966). The dimensions of some horizontally-moving Es-region irregularities. *Planetary and Space Science*, 14(8), 759–771. [https://doi.org/10.1016/0032-0633\(66\)90105-X](https://doi.org/10.1016/0032-0633(66)90105-X)
- Greenwald, R., Baker, K., Dudeney, J., Pinnock, M., Jones, T., Thomas, E., et al. (1995). Darn/SuperDARN. *Space Science Reviews*, 71(1–4), 761–796. <https://doi.org/10.1007/BF00751350>
- Grocott, A., Hosokawa, K., Ishida, T., Lester, M., Milan, S., Freeman, M., et al. (2013). Characteristics of medium-scale traveling ionospheric disturbances observed near the Antarctic Peninsula by HF radar. *Journal of Geophysical Research: Space Physics*, 118(9), 5830–5841. <https://doi.org/10.1002/jgra.50515>
- Habarulema, J. B., Katamzi, Z. T., & Yizengaw, E. (2015). First observations of poleward large-scale traveling ionospheric disturbances over the African sector during geomagnetic storm conditions. *Journal of Geophysical Research: Space Physics*, 120(8), 6914–6929. <https://doi.org/10.1002/2015JA021066>
- Haldoupis, C., Kelley, M. C., Hussey, G. C., & Shalimov, S. (2003). Role of unstable sporadic-E layers in the generation of midlatitude spread F. *Journal of Geophysical Research*, 108(A12), 1446. <https://doi.org/10.1029/2003JA009956>
- Haldoupis, C., Schlegel, K., & Hussey, G. (2000). Auroral E-region electron density gradients measured with EISCAT. In *Annales Geophysicae* (Vol. 18, No. 9, pp. 1172–1181). <https://doi.org/10.1007/s005850000223>
- Hall, G., MacDougall, J., Moorcroft, D., St-Maurice, J.-P., Manson, A., & Meek, C. (1997). Super Dual Auroral Radar Network observations of meteor echoes. *Journal of Geophysical Research*, 102(A7), 14603–14614. <https://doi.org/10.1029/97JA00517>
- Hayashi, H., Nishitani, N., Ogawa, T., Otsuka, Y., Tsugawa, T., Hosokawa, K., & Saito, A. (2010). Large-scale traveling ionospheric disturbance observed by SuperDARN Hokkaido HF radar and GPS networks on 15 December 2006. *Journal of Geophysical Research*, 115(A6). <https://doi.org/10.1029/2009JA014297>
- He, L.-S., Dyson, P., Parkinson, M., & Wan, W. (2004). Studies of medium scale travelling ionospheric disturbances using TIGER SuperDARN radar sea echo observations. In *Annales Geophysicae* (Vol. 22, No. 12, pp. 4077–4088). <https://doi.org/10.5194/angeo-22-4077-2004>
- Hedin, A. (1988). The atmospheric model in the region 90 to 2000 km. *Advances in Space Research*, 8(5–6), 9–25. [https://doi.org/10.1016/0273-1177\(88\)90038-5](https://doi.org/10.1016/0273-1177(88)90038-5)
- Hernández-Pajares, M., Juan, J. M., & Sanz, J. (2006). Medium-scale traveling ionospheric disturbances affecting GPS measurements: Spatial and temporal analysis. *Journal of Geophysical Research*, 111(A7), A07S11. <https://doi.org/10.1029/2005JA011474>
- Hocke, K., & Schlegel, K. (1996). A review of atmospheric gravity waves and travelling ionospheric disturbances: 1982–1995. In *Annales Geophysicae* (Vol. 14, No. 9, pp. 917–940). <https://doi.org/10.1007/s00585-996-0917-6>
- Hosokawa, K., Ogawa, T., Arnold, N., Lester, M., Sato, N., & Yukimatu, A. (2005). Extraction of polar mesosphere summer echoes from SuperDARN data. *Geophysical Research Letters*, 32(12). <https://doi.org/10.1029/2005GL022788>
- Hunsucker, R. D. (1982). Atmospheric gravity waves generated in the high-latitude ionosphere: A review. *Reviews of Geophysics*, 20(2), 293–315. <https://doi.org/10.1029/RG020i002p00293>
- Hussey, G., Meek, C., André, D., Manson, A., Sofko, G., & Hall, C. (2000). A comparison of Northern Hemisphere winds using SuperDARN meteor trail and MF radar wind measurements. *Journal of Geophysical Research*, 105(D14), 18053–18066. <https://doi.org/10.1029/2000JD900272>
- Jenkins, B., & Jarvis, M. J. (1999). Mesospheric winds derived from SuperDARN HF radar meteor echoes at Halley, Antarctica. *Earth Planets and Space*, 51(7–8), 685–689. <https://doi.org/10.1186/BF03353226>
- Kagan, L. M., & Kelley, M. C. (1998). A wind-driven gradient drift mechanism for mid-latitude E-region ionospheric irregularities. *Geophysical Research Letters*, 25(22), 4141–4144. <https://doi.org/10.1029/1998GL900123>
- Kavanagh, A., Honary, F., Rietveld, M., & Senior, A. (2006). First observations of the artificial modulation of polar mesospheric winter echoes. *Geophysical Research Letters*, 33(19), L19801. <https://doi.org/10.1029/2006GL027565>

- Kelley, M. C. (2009). *The Earth's ionosphere: Plasma physics and electrodynamics*. Academic Press.
- Kelly, M. (2012). *The Earth's Ionosphere: Plasma Physics and Electrodynamics* (Vol. 43). Elsevier.
- Keskinen, M., & Ossakow, S. (1983). Theories of high-latitude ionospheric irregularities: A review. *Radio Science*, 18(06), 1077–1091. <https://doi.org/10.1029/RS018i006p01077>
- Kirkwood, S., & Von Zahn, U. (1991). On the role of auroral electric fields in the formation of low altitude sporadic-E and sudden sodium layers. *Journal of Atmospheric and Terrestrial Physics*, 53(5), 389–407. [https://doi.org/10.1016/0021-9169\(91\)90034-5](https://doi.org/10.1016/0021-9169(91)90034-5)
- Kotake, N., Otsuka, Y., Ogawa, T., Tsugawa, T., & Saito, A. (2007). Statistical study of medium-scale traveling ionospheric disturbances observed with the GPS networks in Southern California. *Earth Planets and Space*, 59(2), 95–102. <https://doi.org/10.1186/BF03352681>
- Kotzé, P. B. (2018). Hermanus magnetic observatory: A historical perspective of geomagnetism in southern Africa. *History of Geo-and Space Sciences*, 9(2), 125–131. <https://doi.org/10.5194/hgss-9-125-2018>
- Li, H.-L., Wu, J., Liu, R.-Y., & Huang, J.-Y. (2007). Study on mesosphere summer echoes observed by digital ionosonde at Zhongshan Station, Antarctica. *Earth Planets and Space*, 59(10), 1135–1139. <https://doi.org/10.1186/BF03352056>
- Liu, E., Hu, H., Hosokawa, K., Liu, R., Wu, Z., & Xing, Z. (2013). First observations of polar mesosphere summer echoes by SuperDARN Zhongshan radar. *Journal of Atmospheric and Solar-Terrestrial Physics*, 104, 39–44. <https://doi.org/10.1016/j.jastp.2013.07.011>
- Liu, Y., Hu, H., Yang, H., Zhang, B., Sun, B., Wei, F., et al. (2016). Chinese Antarctic magnetometer chain at the cusp latitude. *Advances in Polar Science*, 27(2), 102–106. <https://doi.org/10.13679/j.advps.2016.2.00102>
- Liu, Y., Zhou, C., Tang, Q., Kong, J., Gu, X., Ni, B., et al. (2019). Evidence of mid-and low-latitude nighttime ionospheric E–F coupling: Coordinated observations of sporadic E layers, F-region field-aligned irregularities, and medium-scale traveling ionospheric disturbances. *IEEE Transactions on Geoscience and Remote Sensing*, 57(10), 7547–7557. <https://doi.org/10.1109/TGRS.2019.2914059>
- Makarevich, R. A. (2014). Symmetry considerations in the two-fluid theory of the gradient drift instability in the lower ionosphere. *Journal of Geophysical Research: Space Physics*, 119(9), 7902–7913. <https://doi.org/10.1002/2014JA020292>
- Miyoshi, Y., Jin, H., Fujiwara, H., & Shinagawa, H. (2018). Numerical study of traveling ionospheric disturbances generated by an upward propagating gravity wave. *Journal of Geophysical Research: Space Physics*, 123(3), 2141–2155. <https://doi.org/10.1002/2017JA025110>
- Nishitani, N., Ogawa, T., Otsuka, Y., Hosokawa, K., & Hori, T. (2011). Propagation of large amplitude ionospheric disturbances with velocity dispersion observed by the SuperDARN Hokkaido radar after the 2011 off the Pacific coast of Tohoku Earthquake. *Earth Planets and Space*, 63(7), 891–896. <https://doi.org/10.5047/eps.2011.07.003>
- Nishitani, N., Ruohoniemi, J. M., Lester, M., Baker, J. B. H., Koustov, A. V., Shepherd, S. G., et al. (2019). Review of the accomplishments of mid-latitude Super Dual Auroral Radar Network (SuperDARN) HF radars. *Progress in Earth and Planetary Science*, 6(1), 1–57. <https://doi.org/10.1186/s40645-019-0270-5>
- Ogawa, T., Igarashi, K., Aikyo, K., & Maeno, H. (1987). NNSS satellite observations of medium-scale traveling ionospheric disturbances at southern high-latitudes. *Journal of Geomagnetism and Geoelectricity*, 39(12), 709–721. <https://doi.org/10.5636/jgg.39.709>
- Ogawa, T., Nishitani, N., Otsuka, Y., Shiokawa, K., Tsugawa, T., & Hosokawa, K. (2009). Medium-scale traveling ionospheric disturbances observed with the SuperDARN Hokkaido radar, all-sky imager, and GPS network and their relation to concurrent sporadic E irregularities. *Journal of Geophysical Research*, 114(A3). <https://doi.org/10.1029/2008JA013893>
- Ogunjobi, O., Sivakumar, V., Stephenson, E., Ann, J., & Mtumela, Z. (2017). PMSE long term observations using SuperDARN SANA HF radar measurements. *Terrestrial, Atmospheric and Oceanic Sciences*, 28(3), 371–383. <https://doi.org/10.3319/TAO.2016.09.19.01>
- Ogunjobi, O., Sivakumar, V., Stephenson, J. A. E., & Sivla, W. T. (2015). Evidence of polar mesosphere summer echoes observed by SuperDARN SANA HF radar in Antarctica. *Terrestrial, Atmospheric and Oceanic Sciences*, 26(4), 431. [https://doi.org/10.3319/TAO.2015.03.06.01\(AA\)](https://doi.org/10.3319/TAO.2015.03.06.01(AA))
- Oinats, A. V., Kurkin, V. I., & Nishitani, N. (2015). Statistical study of medium-scale traveling ionospheric disturbances using SuperDARN Hokkaido ground backscatter data for 2011. *Earth Planets and Space*, 67(1), 22. <https://doi.org/10.1186/s40623-015-0192-4>
- Otsuka, Y., Onoma, F., Shiokawa, K., Ogawa, T., Yamamoto, M., & Fukao, S. (2007). Simultaneous observations of nighttime medium-scale traveling ionospheric disturbances and E region field-aligned irregularities at midlatitude. *Journal of Geophysical Research*, 112(A6). <https://doi.org/10.1029/2005JA011548>
- Otsuka, Y., Shiokawa, K., Ogawa, T., & Wilkinson, P. (2004). Geomagnetic conjugate observations of medium-scale traveling ionospheric disturbances at midlatitude using all-sky airglow imagers. *Geophysical Research Letters*, 31(15), L15803. <https://doi.org/10.1029/2004GL020262>
- Otsuka, Y., Shiokawa, K., Ogawa, T., Yokoyama, T., & Yamamoto, M. (2009). Spatial relationship of nighttime medium-scale traveling ionospheric disturbances and F region field-aligned irregularities observed with two spaced all-sky airglow imagers and the middle and upper atmosphere radar. *Journal of Geophysical Research*, 114(A5). <https://doi.org/10.1029/2008JA013902>
- Palmroth, M., Janhunen, P., Pulkkinen, T., Aksnes, A., Lu, G., Østgaard, N., et al. (2005). Assessment of ionospheric Joule heating by GUMICS-4 MHD simulation, AMIE, and satellite-based statistics: Towards a synthesis. In *Annales Geophysicae* (Vol. 23, No. 6, pp. 2051–2068). <https://doi.org/10.5194/angeo-23-2051-2005>
- Ponomarenko, P. V., Iserhienrhen, B., & Maurice, J.-P. S. (2016). Morphology and possible origins of near-range oblique HF backscatter at high and midlatitudes. *Radio Science*, 51(6), 718–730. <https://doi.org/10.1002/2016RS006088>
- Ponomarenko, P. V., St-Maurice, J., Waters, C., Gillies, R., & Koustov, A. (2009). Refractive index effects on the scatter volume location and Doppler velocity estimates of ionospheric HF backscatter echoes. In *Annales Geophysicae* (Vol. 27, No. 11, pp. 4207–4219). <https://doi.org/10.5194/angeo-27-4207-2009>
- Ponomarenko, P. V., & Waters, C. (2006). Spectral width of SuperDARN echoes: Measurement, use and physical interpretation. In *Annales Geophysicae* (Vol. 24, No. 1, pp. 115–128). <https://doi.org/10.5194/angeo-24-115-2006>
- Ruohoniemi, J., Greenwald, R., Baker, K., Villain, J.-P., Haniuise, C., & Kelly, J. (1989). Mapping high-latitude plasma convection with coherent HF radars. *Journal of Geophysical Research*, 94(A10), 13463–13477. <https://doi.org/10.1029/JA094iA10p13463>
- Samson, J., Greenwald, R., Ruohoniemi, J., Frey, A., & Baker, K. (1990). Goose Bay radar observations of Earth-reflected, atmospheric gravity waves in the high-latitude ionosphere. *Journal of Geophysical Research*, 95(A6), 7693–7709. <https://doi.org/10.1029/JA095iA06p07693>
- Senior, A., Kosch, M., Yeoman, T. K., Rietveld, M., & McCrea, I. (2006). Effects of high-latitude atmospheric gravity wave disturbances on artificial HF radar backscatter. In *Annales Geophysicae* (Vol. 24, No. 9, pp. 2347–2361). <https://doi.org/10.5194/angeo-24-2347-2006>
- Shepherd, S., & Ruohoniemi, J. (2000). Electrostatic potential patterns in the high-latitude ionosphere constrained by SuperDARN measurements. *Journal of Geophysical Research*, 105(A10), 23005–23014. <https://doi.org/10.1029/2000JA000171>
- Sojka, J. J., Subramaniam, M., Zhu, L., & Schunk, R. (1998). Gradient drift instability growth rates from global-scale modeling of the polar ionosphere. *Radio Science*, 33(6), 1915–1928. <https://doi.org/10.1029/98RS02490>
- St.-Maurice, J.-P. (1985). A nonlocal theory of the high-latitude Farley-Buneman Instability. *Journal of Geophysical Research*, 90(A6), 5211–5225. <https://doi.org/10.1029/JA090iA06p05211>
- St.-Maurice, J.-P., & Nishitani, N. (2020). On the origin of far-aspect angle irregularity regions seen by HF radars at 100-km altitude. *Journal of Geophysical Research: Space Physics*, 125(6), e2019JA027473. <https://doi.org/10.1029/2019JA027473>

- Sun, L., Xu, J., Wang, W., Yue, X., Yuan, W., Ning, B., et al. (2015). Mesoscale field-aligned irregularity structures (FAIs) of airglow associated with medium-scale traveling ionospheric disturbances (MSTIDs). *Journal of Geophysical Research: Space Physics*, *120*(11), 9839–9858. <https://doi.org/10.1002/2014JA020944>
- Suzuki, S., Hosokawa, K., Otsuka, Y., Shiokawa, K., Ogawa, T., Nishitani, N., et al. (2009). Coordinated observations of nighttime medium-scale traveling ionospheric disturbances in 630-nm airglow and HF radar echoes at midlatitudes. *Journal of Geophysical Research*, *114*(A7). <https://doi.org/10.1029/2008JA013963>
- Tsugawa, T., Saito, A., & Otsuka, Y. (2004). A statistical study of large-scale traveling ionospheric disturbances using the GPS network in Japan. *Journal of Geophysical Research*, *109*(A6), A06302. <https://doi.org/10.1029/2003JA010302>
- Tsunoda, R. T., & Cosgrove, R. B. (2001). Coupled electrodynamics in the nighttime midlatitude ionosphere. *Geophysical Research Letters*, *28*(22), 4171–4174. <https://doi.org/10.1029/2001GL013245>
- Tsunoda, R. T., Fukao, S., & Yamamoto, M. (1994). On the origin of quasi-periodic radar backscatter from midlatitude sporadic E. *Radio Science*, *29*(01), 349–365. <https://doi.org/10.1029/93RS01511>
- Waldock, J., & Jones, T. (1986). HF Doppler observations of medium-scale travelling ionospheric disturbances at mid-latitudes. *Journal of Atmospheric and Terrestrial Physics*, *48*(3), 245–260. [https://doi.org/10.1016/0021-9169\(86\)90099-1](https://doi.org/10.1016/0021-9169(86)90099-1)
- Woodman, R., Yamamoto, M., & Fukao, S. (1991). Gravity wave modulation of gradient drift instabilities in mid-latitude sporadic E irregularities. *Geophysical Research Letters*, *18*(7), 1197–1200. <https://doi.org/10.1029/91GL01159>
- Zhou, C., Tang, Q., Huang, F., Liu, Y., Gu, X., Lei, J., et al. (2018). The simultaneous observations of nighttime ionospheric E region irregularities and F region medium-scale traveling ionospheric disturbances in midlatitude China. *Journal of Geophysical Research: Space Physics*, *123*(6), 5195–5209. <https://doi.org/10.1029/2018JA025352>

References

- Ables, S. T. and Fraser, B. J. (2005). Observing the open-closed boundary using cusp-latitude magnetometers. *Geophysical Research Letters*, 32(10), L10104. doi: <https://doi.org/10.1029/2005GL022824>.
- Allen, B. and Ottewill, A. (2000). Multi-taper spectral analysis in gravitational wave data analysis. *General Relativity and Gravitation*, 32(3), 385–398. doi: <https://doi.org/10.1023/A:1001911930363>.
- Alves, D. B. M., de Souza, E. M. and Gouveia, T. A. F. (2020). Correlation between ionospheric scintillation effects and GNSS positioning over Brazil during the last solar maximum (2012–2014). *Journal of Atmospheric and Solar-Terrestrial Physics*, 197, 105019. doi: <https://doi.org/10.1016/j.jastp.2019.03.013>.
- Appleton, E. V. and Barnett, M. A. (1925). Local reflection of wireless waves from the upper atmosphere. *Nature*, 115(2888), 333–334. doi: <https://doi.org/10.1038/115333a0>.
- Atilaw, T. Y., Stephenson, J. A. and Katamzi-Joseph, Z. T. (2021). Multitaper analysis of an MSTID event above Antarctica on 17 March 2013. *Polar Science*, 28, 100643. doi: <https://doi.org/10.1016/j.polar.2021.100643>.
- Babadi, B. and Brown, E. N. (2014). A review of multitaper spectral analysis. *IEEE Transactions on Biomedical Engineering*, 61(5), 1555–1564. doi: <https://doi.org/10.1109/TBME.2014.2311996>.
- Baron, M. (1974). Electron densities within aurorae and other auroral E-region characteristics. *Radio Science*, 9(2), 341–348. doi: <https://doi.org/10.1029/RS009i002p00341>.
- Bertotti, B. and Farinella, P. (2012). *Physics of the earth and the solar system: Dynamics and evolution, space navigation, space-time structure*. Vol. 31. Berlin: Springer.
- Bibl, K. and Reinisch, B. W. (1978). The universal digital ionosonde. *Radio Science*, 13(3), 519–530. doi: <https://doi.org/10.1029/RS013i003p00519>.
- Bilitza, D. (2001). International reference ionosphere 2000. *Radio Science*, 36(2), 261–275. doi: <https://doi.org/10.1029/2000RS002432>.
- Bilitza, D. (2003). International reference ionosphere 2000: Examples of improvements and new features. *Advances in Space Research*, 31(3), 757–767. doi: [https://doi.org/10.1016/S0273-1177\(03\)00020-6](https://doi.org/10.1016/S0273-1177(03)00020-6).
- Bilitza, D. (2016). International Reference Ionosphere - IRI (2016) with IGRF-13 coefficients. https://ccmc.gsfc.nasa.gov/modelweb/models/iri2016_vitmo.php.
- Bilitza, D., Altadill, D., Reinisch, B., Galkin, I., Shubin, V. and Truhlik, V. (2016). The international reference ionosphere: model update 2016. *EGU General Assembly Conference Abstracts*, 18, EPSC2016–9671. doi: <https://doi.org/10.1016/j.asr.2015.05.029>.
- Bilitza, D., Altadill, D., Truhlik, V., Shubin, V., Galkin, I., Reinisch, B. et al. (2017). International reference ionosphere 2016: From ionospheric climate to real-time weather predictions. *Space Weather*, 15(2), 418–429. doi: <https://doi.org/10.1002/2016SW001593>.
- Bilitza, D., McKinnell, L.-A., Reinisch, B. and Fuller-Rowell, T. (2011). The international reference ionosphere today and in the future. *Journal of Geodesy*, 85(12), 909–920. doi: <https://doi.org/10.1007/s00190-010-0427-x>.
- Bilitza, D. and Reinisch, B. W. (2008). International reference ionosphere 2007: Improvements and new parameters. *Advances in Space Research*, 42(4), 599–609. doi: <https://doi.org/10.1016/j.asr.2007.07.048>.
- Bilitza, D. et al. (1992). International reference ionosphere 1990. *Planetary and Space Science*, 40(4), 544. doi: [https://doi.org/10.1016/0032-0633\(92\)90174-M](https://doi.org/10.1016/0032-0633(92)90174-M).
- Borchevkina, O., Karpov, I. and Karpov, M. (2020). Meteorological storm influence on the ionosphere parameters. *Atmosphere*, 11(9), 1017. doi: <https://doi.org/10.3390/atmos11091017>.

- Borovsky, J. E. and Denton, M. H. (2006). Differences between CME-driven storms and CIR-driven storms. *Journal of Geophysical Research: Space Physics*, 111(A7), A07S08. doi: <https://doi.org/10.1029/2005JA011447>.
- Brasseur, G. P. and Solomon, S. (2006). *Aeronomy of the middle atmosphere: Chemistry and physics of the stratosphere and mesosphere*. Vol. 32. Berlin: Springer.
- Breedveld, M. J. (2020). Predicting the auroral oval boundaries by means of polar operational environmental satellite particle precipitation data. Master's thesis. Retrieved from (<https://munin.uit.no/bitstream/handle/10037/19283/thesis.pdf?sequence=2>).
- Brekke, A. (1979). On the relative importance of Joule heating and the Lorentz force in generating atmospheric gravity waves and infrasound waves in the auroral electrojet. *Journal of Atmospheric and Terrestrial Physics*, 41(5), 475–479. doi: [https://doi.org/10.1016/0021-9169\(79\)90072-2](https://doi.org/10.1016/0021-9169(79)90072-2).
- Bremer, J., Hoffmann, P., Manson, A., Meek, C., Rüster, R. and Singer, W. (1997). PMSE observations at three different frequencies in northern Europe during summer 1994. Vol. 14. Springer. pp. 1317–1327. doi: <https://doi.org/10.1007>
- Bristow, W. and Greenwald, R. (1997). On the spectrum of thermospheric gravity waves observed by the Super Dual Auroral Radar Network. *Journal of Geophysical Research: Space Physics*, 102(A6), 11585–11595. doi: <https://doi.org/10.1029/97JA00515>.
- Carter, B. and Makarevich, R. (2010). On the diurnal variation of the E-region coherent HF echo occurrence. *Journal of Atmospheric and Solar-Terrestrial Physics*, 72(7-8), 570–582. doi: <https://doi.org/10.1016/j.jastp.2010.02.004>.
- Chapman, S. and Bartels, J. (1940). Geomagnetism, vol. I: geomagnetic and related phenomena. *Geomagnetism*, 1. doi: <https://doi.org/10.1002/qj.49706728810>.
- Chen, C. and Scales, W. (2005). Electron temperature enhancement effects on plasma irregularities associated with charged dust in the Earth's mesosphere. *Journal of Geophysical Research: Space Physics*, 110(A12). doi: <https://doi.org/10.1029/2005ja011341>.
- Cherniak, I. and Zakharenkova, I. (2018). Large-scale traveling ionospheric disturbances origin and propagation: Case study of the December 2015 geomagnetic storm. *Space Weather*, 16(9), 1377–1395. doi: <https://doi.org/10.1029/2018SW001869>.
- Chisham, G., Lester, M., Milan, S. E., Freeman, M., Bristow, W., Grocott, A. et al. (2007). A decade of the Super Dual Auroral Radar Network (SuperDARN): Scientific achievements, new techniques and future directions. *Surveys in Geophysics*, 28(1), 33–109. doi: <https://doi.org/10.1007/s10712-007-9017-8>.
- Cho, J. Y., Kelley, M. C. and Heinselman, C. J. (1992). Enhancement of Thomson scatter by charged aerosols in the polar mesosphere: Measurements with a 1.29-ghz radar. *Geophysical Research Letters*, 19(11), 1097–1100. doi: <https://doi.org/10.1029/92GL01155>.
- Chopde, N. R. and Nichat, M. (2013). Landmark based shortest path detection by using A* and Haversine formula. *International Journal of Innovative Research in Computer and Communication Engineering*, 1(2), 298–302. doi: <https://doi.org/10.1.1.300.5943>.
- Clausen, L., Baker, J., Ruohoniemi, J., Greenwald, R., Thomas, E., Shepherd, S. et al. (2012). Large-scale observations of a subauroral polarization stream by midlatitude SuperDARN radars: Instantaneous longitudinal velocity variations. *Journal of Geophysical Research: Space Physics*, 117(A5), A05306. doi: <https://doi.org/10.1029/2011JA017232>.
- Coleman, C. (1998). A ray tracing formulation and its application to some problems in over-the-horizon radar. *Radio Science*, 33(4), 1187–1197. doi: <https://doi.org/10.1029/98RS01523>.
- Dalin, P., Kirkwood, S., Moström, A., Stebel, K., Hoffmann, P. and Singer, W. (2004). A case study of gravity waves in noctilucent clouds. *Annales Geophysicae*, 22(6), 1875–1884. doi: <https://doi.org/10.5194/angeo-22-1875-2004>.

- Davies, K. (1990). *Ionospheric radio*. number 31. IET.
- Davis, M. (1973). The integrated ionospheric response to internal atmospheric gravity waves. *Journal of Atmospheric and Terrestrial Physics*, 35(5), 929–959. doi: [https://doi.org/10.1016/0021-9169\(73\)90074-3](https://doi.org/10.1016/0021-9169(73)90074-3).
- Davis, M. and Da Rosa, A. (1969). Traveling ionospheric disturbances originating in the auroral oval during polar substorms. *Journal of Geophysical Research*, 74(24), 5721–5735. doi: <https://doi.org/10.1029/JA074i024p05721>.
- Ding, F., Wan, W., Liu, L., Afraimovich, E., Voeykov, S. and Perevalova, N. (2008). A statistical study of large-scale traveling ionospheric disturbances observed by GPS TEC during major magnetic storms over the years 2003–2005. *Journal of Geophysical Research: Space Physics*, 113(A3). doi: <https://doi.org/10.1029/2008JA013037>.
- Drexler, J. and St-Maurice, J.-P. (2005). A possible origin for large aspect angle (HAIR) echoes seen by super-DARN radars in the E region. *Annales Geophysicae*, 23(3), 767–772. doi: <https://doi.org/10.5194/angeo-23-767-2005>.
- Drob, D., Emmert, J., Crowley, G., Picone, J., Shepherd, G., Skinner, W. et al. (2008). An empirical model of the Earth's horizontal wind fields: HWM07. *Journal of Geophysical Research: Space Physics*, 113(A12), A12304. doi: <https://doi.org/10.1029/2008JA013668>.
- Drob, D. P., Emmert, J. T., Meriwether, J. W., Makela, J. J., Doornbos, E., Conde, M. et al. (2015). An update to the horizontal wind model (HWM): The quiet time thermosphere. *Earth and Space Science*, 2(7), 301–319. doi: <https://doi.org/10.1002/2014EA000089>.
- Edberg, N., Wahlund, J.-E., Ågren, K., Morooka, M. W., Modolo, R., Bertucci, C. et al. (2010). Electron density and temperature measurements in the cold plasma environment of Titan: Implications for atmospheric escape. *Geophysical Research Letters*, 37(20), L20105. doi: <https://doi.org/10.1029/2010GL044544>.
- Emmert, J., Hernandez, G., Jarvis, M., Niciejewski, R., Sipler, D. and Vennerstrom, S. (2006). Climatologies of nighttime upper thermospheric winds measured by ground-based Fabry-Perot interferometers during geomagnetically quiet conditions: 2. High-latitude circulation and interplanetary magnetic field dependence. *Journal of Geophysical Research: Space Physics*, 111(A12), A12303. doi: <https://doi.org/10.1029/2006JA011949>.
- Emmert, J., Richmond, A. and Drob, D. (2010). A computationally compact representation of magnetic-apex and quasi-dipole coordinates with smooth base vectors. *Journal of Geophysical Research: Space Physics*, 115(A8), A08322. doi: <https://doi.org/10.1029/2010JA015326>.
- Fabrizio, G. A. (2013). *High frequency over-the-horizon radar: fundamental principles, signal processing, and practical applications*. McGraw-Hill Education.
- Farley, D. (1985). Theory of equatorial electrojet plasma waves-new developments and current status. *Journal of Atmospheric and Terrestrial Physics*, 47, 729–744. doi: [https://doi.org/10.1016/0021-9169\(85\)90050-9](https://doi.org/10.1016/0021-9169(85)90050-9).
- Fejer, B. G. and Kelley, M. (1980). Ionospheric irregularities. *Reviews of Geophysics*, 18(2), 401–454. doi: <https://doi.org/10.1029/RG018i002p00401>.
- Forbes, T. (2000). A review on the genesis of coronal mass ejections. *Journal of Geophysical Research: Space Physics*, 105(A10), 23153–23165. doi: <https://doi.org/10.1029/2000JA000005>.
- Francis, F. C. (2016). *Introduction to plasma physics and controlled fusion*. New York: Plenum Press.
- Frank, L. and Ackerson, K. (1971). Observations of charged particle precipitation into the auroral zone. *Journal of Geophysical Research*, 76(16), 3612–3643. doi: <https://doi.org/10.1029/JA076i016p03612>.
- Frissell, N., Baker, J., Ruohoniemi, J., Gerrard, A., Miller, E., Marini, J., West, M. and Bristow, W. (2014). Climatology of medium-scale traveling ionospheric disturbances observed by the midlatitude Blackstone SuperDARN radar. *Journal of Geophysical Research: Space Physics*, 119(9), 7679–7697. doi: <https://doi.org/10.1002/2014JA019870>.

- Fritts, D. C. and Alexander, M. J. (2003). Gravity wave dynamics and effects in the middle atmosphere. *Reviews of Geophysics*, 41(1). doi: <https://doi.org/10.1029/2001RG000106>.
- Galkin, I. A. and Reinisch, B. W. (2008). The new ARTIST 5 for all digisondes. *Ionosonde Network Advisory Group Bulletin*, 69(8), 1–8. doi: <https://doi.org/10.1.1.510.8066>.
- Galushko, V., Paznukhov, V., Yampolski, Y. and Foster, J. (1998). Incoherent scatter radar observations of AGW/TID events generated by the moving solar terminator. *Annales Geophysicae*, 16(7), 821–827. doi: <https://doi.org/10.1007/s005850050651>.
- Garcia, R. R. and Solomon, S. (1985). The effect of breaking gravity waves on the dynamics and chemical composition of the mesosphere and lower thermosphere. *Journal of Geophysical Research: Atmospheres*, 90(D2), 3850–3868. doi: <https://doi.org/10.1029/JD090iD02p03850>.
- Gauld, J., Yeoman, T., Davies, J., Milan, S. and Honary, F. (2002). SuperDARN radar HF propagation and absorption response to the substorm expansion phase. *Annales Geophysicae*, 20, 1631–1645. doi: <https://doi.org/10.5194/angeo-20-1631-2002>.
- Gillies, D. (2012). Global-scale observations of changes in ionospheric echo occurrence and convection during periods of increased solar wind activity and increased geomagnetic activity. PhD thesis. University of Saskatchewan, Canada. Retrieved from <http://hdl.handle.net/10388/ETD-2012-04-421>.
- Gonzalez, W., Joselyn, J.-A., Kamide, Y., Kroehl, H. W., Rostoker, G., Tsurutani, B. et al. (1994). What is a geomagnetic storm?. *Journal of Geophysical Research: Space Physics*, 99(A4), 5771–5792. doi: <https://doi.org/10.1029/93JA02867>.
- Goodman, J. M. (2004). *Space weather & telecommunications*. Vol. 782. Berlin: Springer.
- Greenwald, R. (1974). Diffuse radar aurora and the gradient drift instability. *Journal of Geophysical Research*, 79(31), 4807–4810. doi: <https://doi.org/10.1029/JA079i031p04807>.
- Greenwald, R., Baker, K., Dudeney, J., Pinnock, M., Jones, T., Thomas, E. et al. (1995). DARN/SuperDARN: A global view of the dynamics of high-latitude convection. *Space Science Reviews*, 71(1-4), 761–796. doi: <https://doi.org/10.1007/BF00751350>.
- Grocott, A., Hosokawa, K., Ishida, T., Lester, M., Milan, S., Freeman, M. et al. (2013). Characteristics of medium-scale traveling ionospheric disturbances observed near the Antarctic Peninsula by HF radar. *Journal of Geophysical Research: Space Physics*, 118(9), 5830–5841. doi: <https://doi.org/10.1002/jgra.50515>.
- Gubenko, V. and Kirillovich, I. (2019). Modulation of sporadic E layers by small-scale atmospheric waves in Earth's high-latitude ionosphere. *Solar-Terrestrial Physics*, 5(3), 98–108. doi: <https://doi.org/10.12737/stp-53201912>.
- Habarulema, J. B., Katamzi, Z. T. and Yizengaw, E. (2015). First observations of poleward large-scale traveling ionospheric disturbances over the African sector during geomagnetic storm conditions. *Journal of Geophysical Research: Space Physics*, 120(8), 6914–6929. doi: <https://doi.org/10.1002/2015JA021066>.
- Haldoupis, C., Schlegel, K. and Hussey, G. (2000). Auroral E-region electron density gradients measured with EISCAT. *Annales Geophysicae*, 18(9), 1172–1181. doi: <https://doi.org/10.1007/s005850000223>.
- Hall, G., MacDougall, J., Cecile, J.-F., Moorcroft, D. and St.-Maurice, J. (1999). Finding gravity wave source positions using the Super Dual Auroral Radar Network. *Journal of Geophysical Research: Space Physics*, 104(A1), 67–78. doi: <https://doi.org/10.1029/98JA02830>.
- Hall, G., MacDougall, J., Moorcroft, D., St.-Maurice, J.-P., Manson, A. and Meek, C. (1997). Super Dual Auroral Radar Network observations of meteor echoes. *Journal of Geophysical Research: Space Physics*, 102(A7), 14603–14614. doi: <https://doi.org/10.1029/97JA00517>.
- Hamza, A. (1999). Perkins instability revisited. *Journal of Geophysical Research: Space Physics*, 104(A10), 22567–22575. doi: <https://doi.org/10.1029/1999JA900307>.

- Hamza, A. and St-Maurice, J.-P. (1993). A turbulent theoretical framework for the study of current-driven region irregularities at high latitudes: Basic derivation and application to gradient-free situations. *Journal of Geophysical Research: Space Physics*, 98(A7), 11587–11599. doi: <https://doi.org/10.1029/92JA02836>.
- Hardy, D. A., Gussenhoven, M. and Brautigam, D. (1989). A statistical model of auroral ion precipitation. *Journal of Geophysical Research: Space Physics*, 94(A1), 370–392. doi: <https://doi.org/10.1029/JA094iA01p00370>.
- Hargreaves, J. K. (1979). *The upper atmosphere and solar-terrestrial relations: - An introduction to the aerospace environment*. New York: Van Nostrand Reinhold Company.
- Hargreaves, J. K. (1995). *The solar-terrestrial environment*. Cambridge: Cambridge University Press, 1, 992.
- Hariri Naghadeh, D. and Keith Morley, C. (2017). Propagation source wavelet phase extraction using multi-taper method coherence estimation. *Journal of Geophysics and Engineering*, 14(1), 69–76. doi: <https://doi.org/10.1088/1742-2140/14/1/69>.
- Havnes, O., Aslaksen, T. and Brattli, A. (2001). Charged dust in the Earth's middle atmosphere. *Physica Scripta*, 2001(T89), 133. doi: <https://doi.org/10.1238/Physica.Topical.089a00133>.
- Havnes, O., Trøim, J., Blix, T., Mortensen, W., Næsheim, L., Thrane, E. and Tønnesen, T. (1996). First detection of charged dust particles in the Earth's mesosphere. *Journal of Geophysical Research: Space Physics*, 101(A5), 10839–10847. doi: <https://doi.org/10.1029/96JA00003>.
- Hayashi, H., Nishitani, N., Ogawa, T., Otsuka, Y., Tsugawa, T., Hosokawa, K. et al. (2010). Large-scale traveling ionospheric disturbance observed by SuperDARN Hokkaido HF radar and GPS networks on 15 december 2006. *Journal of Geophysical Research: Space Physics*, 115(A06309). doi: <https://doi.org/10.1029/2009JA014297>.
- He, L.-S., Dyson, P., Parkinson, M. and Wan, W. (2004). Studies of medium scale travelling ionospheric disturbances using TIGER SuperDARN radar sea echo observations. *Annales Geophysicae*, 22(12), 4077–4088. doi: <https://doi.org/1432-0576/ag/2004-22-4077>.
- Heale, C. J., Bossert, K., Vadas, S., Hoffmann, L., Dörnbrack, A., Stober, G. et al. (2020). Secondary gravity waves generated by breaking mountain waves over Europe. *Journal of Geophysical Research: Atmospheres*, 125(5), e2019JD031662. doi: <https://doi.org/10.1029/2019JD031662>.
- Heaton, J., Jones, G. and Kersley, L. (1996). Toward ionospheric tomography in Antarctica: First steps and comparison with dynasonde observations. *Antarctic Science*, 8(3), 297–302. doi: <https://doi.org/10.1017/S0954102096000430>.
- Hedin, A. (1983). A revised thermospheric model based on mass spectrometer and incoherent scatter data: MSIS-83. *Journal of Geophysical Research: Space Physics*, 88(A12), 10170–10188. doi: <https://doi.org/10.1029/JA088iA12p10170>.
- Hedin, A. (1988). The atmospheric model in the region 90 to 2000 km. *Advances in Space Research*, 8(5-6), 9–25. doi: [https://doi.org/10.1016/0273-1177\(88\)90038-5](https://doi.org/10.1016/0273-1177(88)90038-5).
- Hedin, A. E. (1991). Extension of the MSIS thermosphere model into the middle and lower atmosphere. *Journal of Geophysical Research: Space Physics*, 96(A2), 1159–1172. doi: <https://doi.org/10.1029/90JA02125>.
- Hedin, A., Reber, C., Newton, G., Spencer, N., Brinton, H. et al. (1977). A global thermospheric model based on mass spectrometer and incoherent scatter data MSIS, 2. Composition. *Journal of Geophysical Research*, 82(16), 2148–2156. doi: <https://doi.org/10.1029/JA082i016p02148>.
- Hedin, A., Salah, J., Evans, J., Reber, C., Newton, G. et al. (1977). A global thermospheric model based on mass spectrometer and incoherent scatter data MSIS, 1. N₂ density and temperature. *Journal of Geophysical Research*, 82(16), 2139–2147. doi: <https://doi.org/10.1029/JA082i016p02139>.
- Heinselman, C., Thayer, J. and Watkins, B. (1998). A high-latitude observation of sporadic sodium and sporadic E-layer formation. *Geophysical Research Letters*, 25(16), 3059–3062. doi: <https://doi.org/10.1029/98GL02215>.
- Heppner, J. and Maynard, N. (1987). Empirical high-latitude electric field models. *Journal of Geophysical Research: Space Physics*, 92(A5), 4467–4489. doi: <https://doi.org/10.1029/JA092iA05p04467>.

- Heppner, J. P. (1977). Empirical models of high-latitude electric fields. *Journal of Geophysical Research*, 82(7), 1115–1125. doi: <https://doi.org/10.1029/JA082i007p01115>.
- Hernandez, G., Smith, R. and Conner, J. (1992). Neutral wind and temperature in the upper mesosphere above South Pole, Antarctica. *Geophysical Research Letters*, 19(1), 53–56. doi: <https://doi.org/10.1029/91GL02957>.
- Hervig, M. E., Gordley, L. L., Russell III, J. M. and Bailey, S. M. (2009). SOFIE PMC observations during the northern summer of 2007. *Journal of Atmospheric and Solar-Terrestrial Physics*, 71(3-4), 331–339. doi: <https://doi.org/10.1016/j.jastp.2008.08.010>.
- Hervig, M. E., Rapp, M., Latteck, R. and Gordley, L. L. (2011). Observations of mesospheric ice particles from the ALWIN radar and SOFIE. *Journal of Atmospheric and Solar-Terrestrial Physics*, 73(14-15), 2176–2183. doi: <https://doi.org/10.1016/j.jastp.2010.08.002>.
- Hines, C. O. (1960). Internal atmospheric gravity waves at ionospheric heights. *Canadian Journal of Physics*, 38(11), 1441–1481. doi: <https://doi.org/10.1029/GM018p0248>.
- Hiyadutuje, A., Nsengiyumva, F. and Uwamahoro, J. (2016). Ionospheric disturbances during magnetic storms at SANAE. , pp. 1–90. Retrieved from <https://core.ac.uk/reader/145035538>.
- Hocke, K., Schlegel, K. et al. (1996). A review of atmospheric gravity waves and travelling ionospheric disturbances: 1982–1995. *Annales Geophysicae*, 14(9), 917. doi: <https://doi.org/10.1007/s00585-996-0917-6>.
- Hooke, W. H. (1970). The ionospheric response to internal gravity waves: 1. The F2 region response. *Journal of Geophysical Research*, 75(28), 5535–5544. doi: <https://doi.org/10.1029/JA075i028p05535>.
- Horvath, I. and Lovell, B. C. (2016). Polar tongue of ionization (TOI) and associated Joule heating intensification investigated during the magnetically disturbed period of 1–2 october 2001. *Journal of Geophysical Research: Space Physics*, 121(6), 5897–5913. doi: <https://doi.org/10.1002/2015JA022283>.
- Hosokawa, K., Ogawa, T., Arnold, N., Lester, M., Sato, N. and Yukimatu, A. (2005). Extraction of polar mesosphere summer echoes from SuperDARN data. *Geophysical Research Letters*, 32(12). doi: <https://doi.org/10.1029/2005GL022788>.
- Huang, C.-S., Kelley, M. and Hysell, D. (1993). Nonlinear Rayleigh-Taylor instabilities, atmospheric gravity waves and equatorial spread F. *Journal of Geophysical Research: Space Physics*, 98(A9), 15631–15642. doi: <https://doi.org/10.1029/93JA00762>.
- Huba, J., Joyce, G. and Fedder, J. (2000). Ion sound waves in the topside low latitude ionosphere. *Geophysical Research Letters*, 27(19), 3181–3184. doi: <https://doi.org/10.1029/2000GL003808>.
- Huba, J., Joyce, G., Sazykin, S., Wolf, R. and Spiro, R. (2005). Simulation study of penetration electric field effects on the low-to mid-latitude ionosphere. *Geophysical Research Letters*, 32(23). doi: <https://doi.org/10.1029/2005GL024162>.
- Hunsucker, R. D. (1982). Atmospheric gravity waves generated in the high-latitude ionosphere: A review. *Reviews of Geophysics*, 20(2), 293–315. doi: <https://doi.org/10.1029/RG020i002p00293>.
- Hussey, G., Meek, C., André, D., Manson, A., Sofko, G. and Hall, C. (2000). A comparison of Northern Hemisphere winds using SuperDARN meteor trail and MF radar wind measurements. *Journal of Geophysical Research: Atmospheres*, 105(D14), 18053–18066. doi: <https://doi.org/10.1029/2000JD900272>.
- Hutchinson, J. A., Wright, D. and Milan, S. (2011). Geomagnetic storms over the last solar cycle: A superposed epoch analysis. *Journal of Geophysical Research: Space Physics*, 116(A9). doi: <https://doi.org/10.1029/2011JA016463>.
- Idrus, I. I., Abdullah, M., Hasbi, A. M., Husin, A. and Yatim, B. (2013). Large-scale traveling ionospheric disturbances observed using GPS receivers over high-latitude and equatorial regions. *Journal of Atmospheric and Solar-Terrestrial Physics*, 102, 321–328. doi: <https://doi.org/10.1016/j.jastp.2013.06.014>.
- Imtiaz, N., Younas, W. and Khan, M. (2020). Response of the low-to mid-latitude ionosphere to the geomagnetic storm of september 2017. *Annales Geophysicae*, 38(2), 359–372. doi: <https://doi.org/10.5194/angeo-38-359-2020>.

- Innes, D., Inhester, B., Axford, W. and Wilhelm, K. (1997). Bi-directional plasma jets produced by magnetic reconnection on the Sun. *Nature*, 386(6627), 811–813. doi: <https://doi.org/10.1038/386811a0>.
- Iserhienrhien, B. (2016). On the origin of close-range E region echoes observed by SuperDARN HF radars in the mid-and high latitudes. PhD thesis. University of Saskatchewan. Saskatoon: Canada. Retrieved from (<http://hdl.handle.net/10388/ETD-2016-04-2517>).
- Ishida, T., Hosokawa, K., Shibata, T., Suzuki, S., Nishitani, N. and Ogawa, T. (2008). Superdarn observations of daytime MSTIDs in the auroral and mid-latitudes: Possibility of long-distance propagation. *Geophysical Research Letters*, 35(13). doi: <https://doi.org/10.1029/2008GL034623>.
- Jacchia, L. G. (1971). Revised static models of the thermosphere and exosphere with empirical temperature profiles. *SAO Special Report*, 332, 1–104.
- Jenkins, B. and Jarvis, M. J. (1999). Mesospheric winds derived from SuperDARN HF radar meteor echoes at Halley, Antarctica. *Earth, Planets and Space*, 51(7-8), 685–689. doi: <https://doi.org/10.1186/BF03353226>.
- Johnson, M. and Wygant, J. (2003). The correlation of plasma density distributions over 5000 km with solar illumination of the ionosphere: Solar cycle and zenith angle observations. *Geophysical Research Letters*, 30(24), 2260. doi: <https://doi.org/10.1029/2003GL018175>.
- Kagan, L. M. and Kelley, M. C. (1998). A wind-driven gradient drift mechanism for mid-latitude E-region ionospheric irregularities. *Geophysical Research Letters*, 25(22), 4141–4144. doi: <https://doi.org/10.1029/2003GL018175>.
- Kaifler, N., Baumgarten, G., Fiedler, J., Latteck, R., Lübken, F.-J. and Rapp, M. (2011). Coincident measurements of PMSE and NLC above ALOMAR (69° N, 16° E) by radar and lidar from 1999–2008. *Atmospheric Chemistry and Physics*, 11(4), 1355–1366. doi: <https://doi.org/10.5194/acp-11-1355-2011>.
- Kaifler, N., Kaifler, B., Ehard, B., Gisinger, S., Dörnbrack, A., Rapp, M. et al. (2017). Observational indications of downward-propagating gravity waves in middle atmosphere lidar data. *Journal of Atmospheric and Solar-Terrestrial Physics*, 162, 16–27. doi: <https://doi.org/10.1016/j.jastp.2017.03.003>.
- Kamide, Y. and Rostoker, G. (2004). What is the physical meaning of the AE index?. *Eos, Transactions American Geophysical Union*, 85(19), 188–192. doi: <https://doi.org/10.1029/2004EO190010>.
- Karpachev, A., Beloff, N., Carozzi, T., Denisenko, P., Karhunen, T. and Lester, M. (2010). Detection of large scale TIDs associated with the dayside cusp using SuperDARN data. *Journal of Atmospheric and Solar-Terrestrial Physics*, 72(9), 653–661. doi: <https://doi.org/10.1016/j.jastp.2010.02.018>.
- Kato, S., Tsuda, T. and Watanabe, F. (1982). Thermal excitation of non-migrating tides. *Journal of Atmospheric and Terrestrial Physics*, 44(2), 131–146. doi: [https://doi.org/10.1016/0021-9169\(82\)90116-7](https://doi.org/10.1016/0021-9169(82)90116-7).
- Kelley, M. C. (2009). *The Earth's ionosphere: plasma physics and electrodynamics*. Academic press.
- Kelley, M. C., Farley, D. T. and Röttger, J. (1987). The effect of cluster ions on anomalous VHF backscatter from the summer polar mesosphere. *Geophysical Research Letters*, 14(10), 1031–1034. doi: <https://doi.org/10.1029/GL014i010p01031>.
- Kelley, M., Riggan, D., Pfaff, R., Swartz, W., Providakes, J. and Huang, C.-S. (1995). Large amplitude quasi-periodic fluctuations associated with a mid-latitude sporadic E layer. *Journal of Atmospheric and Terrestrial Physics*, 57(10), 1165–1178. doi: [https://doi.org/10.1016/0021-9169\(94\)00130-G](https://doi.org/10.1016/0021-9169(94)00130-G).
- Keskinen, M. and Ossakow, S. (1983). Theories of high-latitude ionospheric irregularities: A review. *Radio Science*, 18(06), 1077–1091. doi: <https://doi.org/10.1029/RS018i006p01077>.
- Kirkwood, S. (2007). Polar mesosphere winter echoes—A review of recent results. *Advances in Space Research*, 40(6), 751–757. doi: <https://doi.org/10.1016/j.asr.2007.01.024>.
- Kirkwood, S. and Réchou, A. (1998). Planetary-wave modulation of PMSE. *Geophysical Research Letters*, 25(24), 4509–4512. doi: <https://doi.org/10.1029/1998GL900198>.
- Kivelson, A. (1995). *Introduction to space physics*. Cambridge: Cambridge University Press.

- Kotsarenko, N. Y., Enríquez, R. P. and Koshevaya, S. (1996). Excitation of plasma waves in the ionosphere caused by atmospheric acoustic waves. *Astrophysics and Space Science*, 246(2), 211–217. doi: <https://doi.org/10.1007/BF00645641>.
- Kotzé, P. B. (2018). Hermanus magnetic observatory: a historical perspective of geomagnetism in southern Africa. *History of Geo-and Space Sciences*, 9(2), 125–131. doi: <https://doi.org/10.5194/hgss-9-125-2018>.
- Kunduri, B., Baker, J., Ruohoniemi, J., Thomas, E., Shepherd, S. and Sterne, K. (2017). Statistical characterization of the large-scale structure of the subauroral polarization stream. *Journal of Geophysical Research: Space Physics*, 122(6), 6035–6048. doi: <https://doi.org/10.1002/2017JA024131>.
- Kunduri, B. S. R. (2013). A study of interhemispheric magnetic conjugacy and large scale magnetosphere-ionosphere coupling using SuperDARN radars. PhD thesis. Virginia Polytechnic Institute and State University. Blacksburg, VA: USA. Retrieved from <http://hdl.handle.net/10919/24772>.
- Lansangan, J. R. G. and Barrios, E. B. (2009). Principal components analysis of nonstationary time series data. *Statistics and Computing*, 19(2), 173–187. doi: <https://doi.org/10.1007/s11222-008-9082-y>.
- Laštovička, J. (2006). Forcing of the ionosphere by waves from below. *Journal of Atmospheric and Solar-Terrestrial Physics*, 68(3-5), 479–497. doi: <https://doi.org/10.1016/j.jastp.2005.01.018>.
- Latteck, R. and Strelnikova, I. (2015). Extended observations of polar mesosphere winter echoes over Andøya (69 N) using MAARSY. *Journal of Geophysical Research: Atmospheres*, 120(16), 8216–8226. doi: <https://doi.org/10.1002/2015JD023291>.
- Leake, J., DeVore, C., Thayer, J., Burns, A., Crowley, G., Gilbert, H. et al. (2014). Ionized plasma and neutral gas coupling in the Sun's chromosphere and Earth's ionosphere/thermosphere. *Space Science Reviews*, 184(1-4), 107–172. doi: <https://doi.org/10.1007>
- Li, H.-L., Wu, J., Liu, R.-Y. and Huang, J.-Y. (2007). Study on mesosphere summer echoes observed by digital ionosonde at Zhongshan station, Antarctica. *Earth, Planets and Space*, 59(10), 1135–1139.
- Li, W., Raeder, J., Thomsen, M. F. and Lavraud, B. (2008). Solar wind plasma entry into the magnetosphere under northward IMF conditions. *Journal of Geophysical Research: Space Physics*, 113(A4), 5461–5481. doi: <https://doi.org/10.1016/j.icarus.2003.08.005>.
- Lintelman, S. A. and Gardner, C. S. (1994). Observation and interpretation of spectra of atmospheric gravity wave perturbations with upward and downward phase progression. *Journal of Geophysical Research: Atmospheres*, 99(D8), 16959–16971. doi: <https://doi.org/10.1029/94JD01118>.
- Liu, A. Z. and Swenson, G. R. (2003). A modeling study of O₂ and OH airglow perturbations induced by atmospheric gravity waves. *Journal of Geophysical Research: Atmospheres*, 108(D4), 4151. doi: <https://doi.org/10.1029/2002JD002474>.
- Liu, C. and Yeh, K. (1966). Gradient instabilities as possible causes of irregularities in the ionosphere. *Radio Science*, 1(11), 1283–1291. doi: <https://doi.org/10.1002/rds19661111283>.
- Liu, E., Hu, H., Hosokawa, K., Liu, R., Wu, Z. and Xing, Z. (2013). First observations of polar mesosphere summer echoes by superDARN Zhongshan radar. *Journal of Atmospheric and Solar-Terrestrial Physics*, 104, 39–44. doi: <https://doi.org/10.1016/j.jastp.2013.07.011>.
- Liu, Y., Hu, H., Yang, H., Zhang, B., Sun, B., Wei, F. et al. (2016). Chinese Antarctic magnetometer chain at the cusp latitude. *Advances in Polar Science*, 27(02), 102–106. doi: <https://doi.org/10.13679/j.advps.2016.2.00102>.
- Liu, Y., Zhou, C., Tang, Q., Kong, J., Gu, X., Ni, B. et al. (2019). Evidence of mid-and low-latitude nighttime ionospheric *E–F* coupling: Coordinated observations of sporadic *E* layers, *F*-region field-aligned irregularities, and medium-scale traveling ionospheric disturbances. *IEEE Transactions on Geoscience and Remote Sensing*, 57(10), 7547–7557. doi: <https://doi.org/10.1109/TGRS.2019.2914059>.
- Liu, Y., Zhou, C., Xu, T., Tang, Q., Deng, Z., Chen, G. and Wang, Z. (2021). Review of ionospheric irregularities and ionospheric electrodynamic coupling in the middle latitude region. *Earth and Planetary Physics*, 5(5), 462–482. doi: <https://doi.org/10.26464/epp2021025>.

- Loewe, C. and Pröls, G. (1997). Classification and mean behavior of magnetic storms. *Journal of Geophysical Research: Space Physics*, 102(A7), 14209–14213. doi: <https://doi.org/10.1029/96JA04020>.
- Loucks, D., Palo, S., Pilinski, M., Crowley, G., Azeem, I. and Hampton, D. (2017). High-latitude GPS phase scintillation from E region electron density gradients during the 20–21 December 2015 geomagnetic storm. *Journal of Geophysical Research: Space Physics*, 122(7), 7473–7490. doi: <https://doi.org/10.1002/2016JA023839>.
- Mahlangu, D. F. (2017). Statistical study of traveling ionospheric disturbances over South Africa. Master's thesis. Rhodes University. Retrieved from <https://commons.ru.ac.za/vital/access/services/Download/vital:30556/SOURCE1>.
- Mahmoudian, A., Kosch, M. J., Vierinen, J. and Rietveld, M. T. (2020). A new technique for investigating dust charging in the PMSE source region. *Geophysical Research Letters*, 47(19), e2020GL089639. doi: <https://doi.org/10.1029/2020GL089639>.
- Mahmoudian, A., Scales, W. A., Kosch, M., Senior, A. and Rietveld, M. (2011). Dusty space plasma diagnosis using temporal behavior of polar mesospheric summer echoes during active modification. *Journal of Geophysical Research: Space Physics*, 29(11), 2169–2179. doi: <https://doi.org/10.5194/angeo-29-2169-2011>.
- Makarevich, R. A. (2016). Toward an integrated view of ionospheric plasma instabilities: Altitudinal transitions and strong gradient case. *Journal of Geophysical Research: Space Physics*, 121(4), 3634–3647. doi: <https://doi.org/10.1002/2016JA022515>.
- Makarevich, R. A., Crowley, G., Azeem, I., Ngwira, C. and Forsythe, V. (2021). Auroral E-region as a source region for ionospheric scintillation. *Journal of Geophysical Research: Space Physics*, 126(5), e2021JA029212. doi: <https://doi.org/10.1029/2021JA029212>.
- Manchester IV, W. B., Gombosi, T. I., Roussev, I., Ridley, A., De Zeeuw, D. L., Sokolov, I., Powell, K. G. and Tóth, G. (2004). Modeling a space weather event from the sun to the Earth: CME generation and interplanetary propagation. *Journal of Geophysical Research: Space Physics*, 109(A2), A02107. doi: <https://doi.org/10.1029/2003JA010150>.
- Marov, M. Y. (2020). Radiation and space flights safety: An insight. *Acta Astronautica*, 176, 580–590. doi: <https://doi.org/10.1016/j.actaastro.2020.03.022>.
- Martinis, C., Baumgardner, J., Mendillo, M., Wroten, J., MacDonald, T., Kosch, M. et al. (2019). First conjugate observations of medium-scale traveling ionospheric disturbances (MSTIDs) in the Europe-Africa longitude sector. *Journal of Geophysical Research: Space Physics*, 124(3), 2213–2222. doi: <https://doi.org/10.1029/2018JA026018>.
- Matzka, J., Stolle, C., Yamazaki, Y., Bronkalla, O. and Morschhauser, A. (2021). The geomagnetic Kp index and derived indices of geomagnetic activity. *Space Weather*, 19(5), e2020SW002641. doi: <https://doi.org/10.1029/2020SW002641>.
- Mayr, H. and Harris, I. (1977). Diurnal variations in the thermosphere, 2. Temperature, composition, and winds. *Journal of Geophysical Research*, 82(19), 2628–2640. doi: <https://doi.org/10.1029/JA082i019p02628>.
- Mayr, H., Mengel, J., Talaat, E., Porter, H. and Chan, K. (2005). Mesospheric non-migrating tides generated with planetary waves: I. Characteristics. *Journal of Atmospheric and Solar-Terrestrial Physics*, 67(11), 959–980. doi: <https://doi.org/10.1016/j.jastp.2005.03.002>.
- McNamara, L. F. (1991). *The ionosphere: communications, surveillance, and direction finding*. Krieger.
- Mellors, R. J., Vernon, F. L. and Thomson, D. J. (1998). Detection of dispersive signals using multitaper dual-frequency coherence. *Geophysical Journal International*, 135(1), 146–154. doi: <https://doi.org/10.1046/j.1365-246X.1998.00614.x>.
- Milan, S. E. and Lester, M. (2001). A classification of spectral populations observed in HF radar backscatter from the E region auroral electrojets. *Annales Geophysicae*, 19(2), 189–204. doi: <https://doi.org/10.5194/angeo-19-189-2001>.

- Milan, S., Lester, M., Yeoman, T., Robinson, T., Uspensky, M. and Villain, J.-P. (2004). HF radar observations of high-aspect angle backscatter from the E-region. *Annales Geophysicae*, 22(3), 829–847. doi: <https://doi.org/10.5194/angeo-22-829-2004>.
- Milan, S., Yeoman, T., Lester, M., Thomas, E. and Jones, T. (1997). Initial backscatter occurrence statistics from the CUTLASS HF radars. *Annales Geophysicae*, 15(6), 703–718. doi: <https://doi.org/10.1007/s00585-997-0703-0>.
- Miller, C. A., Swartz, W., Kelley, M., Mendillo, M., Nottingham, D., Scali, J. and Reinisch, B. (1997). Electrodynamics of midlatitude spread F: 1. Observations of unstable, gravity wave-induced ionospheric electric fields at tropical latitudes. *Journal of Geophysical Research: Space Physics*, 102(A6), 11521–11532. doi: <https://doi.org/10.1029/96JA03839>.
- Mills, M. J., Toon, O. B. and Thomas, G. E. (2005). Mesospheric sulfate aerosol layer. *Journal of Geophysical Research: Atmospheres*, 110(D24). doi: <https://doi.org/10.1029/2005JD006242>.
- Miyoshi, Y., Jin, H., Fujiwara, H. and Shinagawa, H. (2018). Numerical study of traveling ionospheric disturbances generated by an upward propagating gravity wave. *Journal of Geophysical Research: Space Physics*, 123(3), 2141–2155. doi: <https://doi.org/10.1002/2017JA025110>.
- Miyoshi, Y., Pancheva, D., Mukhtarov, P., Jin, H., Fujiwara, H. and Shinagawa, H. (2017). Excitation mechanism of non-migrating tides. *Journal of Atmospheric and Solar-Terrestrial Physics*, 156, 24–36. doi: <https://doi.org/10.1016/j.jastp.2017.02.012>.
- Moldwin, M. (2008). *An introduction to space weather*. Vol. 1. Cambridge: Cambridge University Press.
- Nakamura, M., Yoneda, A., Oda, M. and Tsubouchi, K. (2015). Statistical analysis of extreme auroral electrojet indices. *Earth, Planets and Space*, 67(1), 1–8. doi: <https://doi.org/10.1186/s40623-015-0321-0>.
- Nishitani, N., Ruohoniemi, J. M., Lester, M., Baker, J. B. H., Koustov, A. V., Shepherd, S. G. et al. (2019). Review of the accomplishments of mid-latitude Super Dual Auroral Radar Network (SuperDARN) HF radars. *Progress in Earth and Planetary Science*, 6(1), 1–57. doi: <https://doi.org/10.1186/s40645-019-0270-5>.
- Norman, R. J., Bennett, J. A., Dyson, P. L., Le Marshall, J. and Zhang, K. (2013). A ray-tracing technique for determining ray tubes in anisotropic media. *IEEE Transactions on Antennas and Propagation*, 61(5), 2664–2675. doi: <https://doi.org/10.1109/TAP.2013.2240647>.
- Occhipinti, G., Kherani, E. A. and Lognonné, P. (2008). Geomagnetic dependence of ionospheric disturbances induced by tsunamigenic internal gravity waves. *Geophysical Journal International*, 173(3), 753–765. doi: <https://doi.org/10.1111/j.1365-246X.2008.03760.x>.
- Ogawa, T., Arnold, N. F., Kirkwood, S., Nishitani, N. and Lester, M. (2003). Finland HF and Esrange MST radar observations of polar mesosphere summer echoes. *Annales Geophysicae*, 21(4), 1047–1055. doi: <https://doi.org/10.5194/angeo-21-1047-2003>.
- Ogawa, T., Igarashi, K., Aikyo, K. and Maeno, H. (1987). NNSS satellite observations of medium-scale traveling ionospheric disturbances at southern high-latitudes. *Journal of Geomagnetism and Geoelectricity*, 39(12), 709–721. doi: <https://doi.org/10.5636/jgg.39.709>.
- Ogawa, T., Nishitani, N., Otsuka, Y., Shiokawa, K., Tsugawa, T. and Hosokawa, K. (2009). Medium-scale traveling ionospheric disturbances observed with the SuperDARN Hokkaido radar, all-sky imager, and GPS network and their relation to concurrent sporadic E irregularities. *Journal of Geophysical Research: Space Physics*, 114(A3), A03316. doi: <https://doi.org/10.1029/2008JA013893>.
- Ogawa, T., Nishitani, N., Sato, N., Yamagishi, H. and Yukimatu, A. S. (2002). Upper mesosphere summer echoes detected with the Antarctic Syowa HF radar. *Geophysical research letters*, 29(7), 61–1. doi: <https://doi.org/10.1029/2001GL014094>.
- Ogunjobi, O., Sivakumar, V., Stephenson, E., Ann, J. and Mtumela, Z. (2017). PMSE long term observations using SuperDARN SANAE HF radar measurements.. *Terrestrial, Atmospheric and Oceanic Sciences*, 28(3), 378–383. doi: <https://doi.org/10.3319/TAO.2016.09.19.01>.

- Ogunjobi, O., Sivakumar, V., Stephenson, J. A. E. and Sivla, W. T. (2015). Evidence of polar mesosphere summer echoes observed by SuperDARN SANA HF Radar in Antarctica. *Terrestrial, Atmospheric & Oceanic Sciences*, 26(4), 431–440. doi: [https://doi.org/10.3319/TAO.2015.03.06.01\(AA\)](https://doi.org/10.3319/TAO.2015.03.06.01(AA)).
- Ogwala, A., Somoye, E. O., Panda, S. K., Ogunmodimu, O., Onori, E., Sharma, S. K. et al. (2020). Total electron content at equatorial and low-, middle-and high-latitudes in African longitude sector and its comparison with IRI-2016 and IRI-PLAS 2017 models. *Advances in Space Research*, 68(5), 2160–2176. doi: <https://doi.org/10.1016/j.asr.2020.07.013>.
- Oinats, A. V., Kurkin, V. I. and Nishitani, N. (2015). Statistical study of medium-scale traveling ionospheric disturbances using SuperDARN Hokkaido ground backscatter data for 2011. *Earth, Planets and Space*, 67(1), 22. doi: <https://doi.org/10.1186/s40623-015-0192-4>.
- Oinats, A. V., Nishitani, N., Ponomarenko, P., Berngardt, O. I. and Ratovsky, K. G. (2016). Statistical characteristics of medium scale traveling ionospheric disturbances revealed from the Hokkaido East and Ekaterinburg HF radar data. *Earth, Planets and Space*, 68(1), 1–13. doi: <https://doi.org/10.1186/s40623-016-0390-8>.
- Olson, W. P. and Pfitzer, K. A. (1974). A quantitative model of the magnetospheric magnetic field. *Journal of Geophysical Research*, 79(25), 3739–3748. doi: <https://doi.org/10.1029/JA079i025p03739>.
- Oppenheim, M., Otani, N. and Ronchi, C. (1996). Saturation of the Farley-Buneman instability via nonlinear electron $\mathbf{e} \times \mathbf{b}$ drifts. *Journal of Geophysical Research: Space Physics*, 101(A8), 17273–17286. doi: <https://doi.org/10.1029/96JA01403>.
- Otsuka, Y., Onoma, F., Shiokawa, K., Ogawa, T., Yamamoto, M. and Fukao, S. (2007). Simultaneous observations of nighttime medium-scale traveling ionospheric disturbances and E region field-aligned irregularities at midlatitude. *Journal of Geophysical Research: Space Physics*, 112(A6), A06317. doi: <https://doi.org/10.1029/2005JA011548>.
- Otsuka, Y., Shiokawa, K., Ogawa, T. and Wilkinson, P. (2004). Geomagnetic conjugate observations of medium-scale traveling ionospheric disturbances at midlatitude using all-sky airglow imagers. *Geophysical Research Letters*, 31(15), L15803. doi: <https://doi.org/10.1029/2004GL020262>.
- Otsuka, Y., Suzuki, K., Nakagawa, S., Nishioka, M., Shiokawa, K. and Tsugawa, a. (2013). GPS observations of medium-scale traveling ionospheric disturbances over Europe. *Annales Geophysicae*, 31(2), 163–172. doi: <https://doi.org/10.5194/angeo-31-163-2013>.
- Palmroth, M., Janhunen, P., Pulkkinen, T., Aksnes, A., Lu, G., Østgaard, N. et al. (2005). Assessment of ionospheric Joule heating by GUMICS-4 MHD simulation, AMIE, and satellite-based statistics: towards a synthesis. *Annales Geophysicae*, 23(6), 2051–2068. doi: <https://doi.org/10.5194/angeo-23-2051-2005>.
- Pashin, A., Belova, E. and Lyatsky, W. (1995). Magnetic pulsation generation by a powerful ground-based modulated HF radio transmitter. *Journal of Atmospheric and Terrestrial Physics*, 57(3), 245–252. doi: [https://doi.org/10.1016/0021-9169\(95\)00045-3](https://doi.org/10.1016/0021-9169(95)00045-3).
- Penney, R. and Jackson-Booth, N. (2015). Mitigating satellite motion in GPS monitoring of traveling ionospheric disturbances. *Radio Science*, 50(11), 1150–1164. doi: <https://doi.org/10.1002/2015RS005767>.
- Perkins, F. (1973). Spread F and ionospheric currents. *Journal of Geophysical Research*, 78(1), 218–226. doi: <https://doi.org/10.1029/JA078i001p00218>.
- Pezzopane, M., Scotto, C., Tomasik, L. and Krasheninnikov, I. (2010). Autoscala: an aid for different ionosondes. *Acta Geophysica*, 58(3), 513–526. doi: <https://doi.org/10.2478/s11600-009-0038-1>.
- Picone, J., Hedin, A., Drob, D. P. and Aikin, A. (2002). NRLMSISE-00 empirical model of the atmosphere: Statistical comparisons and scientific issues. *Journal of Geophysical Research: Space Physics*, 107(A12), SIA 15–1–SIA 15–16. doi: <https://doi.org/10.1029/2002JA009430>.
- Ponomarenko, P., Maurice, J.-P. S. and McWilliams, K. (2018). Calibrating HF radar elevation angle measurements using E layer backscatter echoes. *Radio Science*, 53(11), 1438–1449. doi: <https://doi.org/10.1029/2018RS006638>.

- Ponomarenko, P., St-Maurice, J., Waters, C., Gillies, R. and Koustov, A. (2009). Refractive index effects on the scatter volume location and Doppler velocity estimates of ionospheric HF backscatter echoes. *Annales Geophysicae: Atmospheres, Hydrospheres and Space Sciences*, 27(11), 4207. doi: <https://doi.org/10.5194/angeo-27-4207-2009>.
- Ponomarenko, P. V., Iserhienrhien, B. and Maurice, J.-P. S. (2016). Morphology and possible origins of near-range oblique HF backscatter at high and midlatitudes. *Radio Science*, 51(6), 718–730. doi: <https://doi.org/10.1002/2016RS006088>.
- Ponomarenko, P. and Waters, C. (2006). Spectral width of SuperDARN echoes: measurement, use and physical interpretation. *Annales Geophysicae*, 24, 115–128. doi: <https://doi.org/10.5194/angeo-24-115-2006>.
- Porter, H. and Tuan, T. (1974). On the behavior of the F-layer under the influence of gravity waves. *Journal of Atmospheric and Terrestrial Physics*, 36(1), 135–157. doi: [https://doi.org/10.1016/0021-9169\(74\)90072-5](https://doi.org/10.1016/0021-9169(74)90072-5).
- Rapp, M. and Lübken, F.-J. (2004). Polar mesosphere summer echoes (PMSE): Review of observations and current understanding. *Atmospheric Chemistry and Physics*, 4(11/12), 2601–2633. doi: <https://doi.org/10.5194/acp-4-2601-2004>.
- Rapp, M. and Thomas, G. E. (2006). Modeling the microphysics of mesospheric ice particles: Assessment of current capabilities and basic sensitivities. *Journal of Atmospheric and Solar-Terrestrial Physics*, 68(7), 715–744. doi: <https://doi.org/10.1016/j.jastp.2005.10.015>.
- Rauf, A., Li, H., Ullah, S., Meng, L., Wang, B. and Wang, M. (2019). Investigation of PMSE dependence on high energy particle precipitation during their simultaneous occurrence. *Advances in Space Research*, 63(1), 309–316. doi: <https://doi.org/10.1016/j.asr.2018.09.007>.
- Rawer, K., Bilitza, D. and Ramakrishnan, S. (1978). Goals and status of the international reference ionosphere. *Reviews of Geophysics*, 16(2), 177–181. doi: <https://doi.org/10.1029/RG016i002p00177>.
- Ribeiro, A., Ruohoniemi, J. M., Ponomarenko, P., N. Clausen, L., H. Baker, J., Greenwald, R. et al. (2013). A comparison of SuperDARN ACF fitting methods. *Radio Science*, 48(3), 274–282. doi: <https://doi.org/10.1002/rds.20031>.
- Richmond, A., Ridley, E. and Roble, R. (1992). A thermosphere/ionosphere general circulation model with coupled electrodynamics. *Geophysical Research Letters*, 19(6), 601–604. doi: <https://doi.org/10.1029/92GL00401>.
- Riley, P. and Love, J. J. (2017). Extreme geomagnetic storms: Probabilistic forecasts and their uncertainties. *Space Weather*, 15(1), 53–64. doi: <https://doi.org/10.1002/2016SW001470>.
- Robinson, R. and Vondrak, R. (1984). Measurements of E region ionization and conductivity produced by solar illumination at high latitudes. *Journal of Geophysical Research: Space Physics*, 89(A6), 3951–3956. doi: <https://doi.org/10.1029/JA089iA06p03951>.
- Rodger, A. S., Morrell, C. and Dudeney, J. (1983). Studies of sporadic E (Es) associated with the main ionospheric trough. *Radio Science*, 18(06), 937–946. doi: <https://doi.org/10.1029/RS018i006p00937>.
- Röttger, J. (1981). Equatorial spread-F by electric fields and atmospheric gravity waves generated by thunderstorms. *Journal of Atmospheric and Terrestrial Physics*, 43(5-6), 453–462. doi: [https://doi.org/10.1016/0021-9169\(81\)90108-2](https://doi.org/10.1016/0021-9169(81)90108-2).
- Röttger, J., La Hoz, C., Kelley, M. C., Hoppe, U.-P. and Hall, C. (1988). The structure and dynamics of polar mesosphere summer echoes observed with the EISCAT 224 MHz radar. *Geophysical Research Letters*, 15(12), 1353–1356. doi: <https://doi.org/10.1029/GL015i012p01353>.
- Routledge, G. J. (2011). Polar mesospheric summer echoes studied by active radio wave experiments. PhD thesis. Lancaster University. Lancaster: United Kingdom. Retrieved from <https://ethos.bl.uk/OrderDetails.do?uin=uk.bl.ethos.578270>.
- Ruohoniemi, J. and Greenwald, R. (1996). Statistical patterns of high-latitude convection obtained from Goose Bay HF radar observations. *Journal of Geophysical Research: Space Physics*, 101(A10), 21743–21763. doi: <https://doi.org/10.1029/96JA01584>.

- Russell, C., Chi, P., Dearborn, D., Ge, Y., Kuo-Tiong, B., Means, J. et al. (2008). THEMIS ground-based magnetometers. *Space Science Reviews*, 141(1), 389–412. doi: <https://doi.org/10.1007/s11214-008-9337-0>.
- Rüster, R. and Schlegel, K. (1999). Non-magnetic aspect sensitive auroral echoes from the lower E region observed at 50 MHz. *Annales Geophysicae*, 17(10), 1284–1292. doi: <https://doi.org/10.1007/s00585-999-1284-x>.
- Samson, J., Greenwald, R., Ruohoniemi, J., Frey, A. and Baker, K. (1990). Goose Bay radar observations of Earth-reflected, atmospheric gravity waves in the high-latitude ionosphere. *Journal of Geophysical Research: Space Physics*, 95(A6), 7693–7709. doi: <https://doi.org/10.1029/JA095iA06p07693>.
- Sato, T. (1973). Unified theory of type I and II irregularities in the equatorial electrojet. *Journal of Geophysical Research*, 78(13), 2232–2243. doi: <https://doi.org/10.1029/JA088iA06p04853>.
- Sato, T. (1989). Radar principles: In S. Fukao (ed.), Middle Atmosphere Program: handbook for MAP. *Urbana*, 30, 19–53.
- Schindler, K. (2006). *Physics of space plasma activity*. Cambridge: Cambridge University Press.
- Schmidt, M. J. and Gary, S. P. (1973). Density gradients and the Farley-Buneman instability. *Journal of Geophysical Research*, 78(34), 8261–8265. doi: <https://doi.org/10.1029/JA078i034p08261>.
- Schunk, R. and Nagy, A. (2000, 2009). *Ionospheres: Physics, Plasma physics, and Chemistry*. Cambridge: Cambridge University Press.
- Sen, H. and Wyller, A. (1960). On the generalization of the Appleton-Hartree magnetoionic formulas. *Journal of Geophysical Research*, 65(12), 3931–3950. doi: <https://doi.org/10.1029/JZ065i012p03931>.
- Senior, A., Kosch, M., Yeoman, T. K., Rietveld, M. and McCrea, I. (2006). Effects of high-latitude atmospheric gravity wave disturbances on artificial HF radar backscatter. *Annales Geophysicae*, 24(9), 2347–2361. doi: <https://doi.org/10.5194/angeo-24-2347-2006>.
- Shepherd, S. (2010). A dynamical model of high-latitude convection derived from SuperDARN plasma drift measurements. *Journal of Geophysical Research: Space Physics*, 115(A12), A12329. doi: <https://doi.org/10.1029/2010JA016017>.
- Shepherd, S. (2014). Altitude-adjusted corrected geomagnetic coordinates: Definition and functional approximations. *Journal of Geophysical Research: Space Physics*, 119(9), 7501–7521. doi: <https://doi.org/10.1002/2014JA020264>.
- Shiokawa, K., Otsuka, Y., Nishitani, N., Ogawa, T., Tsugawa, T., Maruyama, T. et al. (2008). North-eastward motion of nighttime medium-scale traveling ionospheric disturbances at middle latitudes observed by an airglow imager. *Journal of Geophysical Research: Space Physics*, 113(A12). doi: <https://doi.org/10.1029/2008JA013417>.
- Smith, A. K. (2000). Structure of the terdiurnal tide at 95 km. *Geophysical Research Letters*, 27(2), 177–180. doi: <https://doi.org/10.1029/1999GL010843>.
- Sojka, J. J., Subramaniam, M., Zhu, L. and Schunk, R. (1998). Gradient drift instability growth rates from global-scale modeling of the polar ionosphere. *Radio Science*, 33(6), 1915–1928. doi: <https://doi.org/10.1029/98RS02490>.
- Søråas, F., Sandanger, M. I. and Smith-Johnsen, C. (2018). NOAA POES and MetOp particle observations during the 17 March 2013 storm. *Journal of Atmospheric and Solar-Terrestrial Physics*, 177, 115–124. doi: <https://doi.org/10.1016/j.jastp.2017.09.004>.
- St.-Maurice, J.-P. and Nishitani, N. (2020). On the origin of far-aspect angle irregularity regions seen by HF radars at 100-km altitude. *Journal of Geophysical Research: Space Physics*, 125(6), e2019JA027473. doi: <https://doi.org/10.1029/2019JA027473>.
- Stefanello, M., Muella, M., Amorim, D., Machado, C., Bageston, J., Pimenta et al. (2015). OI 630.0 nm all-sky image observations of medium-scale traveling ionospheric disturbances at geomagnetic conjugate points. *Journal of Atmospheric and Solar-Terrestrial Physics*, 128, 58–69. doi: <https://doi.org/10.1016/j.jastp.2015.03.012>.

- Strangeway, R., Ergun, R., Su, Y.-J., Carlson, C. and Elphic, R. (2005). Factors controlling ionospheric outflows as observed at intermediate altitudes. *Journal of Geophysical Research: Space Physics*, 110(A3), A03221. doi: <https://doi.org/10.1029/2004JA010829>.
- Subramaniam, M. (1997). A study of the gradient drift instability in the high-latitude ionosphere using the Utah State University time dependent ionospheric model. Master's thesis. Utah State University. Logan, UT: Canada. Retrieved from <https://digitalcommons.usu.edu/cgi/viewcontent.cgi?article=5931&context=etd>.
- Sun, L., Xu, J., Wang, W., Yue, X., Yuan, W., Ning, B. et al. (2015). Mesoscale field-aligned irregularity structures (FAIs) of airglow associated with medium-scale traveling ionospheric disturbances (MSTIDs). *Journal of Geophysical Research: Space Physics*, 120(11), 9839–9858. doi: <https://doi.org/10.1002/2014JA020944>.
- Suzuki, S., Hosokawa, K., Otsuka, Y., Shiokawa, K., Ogawa, T., Nishitani, N. et al. (2009). Coordinated observations of nighttime medium-scale traveling ionospheric disturbances in 630-nm airglow and HF radar echoes at midlatitudes. *Journal of Geophysical Research: Space Physics*, 114(A7). doi: <https://doi.org/10.1029/2008JA013963>.
- Treumann, R. A. and Baumjohann, W. (1997). *Advanced space plasma physics*. Vol. 30. Imperial College Press London.
- Tsugawa, T., Saito, A. and Otsuka, Y. (2004). A statistical study of large-scale traveling ionospheric disturbances using the GPS network in Japan. *Journal of Geophysical Research: Space Physics*, 109(A6). doi: <https://doi.org/10.1029/2003JA010302>.
- Tsunoda, R. T., Fukao, S. and Yamamoto, M. (1994). On the origin of quasi-periodic radar backscatter from midlatitude sporadic E. *Radio Science*, 29(01), 349–365. doi: <https://doi.org/10.1029/93RS01511>.
- Vadas, S. L. (2007). Horizontal and vertical propagation and dissipation of gravity waves in the thermosphere from lower atmospheric and thermospheric sources. *Journal of Geophysical Research: Space Physics*, 112(A6). doi: <https://doi.org/10.1029/2006JA011845>.
- Varney, R. H., Kelley, M. C., Nicolls, M. J., Heinselman, C. J. and Collins, R. L. (2011). The electron density dependence of polar mesospheric summer echoes. *Journal of Atmospheric and Solar-Terrestrial Physics*, 73(14–15), 2153–2165. doi: <https://doi.org/10.1016/j.jastp.2010.07.020>.
- Vlasov, A., Kauristie, K., Van de Kamp, M., Luntama, J.-P. and Pogoreltsev, A. (2011). A study of traveling ionospheric disturbances and atmospheric gravity waves using EISCAT Svalbard Radar IPY-data. *Annales Geophysicae*, 29(11), 2101–2116. doi: <https://doi.org/10.5194/angeo-29-2101-2011>.
- Waldock, J. and Jones, T. (1986). HF Doppler observations of medium-scale travelling ionospheric disturbances at mid-latitudes. *Journal of atmospheric and terrestrial physics*, 48(3), 245–260. doi: [https://doi.org/10.1016/0021-9169\(86\)90099-1](https://doi.org/10.1016/0021-9169(86)90099-1).
- Ware, J. H., Mosteller, F., Delgado, F., Donnelly, C. and Ingelfinger, J. A. (2019). P values. Vol. 2. CRC Press. pp. 181–200. doi: <https://doi.org/10.1201/9780429187445-10>.
- Wilks, D. S. (2011). *Statistical methods in the atmospheric sciences*. Vol. 100. Academic press.
- Wilson, P. (1968). The structure of a sunspot. *Solar Physics*, 3(2), 243–257. doi: <https://doi.org/10.1007/bf00146994>.
- Witvliet, B. A., Van Maanen, E., Petersen, G. J., Westenberg, A. J., Bentum, M. J., Slump, C. H. and Schiphorst, R. (2015). Near vertical incidence skywave propagation: Elevation angles and optimum antenna height for horizontal dipole antennas. *IEEE Antennas and Propagation Magazine*, 57(1), 129–146.
- Woodman, R., Yamamoto, M. and Fukao, S. (1991). Gravity wave modulation of gradient drift instabilities in mid-latitude sporadic E irregularities. *Geophysical Research Letters*, 18(7), 1197–1200. doi: <https://doi.org/10.1029/91GL01159>.
- Xie, H., Ofman, L. and Lawrence, G. (2004). Cone model for halo CMEs: Application to space weather forecasting. *Journal of Geophysical Research: Space Physics*, 109(A3), A03109. doi: <https://doi.org/10.1029/2003JA010226>.

- Yeoman, T. K., Chisham, G., Baddeley, L., Dhillon, R., Karhunen, T. et al. (2008). Mapping ionospheric backscatter measured by the SuperDARN HF radars—Part 2: assessing SuperDARN virtual height models. *Annales Geophysicae*, 26(4), 843–852. doi: <https://doi.org/10.5194/angeo-26-823-2008>.
- Zawdie, K. A., Drob, D. P., Siskind, D. E. and Coker, C. (2017). Calculating the absorption of HF radio waves in the ionosphere. *Radio Science*, 52(6), 767–783. doi: <https://doi.org/10.1002/2017RS006256>.
- Zhang, B.-C. et al. (2015). Diurnal variation of winter F region ionosphere for solar minimum at both Zhongshan station, Antarctica, and Svalbard station, Arctic. *Journal of Geophysical Research: Space Physics*, 120(11), 9929–9942. doi: <https://doi.org/10.1002/2015JA021465>.
- Zhang, B., Lotko, W., Brambles, O., Wiltberger, M., Wang, W., Schmitt, P. et al. (2012). Enhancement of thermospheric mass density by soft electron precipitation. *Geophysical Research Letters*, 39(20), 20102. doi: <https://doi.org/10.1029/2012GL053519>.
- Zhang, Y., Wu, J., Guo, L., Hu, Y., Zhao, H. and Xu, T. (2015). Influence of solar and geomagnetic activity on sporadic-E layer over low, mid and high latitude stations. *Advances in Space Research*, 55(5), 1366–1371. doi: <https://doi.org/10.1016/j.asr.2014.12.010>.
- Zolesi, B. and Ljiljana R, C. (2014). *Ionospheric Prediction and Forecasting*. Vol. 31. Berlin: Springer.
- Zou, K. H., Tuncali, K. and Silverman, S. G. (2003). Correlation and simple linear regression. *Radiology*, 227(3), 617–628. doi: <https://doi.org/10.1148/radiol.2273011499>.